Rita Glenne

Preparation and Transport Properties of $SrFeO_3$ Based Materials with Controlled Microstructure

NTNU Trondheim
Norges teknisk-naturvitenskapelige universitet

Doktor ingeniøravhandling 2001:6
Institutt for kjemi

IUK-thesis:100

This thesis has been submitted

to

Institutt for kjemi
Norges teknisk-naturvitenskapelige universitet

in partial fulfilment of the requirements for
the Norwegian academic degree

DOKTOR INGENIØR

February 2001

ACKNOWLEDGEMENTS

This work was carried out at Norsk Hydro Research Centre, Porsgrunn in the period 1997-2001.

I wish to express my gratitude to Professor Dr. Techn. Stein Julsrud for his supervision of the present work. His fundamental knowledge, experience and interest in solid state chemistry have been invaluable throughout these years.

During the period of research I have benefited from many discussions with my colleagues at Norsk Hydro. I am particularly grateful for many good advice and stimulating conversations with Dr. Ing. Bent E. Vigeland. The experimentally study would not have been possible without the support from Norsk Hydro. The support from the Section for Material Development, Research Centre and Section Manager Erik Hans Eriksen is gratefully acknowledged.

The Research Council of Norway has funded the present work and is gratefully acknowledged.

Finally, I want to thank Hilde Kari Nylund and Heidi Berg for the kindness of helping me when I struggled with "unsolvable" equations, software problems, the English language or just to be clear-sighted. I also want to thank Elin Aksnes for her continued support and sensible advice.

CONTENTS

SUMMARY

This work consists of mainly two parts. The first part deals with the sintering behaviour and the microstructural stability of $SrFe_{1-x}Cr_xO_{3-\delta}$, and the second with transport properties of membranes of the same compositions. The most important experimental tools have been dilatometry and oxygen permeability measurements. Supplementary tools were x-ray diffraction analysis (XRD), scanning electron microscope (SEM) and particle size distribution analysis.

The first part describes the demanding and time-consuming work of making dense membranes with controlled microstructure. The aim was to obtain a density near to 100 % of theoretical, and with a negligible variation in density between the different membranes. In addition, we made demand on the final microstructure without changing the chemistry.

The most remarkable observation while struggling with sintering dense membranes was a total expansion of the samples after having first attained a relatively high density. The sintering behaviour of $SrFeO_{3-\delta}$ exhibiting comprehensive swelling is given in Figure 1.

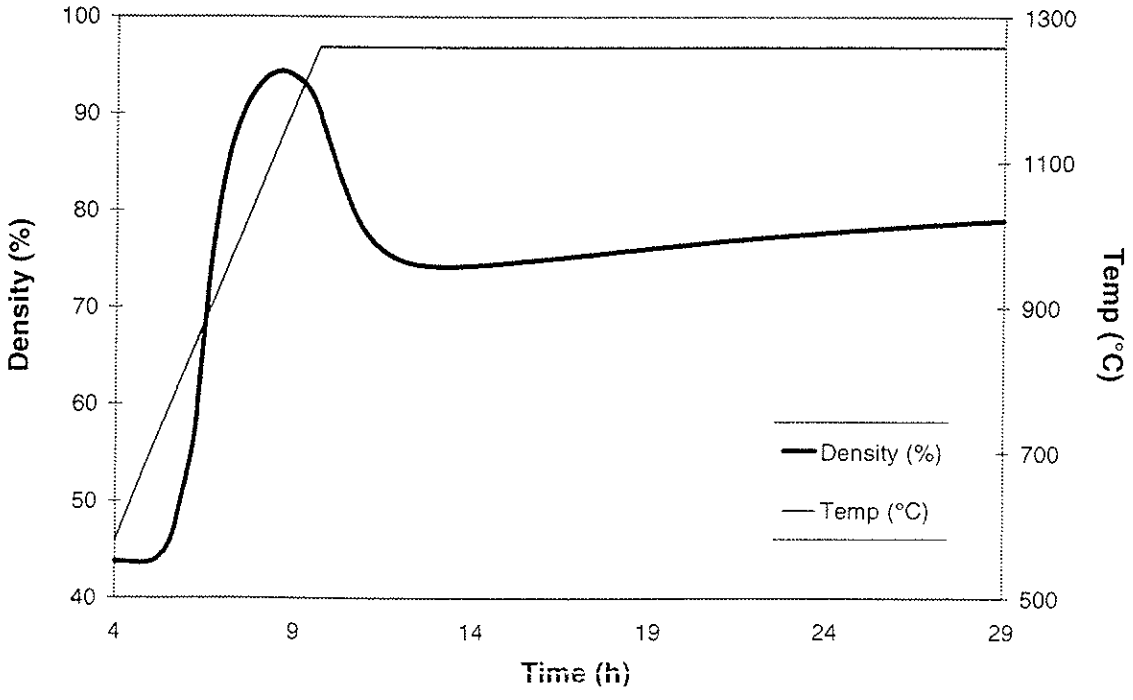

Figure 1 Sintering behaviour of $SrFeO_{3-\delta}$ with broad particle size distribution.

To examine this phenomenon, a number of dilatometry experiments and microstructure characterisations were carried out. It is concluded that the apparent determining factor for this kind of behaviour is the pore size/grain size ratio. The swelling process is favoured by high pore coordination and is typically observed in highly agglomerated powder. Grain growth will accordingly reduce the pore expansion because it lead to a reduction in pore coordination.

Sintered samples of $SrFeO_{3-\delta}$ develop cracks under normal cooling rates or abrupt changes in the oxygen partial pressure. Mechanical stresses are generated by change in the unit cell volume caused by change in oxygen vacancy concentration. A higher yield of crack-free membranes was obtained through a limited substitution of iron for chromium in the ferrates. Measurements of relative oxygen vacancy concentration as a function of Cr-substitution confirms a decrease in the oxygen vacancy concentration with limited chromium substitution.

In the second part of this work, attention is paid to the oxygen permeation of a number of chromium substituted strontium ferrate membranes. The influence of temperature, driving force, membrane thickness and microstructure are investigated. Of special interest was the influence of microstructure on the oxygen permeation. Moreover, an important issue was also to determine the surface exchange limitation.

The oxygen permeation experiments were restricted to oxygen partial pressure gradients in the range 0.001 - 0.9 bar and temperatures in the range 900 - 1030 °C. The slow process of vacancy ordering limited the window of investigation, even though oxygen transport in $SrFeO_{3-\delta}$ based materials can be observed at temperatures down to 400 °C.

The ceramics of $SrFe_{0.97}Cr_{0.03}O_{3-\delta}$ exhibit high oxygen permeation with relatively low apparent activation energy of 60 ± 8 kJ/mol for the overall transport process. Permeability of an one millimetre thick membrane is measured to be≈ 0.015 mol m^{-2} s^{-1} at 1273 K and $\Delta \log P_{O_2} = 2$. The oxygen permeation is partly governed by the surface oxygen exchange kinetics. Results from thickness dependent permeation implies approximately 50 % surface exchange limitations for the permeability of a 1 mm thick membrane. The calculated activation energy for the total oxygen exchange process was ≈

55 kJ/mol, while diffusion through the bulk is activated with an energy in the same range.

Modelling of the oxygen exchange rates give higher surface exchange limitation on the permeate side than the feed side of the membrane. On the permeate side the exchange rate increases with increasing temperature, and the activation energy is calculated to 98 ± 8 kJ/mol. On the feed side the oxygen exchange rate decreases with increasing temperature. Figure 2 shows the chemical potential drop as a fraction of the total driving force for $SrFe_{0.97}Cr_{0.03}O_{3-\delta}$. These results indicate different rate determining step in the exchange process on the two surfaces. The calculated apparent activation energy of ≈55 kJ/mol for the total exchange process is thus not inconsistent with the modelling results.

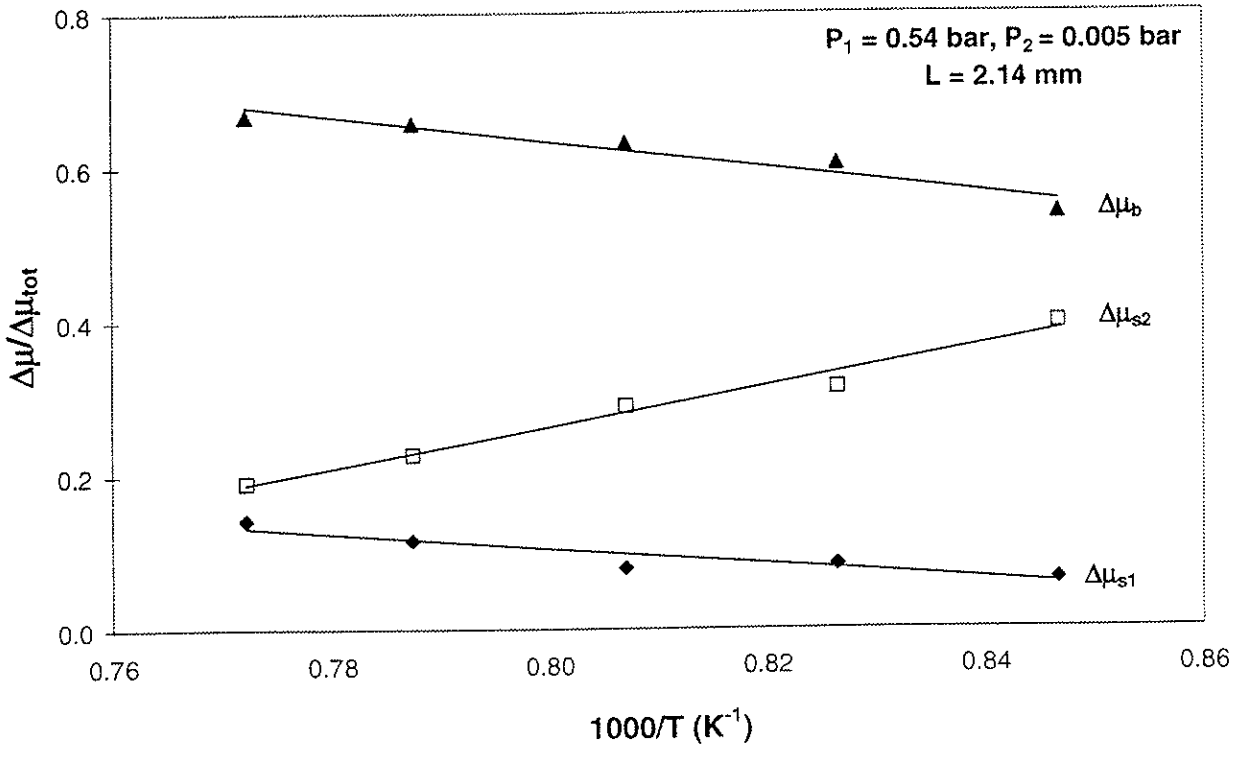

Figure 2 The fraction of the chemical potential drop on the feed surface ($\Delta\mu_{s1}$), permeate surface ($\Delta\mu_{s2}$) and through the bulk ($\Delta\mu_b$), as a function of inverse temperature. Membrane of composition $SrFe_{0.97}Cr_{0.03}O_{3-\delta}$ and thickness 2.14 mm.

Increased oxygen permeability was observed by increasing the grain boundary length in the membranes. Increased surface area depressed this effect, suggesting grain boundary dependent surface exchange kinetics. A model for microstructure dependent oxygen permeation is described.

The oxygen sub-lattice of $SrFeO_{3-\delta}$ is highly defect, and a description of the vacancy concentration based on an ideal point defect model is expected to be too simple. Surprisingly, the model fits well with thermodynamic values from the literature, as shown in Table 1. It does not appear necessary to consider the interaction of the large number of defects and the resulting defect clustering, to describe an oxygen defect model for $SrFeO_{3-\delta}$ at the selected conditions.

Table 1 Thermodynamic quantities for oxygen vacancy formation and charge disproportionation of $SrFeO_{3-\delta}$ (equations [4.1] and [4.2]), compared with literature data for $La_{1-x}Sr_xFeO_{3-\delta}$.

x	$\Delta H_{4.1}$ (kJ/mol)	$\Delta S_{4.1}$ (J/K mol)	$\Delta H_{4.2}$ (kJ/mol)	$\Delta S_{4.2}$ (J/K mol)	References
0	125	71	196	25	Mizusaki et al., 1985
0.1	113	67	163	13	["]
0.25	117	75	184	31	["]
0.4	105	70	125	-4	["]
0.6	113	82	138	6	["]
1.0	80	75	-	-	Holt et al., 1999
1.0	110	90	155	22	This study

1 INTRODUCTION

1.1 Background

1.1.1 Air separation

The market for oxygen has grown significantly because many industrial processes benefit from the use of oxygen where air is traditionally used. The consumption of oxygen has increased steadily by amount 5 % per year during the last 30 years. By oxygen-enrichment of air, the process rates can be increased or the amount of process gas decreased. The metallurgical industry, especially steel manufacturing, is the largest consumer of oxygen or oxygen-enriched air. Volatilisation of carbon dioxide and other non-metal impurities in the metals is controlled more easily by using oxygen gas instead of air. Dissolved nitrogen in unalloyed steel reduces the ductility. Nitrogen can form nitrides with Fe, Al and other elements in steel. Depending on the conditions, the precipitation can either improve the microstructure by preventing grain growth, or lead to unfavourable properties of lower ductility and poorer impact strength. Apparently the aluminium nitride formed at the grain boundaries increases the mechanical strength of the steel (Davies, 1970; Encyclopædia Britannica, 2000; Praxair, 2000).

The chemical industries consume large amounts of oxygen for the manufacturing of chemicals such as methanol and acetylene. To a lesser extent, oxygen is used in the wood products industry, treatment of sewage, incineration of wastes, pottery manufacturing and other processes that use kilns. Medical applications of oxygen include use in oxygen tents, inhalers and a multitude of breathing devices. The total world market for oxygen is in the range of 80 million tons/year, and the production increases mainly due to a growing demand in combustion applications (Encyclopædia Britannica, 2000; Chemical Week, 2000; Praxair, 2000).

Oxygen prices vary widely depending on volumes, qualities, the supplier-customer distance, electrical energy costs and plant-operating rate. Average price level for the merchant business is approximately 0.1 \$/m^3 O_2 (Chemical Week, 2000).

Production methods for oxygen depend on required purity and quantity of the gas. Today, the major conventional technique for air separation is cryogenic distillation. In this process air is compressed and a water cooled heat exchanger removes the heat of compression. This condenses most of the water, and an adsorbent subsequently removes the residual water and other impurities. A portion (7-12 %) of the water cooled compressed gas is allowed to expand and this cools the system. Additional cooling of the air is done by heat exchange a portion of the product stream, until the air becomes a liquid (-196 °C, boiling point of nitrogen). The liquid air is warmed, and the rare gases are distilled off first, then the nitrogen gas, leaving only liquid oxygen (T_b = -183 °C). By multiple fractional distillation, oxygen of 99.9 percent purity can be produced.

Pressure-swing adsorption (PSA) is generally used for small-scale air separation. This process uses a zeolite based adsorbent that preferentially adsorbs nitrogen, while the targeted oxygen gas passes through. A complex PSA scheme uses three or four beds of zeolites, with one adsorbing nitrogen at several bar pressure while the others are depressurized, purged or repressurized. The resulting oxygen gas is in the 95-99 percent purity. Vacuum-swing adsorption (VSA) is also used industrially. The basic concept behind PSA and VSA is the same. In PSA the bed is vented to atmospheric pressure, while in VSA the bed is taken down to much lower pressure.

Cryogenic separation is cost competitive in large volume applications, especially in high-purity applications. Figure 1.1 illustrates the relative ranges in which the various technologies are economical.

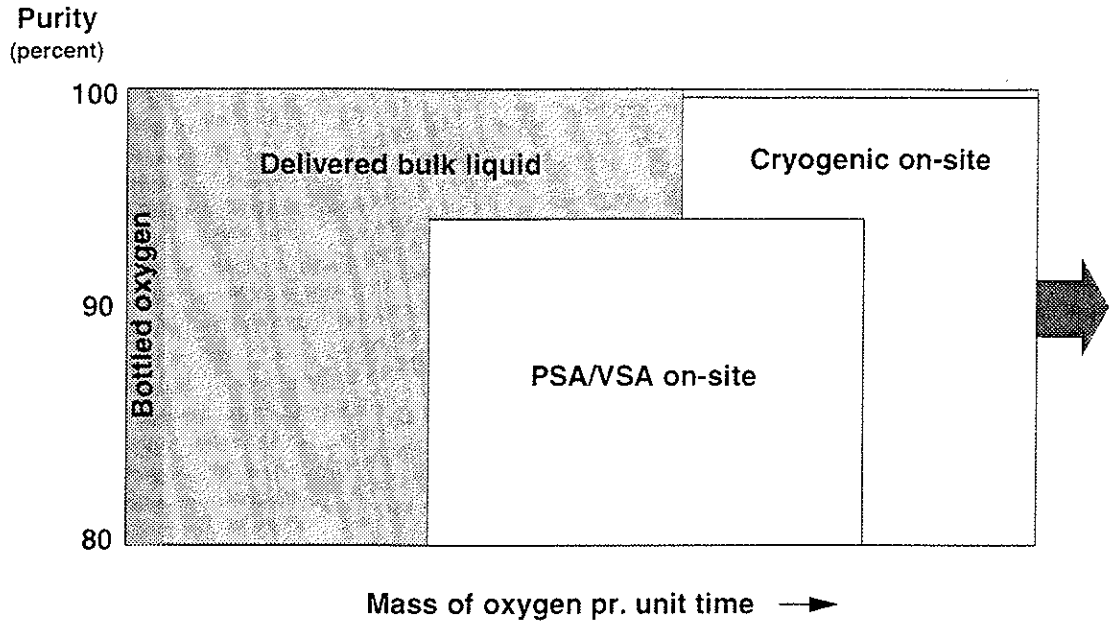

Figure 1.1 Economical oxygen production technologies shown as a function of purity and required supply rate.

The cryogenic distillation of oxygen has a world market share of more than 95 percent. Adsorption systems can be operated economically on a smaller scale, but their disadvantage is the discontinuous process. In addition, high purity requirements for the oxygen exclude the PSA method. However, PSA systems are portable, which permits on-site temporary applications (Ullmann, 1991; Encyclopædia Britannica, 2000).

During the last 20-30 years, especially during the nineties, efforts have focused on development of dense ceramic membranes for air separation (Jagannathan et al., 1980; Iwahara, 1981; Mazanec & Velenyi, 1992). Two categories of dense membranes can be distinguished; the ionic conductor (ICM) and the mixed conducting membrane (MCM) (Steele, 1996). The oxygen permeation of ICM and MCM is established by different driving forces; electric and pressure potential gradient. Figure 1.2 illustrates the principle of operation of the two membrane types. Figure 1.2a shows a purely oxygen ionic conductor used as an electrochemical pump. The membrane has electrodes attached on both sides with connections to an external electrical circuit. So far, this concept for an oxygen generator has not found a successful technological application. Calcia-stabilised zirconia is, however, a widely used example of an oxygen-ion conducting material in a commercial

application. Zirconia is used as an oxygen sensor for the control of the air to fuel ratio in automobiles.

The solid electrolyte membrane can also be operated in a solid oxide fuel cell mode (SOFC). With a load on the external circuit and an oxygen pressure gradient across the membrane, the system will generate electrical energy. Hydrocarbon gases are added as fuel to the anode compartment. In spite of intensive development efforts by many companies, this technology has so far not reached commercialisation.

A dense mixed conducting material with both high oxygen ionic and electronic conductivity can separate oxygen from air without an external electrical circuit. This is shown in Figure 1.2b. This type of membrane is the subject of the present study, and will be described in more detail. Oxygen dissociates and is transported in the structure via vacant oxygen sites. In addition to available vacant positions, a certain mobility of the oxygen ions is required. The flux of oxygen ions is charge compensated by a simultaneous flux of electronic charge carriers. The vacancy concentration depends on the oxygen partial pressure and temperature. The driving force for oxygen transport through the membrane is a gradient in the chemical potential of oxygen across the membrane. This again establishes an oxygen ion concentration gradient.

a) **Electrochemical oxygen pump**

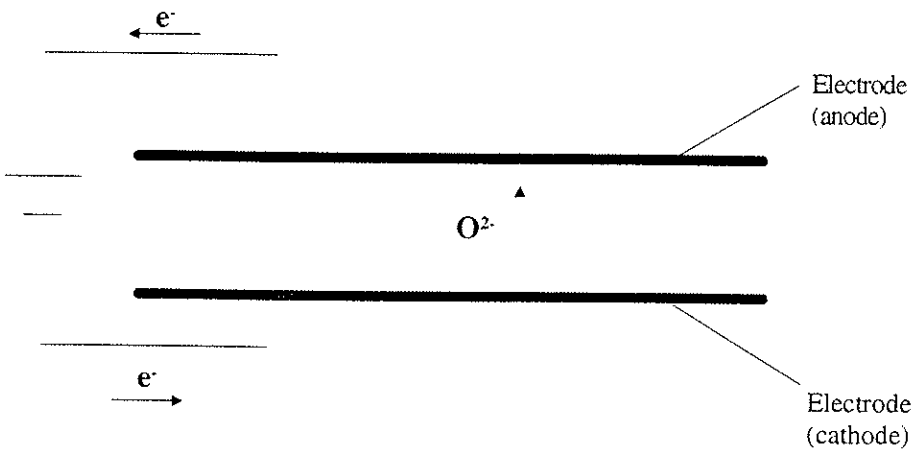

b) **Mixed conducting membrane, $P^{I}(O_2) > P^{II}(O_2)$**

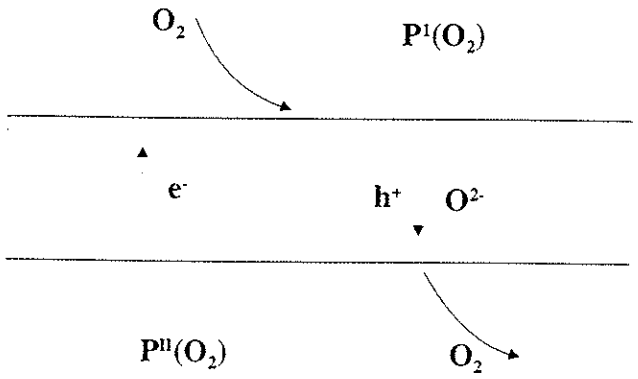

Figure 1.2 Oxygen ion conductors in different membrane concepts.

The desired oxygen transport occurs by a diffusion process which requires a high temperature since it is an activated process. To get an industrially acceptable permeation rate of oxygen, the membrane has to be operated at temperatures as high as 800-1200 °C. In addition, the gradient in chemical potential of oxygen across the membrane must correspond to a oxygen partial pressure in the range of 1-5 bar. Most technological applications probably require oxygen permeabilities as high as 100 kg/(m^2 day), depending of course on the process. This corresponds to 5.2 $Scm^3/(cm^2$ min) or an ambipolar current density of 1.5 A/cm^2. The design criteria of permitted maximum membrane area in the module will most likely determine the need of oxygen transport in the process.

The use of MCM's has become a potentially economical method for producing oxygen by separation from a hot air stream. The particularly attractive option is the integration of a membrane reactor with a gas turbine for cogeneration of oxygen and electricity (Kang et al., 1996). Compared to existing technologies, the membrane installation will presumably reduce both energy consumption and investment costs.

Cheaper oxygen production technology will open up new markets. The ion-conducting membrane has the advantage of inherently producing 100 % oxygen. Thus, the purity of the product depends only on sealing and mechanical integrity of the module. For processes that require high purity oxygen, the high oxygen selectivity of MCM's can oust other technological concepts. Industrial and technology companies are most likely carrying out feasibility studies and technical-economical evaluations for an extensive range of applications.

Market opportunities for MCM's include oxygen generators for various purposes, or as units where the membrane module is incorporated in a process plant. An example of the latter is the research activities to develop a membrane for converting natural gas to synthesis gas (H_2 + CO) (Nataraj et al., 1998). BP Chemicals initiated this research, and the project is now funded by Praxair, BP-Amoco, Sasol and Statoil (Prasad, 1999). Figure 1.3 shows the principle of the process. Oxygen is fed to the natural gas by MCM separation of heated air. The driving force is provided by the difference in P_{O_2} between air and the reducing atmosphere of natural gas.

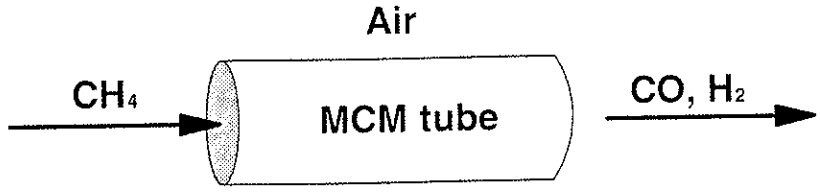

Figure 1.3 Conversion of natural gas to synthesis gas with oxygen produced by a MCM tube.

The U. S. Department of Energy has estimated that if a one-step process can be developed to separate oxygen from air and combine it with natural gas to form synthesis gas, costs could be reduced by 25 percent or more (DOE, 1999). Synthesis gas is a source of energy for various processes, and two main products are ammonia and methanol. Another alliance, led by Air Products and Chemicals is competing in the commercialisation of the MCM based synthesis gas production (J. E. Sinor Consultants Inc., 1998).

Compared to traditional synthesis gas production, the investment in an aeration plant is avoided. Furthermore, offshore conversion of natural gas can become a reality with a more compact synthesis gas technology.

1.1.2 Material properties of mixed conducting membranes

The high oxygen permeability of MCM materials originates in the high concentration of oxygen vacancies and high oxygen ion mobility at elevated temperatures. Most materials of interest are based on perovskite related structures (ABO_3) with high concentrations of vacancies in the oxygen sub-lattice. The ideal perovskite structure is shown in Figure 1.4. Alternatively, the conduction mechanism can occur via occupation of interstitial oxygen sites, as in structures of the Ruddlesden-Popper type.

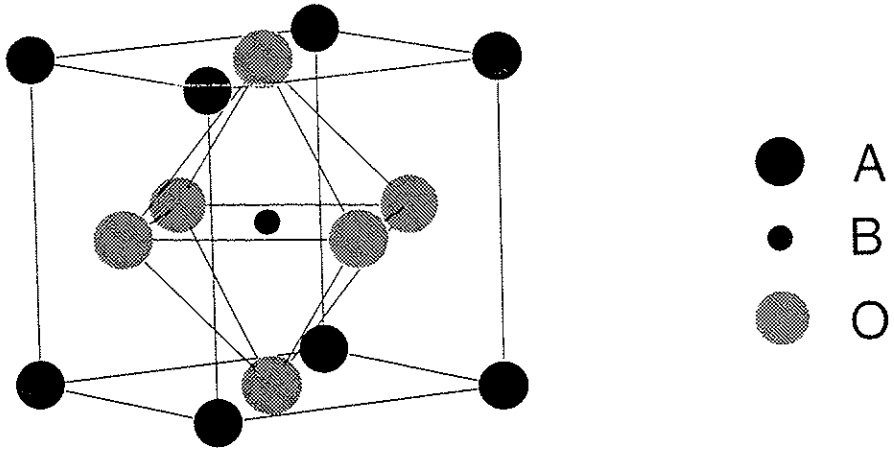

Figure 1.4 The ideal perovskite structure (ABO_3).

The research activity has focused on $ABO_{3-\delta}$ with a fair amount of oxygen vacancies. The oxygen nonstoichiometry is defined by δ and describes the average number of vacant oxygen sites per unit formula cell. In general, the large A-site cation is a trivalent rare earth element, while the smaller B-cation is a transtition metal. The oxygen content varies with temperature, partial pressure of oxygen and degree of substitution on A- and B-sites. A publication by Anderson (1992) illustrates how the concentration of oxygen vacancies can be influenced by substitution of a divalent element (A') for the trivalent A-site cation. The oxygen content of $A_{1-x}A'_xBO_{3-\delta}$ as a function of P_{O_2} is drawn schematically in Figure 1.5.

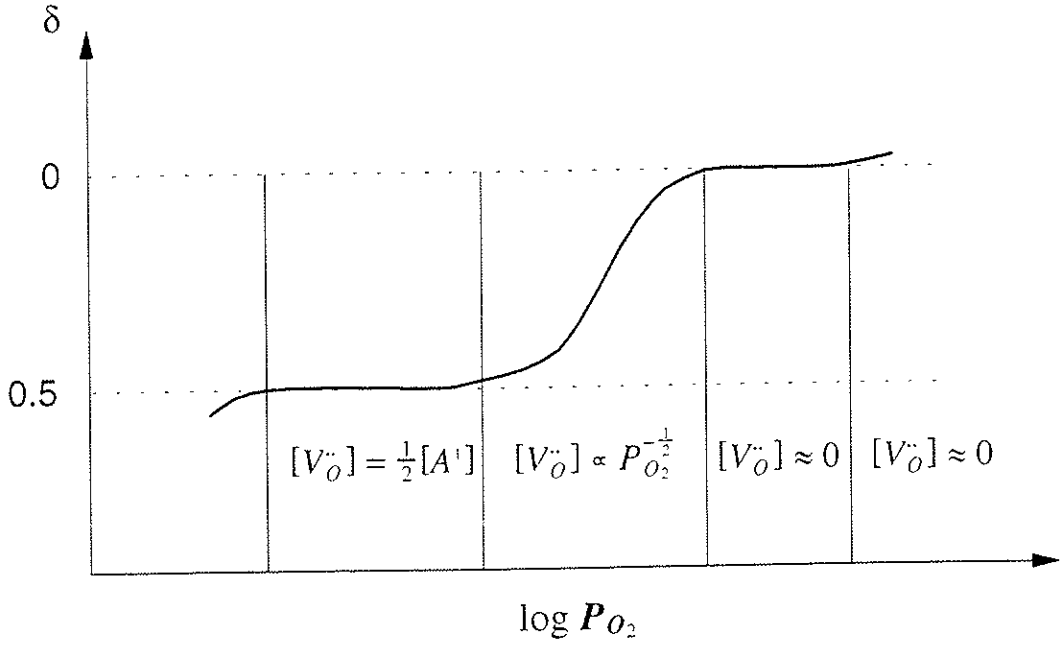

Figure 1.5 The oxygen nonstoichiometry as a function of P_{O_2} for a perovskite with composition $A(III)_{1-x}A'(II)_xB(III)O_{3-\delta}$ $[V_O^{\cdot\cdot}]$ denotes the oxygen vacancy concentration and $[A']$ the concentration of divalent A' on the trivalent position A.

An example of such a complex system is the composition with the general formula $La_{1-x}Sr_xCo_{1-y}Fe_yO_{3-\delta}$ (Teraoka et al., 1985). This was one of the first studies on MCM's reported in the literature. Introducing divalent Sr cations on the La-site involves not only creation of oxygen vacancies, but also oxidises a fraction of three valent chromium- and/or iron-ions. This contributes to higher concentrations of mobile ionic and electronic charge carriers. An alteration in the oxygen vacancy concentration can also be accomplished by partial substitution on the B-site by other mixed-valent transtition metals such as Mn, Cr, Ni, Cu (Bouwmeester & Burggraf, 1997). Partial substitution on either A- or B-sites affects the thermodynamic stability, and is a key factor for designing a thermodynamically stable MCM material.

The simple point defect model is hardly applicable to materials with high defect concentrations. Defect-defect interactions lead to an ordering of the defects in order to minimise the lattice energy, particularly at low temperature. The vacancy ordering depends both on temperature and oxygen partial pressure. The interaction between oxygen defects results in fewer

vacancies available for the oxygen transport. The brownmillerite structure is ordered and can be derived from the ideal perovskite lattice. One of six oxygen sites in this structure is vacant and ordered, as in $Sr_2Fe_2O_5$ (Rao & Gopalakrishnan, 1997). An *order-disorder* transition for the $SrFeO_{3-\delta}$ perovskite can occur for $0 < \delta$. but leads to a phase decomposition for an unidentified value in the range $0.5 < \delta < 1$. The disorder state is favoured when decreasing the vacancy concentration or increasing the temperature. Ordering of oxygen vacancies into microdomains having the brownmillerite unit cell is observed by High Resolution Transmission Electron Microscopy (van Doorn, 1996).

When an initially homogenous multicomponent oxide is placed in an oxygen potential gradient, a gradient in the chemical potential of the constituent binary oxides is established. At steady state diffusion, the mobility of different cations at the same sub-lattice leads to an enrichment of the high-mobility cations at the oxygen rich side of the membrane. This causes a *kinetic demixing* of the material. *Kinetic decomposition* occurs if the demixing exceeds the stability limit of the material, even though the material is stable under static conditions in the same P_{O_2} range (Schmalzried & Laqua, 1981). Cation diffusion is some order of magnitudes lower than the oxygen diffusion in the relevant materials.

The crystallographic cell volume expands when the oxygen vacancy concentration increases, and will in the present work be referred to as *chemical expansion*. It leads to mechanical stress of the membrane in an oxygen potential gradient. A sufficiently low value of this chemical expansion is important to avoid cracking of the membranes.

Chemical compatibility and thermal expansion match with adjacent materials is important for sufficient strength. In addition, good creep resistance is essential. An important issue for functional ceramics is the stability of the microstructure under operating conditions. Extended grain growth decreases the mechanical strength, and the bulk transport properties are usually improved by diffusivity paths along grain boundaries (Bouwmeester & Burggraf, 1997). As a whole, this implies a desire for a microstructure with small grains. The number of microstructural investigations of perovskites membrane materials, found in the literature is very limited.

1.2 Oxygen transport parameters

The oxygen permeation of a dense ceramic membrane is essentially controlled by the rate of bulk diffusion and the interfacial oxygen exchange on either side of the membrane. Molecular oxygen from the gas phase dissociates and ionises on the high-pressure surface. In the bulk, coupled diffusion of oxygen ions, electrons and/or electron holes take place. On the low-pressure side, the diffusing oxygen ions recombine to form molecules. Varying conditions on the membrane surfaces can cause considerable difference in surface exchange limitations. The bulk diffusion depends on temperature, oxygen partial pressure and microstructure of the bulk. The surface exchange kinetics are, additionally, presumably dependent on the surface structure and area.

Oxygen permeation leads to a drop in the chemical potential of oxygen across the membrane. This is illustrated schematically in Figure 1.6. The membrane can be divided into three regions, but the oxygen flux is obviously the same through these three under steady state conditions. The available driving force is distributed across the membrane with the rate-limiting step expending the greater proportion. This macroscopic description leads to a need for rate constants to describe the oxygen permeation of the various zones. The following chapter will describe the different coefficients, and mention the conceptionally different experimental techniques which lead to data on these rate constants. Based on a review of the relevant literature, some attention is paid to the relationships between these rate constants (Maier, 1998).

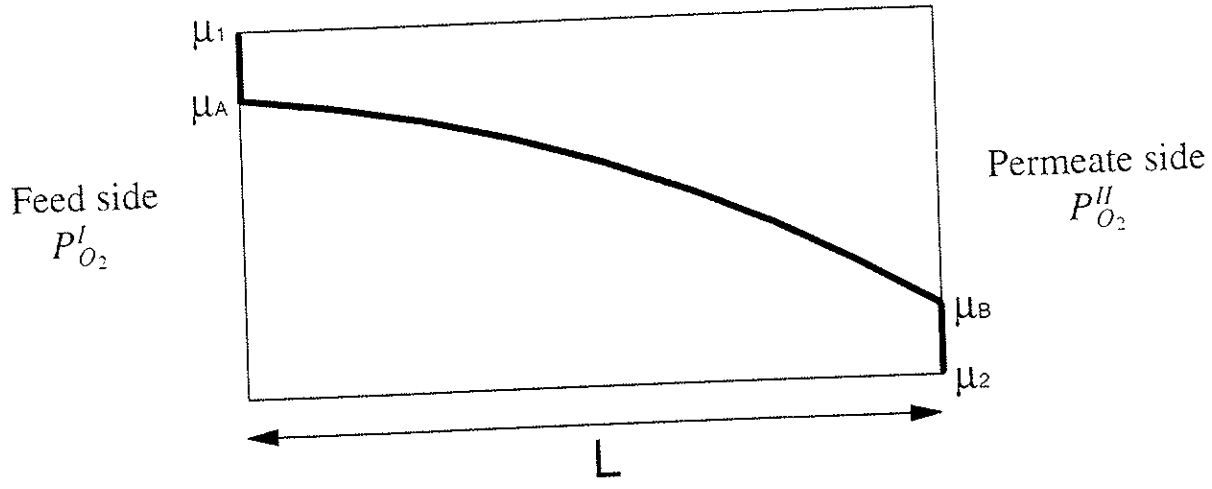

Figure 1.6 A possible draw of the profile of the chemical potential of oxygen across a permeating membrane with thickness L. $P^{I}_{O_2} > P^{II}_{O_2}$

Bulk diffusion

The chemical diffusion is used to describe the combined diffusion processes involving one or more species occurring under a chemical potential gradient. Relevant to the present work is the simultaneous diffusion of oxygen ions and electrons in the dense membrane. Most of the MCM's which have been investigated in the past have electronic conductivities of magnitudes larger than the ionic conductivities. This is also valid for $SrFeO_{3-\delta}$ based materials (Smyth et al., 1996). Hence, the bulk diffusion of $SrFeO_{3-\delta}$ can be simplified by the transport only limited by the oxygen ions. In addition, the simultaneous flux of ions and electrons are assumed to be ideally diluted with no interactions. Cross-coefficients between ionic and electronic fluxes are thus neglected.

The permeation J_o of component o, can be described by the phenomenological relation from irreversible thermodynamics (Prigogine, 1967):

$$J_o = -\mathcal{L} \cdot \nabla \mu_o \qquad [1.1]$$

where $\mathcal{L}$ is the transport coefficient and $\nabla\mu_o$ is the gradient in chemical potential. The transport coefficient can be expressed by the product of the concentration and mobility of species o:

$$\mathcal{L} = c_o \cdot B_o \qquad [1.2]$$

The mobility B_o is defined as the ratio between the mean velocity and the driving force, and is given by:

$$B_o = \frac{D_o}{RT} \qquad [1.3]$$

where D_o is termed the self diffusion coefficient of species o, and is often reported in units of cm^2/s. Integration of equation [1.1] across the membrane thickness, L, using the relationship $\nabla\mu_{O_2} = RT \nabla \ln P_{O_2}$ and assuming predominant electronic conductivity, gives the Wagner equation for oxygen permeation (Wagner, 1933/1936):

$$J_{O_2} = -\frac{1}{4L} \int_{\ln P'O_2}^{\ln P''O_2} D_o \cdot c_o \, d\ln P_{O_2} \qquad [1.4]$$

where P_{O_2} is the oxygen partial pressure. Superscripts ' and " represents the oxygen partial pressure on the two sides of the membrane.

The bulk diffusion of oxygen through mixed conducting oxides is commonly described using Wagner's theory. Originally, Wagner derived the equation to describe the high temperature oxidation of metals, and the parabolic growth rate of the oxide scales.

The relationship between the oxygen ionic conductivity, σ_o, and the oxygen self-diffusion coefficient, D_o, is given by the Nernst-Einstein equation:

$$\sigma_O = \frac{z_O^2 F^2 D_O c_O}{RT} \qquad [1.5]$$

where R is the gas constant, T is the temperature, z_O is the valence of lattice oxygen ions (i.e. -2), F the Faraday constant and c_O is the concentration of lattice oxygen ions.

The common expression of the Wagner equation appears by introducing the Nernst-Einstein equation [1.5] into equation [1.4]. Generalisation by taking the electronic conductivity into account gives (Bouwmeester & Burggraaf, 1997):

$$J_{O_2} = -\frac{RT}{4^2 F^2 L} \int_{\ln P'O_2}^{\ln P''O_2} \left[\frac{\sigma_O \cdot \sigma_e}{\sigma_O + \sigma_e}\right] d\ln P_{O_2} \qquad [1.6]$$

where σ_e is the total electronic conductivity (i.e. the sum of the electron and hole conductivity). The expression in the brackets in equation [1.6] is named the *ambipolar conductivity* and defines the coupled diffusion of charged species.

The transport of oxygen ions is equal to the transport of oxygen vacancies in the opposite direction. This implies the relation:

$$D_O c_O = D_v c_v \qquad [1.7]$$

The oxygen vacancy concentration is related to the vacant oxygen sites per unit formula cell, δ, by the molar volume of the crystallographic cell, V_m:

$$c_v = \frac{\delta}{V_m} \qquad [1.8]$$

In view of equations [1.4] and [1.7], it is presumed that all oxygen vacancies contribute equally to the oxygen permeation. The mobility, expressed by the self-diffusion coefficient, is generally assumed to be independent of the oxygen vacancy concentration (van Hassel et al., 1993). This assumption may hold when the vacancy concentration is low. Variation in mobility as a function of P_{O_2} may be essential for systems with a considerable number of oxygen vacancies (e.g. $SrFeO_{3-\delta}$) (Yasuda & Hishinuma, 1995).

The self-diffusion coefficient of oxygen ions can be determined from tracer diffusion experiment using the ^{18}O isotope. The diffusion of tracers are studied at what is essentially thermodynamic equilibrium. The driving force for transport is only the mixing of isotopes under the influence of their concentration gradients. Surface reaction between $^{18}O_2$-enriched gas phase and lattice oxygen is carried out at high temperature for a selected time before the isotope penetration profile is analysed. The tracer diffusion is usually monitored by depth probing of the ^{18}O-fraction, $^{18}O/(^{16}O+^{18}O)$, diffusion profiles. Analysing the profile is commonly performed by secondary ion mass spectroscopy (SIMS) (Kilner et al., 1984).

The tracer diffusion coefficient is smaller than the random diffusion coefficient, due to the probability that a vacancy will re-exchange with the tracer atom. This implies that the jump is dependent on the previous. This is accounted for by a correlation factor f, which is less than unity. The factor depends on the diffusion mechanism and the crystal structure. For a vacancy diffusion mechanism, the oxygen tracer diffusion coefficient, D^*, is related to the random self-diffusion coefficient, D_o, through the tracer correlation factor f as:

$$D^* = f \cdot D_o \qquad [1.9]$$

The correlation factor for a perovskite anion sublattice was calculated to 0.69 for minor oxygen vacancy concentration (Ishigaki et al., 1988).

The transport of species o in a concentration gradient can be expressed by Fick's first law:

$$J_o = -\tilde{D}\frac{\partial c_o}{\partial x} \qquad [1.10]$$

where $\tilde{D}$ is the chemical diffusion coefficient. A relationship between the self-diffusion coefficient D_o and the chemical diffusion coefficient $\tilde{D}$ can be derived by combining the Wagner equation [1.4] and Fick's first law [1.10], and introducing $a_o = \gamma_o^* \cdot c_o$ where γ_o^* is the activity coefficient (Schmalzried, 1981; Atkins, 1986). The details are given in Appendix 1.

$$\tilde{D} = D_o(1 + \frac{\partial \ln \gamma_o^*}{\partial \ln c_o}) \qquad [1.11]$$

Simply combining the Wagner equation [1.4] and Fick's first law [1.10] gives the relation, details of which are given in Appendix 1:

$$\tilde{D} = D_o \frac{1}{2}\frac{\partial \ln P_{O_2}}{\partial \ln c_o} = -D_v \frac{1}{2}\frac{\partial \ln P_{O_2}}{\partial \ln c_v} \qquad [1.12]$$

Part of this expression is defined in the literature as the *thermodynamic enhancement factor* given by (Bouwmeester & Burggraf, 1997; ten Elshof, 1997[1]; Lane et al., 1999):

$$\gamma_o = \frac{1}{2}\frac{\partial \ln P_{O_2}}{\partial \ln c_o} \qquad \gamma_v = -\frac{1}{2}\frac{\partial \ln P_{O_2}}{\partial \ln c_v} \qquad [1.13]$$

This expression shows that the thermodynamic enhancement factor, γ_o which is generally reported in the literature is defined differently from the thermodynamic activity coefficient γ_o^* which is defined in classical thermodynamic.

For perovskite oxides the thermodynamic enhancement factor has been reported to values as high as $\approx 10^5$, which mean a P_{O_2} range with limited changes in oxygen stoichiometry (Belzner et al., 1992). The value depends on

temperature and composition. Hence the curve shape of $\tilde{D}$ and D_o as a function of P_{O_2} will show a different characteristic.

Surface exchange kinetics

The surface exchange of oxygen involves a sequence of reaction steps, each of which may be rate determining (Nowotny & Wagner, 1981; Adamczyk & Nowotny, 1991; Gellings & Bouwmeester, 1992). Possible steps involve oxygen adsorption to the surface, dissociation of molecular oxygen, diffusion on the surface, charge transfer and incorporation of O_{ads}^{2-} into the lattice. Several species can occur as intermediates for the reduction of molecular oxygen. A sketch of some possible rate determining steps is shown below:

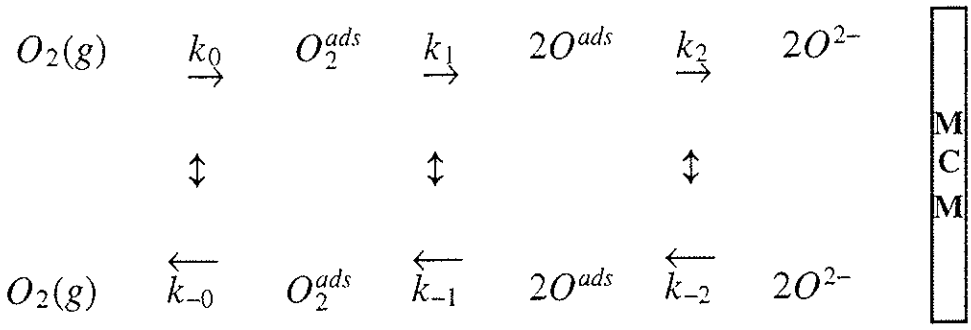

The oxygen permeation can be described by the exchange rate of oxygen on the surface, as defined in irreversible thermodynamics (Prigogine, 1967). On the feed surface, the oxygen permeation can be expressed by:

$$J_{O_2} = J_{O_2}^{in} - J_{O_2}^{out} = J_{O_2}^{ex} - J_{O_2}^{out} = J_{O_2}^{ex}(1 - \frac{J_{O_2}^{out}}{J_{O_2}^{ex}}) \qquad [1.14]$$

where $J_{O_2}^{in}$ and $J_{O_2}^{out}$ are the oxygen flux into and out of the sample surface. At thermodynamic equilibrium there are two equal and opposite fluxes into and out of the sample surface. The parameter $J_{O_2}^{in}$ is equal to $J_{O_2}^{ex}$, which expresses the oxygen exchange rate in absence of an oxygen potential gradient. The exchange rate is a fundamental quantity and gives the maximum oxygen permeation rate which can occur. The exchange rate is a material parameter and depends of the temperature and P_{O_2}. Perturbation from equilibrium

results in oxygen permeation, and the flux increases with increasing perturbation. The variable, $J_{O_2}^{out}$, depends of the oxygen potential gradient. The rates are proportional to the oxygen activity and can be defined as:

$$J_{O_2}^{ex} = k \cdot a_1 \; J_{O_2}^{out} = k \cdot a_A \qquad [1.15]$$

where k is a constant. The subscripts given on the activities (1 and A) are related to the chemical potentials on the feed surface, defined in Figure 1.6. Using the relationship $\mu_{O_2} = RT \ln a_{O_2}$ gives the expression:

$$J_{O_2} = J_{O_2}^{ex}(1 - \exp(\tfrac{\mu_A - \mu_1}{RT})) \qquad [1.16]$$

where $\mu_A - \mu_1$ is the chemical potential drop for molecular oxygen on the feed surface.

Equation [1.16] expresses the general relation between the oxygen permeation and the chemical potential drop on the surface. A similar expression is valid on the permeate surface of the membrane with the chemical potential drop $\mu_2 - \mu_B$ (see Figure 1.6).

For perturbation close to equilibrium, the equation [1.16] can be simplified (Bouwmeester & Burggraf, 1997):

$$J_{o_2} = -J_{O_2}^{ex} \tfrac{(\mu_A - \mu_1)}{RT} \qquad [1.17]$$

This linear equation will only be valid when $\mu_A - \mu_1$ is much smaller than RT, i. e. when the transport process is limited considerably by the surface exchange kinetics.

The tracer exchange rate is assumed to be proportional to the difference between the concentration in the gas and the concentration in the surface at

any time. The expression of k^* and D^*, with the appropriate boundary conditions, can be expressed as (Kilner, 1994):

$$k^*(c_g - c_s) = -D^* \frac{\partial C(x)}{\partial x} \mid_{x=0} \qquad [1.18]$$

where c_g and c_s are the ^{18}O isotope fraction in the gas phase, and in the solid surface, respectively. The isotopic fraction at any depth x is defined as $c(x) = c_o^{18}/(c_o^{16} + c_o^{18})$. The tracer self-diffusion coefficient of oxygen is given as D^* and the variable k^* is the first order rate constant for the kinetic exchange of oxygen.

The net flux of the isotope, J_O, into the solid is given as:

$$J_O = J_O^{ex}(c_g - c_s) = -D^* c_o \frac{\partial C(x)}{\partial x} \mid_{x=0} \qquad [1.19]$$

where c_o is the bulk oxygen concentration. Combining equations [1.18] and [1.19] leads to a simple relationship between the tracer exchange coefficient and the oxygen exchange flux (Kilner, 1994):

$$J_O^{ex} = k^* c_o = 2J_{O_2}^{ex} \qquad [1.20]$$

The surface exchange rate as a function of P_{O_2} can be determined from oxygen permeation data versus driving force. This topic is discussed in Chapter 4.2.

The oxygen permeation, J_{O_2}, is commonly measured by experimental techniques where electrical or chemical driving forces are applied. The oxygen transport can be described by the chemical diffusion coefficient, $\tilde{D}$ and chemical surface exchange coefficient, $\tilde{k}$. The units are often given in cm^2/s and cm/s, respectively. A method by which to determine the chemical rate coefficients is the monitoring of the time-dependence of the mass change

or the change in gas composition surrounding the sample, when an abrupt change in P_{O_2} is applied (Holt et al., 1999).

More established is the electrochemical method by investigation the oxygen relaxation with potential step technique. Briefly, this technique involves the measurement of the time dependent of the flux of oxygen ions in response to a rapid change in the surrounding oxygen partial pressure. The sample is placed in an electrochemical cell, whose P_{O_2} is controlled with a potentiostat. The cell is generally made of yttria-stabilised zirconia with platinum electrodes. A potential step is applied to the electrodes of the cell whereby oxygen is pumped through the zirconia electrolyte. The sample exchanges oxygen with the surrounding volume in order to attain a new equilibrium, and the oxygen flow is recorded as an electrical current. From the time-dependence of the change in current, the chemical rate coefficients can be obtained. A simple expression of $\tilde{k}$ and $\tilde{D}$ with appropriate boundary conditions is (Bouwmeester & Burggraf, 1997, Diethelm et al., 1999):

$$\tilde{k}(c - c_{eq}) = -\tilde{D}\frac{\partial c}{\partial x} \mid_{x=0} \qquad [1.21]$$

where c_{eq} is the concentration of oxygen ions at the solid surface at infinite time.

A simple relationship can be derived between the tracer and chemical exchange coefficients. This is done by combination the equations [1.17], [1.20] and [1.21] (Lane et al., 1999; ten Elshof et al., 1997[III]):

$$\tilde{k} = k^* \cdot \frac{c_O \Delta\mu_s}{\Delta c_O RT} = k^* \cdot \gamma_O \qquad [1.22]$$

Accordingly, this is a similar to the correlation between the diffusion coefficients [1.12].

The degree to which the surface oxygen exchange limits the oxygen permeation process is often reported as a characteristic membrane thickness L_c. The parameter L_c determines the transition from dominantly bulk limited

diffusion to a dominantly surface exchange limited process. Accordingly, L_c is defined by the ratio between the tracer diffusion coefficient, D^* and the tracer surface exchange coefficient k^*, as given in equation [1.23] (Bouwmeester et al., 1994). The characteristic thickness is a function of P_{O_2}, temperature and the microstructure of the bulk and the membrane surface. The value of L_c may therefore be a characteristic of the sample or the experimental conditions. Kilner and co-workers (1984) introduced the ratio between k^* and D^* as a parameter h, which is the inverse of the characteristic membrane thickness, L_c.

$$L_c = \frac{D^*}{k^*} = \frac{1}{h} \qquad [1.23]$$

1.3 Ceramic processing of advanced ceramics

Ceramic fabrication of *traditional* ceramics such as refractories, pottery and structural clay products has been developed through several millennia. The processing has entailed the mixing of raw materials, forming by turning, slip casting or pressing, followed by one or more high temperature treatments of liquid phase or viscous flow sintering. Depending on the application, the parameters important to the performance of the product has varied. It is a different challenge to produce thin Chinese porcelain than fire bricks.

Advanced ceramics have attracted attention lately as wear-resistant materials, ceramic-fibre composites, cutting tools and for other applications where the mechanical or physical properties are important. The advanced ceramics are often divided into *structural* and *functional* ceramics (Rahaman, 1995). Structural ceramics are used as structural construction materials, due to their enhanced mechanical properties. Ceramics used in applications where the magnetic, electronic or optical properties are essential, are often referred to as functional ceramics.

Introduction of ceramics in the high-technology domain has led to the development of advanced processing techniques in order to make ceramic parts of special design and good quality. Control of the microstructure is of major importance. Thin film applications have become of interest concerning functionality and considerations of space and weight, and lead to new

challenges in designing the powder morphology and controlling the sintering behaviour. Sintering of films attached to substrates and problems related to how the sintering rate is influenced by the constraints imposed by the substrate have attracted especial attention (Garino & Bowen, 1990; Bordina & Jagota, 1993). Of interest to application of oxygen permeable membranes, is the possibility of obtaining a thin, high density membrane on a porous substrate. An additional challenge is to keep a stable microstructure under the operating conditions. Generally, sintering temperatures should be chosen at least 30 % higher than the operating temperature (K), to ensure that the microstructure of the ceramic is not altered during time.

Maintenance of the functional property of a material usually demands densification by solid state sintering. The sintering process is the core of ceramic fabrication whether the component is required in a dense or porous state, and the key to success is often the morphology of the powder.

In the research activity on mixed conducting membranes, limited effort has so far been focused on the solid state sintering process. Densification by solid state sintering is essential to maintain the desired transport properties of the bulk material, as well as the mechanical properties.

1.4 Scope of the present work

The ambition of the present work has been to contribute to the understanding of the parameters that determine the oxygen permeation of dense ceramic mixed-conducting membranes. Specifically, the aim was to determine the influence of microstructure on the oxygen permeation. To be able to do this investigation, an understanding of the sintering properties and influence upon the microstructure was necessary. Hence, the present study has been divided into two parts. First, the development of dense membranes with varying microstructure, but as similar as possible in all other respects. Second, to obtain a physical description of oxygen transport through the membrane based on oxygen permeation data. The plan was to investigate the effects of temperature, driving force, membrane thickness and the microstructure of bulk and surface.

2 PREPARATION OF MATERIALS IN THE SYSTEM $SrFe_{1-x}Cr_xO_{3-\delta}$

2.1 Introduction

The object of this part of the work was to prepare $SrFeO_{3-\delta}$ membranes for transport studies. It turned out to be a more difficult task than expected, due to swelling and high chemical expansion of these materials.

Sintering is the process where a heat treatment is used to convert a powder compact into a polycrystalline solid with higher strength. The sintering process is controlled by the slowest ions moving along its fastest path. Whether the material leads to a porous or a dense solid depends on the two competing processes; *densification* or *coarsening*. The term coarsening describes the processes which consumes the sintering driving force without densification. The powder morphology and the chosen sintering conditions determine the rate controlling process. Figure 2.1 shows the two different processes and the effect on the microstructure.

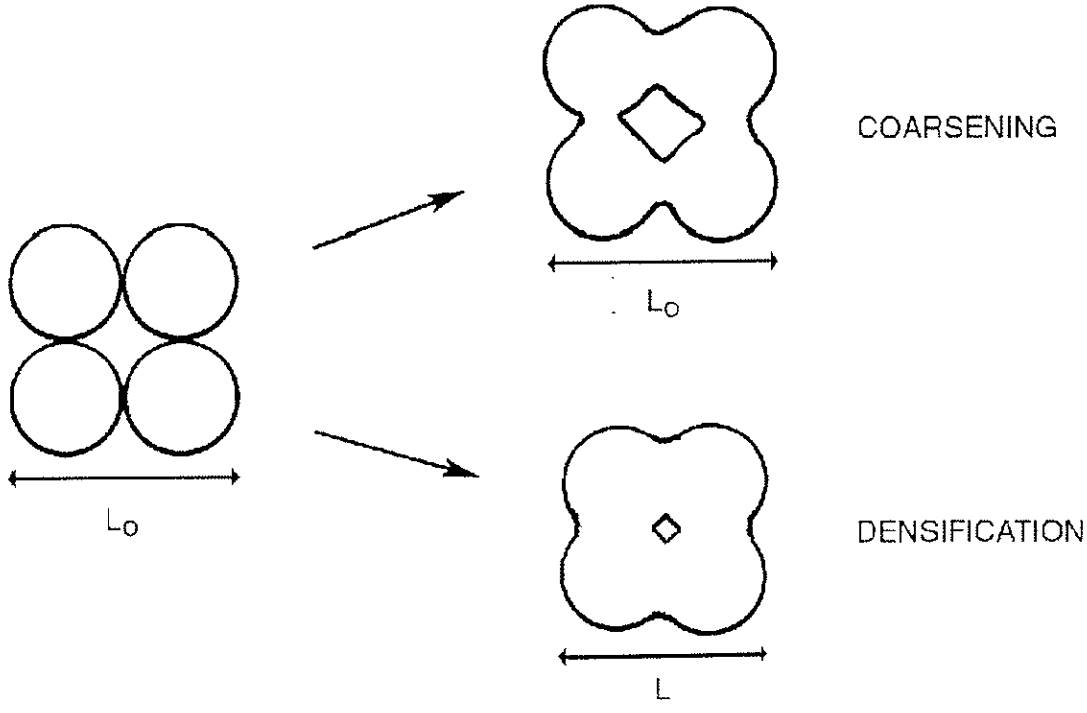

Figure 2.1 The densification and coarsening processes of a powder compact.

For oxygen permeable membranes, open porosity must be eliminated to obtain the oxygen selectivity. The density must exceed approximately 92 % in order to ensure that only closed pores remain (McColm & Clark, 1988). To achieve this, a compact powder body with density in the range of 40 to 60 % is required. This compact is often called a green body.

Driving forces for sintering

Coarsening and densification are mechanisms which compete for the total available driving force. The main challenge is to promote densification over coarsening.

The macroscopic driving force for sintering is the decrease in the surface energy by reduction of surface area of the powder particles. A fraction of the driving force is consumed in the formation of grain boundaries. Typical values of surface energy for oxides are around 1 J/m^2. This gives an energy change of 1.2 kJ/kg when a powder with 1 μm spherical particle size and density 5 g/cm^3, sinter to form a single sphere (McColm & Clark, 1988). We see from the example that the macroscopic driving force for sintering is small. In reality it is even smaller since we disregarded the energy required for grain boundary formation. The energy associated with the surfaces represents a small driving force compared to the local driving forces for sintering.

Curved surfaces have different energies than flat surfaces, and this gives the local driving forces for redistribution of matter. To understand these local driving forces, we must consider the activity difference which exists at equilibrium across a curved surface defined by the Laplace equation:

$$\sigma = \gamma_{sv} \left(\frac{1}{r_1} + \frac{1}{r_2} \right) \qquad [2.1]$$

where σ is the stress, γ_{sv} is the surface energy and r_1 and r_2 are the principal radii of curvature of the surface. This equation shows that tensile stresses are present under a concave surface ($r < 0$). Under a convex curvature ($r > 0$) compressive stresses exist. A flat surface is stress free. During sintering, any curved surface will tend to flatten over time to remove the stress. The stress

defined by the Laplace equation describes a change in the chemical potential at each side of the curved surface:

$$\mu - \mu_0 = \sigma V_m = \gamma_{sv} V_m (\frac{1}{r_1} + \frac{1}{r_2}) \qquad [2.2]$$

where V_m is the molar volume, μ and μ_0 are the chemical potential of atoms in and near, a curved and a flat surface. From this equation and the definition of the chemical potential, μ-μ_0 = RT ln $\frac{a}{a_0}$, we obtain the Kelvin equation for the difference in activity:

$$\ln(\frac{a}{a_0}) = \left(\frac{\gamma_{sv} V_m}{RT}\right) (\frac{1}{r_1} + \frac{1}{r_2}) \qquad [2.3]$$

This equation shows that the activity of a material depends on the particle radii. The activity increases with decreasing particle size. The activity of a surface with negative radius of curvature will be lower than for a flat surface, while a convex curvature has higher activity than the flat surface.

The driving force for the sintering process arises from the reduction of free energy when the local convex curvature decreases. A pore with convex curvature will thus disappear if mass transport occurs. The pore and grain stability is discussed in Chapter 2.3.

The driving force for mass transport can also be derived through the deviation from the equilibrium dihedral angle, as shown by Cannon and Carter (1989). The angle of the intersection between the surface and the grain boundary is defined as the dihedral angle ϕ (Kingery et al., 1976):

$$\cos(\frac{\phi}{2}) = \frac{\gamma_{ss}}{2\gamma_{sv}} \qquad [2.4]$$

where γ_{ss} is the grain boundary energy per unit area and γ_{sv} is the solid-vapour surface energy per unit area. This is illustrated in Figure 2.2. The

curvatures will tend to flattened until the equilibrium dihedral angle is reached. It appears that the equilibrium dihedral angle for many oxides ranges from 120° to 150°, although values as low as 88° is measured for carbon-doped UO_2 (Kingery et al., 1976; Handwerker et al., 1990).

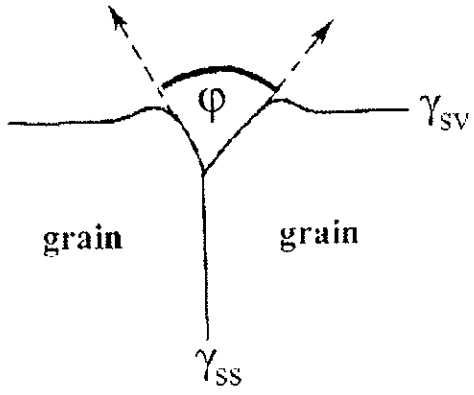

Figure 2.2 The angle of intersection between the surface and the grain boundary, defined as the dihedral angle (φ).

Sintering mechanisms

As shown in Table 2.1 several mechanisms for material transport in the green compact can play a role. Due to the relative importance of some of the transport mechanisms for densification, three sintering categories are defined.

In materials densified by viscous flow sintering, particles deform and grow together by viscous flow. This mechanism is important for the sintering of glass and amorphous materials.

Liquid phase sintering plays a vital role in the densification of highly covalent ceramics. They have low mobility in the lattice. A sintering additive is generally used which forms a liquid phase between the grains at the sintering temperature. An appropriate liquid phase must be chosen in order to give partly soluble ceramic particles. The mass transport occurs by solution-reprecipitation. The driving force for this mass transport is determined by the curvature of the particles and the pressure at contact points between particles. The latter is due to capillary forces and results in solution and transfer of matter away from the contact points. The particle centre-centre distance

decreases and they are flattened along neighbouring faces (contact flattening).

Solid state sintering is important in the densification of typical ionic compounds and functional materials. Only solid state sintering will be described in the following presentation. Several textbooks have described the different sintering categories in detail (McColm & Clark, 1988; Rahaman, 1995; German, 1996).

Table 2.1 The mechanisms of mass transport in a solid body and the effect on the microstructure.

Transport mechanism	**Effect on the microstructure**	**Sintering category ***
Bulk diffusion	densification, grain growth	sss, lps
Surface diffusion	coarsening, grain growth	sss, lps
Grain boundary diffusion	densification, grain growth	sss, lps
Solution-reprecipitation	coarsening	lps
Evaporation-condensation	coarsening, grain growth	sss, lps
Viscous flow (deformation)	densification	vfs

* Solid state sintering : sss
Liquid phase sintering: lps
Viscous flow sintering: vfs

2.2 Solid state sintering

The performance of oxygen permeable membranes will to some extent depend on the purity of the materials used. Impurity phases are detrimental to the high temperature mechanical and oxygen transport properties. To avoid impurity phases, solid state sintering is the only acceptable process for producing dense membranes.

Diffusion is the major mechanism for densification. Diffusion can consist of movement of atoms or vacancies along a surface, a grain boundary or through the grains of the material. If transport is along grain boundaries or through lattice dislocations, diffusion results in densification. Surface diffusion or

evaporation-condensation leads to coarsening. Figure 2.3 shows the transport mechanisms leading to densification or coarsening, applied to a two-sphere model.

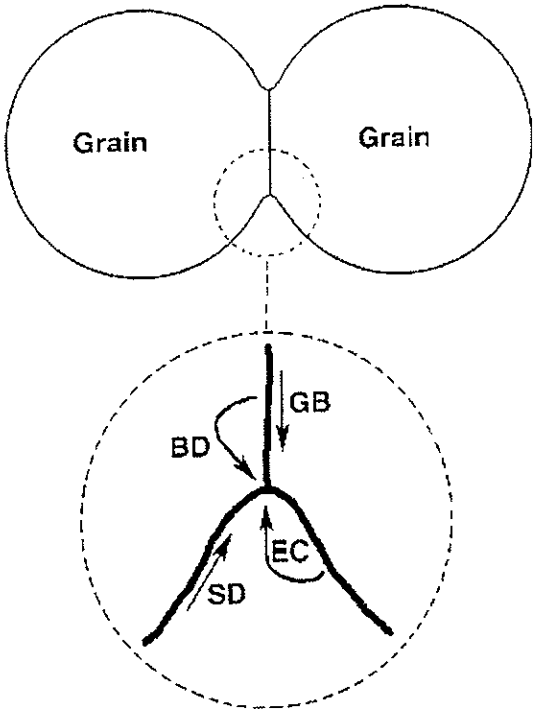

Figure 2.3 Alternative transport mechanisms applied to a two sphere sintering model. EC: evaporation-condensation, SD: surface diffusion, BD: bulk diffusion, GB: grain boundary diffusion

Sintering stages

The densification process is often divided into three stages, according to the sequence of the physical changes which occur (McColm & Clark, 1988; German, 1996). The *initial stage* involves rearrangement of particles and neck formation between particles. The rearrangement consists of movement of adjacent particles to increase the interparticle contact area, thus forming grain boundaries. This stage gives limited densification.

The second stage of densification is referred to as the *intermediate stage*. In this stage the grains and the open pore structure establish a network of interlinked cylindrical channels. Densification occurs when matter diffuses toward the pore channels, or vacancies diffuse in the opposite direction. Grain growth can occur in the last part of this stage.

The *final stage* begins when the pore channels are pinched off, resulting in isolated pores. Pores move and shrink to a stable size or disappear during this stage. The elimination of pores along the grain boundaries is a competition between the pore mobility and grain growth. The grain growth is determined by the grain boundary velocity, which is the product of the mobility and force. The grain boundary mobility decreases with pinning by pores and decreasing temperature, while the force is determined by the grain boundary curvature. At this sintering stage, the grain boundary velocity must be controlled to avoid pore-boundary separation. If grains grow rapidly, pores can be trapped within the grains instead of moving along the grain boundaries and shrink. Figure 2.4 illustrates the process leading to pore isolation. Isolated pores result in slow densification by long-range bulk diffusion. This often leads to residual porosity.

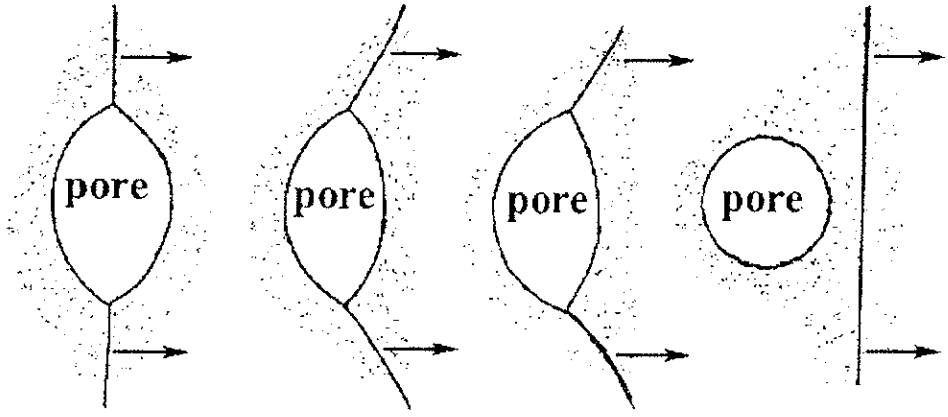

Figure 2.4 Grain growth and pore drag, leading to an isolated pore caused by high grain boundary velocity.

Sintering parameters

The factors that control solid state sintering are limited to five parameters. Increasing *temperature* will enhance the densification rate. The activation energies for surface, grain boundary, and bulk diffusion usually increase in that order (Kingery et al., 1976). Therefore, increasing the temperature often improves the densification because this favours lattice- and grain boundary diffusion mechanisms. A rule of thumb in the sintering field is to use a sintering temperature $\frac{2}{3}$ of the melting point (in Kelvin) of the material (Rahaman, 1995).

The *atmosphere* can alter the diffusivity of the rate-controlling species, for instance by influencing the defect structure of the materials. In some cases a particular atmosphere is chosen to avoid decomposition of the material or reduce evaporation of specific elements. Another issue to be aware of is the effect of an insoluble gas in the final stage sintering. Once the pores close, the internal gas pressure increases as the pore shrinks. The increasing pressure hinders full densification.

The *particle size distribution* can be critical for densification, and is the most important parameter for solid state sintering. The macroscopic- and microscopic driving force decreases with decreasing particle size. The different mechanisms of material transfer depend on square to fourth power of the particle size (McColm & Clark, 1988). Generalised, small particles lead to surface or grain boundary diffusion and large particles favour evaporation-condensation. Broad particle size distributions will increase the tendency for abnormal grain growth, where a few grains grow very fast, consuming smaller grains. Another relevant factor is the presence of agglomerates. (They are often generated in wet-synthesis methods, due to high surface forces during synthesis of the small particles.) Agglomerates introduce problems in the densification by causing an inhomogenous green body. Upon heating, the agglomerates sinter together and create large pores between the partially sintered particles. These pores are subsequently difficult to eliminate. The importance of particle size distribution and agglomerates is discussed in greater detail in Chapter 2.3. and 2.5.

Additions of a proper *dopant* to the sub-lattice of the ion whose transport is limiting the densification rate, can create vacancies and improve the densification kinetics. A dopant can potentially influence all the kinetic and thermodynamic factors in the sintering process.

Applying *pressure* introduces an additional contribution to the internal driving forces for sintering, which is specific to the densification. Less important, the pressure enhances particle deformation and particle-particle contacts, and thereby increases the densification. The application of pressure can allow a reduction in the sintering temperature of 300-500 °C compared to pressureless sintering. This can help avoid the region of rapid grain growth which can lead to residual porosity and mechanically weak materials.

2.3 Pore stability

Pores are subjected to the same driving forces as the grains, and this affects the stability of the microstructure. Differences in the pore curvature lead to growth of the larger pores at the expense of the smaller ones. The surface curvature depends on the number of grains surrounding the pore and on the dihedral angle. Pore coarsening is known as Oswald ripening, and will not give further densification of the body. The analogous theory of grain coarsening is also referred to as Oswald ripening. The phenomenon was first observed for grain growth by Rhines et al. (1950). The basic theory of Oswald ripening was developed independently by Lifshitz and Slyozov (1961), and Wagner (1961). These studies are often referred to as the LSW theory.

The transition from convex to concave pore surfaces is defined by a critical coordination number, R_c. Figure 2.5 illustrates pore stability in two dimensions for different grain coordination for an equilibrium dihedral angle of 120 °. Pores with three neighbours will shrink, because of the convex curvatures. Six neighbouring grains give stable pores, while pores coordinated by a larger number of grains will expand because of the concave surface curvature (Rahaman, 1995).

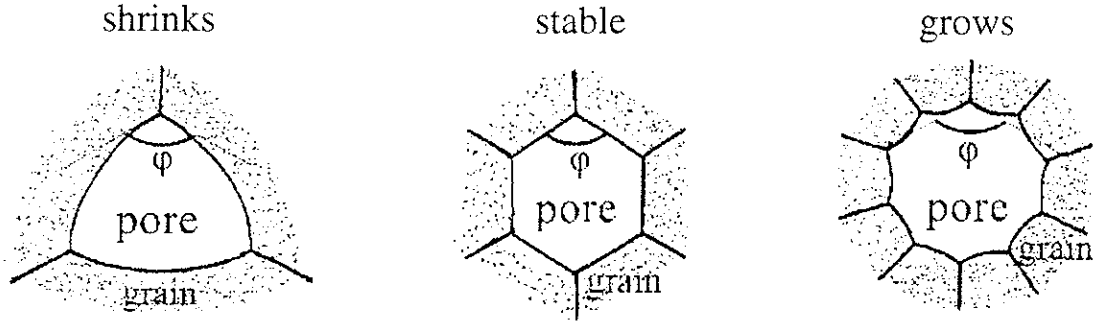

Figure 2.5 Pore stability in two dimensions for an equilibrium dihedral angle (φ) of 120 °.

The critical coordination number is a function of the dihedral angle as shown in Figure 2.6 (Kingery & Francois, 1967). Whether a pore shrinks or grows depends on the ratio of pore size to grain size (i.e. R_c). Large pores and small grains favour pore growth, while the opposite situation favours densification. Agglomerates can often cause large pores. Kingery & Francois have modelled

the pore stability of oxides as a function of the pore to grain size ratio as shown in Figure 2.7.

The pore stability is always relative to pores in the surroundings. This means that a pore with convex curvatures can expand if a pore with higher convex curvature is near to it. Where the material from the unstable pore with convex curvature is transported to, is a trade-off between the distance to a possible sink and the curvature of the pores in the local environment. Matter can be transported to an apparently stable pore if the bulk diffusion is slow and the distance to an unstable pore with concave curvature is relative long.

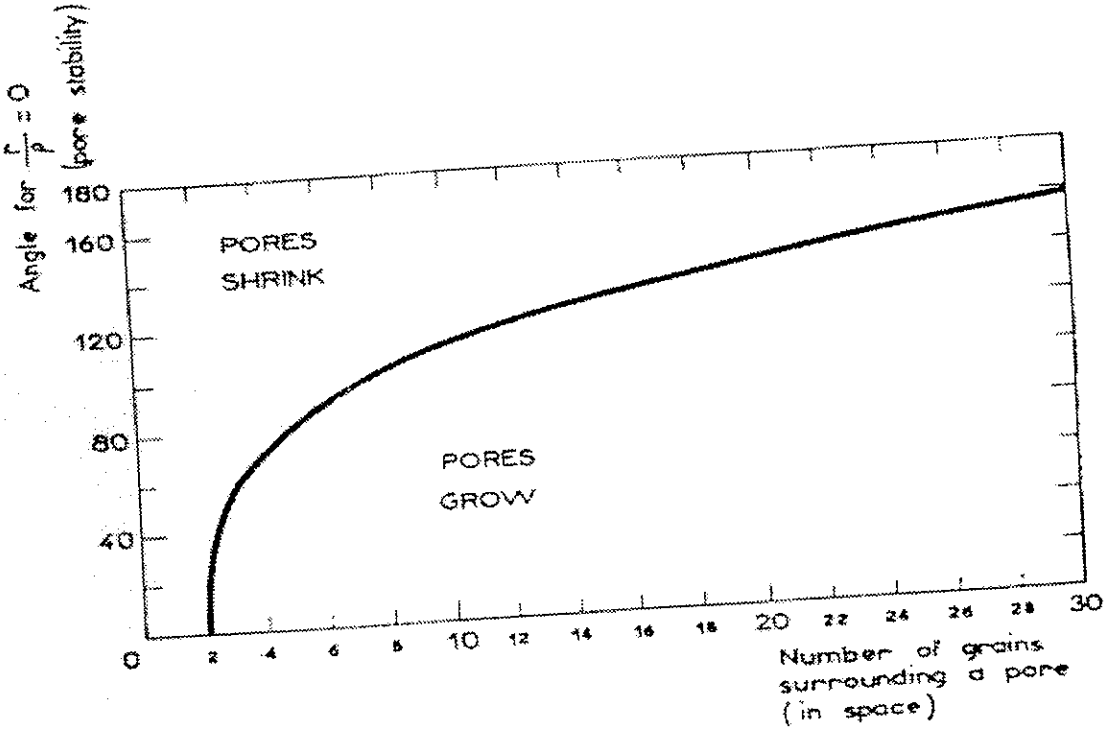

Figure 2.6 Pore stability for oxides as a function of the coordination number (Kingery & Francois, 1967).

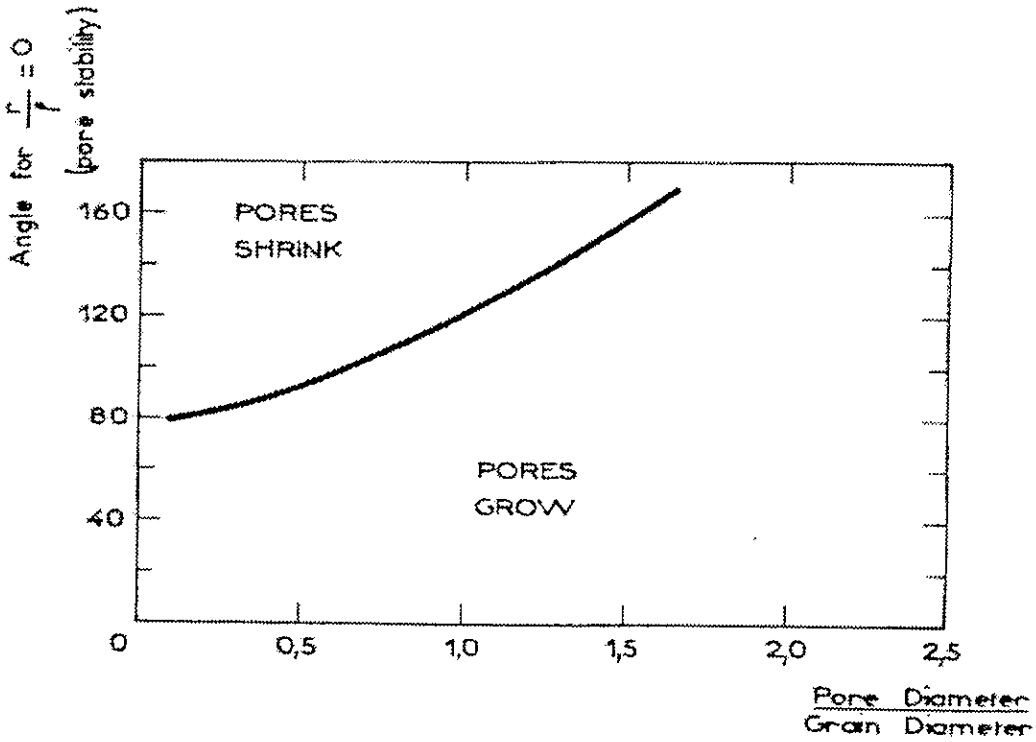

Figure 2.7 Pore stability for oxides as a function of the pore to grain size ratio (Kingery & Francois, 1967).

Swelling

Several factors that inhibit full densification are reported, especially trapped gas in the pores (German & Churn, 1984). The insoluble gas can be introduced from the sintering atmosphere or from a decomposition reaction which gives products with high vapour pressure. Densification stops when the pore pressure equals the surface tension force. If the pressure increases further, the pore will start to swell or the specimen will crack.

A powder with two different particle size fractions can result in two different sintering rates in the initial stage, followed by pore growth (Whittermore & Sipe, 1974). As the fine particles densify, large voids develop through the interstices of the large particles. These large pores have higher coordination number than R_c and will continue to grow, and matter is transported away. If the diffusion rate of cations is fairly high, as it must be during sintering, a total expansion of the sample may occur due to mass transport from the body to the external surface. Ultimately, this behaviour will lead to a pore free surface of the material. The topography of the external surface with the

generally weak concave curvatures may affect the swelling behaviour. The dihedral angle and the grain size at the surface influence the pore stability.

Grain growth can have detrimental effects on the mechanical properties of high-density membranes. It can also be favourable in the densification process (Harmer & Zhao, 1988). Consider an unstable pore with several surrounding grains. Grain growth will reduce the coordination number of the pores. The remaining pores could then have reduced the coordination number to less than R_c, as illustrated in Figure 2.7. This reasoning leads us to assume that grain growth during sintering can be helpful to avoid pore swelling.

German (1996) has described coarsening where pores become too large and continue to grow. He reports that this will occasionally lead to a total swelling of the compact. Enhancement of the grain growth to inhibit swelling of the ceramic material is also briefly described. However, no detailed description of the sintering progress is given, nor any examples of systems which expand.

2.4 Experimental

2.4.1 Powder synthesis

Powders of various compositions were synthesised by three different methods: conventional solid state reaction, wet complexing route and a continuous spray pyrolysis technique. The idea was to obtain various powder morphologies to study the effect on the sintering properties and the final microstructure. The powders were synthesised from the commercial chemicals listed in Appendix 2. Powder morphologies which sintered to high density membranes determined the standard synthesis method for processing membranes.

Conventional route

A standard ceramic synthesis method with high purity materials of $SrCO_3$, iron, and cobalt as starting materials was used to prepare powders of general composition $SrFe_{1-x}Co_xO_{3-\delta}$. The starting mixture was initially ball milled for 3 hours followed by heating to 900 °C in an alumina crucible and calcined for 10 hours in flowing air. The powder batch was subsequently ground in a planetary mill. Calcination and milling were repeated until the solid state

reactions were completed. The progress was monitored by x-ray diffraction (Chapter 2.4.2) of the intermediate powders.

Wet complexing route

Powders of $SrFe_{1-x}Cr_xO_{3-\delta}$ ($0 \leq x \leq 0.10$) were prepared by thermal decomposition of precursor complexes obtained from standardised metal nitrate solutions with ethylenediaminetetraacetetic acid (EDTA) or citric acid as the complexing agent.

The metal nitrates were dissolved in distilled water and diluted to solutions of approximately 1 molar. Accurate determinations of the cation concentration of stock solutions were performed indirectly by analysing the nitrate quantity by ammonia distillation (Kjeldahl method) (Skoog & West, 1976). The nitrates were reduced to ammonium ions with Devarda's alloy (50 % Cu, 45 % Al, 5 % Zn) as the reducing agent, in a strongly alkaline solution. The stock solution of iron nitrate was also analysed gravimetrically to verify the analysis results of the ammonia distillation. The standard deviation of the molarity of the stock solutions was calculated to less than ± 0.003 M. Graded cylinders and volumetric pipettes were used to obtain the desired nominal composition of cations.

Sulphur impurities were observed in some of the batch synthesised powder, appearing as $SrSO_4$ on the surface of thermally etched membranes. The sulphur content in the EDTA used for the synthesis was determined to 140 ppm by ICP-AES analysis (Chapter 2.4.2), which is sufficient to explain the amount observed. Sulphur was not detectable in the citric acid. Citric acid was therefore used for complexing metal solutions in the batch synthesis.

The different metal ion solutions were added in the appropriate proportions and mixed with the citric acid. Excess complexing agent was used with a ratio of citric acid/equivalent cations equal to 2. The solution was left for a few hours at 150 °C to remove water and achieve good complexing of the cations. At this point the heating was carefully controlled to prevent decomposition of the citric acid. The solution was dried over night at 160 °C, and the porous product crushed before organic matter was removed by subjecting the sample to 500 °C until glowing had ceased. After the organic burn out, the char was crushed manually before the powder was calcined at 700-1000 °C for several hours (usually 10 hours) in flowing air. The

maximum quantity was approximately 50 gram product in each batch synthesis.

Spray pyrolysis technique

Oxide powders of $SrFe_{1-x}Cr_xO_{3-\delta}$ ($0 < x < 0.05$) were prepared by continuous thermal decomposition of standardised metal nitrate solutions. The spray pyrolysis process basically consists of the atomisation of a precursor solution into droplets that are driven by a carrier gas through a tube furnace. Inside the furnace the solvent evaporates and the pyrolysis reaction occurs which leads to the powder product. The powder is collected in a filter bag with an ejector or other equipment generating a small under-pressure. The spray pyrolysis technique is well established and details are described in the literature (Messing et al., 1993; Gordes et al., 1995). Figure 2.8 shows a sketch of the spray pyrolysis equipment (Norsk Hydro ASA[1]) used in the present work.

[1] The engineering workshop, Corporate Research Centre, Porsgrunn, Norway.

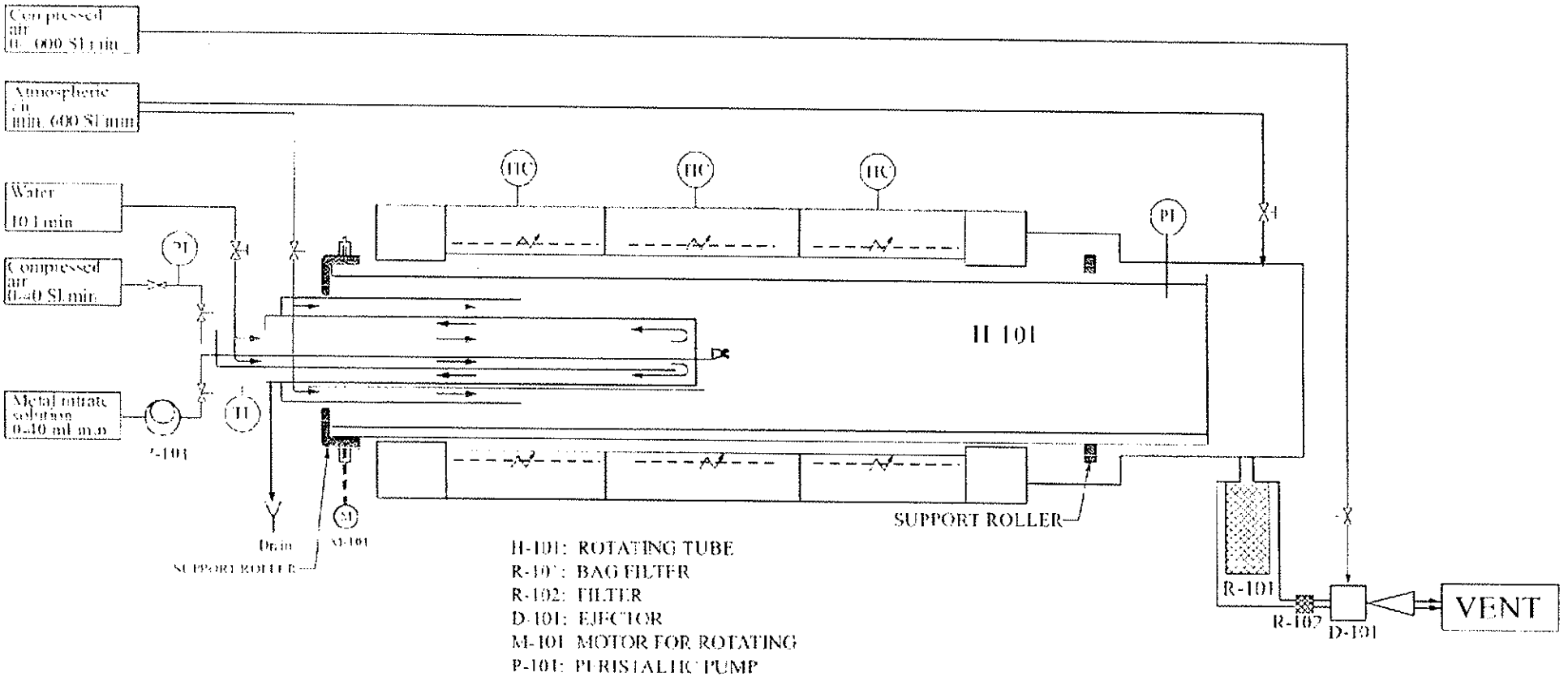

Figure 2.8 Sketch of the spray pyrolysis equipment. The instrument coding is explained in Appendix 3.

The different metal ion solutions were added to the desired nominal composition and the solutions were diluted to approximately 0.7 M. The bottle with the mixed solution was stirred with a propeller for five hours to ensure proper homogeneity.

The mixed feed solution was sprayed through an air atomizing nozzle into the hot zone of a rotating tube (Ø17 cm). The nozzle is placed at the end of a water cooled lance. The tube rotated at a speed of 10 rpm. A peristaltic pump (Watson Marlow[2], PX705) fed the solution at a rate of 10 ml/min. The solution was driven through the nozzle by pressurised air (2 bar) and was sprayed in a cone angle of approximately 18 °. The temperature was set to 750 °C in the hot zone. Near the nozzle a type K (Ni/Cr-Ni/Al) thermocouple measured the temperature to 650 °C. The powder was collected in a Gore-Tex bag at about 150 °C, with a NorClean[3] ejector.

The as-produced particles ranged from approximately 100 µm agglomerates to sub-micrometer primary particles. Particles smaller than 1 µm are entrained in the exhaust gas and represent losses of approximately 10 wt%. On-line gas analysis of the exhaust, when heating the powder proved this product contained unreacted nitrates and carbonates. The analysis of decomposed products such as CO, CO_2, and NO_x was performed by a quadrupole mass spectrometer (Balzers[4], QMG 421C). Single phase powder were obtained by calcining at 900 °C for 5 hours in flowing air. Powders used for some selected sintering measurements were annealed in vacuum (P $\approx 10^{-5}$ bar) at 700 °C to remove carbonates without altering the powder morphology.

The spray pyrolysis equipment used has a powder production capacity of approximately 10 kg/day, and a maximum temperature limit of 1100 °C.

2.4.2 Powder characterisation

After calcination the resulting powders were examined by X-ray diffraction (XRD) for phase identification and structural analysis. Spectra were recorded

---

[2] www.watson-marlow.com, Wilmington, USA.
[3] www.norclean.com, Sandefjord, Norway.
[4] www.pfeiffer-vacuum.de, Asslar, Germany.

on a Rigaku[5] Miniflex diffractometer with Mn-filtered $Fe_{K\alpha}$ radiation and 2θ in the range 10-130°. The iron target was used to decrease the background fluorescence from the iron-containing samples, compared to $Cu_{K\alpha}$ radiation (Klug & Alexander, 1974). The step size was set to 0.02° with a counting time of 3 seconds for phase identification and 6 seconds for structural analysis. Silicon has been used as an internal standard in experiments for the structural refinement. Cell refinement was performed on a XRD pattern-processing program, Jade[6].

Judging from XRD, single phase powders of batch synthesis $SrFe_{1-x}Cr_xO_{3-\delta}$ ($0 \leq x \leq 0.1$) were obtained at 750 °C, but gas analysis of the exhaust during heating indicated the release of small amounts of unreacted carbonates and nitrates up to 900 °C. The powders were generally calcined at 900 °C for 10 hours in flowing air.

The powder morphologies were studied with a JEOL[7] JSM-840A scanning electron microscope (SEM). For the spray pyrolysis powders, the particle shapes (primary particles and agglomerates) were investigated at various stages in the processing. A laser diffraction particle size analyser (Coulter[8] LS 200) was used to analyse the particle size distribution (PSD) for investigation of the effect of different calcination and grinding procedures. The measurements were carried out in water with 1 vol% Na-hexametaphosphate as a dispersing agent, and with an internal ultrasonic treatment of 60 seconds prior to the analysis. Some problems were encountered when performing the particle size distribution analysis with regard to possible agglomeration of powder in water and uncertainty in selecting the appropriate shape and refractive index in the input file for particle size calculation.

The specific density of $SrFe_{1-x}Cr_xO_{3-\delta}$ ($0 \leq x \leq 0.10$) as a function of chromium substitution was determined from the crystallographic lattice parameters obtained from XRD results of powder samples. Crystallographic density (D_x) is calculated from the formula:

---

[5] www.rigaku.com, Tokyo, Japan.
[6] www.materialsdata.com, Livermore, CA USA.
[7] www.jeol.com, Tokyo, Japan.
[8] www.beckmancoulter.com, Fullerton, CA USA.

$$D_X = \frac{M_W \cdot Z}{V_X \cdot N_A} \qquad [2.5]$$

where M_W is the molecular weight of the sample, Z is the number of these formula in a unit cell, V_X is the volume of the unit cell and N_A is the Avogadros number.

Elemental composition and impurities of tracers have been examined by X-ray fluorescence spectrometry, (Phillips[9] PW 2400) and inductively coupled plasma-atomic emission spectroscopy, ICP-AES (Thermo Jarrell Ash[10] 61E).

2.4.3 Sample preparation

The quality of the green body ceramic is influenced by the powder morphology and the pressing technique. Some efforts were focused on describing the variation in PSD by different synthesis techniques, calcination temperatures and grinding procedures.

Calcined powders (900 °C/10h) were ground in isooctane in a planetary mill (Retsch[11] PM 400), using grinding media and a container of yttria stabilised zirconia. A standard grinding recipe was used to achieve a proper morphology, consisting of 15 g powder, 20 ml isooctane and 20 ml of Ø3 mm ZrO_2 balls. The mixture was ground in a 50 ml ZrO_2 lined container. Grinding conditions of 340 rpm in 30 minutes were used. ICP-AES analysis of the powder ground for more than 30 minutes showed traces of zirconia from the grinding media. The grinding time was reduced when examining the effect of broader particle size distribution on the sintering properties. In addition, ball milling overnight in a polyethylene bottle with media of acetone and Ø10 mm ZrO_2 balls was carried out in some few cases.

Organic additives were premixed into the ceramic powders to enhance the redistribution during compaction and to provide extra cohesion. In addition, the additives decrease the particle-particle friction. The powders were mixed

[9] www-eu.analytical.philips.com, Almelo, The Netherlands.
[10] www.tjasolutions.com, Winsford, England.
[11] www.labstars.com, Haan, Germany.

with two wt% polyacrylate binder diluted in ethyl acetate (1:1 of B-66 + B-72). The powder and the binder were mixed manually in an agate mortar followed by evaporation of the ethyl acetate at room temperature. The dried powder was sieved (60 mesh) into the die to avoid lumps of powder. This enhanced the flow properties of the powder. The die was coated with diluted paraffin wax prior to filling. The filled die was put on a vibration plate for a few seconds in order to assure good compaction of the powder. Generally, non-uniform density of the green body caused warping and cracking during the sintering process.

Small pellets with a diameter of Ø7-13 mm and a thickness of 1-7 mm were normally obtained by doble-action uniaxial cold pressing at 100-200 MPa. Some larger membrane discs were pressed uniaxially (< 20 MPa) followed by cold isostatic pressing (Loomis[12] #9820) at 140 MPa. Burn out of organic additives was performed at 500 °C with a heating rate of 3 °C/min. The density of the green body was measured geometrically after the organic burn out. The pressed pellets have typically 58-60 % of theoretical density. The quality of the green bodies was inspected with an optical microscope. Samples with visible inhomogeneities were rejected.

2.4.4 Sintering studies

Sintering studies were performed with a Bähr[13] DIL 802 dilatometer, generally with a heating rate of 10 °C/min in stagnant air. The dwell time at maximum temperature (900-1300 °C) was selected from 1-20 hours. The samples were cooled to room temperature at 2-10 °C/min. Investigations of the sintering behaviour at different oxygen partial pressures were performed in an enclosed chamber with flowing gas of approximately 50 ml/min. Different P_{O_2} was obtained by using oxygen, air or nitrogen gas. Uniaxially pressed pellets of Ø7.5 mm diameter and 5-7 mm length were used in the sintering experiments. Spacers made from platinum foil were used on both sides of the sample to avoid reaction with the alumina push rod and the end plate.

---

[12] www.loomisproducts.com, Levittown, PA USA.

[13] www.baehr-thermo.de, Hüllhorst, Germany.

2.4.5 Characterisation of the microstructure of sintered samples

Microstructures of dense materials were investigated using SEM and optical microscope. Energy Dispersive Spectroscopy, EDS (Noran[14] Vantage DI+) was used for elemental analysis to check for unexpected and unidentified phases on the surface of the samples.

The density of sintered samples were determined by the Archimedes method in isopropanol at room temperature. Density variations of the isopropanol, due to small temperature changes in the laboratory, have been taken into account in the calculation.

2.4.6 Thermal and chemical expansion

The thermal expansion coefficient (α) of membranes were determined in a Bähr dilatometer at a heating rate of 1 °C/min to 900 °C in stagnant air. The sample geometry was bars of approximately 8 mm length and 2-3 mm width. It is estimated that the uncertainty in the measured α value is $< \pm 0.5 \cdot 10^{-6}$ K^{-1}. The uncertainty is relatively high for these short sample lengths, compared to more standard experiments where sample lengths are > 15 mm. Calibration data was obtained by measuring a standard sapphire sample under similar conditions as the membrane materials.

The chemical expansion of dense materials was assessed by measuring the change in sample length while subjecting it to gas atmospheres with different oxygen partial pressures ($\Delta \log P_{O_2} \approx 3.3$). Constant temperatures in the range 700-900 °C were selected. The experiment was carried out by heating the sample at 1 °C/min in a flow of synthetic air while measuring the thermal expansion. The sample was then held at constant temperature and the atmosphere was changed to nitrogen. When the membrane had expanded to equilibrium, the atmosphere was changed back to air and the contraction was recorded until equilibrium was reached. The measurements at low oxygen partial pressure are subject to some uncertainty, due to the use of non buffered gas of nitrogen and possible air leakage.

[14] www.noran.com, Naarden, The Netherlands.

Most often in this type of experiment, the system is pumped out prior to changing the gas. This reduces the measuring time and thereby minimises the uncertainty due to drift in the measurement. This is not feasible with the $SrFeO_{3-\delta}$ based materials due to cracking of the membranes when exposed to a rapid change in the oxygen partial pressure. In these experiments, a twin push rod set up was used to correct for the dimensional change in the alumina push rod. The change in length arose from the alteration in the temperature profile when changing the gas composition. The sample geometry was the same as for the thermal expansion measurements. Indeed, measurements of thermal and chemical expansion were generally performed in one experiment, by first measuring the α value while heating up and thereafter investigating the chemical expansion at constant temperature. The gas flow in the experiments was maintained at 50 ml/min. The uncertainty in the measured change in relative length was estimated to be as high as 5-10 %. The evaluation is based on variation in results of different parallels.

2.4.7 Oxygen nonstoichiometry

The relative change in oxygen vacancy concentration of $SrFe_{1-x}Cr_xO_{3-\delta}$ ($0 \leq x \leq 0.05$) was conducted by thermogravimetric analysis (TGA). The temperature dependence was studied in air in the range 200-1000 °C. A combined instrument of TGA and differential scanning calorimeter (DSC) was used in the experiments (Netzsch[15] STA 409). The relative change in defect concentration ($\Delta\delta$) of $SrFe_{1-x}Cr_xO_{3-\delta}$ as a function of Cr-substitution was measured by alteration of the gas stream from air to nitrogen ($\Delta \log P_{O_2} \approx 3.3$) isothermally in the temperature range 700 - 900 °C. The gas flow in the experiment is maintained at 100 ml/min. The measurements at low pressure are subject to some uncertainty, due to the use of non buffered gas of nitrogen and possible air leakage.

The absolute oxygen stoichiometry of $SrFeO_{3-\delta}$ was found by reducing the phase in diluted hydrogen at 1000 °C ($P_{O_2} \approx 10^{-17}$ bar). The perovskite decomposes to SrO and Fe under these conditions. The uncertainty is estimated to maximum ±0.08 mg. This is due to noise generated by variation in the ventilation system and long term drift.

---

[15] www.ngb.netzsch.com, Selb, Germany.

The absolute oxygen content of $SrFe_{1-x}Cr_xO_{3-\delta}$ ($0 \leq x \leq 0.10$) was estimated from the measured oxygen content of $SrFeO_{3-\delta}$. This data was used in the calculation of the crystallographic density. It is assumed that the ratio of the concentrations of Fe(IV) and Fe(III) is independent of the substitution level in the perovskite (ideal solution). Chromium valence was set constant to Cr(III) at these low substitution levels.

2.5 Results and discussion

2.5.1 Characterisation of $SrFeO_{3-\delta}$

Successful sintering of a dense membrane often depends on small particle size and a narrow particle size distribution in the powder.

The different synthesis routes lead to different particle sizes for $SrFeO_{3-\delta}$ powder. Conventional methods led to the largest crystallites and the spray pyrolysis technique to the smallest ones. Powder from spray pyrolysis contains spheres and other shaped agglomerates in the size range 1-100 μm with crystallites in the sub-micron range. A micrograph of spray pyrolysed $SrFeO_{3-\delta}$ powder is shown in Figure 2.9.

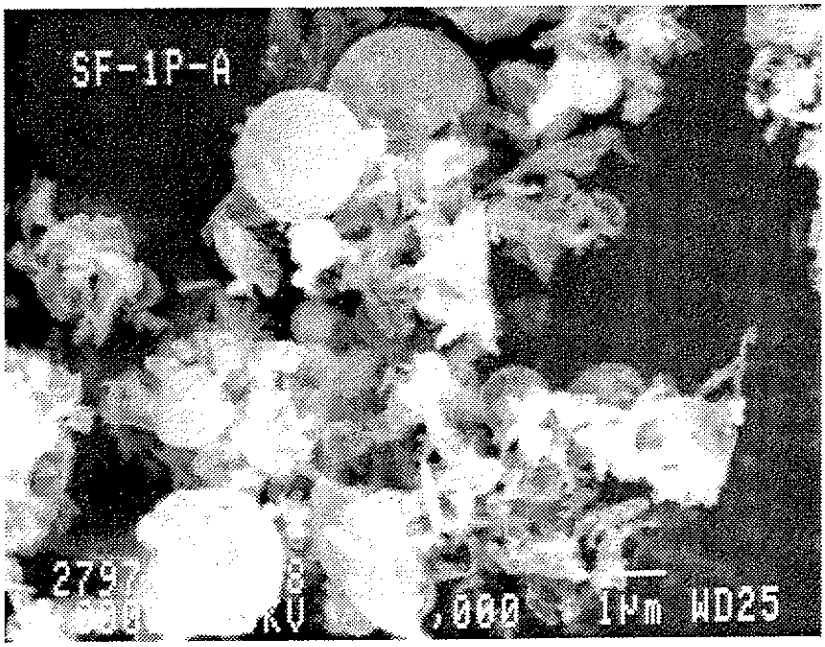

Figure 2.9 SEM micrograph of $SrFeO_{3-\delta}$ powder, spray pyrolysed at 700 °C.

This particular powder batch, with nominal composition $SrFeO_{3-\delta}$, is thoroughly studied by Kleveland et al. (2001). They have reported the powder to be nonstoichiometric with a Sr/Fe ratio of 1.05. XRD analysis indicated single phase powder, but atomic absorption spectroscopy implied a nonstoichiometric composition. Analytical instruments which can determine the ratio of the cations in the prepared oxides to a satisfactory level of accuracy <1 % are not known. To prepare materials with the intended Sr/Fe ratio we had to rely on the standardised cation solutions and the concentrations of the raw materials stated by the suppliers.

A fraction of the agglomerates from the spray pyrolysed powders were difficult to grind. Hence, milled powders were characterised by a bimodal particle size distribution of small primary particles and larger agglomerates. Figure 2.10 illustrates the particle size distribution of spray pyrolysed $SrFeO_{3-\delta}$, processed by various grinding procedures. It appears that a fraction of hard agglomerates is formed in the spray pyrolysis.

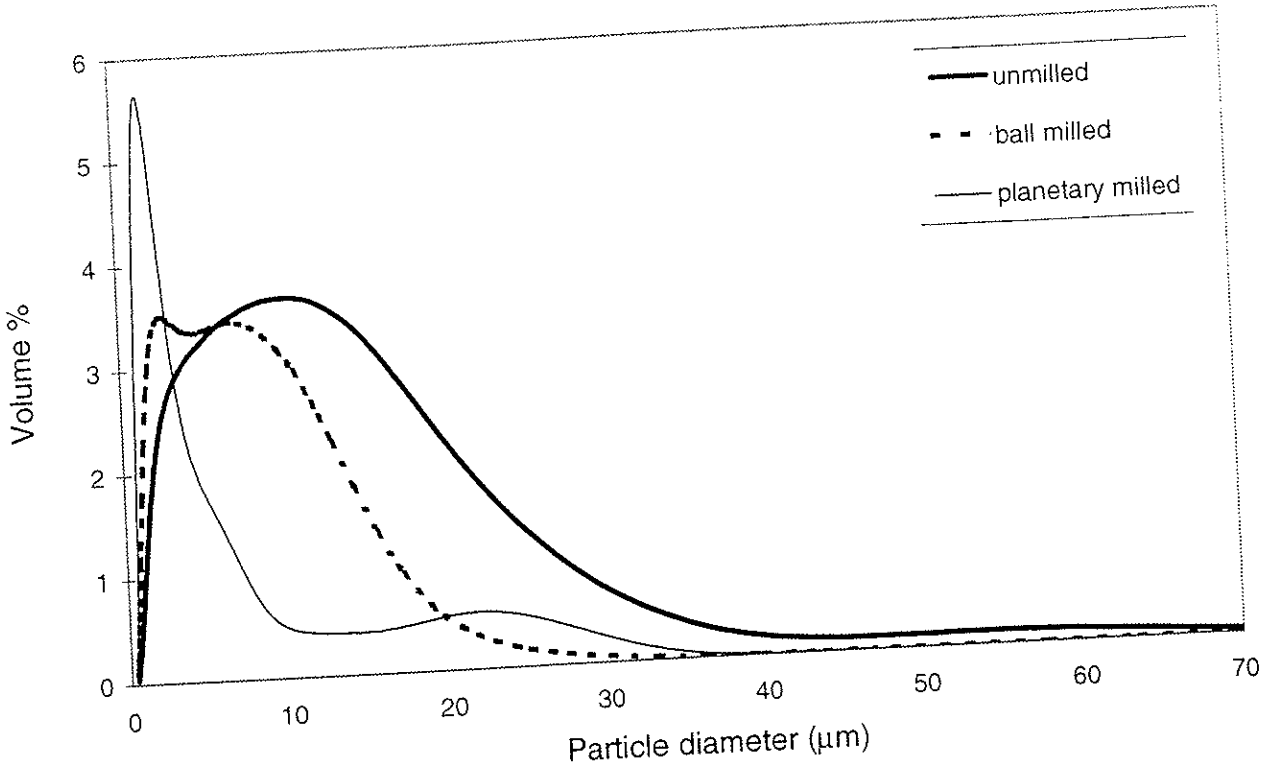

Figure 2.10 Particle size distribution of spray pyrolysed $SrFeO_{3-\delta}$ powder, calcined at 900 °C for 10 hours.

The wet complexing route produced softer agglomerates and a more Gaussian particle size distribution. The conventional route gave narrow and Gaussian distributions, but the synthesis process was time consuming. Single phase $SrFeO_{3-\delta}$ was obtained by repeating the calcination and regrinding step 3-4 times. The wet complexing synthesis technique is used as the standard route for producing membrane materials for the present work. An optimal grinding procedure was obtained by wet milling in a planetary mill. The particle size distributions of powders from the three different synthesis routes are given in Figure 2.11. The three powders were calcined at 900 °C/10 h followed by planetary milling at 340 rpm/30 min. The annealing and milling procedure was repeated three times for the powder made by the solid state reaction to obtain single phase powders.

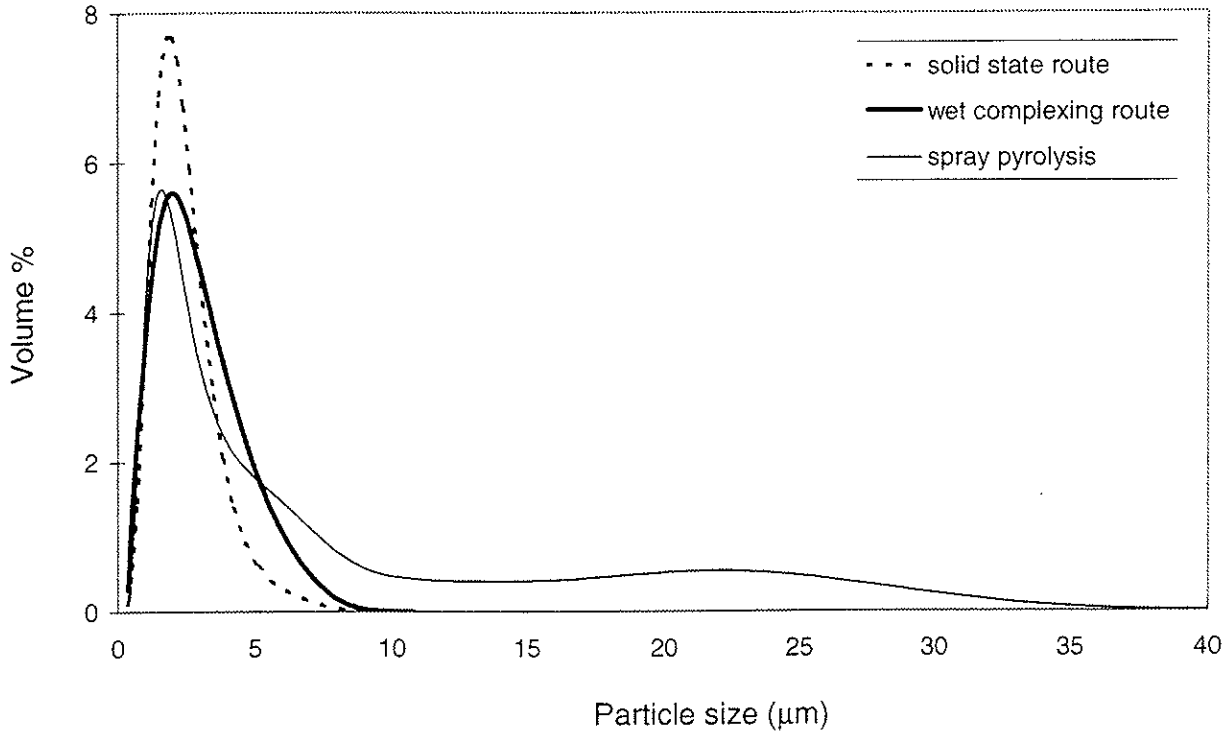

Figure 2.11 Particle size distribution of $SrFeO_{3-\delta}$ powder synthesised by different methods. Detailed description of the powder processing is given in the text.

Sintering behaviour

The surface of sintered samples of spray pyrolysed $SrFeO_{3-\delta}$ appears almost fully dense, as seen in Figure 2.12a. Density measured by the Archimedes method indicated however a lower density which was confirmed by SEM micrographs of the bulk structure. The microstructure of the porous interior of the sintered sample is clearly visible from the fracture surface shown in Figure 2.12b.

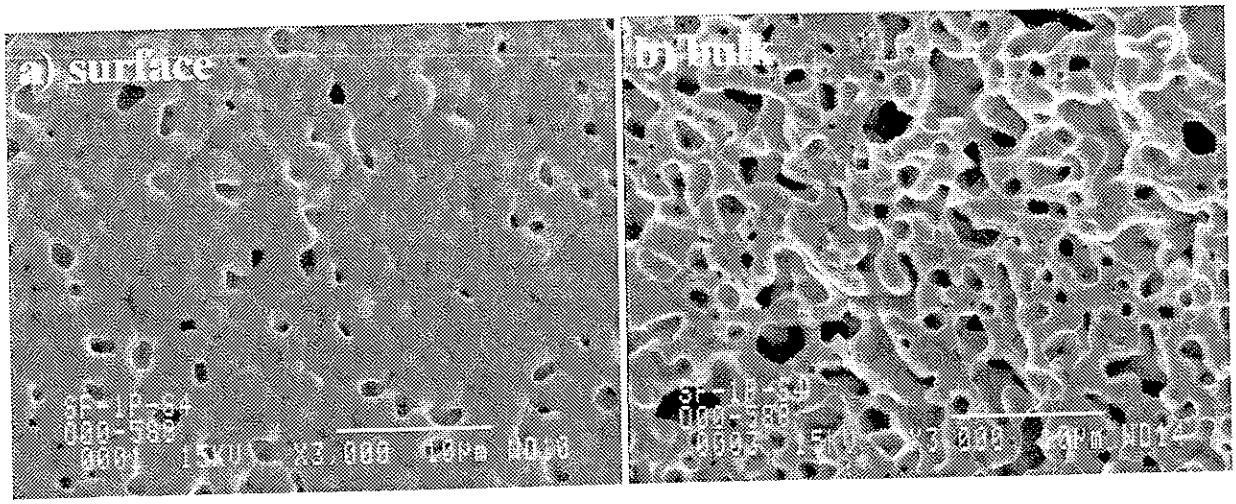

Figure 2.12 SEM micrographs of sintered $SrFeO_{3-\delta}$, showing the almost dense surface, and the fracture of the porous bulk. Maximum sintering temperature was 1250 °C.

The sintering behaviour of $SrFeO_{3-\delta}$ powder, calcined at 700 °C and with particle sizes from submicron to 40 μm, is shown in Figure 2.13. The measurement was carried out in air at a constant heating rate of 2 °C/min with a dwell time of 20 hours at 1260 °C. After the temperature reached 700 °C, the sintering process starts. The specimen reach approximately 94 % of theoretical density before starting to expand considerably at around 1100 °C. The sample continues to swell isothermally at 1260 °C for four hours until the density is down to approximately 74 %. Subsequently the material begins to densify again, but at a considerably reduced rate. The final density never reaches the maximum density the sample had before swelling became the dominant process. It should be noticed that densification began at an exceptional low temperature, and the density was 90% before the temperature reached 1000 °C. This indicates high mobility of the slowest moving ions even at 700 °C.

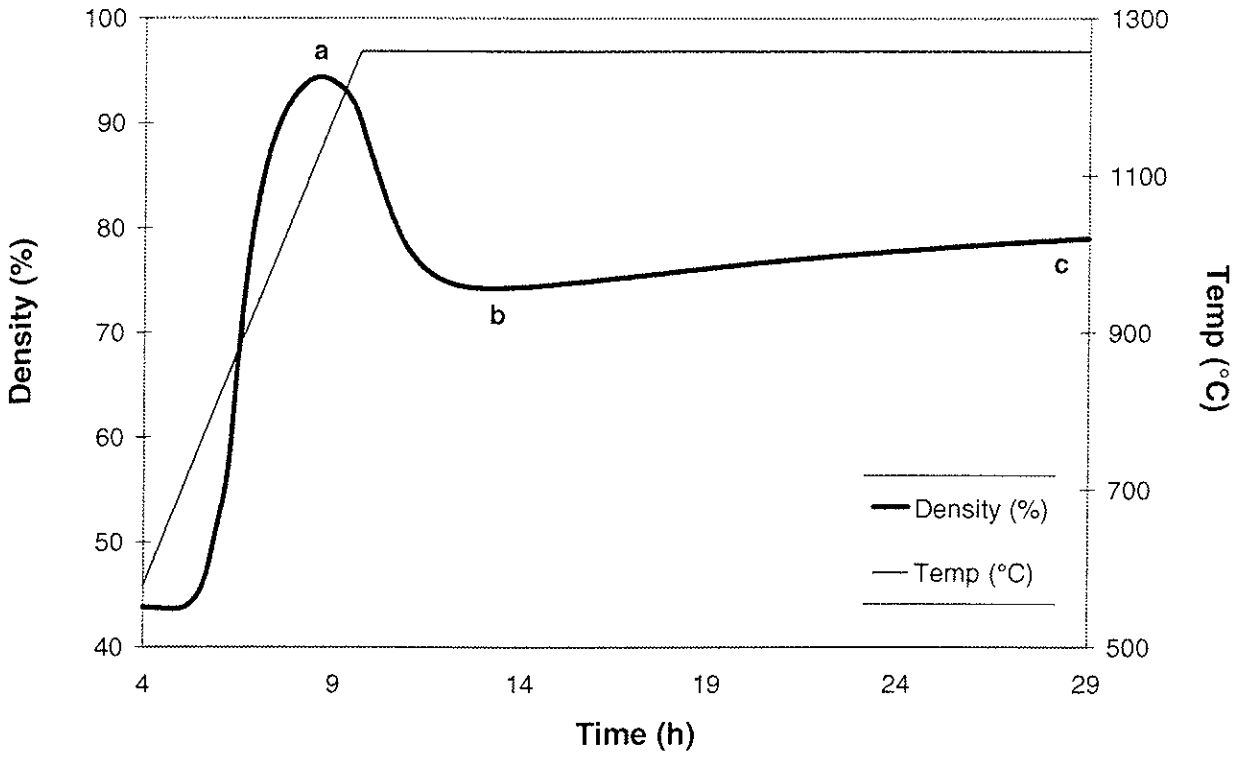

Figure 2.13 Sintering behaviour of agglomerated $SrFeO_{3-\delta}$ powder in air.

Swelling occurred simultaneously with densification and the sum of the effects dictate the sintering characteristic. In the dilatometer we observe the dominant process at each stage.

Additional sintering measurements were carried out at lower temperatures to achieve high density materials. Swelling also occurred in these experiments, but at lower swelling rates. Samples held for more than 30 hours at 1000 °C show slow swelling, which appears to continue indefinitely. This shows that the swelling behaviour is determined by both the temperature and the dwell time. Higher temperature accelerates the swelling.

Table 2.2 shows the densities of the samples at different stages in the sintering process, presented in Figure 2.13. Deviation from isotropic sintering due to the force of the push rod will give an error in the calculated density, from dilatometry data. Normally, the data measured with Archimedes method would be more reliable, but the samples cracked into small pieces during cooling and probably also contained microcracks. This decreased the reliability on the Archimedes density data. However, both measurements gave the same trend in density.

Table 2.2 Relative density of $SrFeO_{3-\delta}$ at different stages in the sintering process, marked in Figure 2.13.

Method	a (%) (max. densification)	b (%) (max. expansion)	c (%) (end of experiment)
Dilatometry	94	74	79
Archimedes	90	68	70

SEM micrographs at three different stages in the process (marked a, b and c in Figure 2.13) are shown in Figure 2.14. The microstructure characteristic of the different intermediate stages is obtained by interrupting dilatometer experiments at the relevant times. Unfortunately, the photo in Figure 2.14a shows a sample which is annealed approximately 5 minutes after maximum density was reached, and thereby has expanded 1-2 vol%. The micrographs illustrate the pore swelling behaviour given in Figure 2.13. There is no indication of abnormal grain growth.

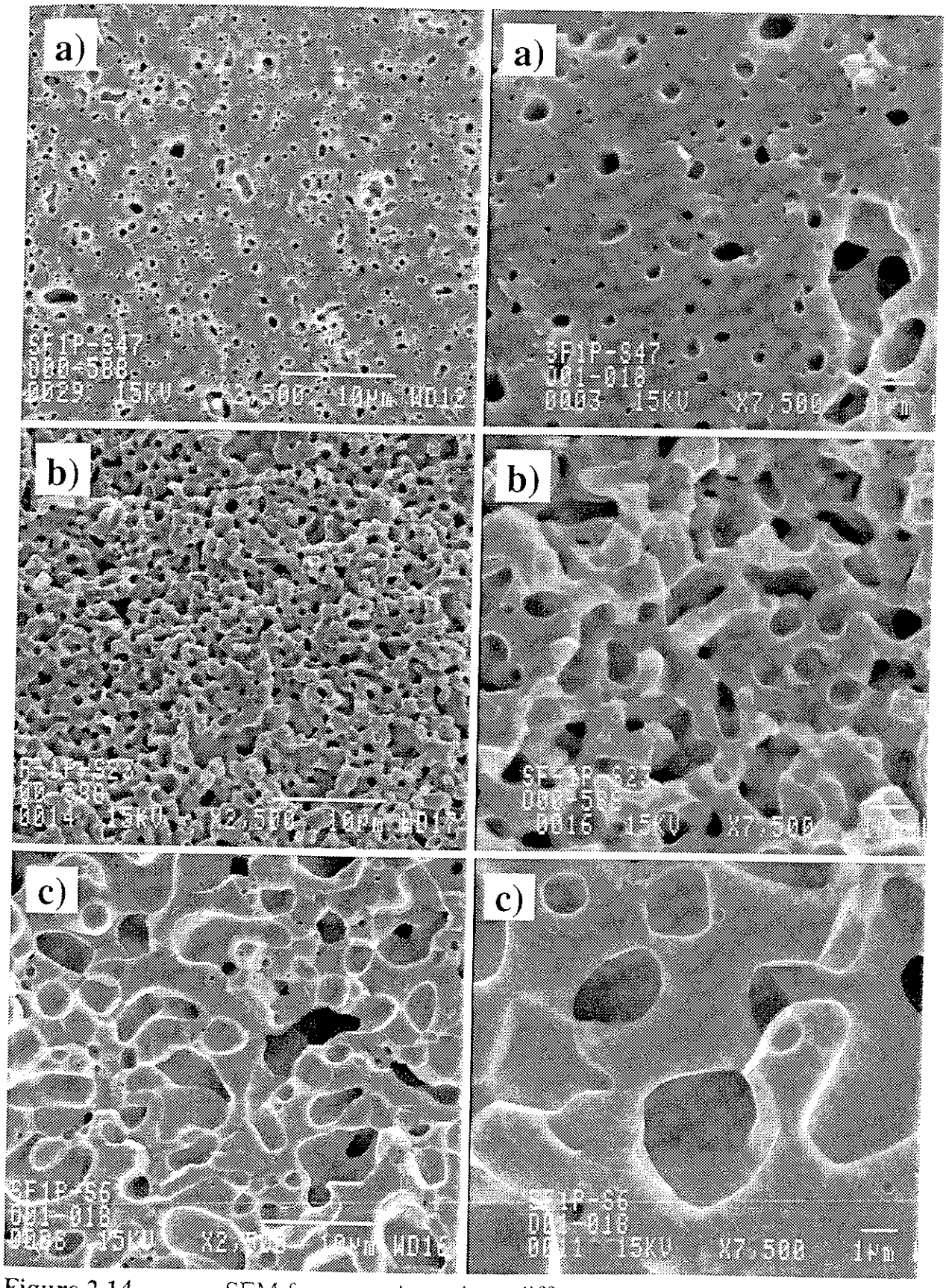

Figure 2.14 SEM fractographs at three different stages (two magnifications) in the sintering process of $SrFeO_{3-\delta}$. The stages are marked in Figure 2.13.

The fraction of small pores located at the grain boundaries decreases while the sintering continues. Likewise, there is a decrease in the fraction of small grains, while the fraction of larger grains seems to increase more than the fraction of larger pores. Normal grain growth occurs in the final part of the annealing. It should be noticed that the apparent grain and pore size, determined from the SEM photos, can be smaller than the real size due to the cut of grains and pores in the two-dimensional pictures.

Discussion of the swelling behaviour

The unstable large pores expand during sintering and causing the swelling behaviour. The large pores are created due to the existence of agglomerates in the green body. Both the small pores and the external surface act as a sink for the mass transport during the sintering. The pore growth process continues until there has been sufficient grain growth to increase the grain size relative to the pore size. The swelling process is not favoured when the pore coordination number become below R_c. Grain growth causes large pores to become stable and smaller pores to become unstable and disappear. This can explain the slow densification which is observed in the last part of the sintering measurements, shown in Figure 2.13. Another explanation for the apparently slow densification in the final part is creep. Nevertheless, Archimedes measurements indicate an increase in the sample density from position *b* to *c* in Figure 2.13.

Figure 2.15 shows micrographs of unstable pores shortly after the swelling is first observed in the dilatometer curve (Figure 2.13). The coordination number is > 10 in the two-dimensional picture of the large pores. With a suggested equilibrium dihedral angle of 100-120°, these pores have a coordination number higher than R_c and are probably unstable. The pores are > 3 times larger than the grains and will expand, according to the information given in Figure 2.7.

One possible transport mechanism for the pore swelling is expansion by opening the grain boundaries around unstable pores. This leads to a dihedral angle far from equilibrium and will accelerate the expansion. The large pore in Figure 2.15b expands by opening the grain boundary against a smaller pore. The pore shown in Figure 2.15c is an example of a very large hole created because of agglomerated powder. These cavities contain large number of unstable curvatures and will continue to swell.

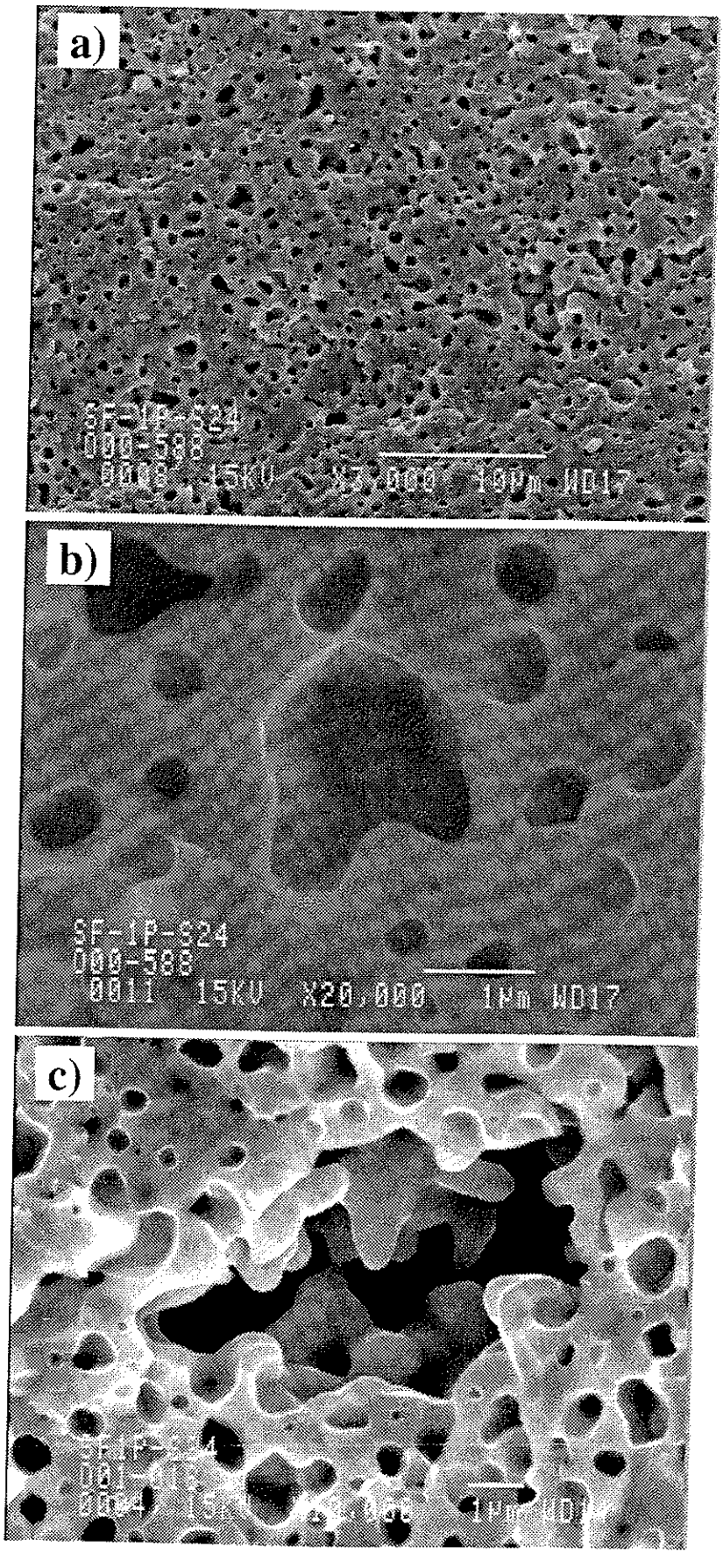

Figure 2.15 SEM micrographs of unstable pores in partially sintered $SrFeO_{3-\delta}$, when the swelling has initiated.

To study the sintering behaviour of an agglomerate-free powder, sintered (1100 °C) $SrFeO_{3-\delta}$ ceramics were reground. The load during uniaxial pressing of the pellets of this powder could be decreased by approximately 30 % relative to that required for the powder calcined at 700 °C, to achieve a green density in the same range. This is as expected, since a relatively higher load is necessary to break the agglomerates and obtain a suitable green density. In addition, extensive growth of the primary crystallites at 1100 °C leads to particles with significantly higher density when the sintered material is milled.

Figure 2.16 displays the sintering behaviour in air of agglomerate-free $SrFeO_{3-\delta}$ powder. The powder was annealed at 1100 °C and crushed to a particle size distribution shown in Figure 2.17, before the sintering measurement. SEM analysis confirmed that the powder was agglomerate-free. Notice that the maximum sintering temperature is increased by several hundred degrees to get densification. This can be explained by growth of the primary crystallites during the previous heat treatment and the coarser particle size. Almost 95 % relative density is obtained and no swelling was observed. The Archimedes method showed a density of 92 % for the sintered sample.

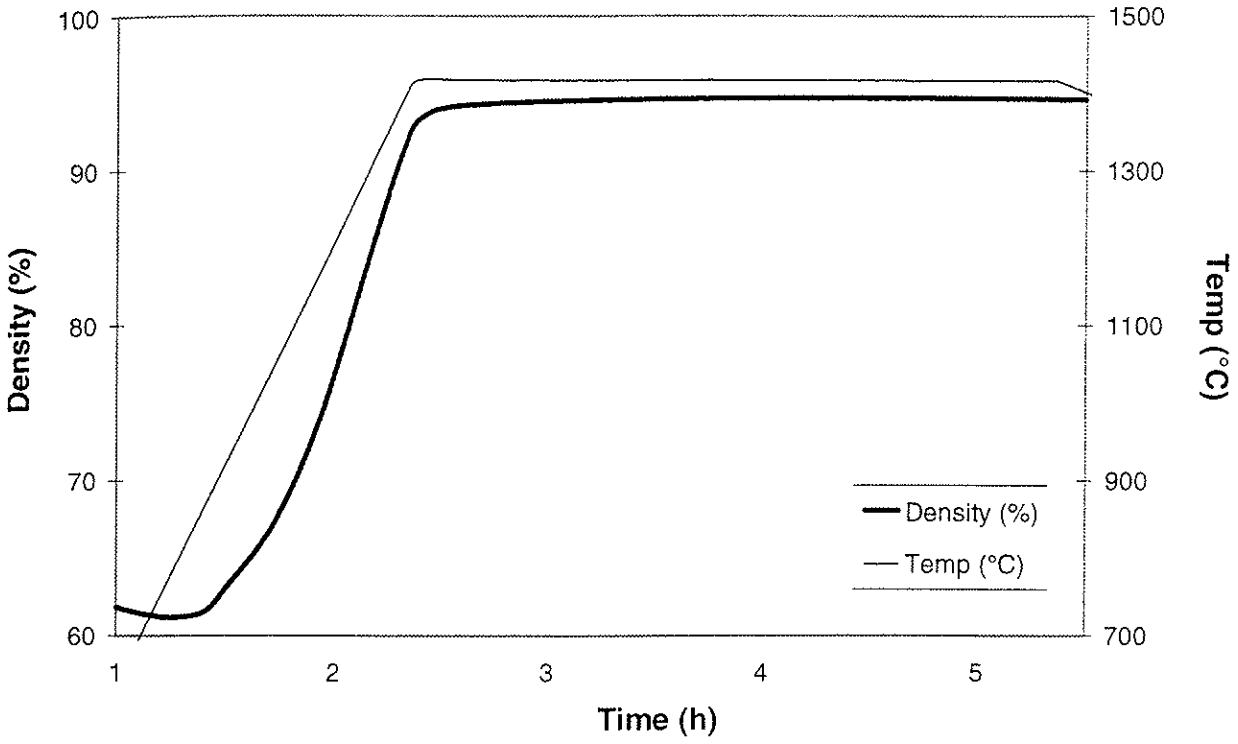

Figure 2.16 Sintering behaviour of $SrFeO_{3-\delta}$ in air. The powder is annealed at 1100 °C and reground before the sintering measurement.

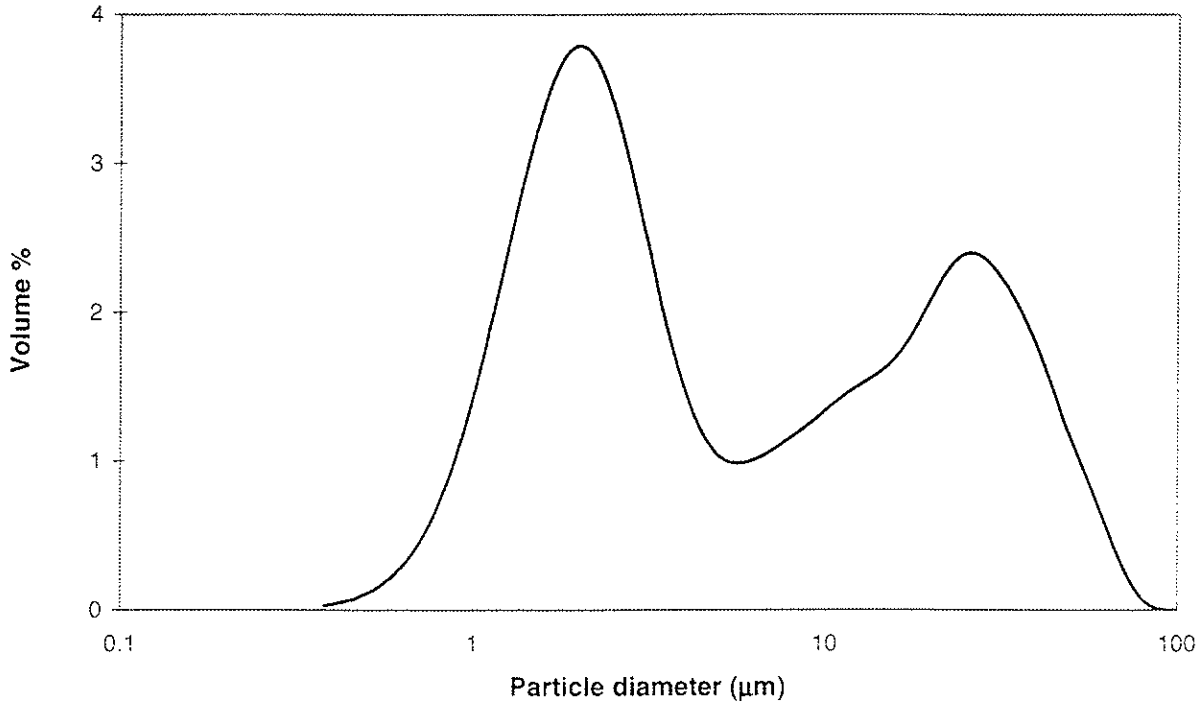

Figure 2.17 Particle sized distribution of $SrFeO_{3-\delta}$ powder calcined at 1100 °C followed by extensive regrinding.

Kleveland et al. (2001) have published a sintering study of $Sr(Fe_{1-x}Co_x)O_{3-\delta}$ materials and were able to obtain $SrFeO_{3-\delta}$ membranes with 98 % of theoretical crystallographic density. The authors observed swelling and claim that small variations in cation stoichiometry influences the sintering process dramatically. They explain the swelling behaviour of $SrFeO_{3-\delta}$ related material as caused by oxygen evolution. The expansion mechanism is related to heterogeneous phase equilibria, due to cation nonstoichiometry in the materials. The reactions which lead to evolution of oxygen gas are given by:

Fe-excess:

$$Sr_4Fe_6O_{13}\ (s) = Sr_2Fe_2O_5\ (s) + 2SrFe_2O_3\ (l) + O_2\ (g) \qquad [2.6]$$

Sr-excess:

$$Sr_{2+x}Fe_2O_{5+\delta}\ (s) = (1-x)Sr_2Fe_2O_5\ (s) + xSr_3Fe_2O_6\ (s) + \frac{\delta-x}{2}O_2\ (g) \qquad [2.7]$$

For the Fe-excess material, rapid swelling initiated at a temperature coinciding with the peritectic decomposition of $Sr_4Fe_6O_{13}$ at 1243 °C (Batti, 1962). The rapid mass transport is explained by viscous flow, because a liquid phase was formed. The swelling terminated after 15 minutes. The swelling of the Sr-excess material was observed to different. The sample started to expand slowly at 1250 °C and continued to swell isothermally at 1320 °C for 4 hours. Similar swelling behaviour is observed in the present work for a certain powder morphology. Kleveland et al. propose that the swelling is related to a narrowing solid solution range of SrO in $SrFeO_{3-\delta}$ with increasing temperature. $Sr_3Fe_2O_6$ will precipitate during heating and simultaneously produce oxygen gas. This mass transport is slower because only solid phases are present.

Sagdahl et al. (2000[I]) reported swelling in $LaFeO_3$ and explain the mechanism in relation to cation nonstoichiometry, as discussed above. However, recent work shows considerable expansion also in stoichiometric $LaFeO_3$ (Sagdahl, 2000[II]).

Kokhanovskii et al. (1999) describe the swelling observed in $Sr(Co_{1-x}Fe_x)O_{3-\delta}$ ($0.0 \leq x \leq 1$) by gas trapped in the pores, due to rapid evolution of oxygen

near the melting point of the material. They observed significant swelling of $SrFeO_{3-\delta}$ at approximately 1400 °C. According to the phase diagram of Batti (1962), the melting point of $SrFeO_{3-\delta}$ is near 1600 °C.

The explanation of the swelling by trapped oxygen gas is hard to reconcile with the results of Holt et al. (1999) who showed a rapid change in the oxygen vacancy concentration of $SrFeO_{3-\delta}$ membranes at the relevant temperature. Thermal gravimetry analysis in the present study showed a significant oxygen exchange in $SrFeO_{3-\delta}$ even at temperatures as low as 400 °C. This result is shown in Figure A4.1. Thermodynamic equilibrium of the sample occurs almost instantaneous at these high temperatures, while the swelling behaviour continues for hours.

Estimation of the maximum pressure in a pore at the relevant conditions is carried out from dynamic TGA results. The oxygen loss data is obtained from heating a dense $SrFeO_{3-\delta}$ membrane in air at 5 °C/min. The task was simplified to a plate with relevant thickness and infinite extension. The calculation is given in Appendix 5, and shows a maximum total pressure of 0.4 bar in the pores at the relevant sample geometry, temperature and heating rate. Consequently, the total pressure in the pore is lower than the ambient pressure, which is inconsistent with the explanation involving trapped oxygen gas.

Sintering experiments of $SrFeO_{3-\delta}$ in varying atmospheres were performed to study the swelling phenomenon. The influence of the atmosphere on sintering behaviour of $SrFeO_{3-\delta}$ is shown in Figure 2.18. Swelling is observed to a considerable extent and is nearly independent of the atmosphere. Altering the oxygen partial pressure can influence the sintering behaviour, since the cation diffusivity depends on the oxygen stoichiometry. This can explain the small difference in the observed sintering behaviour as a function of oxygen partial pressure. It is highly questionable if oxygen evolution can explain the pore swelling phenomenon.

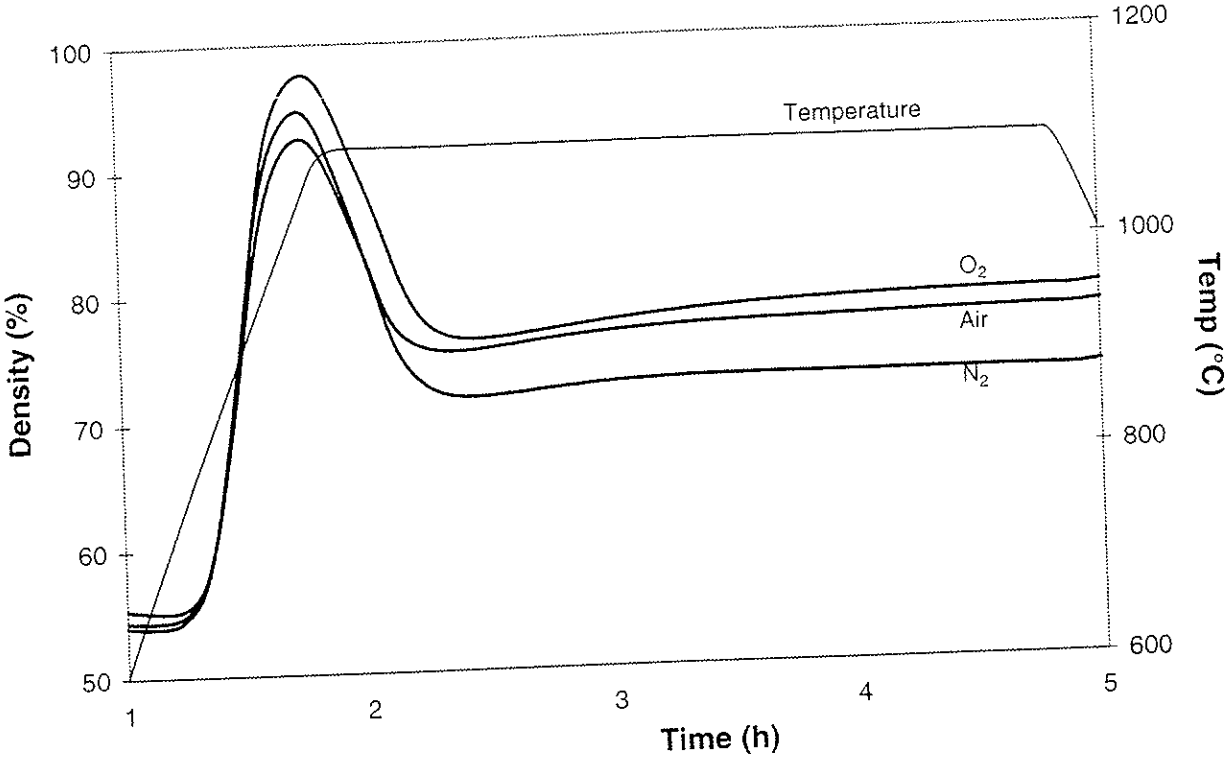

Figure 2.18 Sintering behaviour of $SrFeO_{3-\delta}$ at different oxygen partial pressure.

As discussed, grain growth should inhibit swelling according to the present hypothesis. Attempts to verify this conjecture were however not successful, without observing the swelling. To avoid swelling, the sintering temperature must be lower than 1000 °C. At these conditions the grain boundary velocity is negligible.

Different heating rates do not influence the swelling behaviour. The effect of different cation stoichiometry on the swelling behaviour was not investigated in the present study. Cation nonstoichiometry can influence the cation diffusivity, which may affect the swelling (and densification) behaviour.

In our research group, we have observed the influence of powder morphology on pore swelling, in other oxides as well. As an example, planetary and ball milled powders have shown a totally different swelling characteristic than a unmilled powders of the same batch. Figure A6.1 shows sintering behaviour of a $SrFe_{0.67}Co_{0.33}O_{3-\delta}$ powder, calcined at 900 °C and ground to various degrees. These results support the theory that the swelling behaviour is mainly determined by the powder morphology.

2.5.2 Characterisation of $SrFe_{1-x}Cr_xO_{3-\delta}$

Sintered samples of $SrFeO_{3-\delta}$ develop cracks during cooling at rates in excess of 1-5 °C/min. These cracks propagate from the surface towards the centre of the sample and are caused by chemical contraction of the perovskite due to the oxidation of Fe^{3+} to Fe^{4+} followed by a decrease in the oxygen vacancy concentration. A considerable increase in the sample length is observed at high temperature on changing from air to a nitrogen atmosphere. This is shown in Figure A7.1. The relative change in sample length was approximately 0.5 % at 900 °C, and corresponds to a volume increase of 1.5 %. This high level of chemical expansion causes cracking problems during heating and cooling as well as for the oxygen permeation experiments. The problem increases with increasing membrane thickness. Heating and cooling rates of densified membranes (L < 3 mm) must be less than 1 °C/min to avoid cracks, and the material should not be exposed to abrupt changes in the oxygen partial pressure. The critical temperature range for slow cooling is 200-800 °C. Considerable residual stress often remains in the membranes after sintering, causing a mosaic of cracks in the surface during grinding and polishing. The yield of crack free machined membranes increased by decreasing the cooling rate to 0.5 °C/min for the densified materials.

In the absence of mechanical property data, it is difficult to estimate the highest tolerable level of chemical expansion for oxygen permeable membranes. In general it can however be assumed that the chemical expansion of $SrFeO_{3-\delta}$ is too high to be useful in any commercial application. Even for fundamental studies it would be advisable to choose another model system, due to the difficult and time-consuming experimental work related to densification of $SrFeO_{3-\delta}$ materials.

Kharton et al. (1998) reported improved processing properties by introducing chromium in $SrCo_{0.90-x}Fe_{0.10}Cr_xO_{3-\delta}$. In addition, they observed improved mechanical properties and were able to optimise the microstructure. This reported work was the motivation to investigate chromium substitution in $SrFeO_{3-\delta}$.

Lattice parameter and crystallographic density

Cell refinements of $Sr(Fe_{1-x}Cr_x)O_{3-\delta}$ ($0.01 \leq x \leq 0.1$) show an increase in the crystallographic lattice with increasing chromium substitution. This is shown

in Figure 2.19. The calculation is based on cubic symmetry with the space group Pm3m. The maximum standard deviation was ± 0.02 %. According to Takeda et al. (1986), the phases are probably pseudo cubic. Deviation from cubic symmetry has not been investigated in the present study.

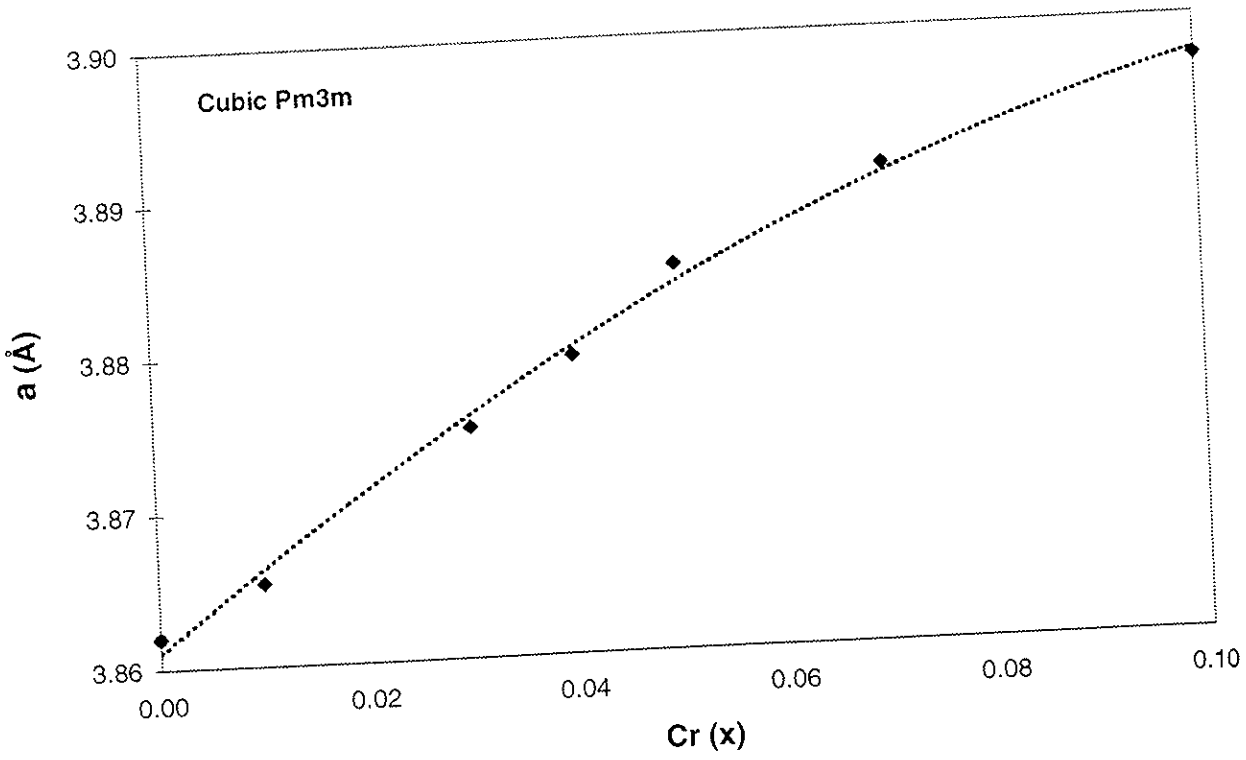

Figure 2.19 Lattice parameter as a function of chromium substitution in $SrFe_{1-x}Cr_xO_{3-\delta}$. The samples were cooled in flowing air at 5 °C/min.

The effective ionic radii of tri- and tetravalent iron ions are slightly larger than the corresponding chromium ions (Shannon, 1976). The data are shown in Table 2.3. If the ratio of tri- to tetravalent B-cations were not influenced by the Cr-substitution, a decrease in the lattice parameter with increasing Cr-substitution should be expected.

Table 2.3 Effective ionic radii with octahedral oxygen coordination (Shannon, 1976).

Ion	Fe^{3+} (HS)	Fe^{4+} (HS)	Cr^{3+}	Cr^{4+}
radius (Å)	0.645	0.585	0.615	0.55

Chemical expansion measurements showed a volume change corresponding to an increase in the lattice parameter of 0.03 Å, in a oxygen defect range of $\Delta\delta = 0.16$. The expansion measurement is performed for highly nonstoichiometric $SrFeO_{3-\delta}$ (900 °C) and is discussed in detail in the subsequent section. Assuming linearity between *a* and δ, the cell refinements indicate a considerable increase in the oxygen vacancy concentration with Cr-substitution up to 10 mol%. The results imply substitution of trivalent chromium and a strong interaction between Cr(III) and Fe(III). Ideal solution of 10 mol% Cr(III) in the iron sublattice gives only an increase in δ of 0.03 as seen from the equation:

$$0.9SrFe^{3+}_{0.36}Fe^{4+}_{0.64}O_{2.82} + 0.1SrCr^{3+}O_{2.5} = SrFe^{3+}_{0.32}Fe^{4+}_{0.58}Cr^{3+}_{0.1}O_{2.79} \qquad [2.8]$$

The interaction between Cr(III) and Fe(III) is expected to decrease when the concentration of Cr(III) increases, and is in agreement with the positive deviation from Vegard's Law, as shown in Figure 2.19.

The uncertainty in assuming linear correlation between vacancy concentration and unit cell length should have been avoided by measuring the absolute oxygen content as a function of Cr-substitution.

Kharton et al. (1998) reported an increase in the unit cell volume with chromium substitution in $SrCo_{0.90-x}Fe_{0.10}Cr_xO_{3-\delta}$. They claimed the volume expansion was caused by a decrease in the oxygen vacancy concentration, which is not the general interpretation.

The crystallographic density as a function of Cr-content is calculated from the cell refinement. The calculation is based on an estimation of the oxygen content from a linearity between *a* and δ, with $SrFeO_{2.82}$ as the reference

point. The calculated crystallographic density as a function of Cr-substitution is given in Figure 2.20.

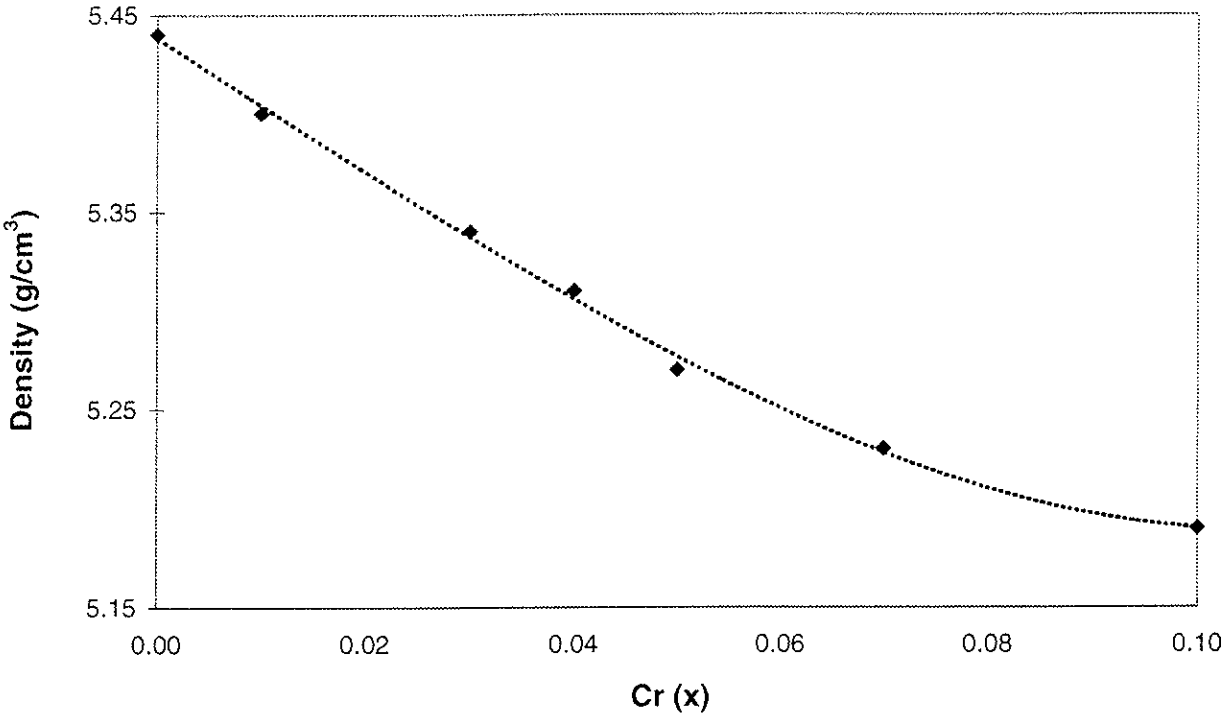

Figure 2.20 Crystallographic density as a function of Cr-substitution in cubic $SrFe_{1-x}Cr_xO_{3-\delta}$.

Sintering behaviour

The swelling phenomenon which was discussed for $SrFeO_{3-\delta}$ (Chapter 2.5.1) is also observed in the chromium substituted samples. Figure 2.21 shows the sintering behaviour and the corresponding particle size distributions of $SrFe_{0.97}Cr_{0.03}O_{3-\delta}$ powders. The two particle size distributions are obtained by calcining at different temperatures. These curves indicate that the swelling accelerates by broadening the particle size distribution, and substantiate the arguments discussed in Chapter 2.5.1. Notice that the swelling starts even before the material has reached closed porosity.

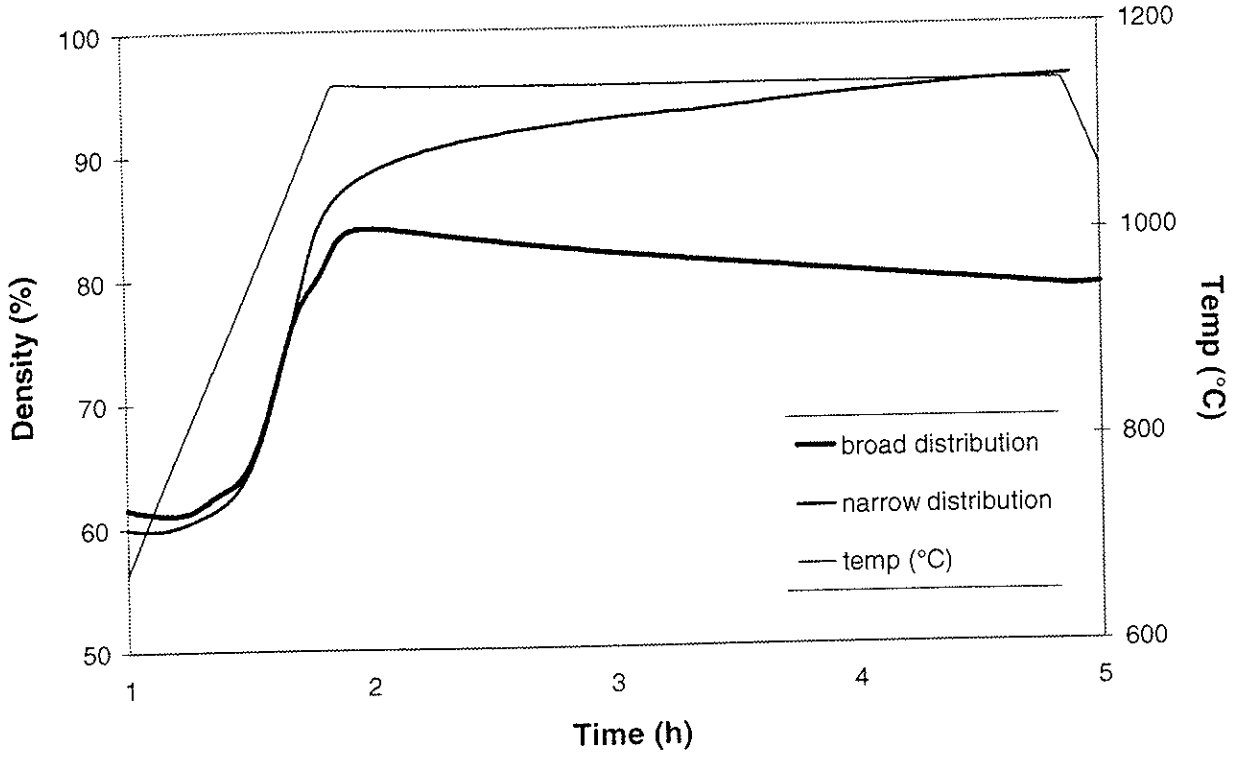

Figure 2.21a Sintering behaviour of $SrFe_{0.97}Cr_{0.03}O_{3-\delta}$ powders with different particle size distributions.

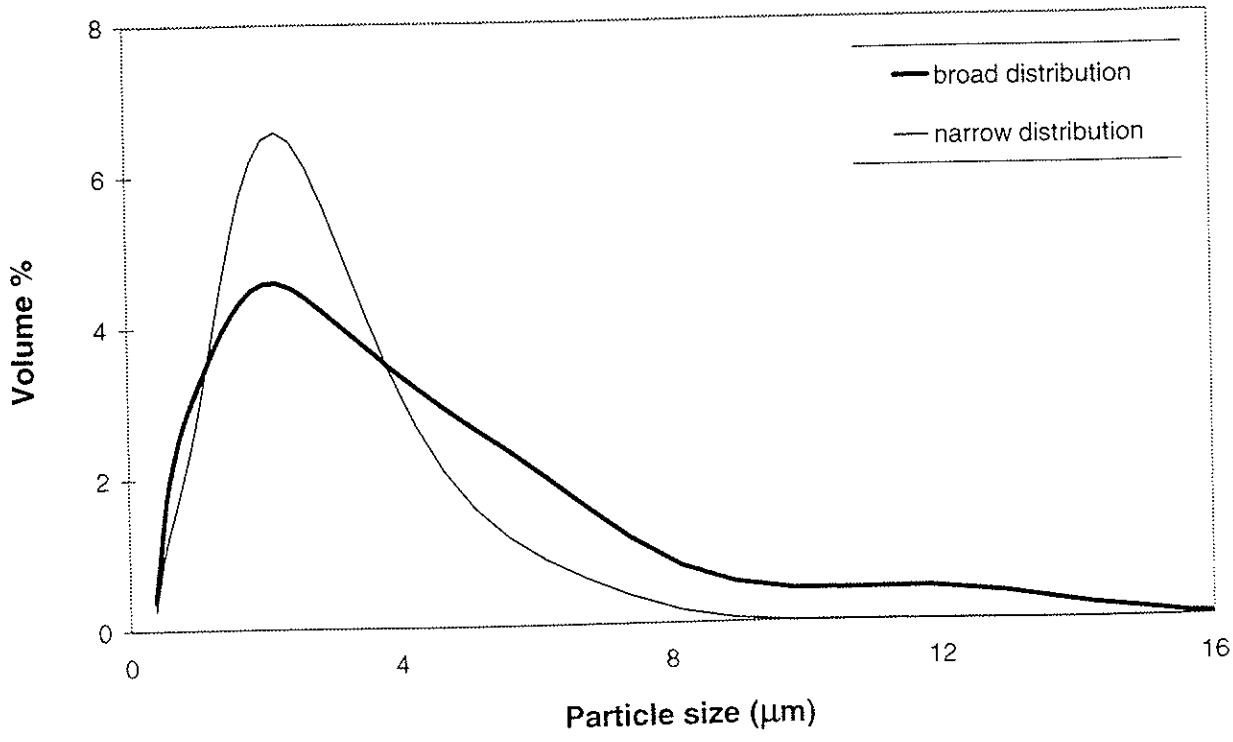

Figure 2.21b Particle size distribution of $SrFe_{0.97}Cr_{0.03}O_{3-\delta}$ powders used in the sintering experiments shown in Figure 2.21a.

Chromium substitution in $SrFeO_{3-\delta}$ improved the sintering behaviour and mechanical strength considerably. Figure 2.22 shows an increase in the maximum sintering rate by increasing the chromium content and confirmed the improvement in sintering behaviour with chromium substitution.

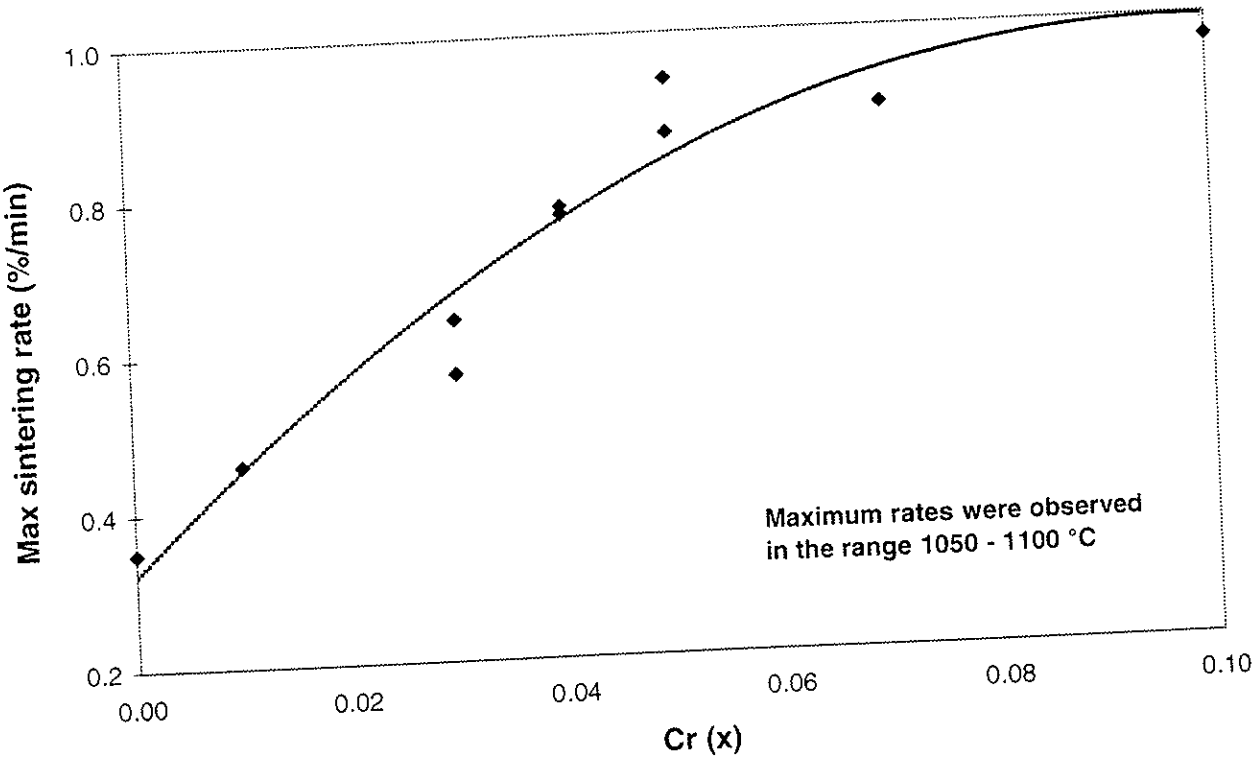

Figure 2.22 Maximum sintering rate as a function of Cr-substitution for $SrFe_{1-x}Cr_xO_{3-\delta}$. The heating rate was 10 °C/min.

Optimised EDS line-scan across a grain boundary showed no grain boundary segregation for a sample with nominal composition $SrFe_{0.97}Cr_{0.03}O_{3-\delta}$. Cell refinement of the compositions with increasing chromium content confirmed the substitution of iron by chromium up to at least 10 mol%, as seen in Figure 2.19.

Chemical expansion and oxygen nonstoichiometry

The most evident parameter that affects the chemical expansion is the level of oxygen nonstoichiometry. This also involves polyhedron preference and Jahn-Teller deformation. Another feasible parameter which can influence the chemical expansion is phase transformation.

Chemical expansion and relative change in vacancy concentration ($\Delta\delta$), have been measured isothermally as a function of Cr-substitution in $SrFe_{1-x}Cr_xO_{3-\delta}$. The change in defect concentration decreased with increasing Cr-substitution, as shown in Figure 2.23. This indicates a movement of the 'flat' region of vacancy concentration ($\delta = 0.5$) towards higher P_{O_2} with increasing Cr-content. In addition, the data show a decreasing dependency on Cr-substitution with increasing temperature. Data on absolute oxygen content is unfortunately lacking in this study.

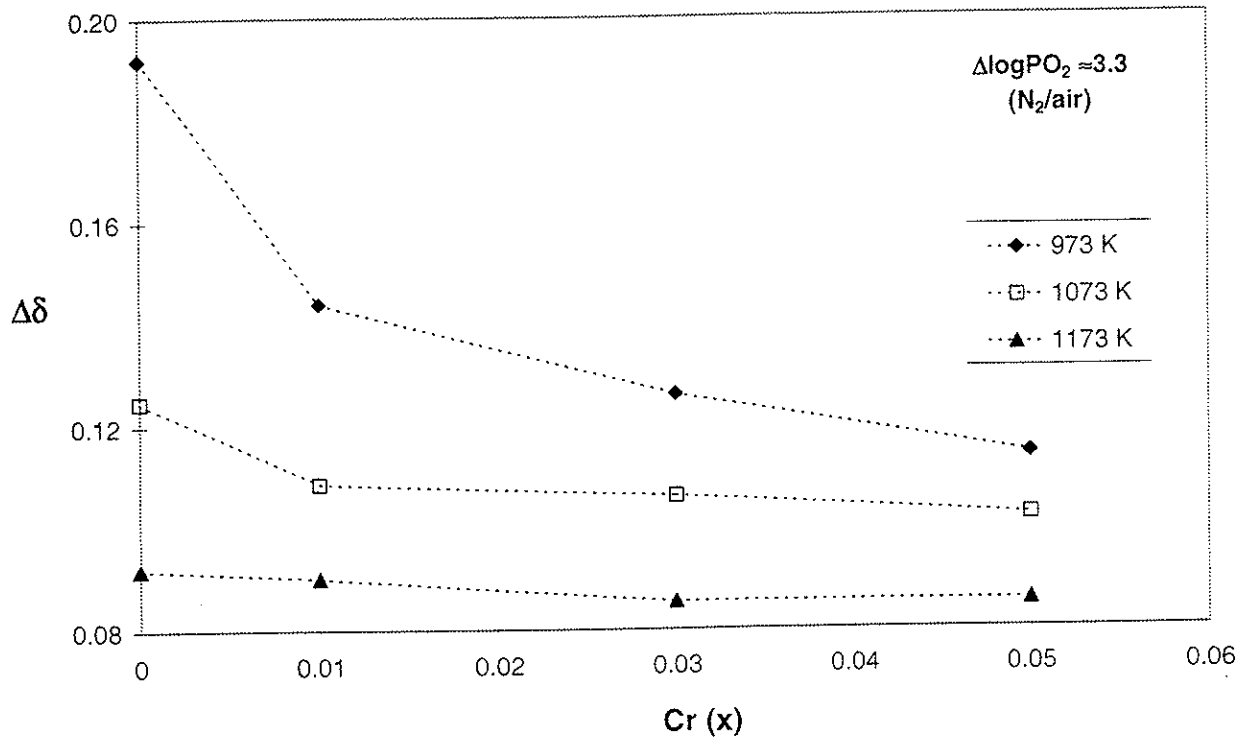

Figure 2.23 Relative change in oxygen vacancy concentration as a function of Cr-content for $SrFe_{1-x}Cr_xO_{3-\delta}$.

The chemical expansion decreases with increasing Cr-content, as shown in Figure 2.24. The effect of Cr-substitution decreases with increasing temperature, and is in agreement with the oxygen stoichiometry measurements. The linear chemical expansion is plotted against relative vacancy concentration in Figure 2.25. As expected, the expansion of the membrane increases with larger changes in defect concentration.

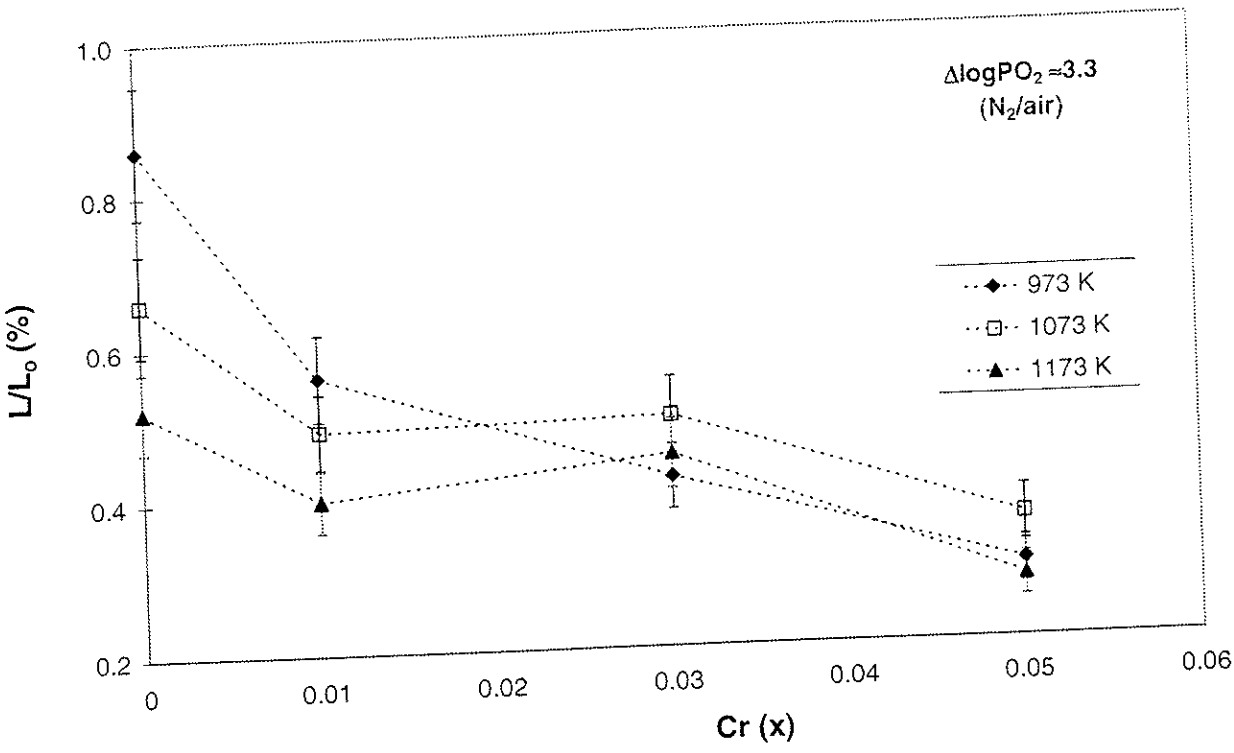

Figure 2.24 Chemical expansion as a function of Cr-content for $SrFe_{1-x}Cr_xO_{3-\delta}$.

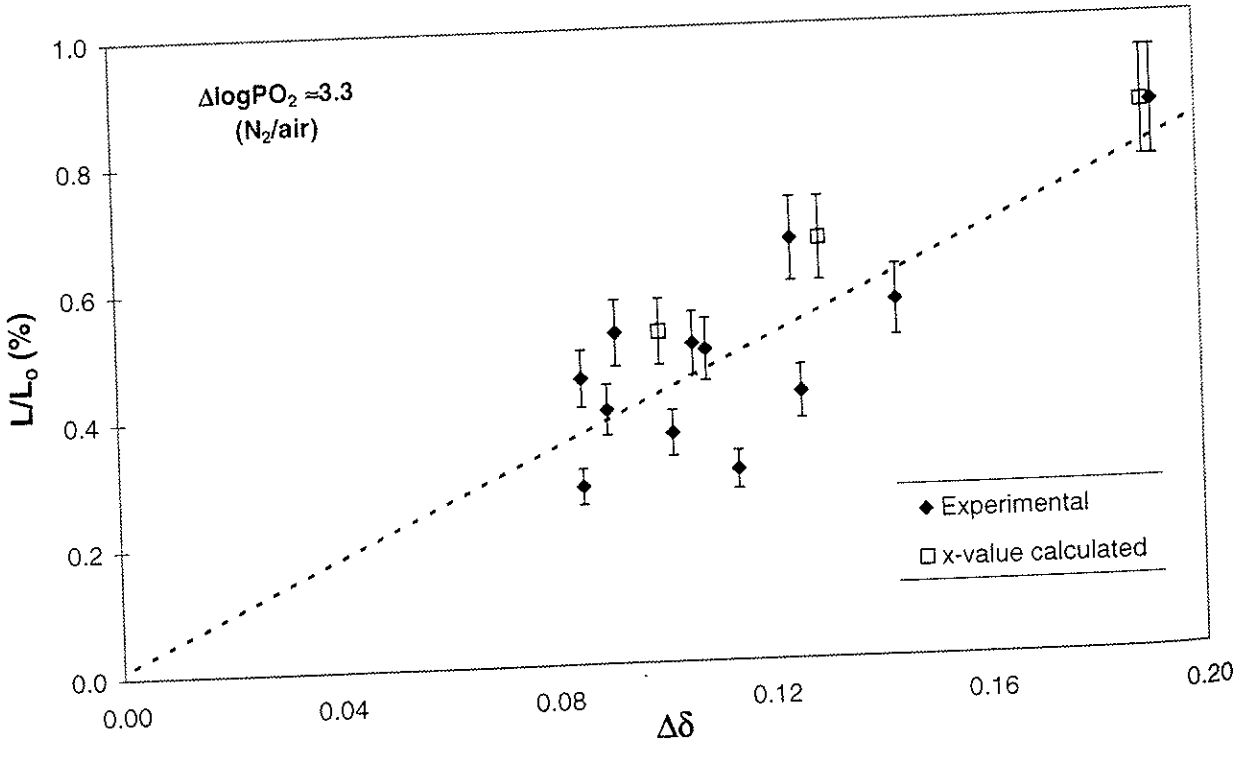

Figure 2.25 Chemical expansion as a function of relative change in oxygen vacancy concentration for $SrFe_{1-x}Cr_xO_{3-\delta}$ $(0 \leq x \leq 0.05)$.

The measurements of chemical expansion are subject to significant uncertainty. Small deviations in cation stoichiometry leads to growth of a plate shaped phase of either $Sr_4Fe_6O_{13+\delta}$ or $Sr_3Fe_2O_{7-\delta}$ from the matrix. This is described in Chapter 3.4.7. The rate of formation of these secondary phases may depend on P_{O_2}. This can results in an apparent expansion in the dilatometry measurement, as a consequence of the way the phases grows out of the matrix. This shows up as an evident drift in the experiment. The long term growth of secondary phases could be avoid by changes the oxygen partial pressure abruptly. Unfortunately, this leads to a cracked sample.

Thermal expansion

Linear dimensional change ($\Delta L/L_o$) and expansivity ($\partial(\Delta L/L_o)/\partial T$) of $SrFe_{0.97}Cr_{0.03}O_{3-\delta}$ is shown in Figure 2.26. The sample was heated in air at 1 °C/min. The abrupt change in expansivity is probably related to a phase transition. This is expected from the phase diagram for $SrFeO_{3-\delta}$, which is given in Figure A8.1 (Takeda et al., 1986; Mizusaki et al., 1992).

The thermal expansion is plotted as expansivity instead of the more common quantity, thermal expansion coefficient (TEC). This is useful when a phase transition appears in the relevant temperature range, since TEC is an average value.

The phase transition is not observed during cooling. This is probably due to the slowness of the phase transition at these low temperatures. Hence, the determination of the phase transition is not possible from these experiments. However, we observe a change in the position of maximum expansivity, towards lower temperature with increasing chromium content. The data are given in Table 2.4. The phase transition was not observed in the sample with 5 mol% Cr-substitution. The phase transitions involve oxygen exchange and the apparently phase stabilisation can be due to different kinetic conditions.

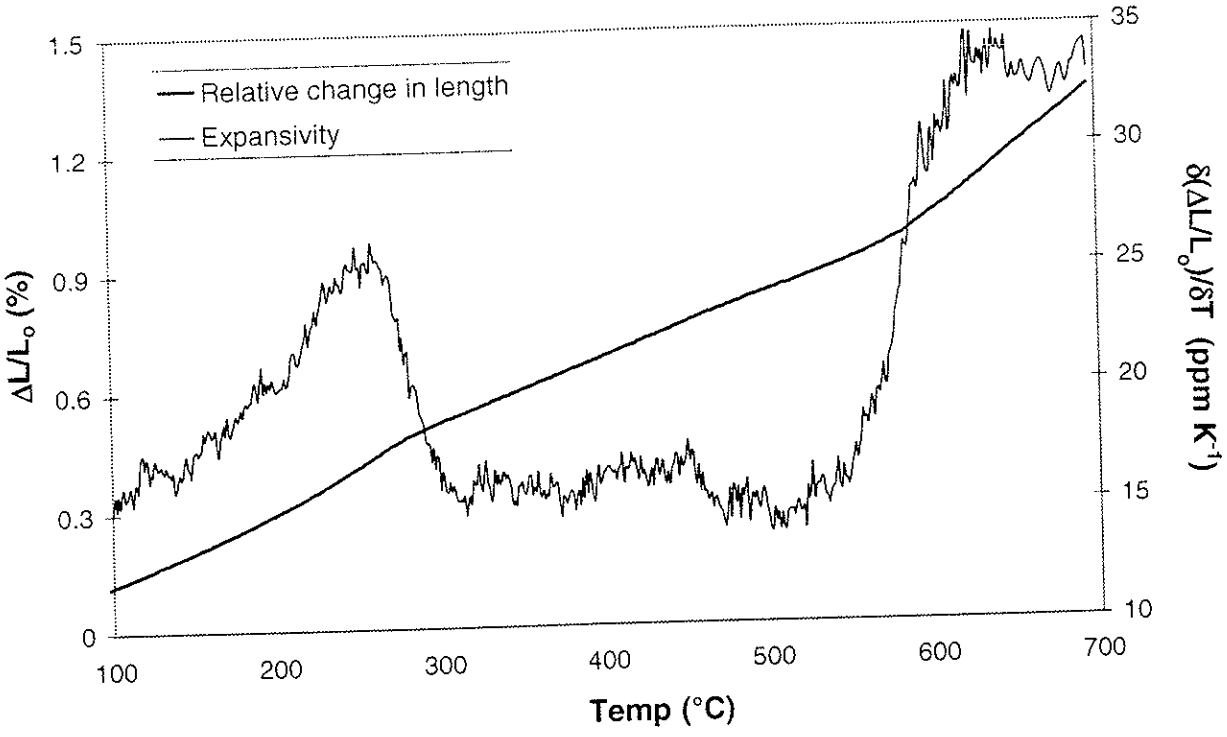

Figure 2.26 Relative change in length and expansivity for $SrFe_{0.97}Cr_{0.03}O_{3-\delta}$, heated at 1 °C/min in air.

The expansivities are in the range 15-20·10^{-6} K^{-1} in air at 500 °C as shown in Table 2.4. The expansion data are reported at 500 °C because of the phase transitions at lower temperatures. The large increase in measured expansion above 550 °C is due to loss in oxygen (chemical expansion).

Table 2.4 Expansivity as a function of Cr-content in $SrFe_{1-x}Cr_xO_{3-\delta}$. The heating rate was 1 °C/min.

x	Expansivity at 500 °C (10^{-6} K^{-1})	Maximum of expansivity in the temperature range 100-500 °C
0	19	400 °C
0.01	16	350 °C
0.03	15	260 °C
0.05	17	-

2.6 Conclusions

Sub-micron powders of $SrFeO_{3-\delta}$ start sintering at < 800 °C. This is close to the temperature required for obtaining single phase perovskite of the material.

Agglomerated $SrFeO_{3-\delta}$ powder exhibited an extended swelling during sintering at high temperature. The pore swelling is nearly independent of the oxygen partial pressure and the heating rate, but is influenced by the powder morphology. The swelling rate is accelerated by increasing the temperature. However, grain growth is the key factor to stop the swelling.

It is suggested that a significant number of unstable large pores, expand during sintering. Both the small pores and the external surface act as a sink for the mass transport. Unstable pores have been observed to open up grain boundaries to coalesce with neighbouring pores, and this is suggested as one of the transport mechanism.

Calculation of the maximum pressure in pores of $SrFeO_{3-\delta}$ membranes at high temperatures implies a lower pressure than in the surrounding atmosphere. This shows that trapped gas can not explain the swelling phenomenon.

A chemical expansion of $\approx$ 1.5 vol% is measured for $SrFeO_{3-\delta}$ at a relevant gradient in oxygen partial pressure. As a consequence, small steps in temperature and P_{O_2} are required to keep the membrane crack free. Limited chromium substitution improved the thermomechanical properties of the material due to a decrease in the chemical expansion. The chemical expansion decreases with increasing Cr-content. In addition, controlled microstructure and enhanced density is obtained for the substituted materials. The solubility limit of chromium on the iron-site in $SrFeO_{3-\delta}$ is at least 10 mol%.

The relative change in oxygen vacancy concentration decreases with increasing Cr-content at 700 °C in a given P_{O_2} gradient. The change in vacancy concentration is less at higher temperatures. This implies that the nonstoichiometry plateau at δ = 0.5 moves to higher P_{O_2} with increasing chromium. The TGA results are in agreement with the chemical expansion measurements.

3 OXYGEN PERMEABILITY OF $SrFe_{1-x}Cr_xO_{3-\delta}$

3.1 Introduction

General characteristics of mixed conducting membranes are given in Chapter 1.1. Oxygen permeation of such dense membranes is mainly controlled by the solid state diffusion and the surface oxygen exchange kinetics. The available driving force is distributed across the membrane, as illustrated in Figure 1.6. This chapter deals with the results of oxygen permeation measurements of $SrFe_{1-x}Cr_xO_{3-\delta}$ as a function of temperature, membrane thickness, microstructure and driving force.

3.2 A survey of the relevant literature

Oxygen diffusion in binary oxides has been studied over the past 70 years. Initial studies originated in the high temperature corrosion field, but later attention was paid to materials with high ionic conductivity. These materials can potentially be used as oxygen sensors, oxygen pumps and electrolytes in the solid oxide fuel cell (SOFC) (Kofstad, 1972, Steele et al., 1986, Manning et al., 1997). More recently materials with mixed ionic and electronic conductivity have attracted attention as dense "self-supported" membranes (Bouwmeester & Burggraf, 1997).

Oxygen permeability in mixed conducting perovskites

Teraoka et al. (1985) published the first data on oxygen permeation of dense membranes. The material in question was the perovskite $La_{1-x}Sr_xCo_{1-y}Fe_yO_{3-\delta}$. The permeation rate was found to increase with an increase in Sr or Co content, indicating that the permeability was mainly controlled by the number of oxygen vacancies. Later on, Teraoka et al. (1988[II]) reported the effect of substitution on both A- and B-sites in perovskites containing cobalt. They observed the highest oxygen permeability in $La_{0.6}A_{0.4}Co_{0.8}Fe_{0.2}O_{3-\delta}$ when A = Ba and in $La_{0.6}Sr_{0.4}Co_{0.8}B_{0.2}O_{3-\delta}$ when B = Cu. Substitution of rare earth cations in $Ln_{0.6}Sr_{0.4}CoO_{3-\delta}$ gave an increased permeation with decreasing ionic radius. The effects of the cation substitution are summarised in Table 3.1.

Table 3.1 Effect of cation substitution on the oxygen permeability of perovskite-type oxides (Teraoka et al., 1988[II]).

Composition	Effect on the oxygen permeability
$La_{0.6}A_{0.4}Co_{0.8}Fe_{0.2}O_{3-\delta}$	A: Ba > Ca > Sr > Na
$La_{0.6}Sr_{0.4}Co_{0.8}B_{0.2}O_{3-\delta}$	B: Cu > Ni > Co > Fe > Cr > Mn
$Ln_{0.6}Sr_{0.4}CoO_{3-\delta}$	Ln: Gd > Sm > Nd > Pr > La

Later, a considerable research effort on the $La_{1-x}Sr_xCo_{1-y}Fe_yO_{3-\delta}$ system was initiated, for instance at Imperial College and University of Twente (Kilner, 1994; ten Elshof et al., 1995/1997[II]; Lane et al., 1999). The Ruddlesden-Popper phase $Sr_4Fe_{6-x}Co_xO_{13+\delta}$ has been studied by Ma et al. (1996[I/II]) who reported an extraordinarily high ionic conductivity. More recent results indicate a lower ionic conductivity and degradation in performance under a reducing atmosphere, which imply that the phase is not thermodynamically stable at the given conditions (Holt et al., 1998; Wang et al., 1999).

A number of oxygen permeation studies have investigated the composition $SrCo_{0.8}Fe_{0.2}O_{3-\delta}$, and the data are summarised by Bouwmeester and Burggraaf (1997). This composition has been particularly attractive because of the maximum permeability reported in the system $SrCo_{1-x}Fe_xO_{3-\delta}$ where $0 \leq x \leq 1$ (Teraoka et al., 1985). The oxygen permeability increased with Fe-content up to $x = 0.2$, and then decreased with further substitution. The permeability for $x = 1$ was slightly higher than for $x = 0$. The $SrCoO_{3-\delta}$ phase is probably partly ordered under the experimental conditions of the study. The permeability data by Teraoka et al. are higher than have been measured by others (Kruidhof et al., 1993; Bouwmeester et al., 1994; Qiu et al., 1995). Table 3.2 summarised the oxygen permeability of $SrCo_{1-x}Fe_xO_{3-\delta}$, reported from several groups.

Table 3.2 Oxygen permeability data and the apparent activation energy for $SrCo_{1-x}Fe_xO_{3-\delta}$. Experimental conditions: $\Delta \log P_{O_2} \approx 2$ and membrane thickness of 1 mm.

Composition	T (°C)	Oxygen permeability (mol m^{-2} s^{-1})	Activation energy (kJ/mol)	References
$SrCoO_{2.5+\delta}$	850	0.0118*	-	Teraoka et al., 1985
$SrCo_{0.8}Fe_{0.2}O_{3-\delta}$	850	0.0215	≈ 60	Teraoka et al., 1985
	850	0.0050	≈ 50	Qiu et al., 1995
	850	0.0020	≈ 50	Kruidhof et al., 1993
	1000	0.0030	"	"
$SrCo_{0.67}Fe_{0.33}O_{3-\delta}$	992	0.0278	100±36	Hansen, 1999
$SrCo_{0.4}Fe_{0.6}O_{3-\delta}$	850	0.0153	-	Teraoka et al.,1985
$SrCo_{0.33}Fe_{0.67}O_{3-\delta}$	1000	0.0190	88-108	Aasland et al., 2000
$SrFeO_{3-\delta}$	850	0.0139	-	Teraoka et al., 1985
	992	0.0073	94-101	Hansen, 1999

* Non-perovskite structure observed (Brownmillerite)

The high permeability observed by Teraoka et al. is later explained by absence of surface exchange limitation (Qiu et al., 1995). However, the vacancy ordering for this perovskite should have been noticed under the reported conditions (Kruidhof et al., 1993). There is some inconsistency in that the permeability of membranes with the highest surface exchange rates, do not exhibit the oxygen vacancy ordering behaviour. A more plausible explanation to these specific results is that the experimental temperatures were higher than reported.

The activation energy for the bulk diffusion in $SrCo_{1-x}Fe_xO_{3-\delta}$ seems to increase with increasing cobalt content from approximately 50 to 100 kJ/mol (Holt et al., 1999; Larsen, 1999; Aasland et al., 2000). Qiu et al. (1995) reported an apparent activation energy of approximately 92 kJ/mol for a predominantly surface exchange controlled process for $SrCo_{0.8}Fe_{0.2}O_{3-\delta}$ (650-780 °C). However, this measurement was performed in the temperature range of an ongoing slow ordering process, which makes the calculated activation energy quite uncertain.

The majority of the authors report that oxygen surface exchange kinetics exert partial or dominant control over the oxygen permeation of $La_{1-x}Sr_xCo_{1-y}Fe_yO_{3-\delta}$ membranes with thickness 1-5 mm (Bouwmeester et al., 1994; Qiu et al., 1995; Lee et al., 1997; Kharton et al., 1998). Measurements of thickness and oxygen pressure dependent permeation show that the surface exchange limitation is higher on the permeate side than on the feed side of the membrane.

The characteristic membrane thickness, L_c, is the point of transition between the predominantly bulk diffusion and the surface exchange controlled reaction, as defined in equation [1.23]. The characteristic membrane thickness for a series of compositions is reviewed by Bouwmeester and Burggraaf (1997). The L_c is reported to increase with increasing Sr-content in $La_{1-x}Sr_xFeO_{3-\delta}$, with $L_c = 0.45$ mm for $x = 0.4$ 1273 K (Ishigaki et al., 1984/1988). The parameter L_c as a function of Sr-content is given in Figure 4.19. Kilner et al. found a correlation between L_c and different structure types; perovskite and fluorite oxides (Kilner, 1994; De Souza & Kilner, 1999).

Improvement of the surface exchange kinetics

Enhanced oxygen permeation can be achieved by improving the inherent surface exchange kinetics. Benson et al. (1998) measured that the tracer surface exchange coefficient increased with increasing P_{O_2} for $La_{0.6}Sr_{0.4}Fe_{0.8}Co_{0.2}O_{3-\delta}$, which implies higher limitation on the permeate surface than the feed side. Lee et al. (1997) observed approximately 40 % enhancement of the permeation rate of $SrCo_{0.8}Fe_{0.2}O_{3-\delta}$ by coating both surfaces of the membrane with porous $SrCo_{0.8}Fe_{0.2}O_{3-\delta}$. At high temperatures the effect of coating the permeate side was larger than coating the feed side. This indicates that surface exchange limitation is greater on the oxygen lean side. No effect was observed when coating with a porous layer of Ag or Pt. The same research group has suggested a model to quantitatively predict the enhancement of oxygen permeation when porous layers are added to one or both surfaces of the membrane (Jacobson et al., 1997). The model includes the effect of tortuosity and gas diffusion in the pores. They claimed that the calculated values of the oxygen permeation rate agreed well with the experimental data. Parts of the work are based on previous studies by Deng et al. (1994/1995) which confirm that an enlargement of the specific surface area had a pronounced effect on the oxygen permeation.

Another study investigated a pretreatment of the oxygen lean surface in a CO-containing atmosphere (ten Elshof, 1997[1]). The authors observed an enhanced oxygen permeability of $La_{1-x}Sr_xFeO_{3-\delta}$ and a decreased time to reach steady state condition. X-ray photoelectron spectroscopy (XPS) analysis indicated strontium enrichment up to 20 % in the permeate membrane surface, probably present as SrO or $SrCO_3$. Surface profile measurements showed an increased surface area by a factor of 1.4-1.6. They propose that this explains the increased oxygen permeability, which agrees with other reports.

Miura et al. (1995) found an improved oxygen permeation for $La_{0.6}Sr_{0.4}Co_{0.8}Fe_{0.2}O_{3-\delta}$ membranes when the surface was treated with acid. The XPS peak assigned by the authors to SrO or $SrCO_3$ disappeared after the acid treatment. Others reported that this specific energy peak is due to strontium in the perovskite (Bocquet et al., 1989; ten Elshof, 1997[1]). Enhanced oxygen permeation when the membranes were treated with acid was also observed by ten Elshof et al. They concluded that the acid treatment decomposes the perovskite at the surface and form SrO or $SrCO_3$, and they interpret the XPS spectra by Miura et al. to agree with this explanation.

Small deviations from stoichiometry or tracer impurities will normally segregate at the grain boundaries, causing a reduction in the oxygen permeation rates. Silica from kiln linings and sodium from surroundings are typical examples of impurities (Machkova et al., 1997). Acid treatment can dissolve segregated phases and apparently improve the oxygen permeability of a specific membrane composition.

Under reducing conditions (CO/CO_2), ten Elshof et al. (1996) observed an enhanced oxygen permeation of $La_{0.8}Sr_{0.2}FeO_{3-\delta}$ when Pt was sputtered on the permeate surface. From this result they concluded that the surface reaction of CO with lattice oxygen was the rate-limiting step in the overall permeation process.

Grain boundary transport

Studies of oxygen diffusivity along grain boundaries are reported by few authors. High diffusivity paths along the grain boundaries in $La_{1-x}Ca_xCrO_{3-\delta}$ are confirmed by depth profiling measurements with SIMS (Yasuda et al., 1994; Kawada et al., 1995; Sakai et al., 2000). Sakai et al. reported a grain

boundary diffusion which was 10^4 times higher than the bulk diffusion at 1273 K. The activation energy was calculated to approximately 165 kJ/mol for both processes. A similar behaviour was observed for $La_{0.87}Sr_{0.13}CrO_3$, with the grain boundary transport increasing proportionally with $\sqrt{P_{O_2}}$ in the range 10^{-3} to 1 bar (Sasaki et al., 1996). With impedance spectroscopy, Rauch & Meilin (1997) observed an effect of the microstructure on the resistance in $BaCe_{1-x}Nb_xO_{3-\delta}$. The oxygen transport was dominated by diffusion through grains above 550 °C and by grain boundary transport at lower temperatures.

Benson et al. (1998) observed predominantly grain boundary diffusion for the composition $La_{0.6}Sr_{0.4}Co_{0.8}Fe_{0.2}O_{3-\delta}$ below 500 °C and P_{O_2} in the range 10^{-3} to 1 bar. The activation energy is estimated to be ≈100 kJ/mol for grain boundary diffusion and 186±14 kJ/mol for the bulk transport. The diffusion profiles above 500 °C did not indicate a significant contribution of the grain boundaries to the oxygen transport.

The chromites discussed above have oxygen defect concentration close to zero under the given conditions (Boroomand et al., 2000). The oxygen nonstoichiometry of $La_{0.6}Sr_{0.4}Co_{0.8}Fe_{0.2}O_{3-\delta}$ is significant under the same conditions, but limited below 500 °C (Benson et al., 1997). It is reasonable to expect higher transport rates of oxygen along the grain boundaries relative to intra grain, for materials with negligible oxygen defect concentrations. Defects and disorder at the grain boundaries will increase the diffusion rates when the oxygen sub-lattice is almost fully occupied. When the number of vacancies is significant, the bulk diffusion is enhanced by paths through the vacant positions in the lattice.

Reports on microstructure dependent permeability in the $SrFe_{1-x}M_xO_{3-\delta}$ systems are presently limited to a single paper (Kharton et al., 1998). Kharton et al. measured a decreasing oxygen permeability with increasing grain boundary length for $SrCo_{0.60}Fe_{0.25}Cu_{0.15}O_{3-\delta}$ membranes. Membranes with different microstructures were made by mixing powder with various morphologies, obtained by different synthesis routes. The paper, however, does not include a discussion of the possibility of grain boundary segregation in membranes made from different powders. Impurities in the chemicals for synthesis of fine particle powders or small deviations from cation stoichiometry may very well explain the variation in permeation behaviour. Various grinding procedures will introduce tracer impurities that can

segregate at the grain boundaries, and thus influence the oxygen flux. Small deviations from stoichiometry are not detectable using common analytical techniques. However, the results are in agreement with the assumption of high diffusivity paths through the lattice of these nonstoichiometric materials.

Oxygen vacancy ordering

The tendency for ordering of oxygen vacancies in the structure grows with increasing oxygen defect concentration, and has a negative influence on the permeation. A study by Shin et al. (1978) reported a phase transition from orthorhombic brownmillerite structure to a completely disordered cubic structure of $SrFeO_{3-\delta}$ at 700 °C in nitrogen atmosphere. This was observed in high temperature XRD. Phase relationships and oxygen nonstoichiometry of $SrFeO_{3-\delta}$ at high temperatures and varying oxygen partial pressures have been thoroughly studied by Takeda et al. (1986) and Mizusaki et al. (1992). Figure A8.1 gives the phase diagram of $SrFeO_{3-\delta}$ as a function of oxygen content and temperature. In view of the article by Mizusaki, a cubic perovskite type phase is stable above 900 °C in the range $0<\delta<0.5$. The transition temperature from a brownmillerite to a perovskite-type phase increases to 900 °C with decreasing P_{O_2}. For the $SrCo_{0.8}Fe_{0.2}O_{3-\delta}$ material, an order-disorder temperature at 790 °C was observed in permeation experiments with an inert atmosphere on the permeate side and air on the feed side (Kruidhof et al., 1993; Qiu et al., 1995). Results from XRD at 800 °C showed a change in the diffraction pattern when the P_{O_2} was switched from 0.1 to 0.05 bar (Pei et al., 1995). The material consisted of a mixture of brownmillerite and perovskite at $P_{O_2} = 0.05\ bar$.

Kinetic demixing and decomposition

As mentioned in Chapter 1.1.2, a counter flux of mobile cations under steady state oxygen permeation can lead to kinetic demixing or decomposition. Several studies have investigated the demixing process in substituted binary metal oxides, as in (Co,Mg)O (Schmalzried et al., 1979; Monceau et al., 1992; Hong et al., 1999).

Kinetic decomposition of $La_{0.3}Sr_{0.7}CoO_{3-\delta}$ membranes under oxygen permeation experiments was observed by van Doorn et al. (1998). The phase separation occurred on the oxygen-lean side of the membrane, observed as SrO on the surface. Because strontium enrichment was observed at the permeate side, it can be concluded that this is the cation with the slowest

diffusion rate. The oxygen permeation rate remained unaltered after 500 hours at 900-1100 °C. This is probably caused by the high porosity of the SrO layer.

Uncertainty in the literature permeability data

It is difficult to make comparisons between the various data presented in the literature for several reasons. Recalculation of the permeability values to unit thickness are often subject to great uncertainty, due to unknown surface exchange limitations. The driving force can also be difficult to estimate. A number of studies used a relatively low sweep gas flow of 1-50 Sml/min, and the distance from the sweep gas outlet to the membrane surface is not given (Teraoka et al., 1985; Kruidhof et al., 1993; ten Elshof et al., 1996). The inner diameter of the sweep tube is not reported, and the gas velocity can thus not be estimated. The low sweep gas flow can result in a stagnant film of oxygen on the membrane surface, and consequently a lower driving force than assumed is established. Additional data and discussion are given in Chapter 3.4.1.

Unfortunately, oxygen permeability data reported in the literature scatter wildly even for apparently similar experiments, as shown in Table 3.2. The large scatter in the permeability data can partly be explained by differences in experimental set-up and variations in membrane processing. Some of the possible sources which contribute to the large scatter are outlined below.

The real temperature of the membrane could be different from that measured if the thermocouple is incorrectly placed or far from the membrane surface. More important is perhaps contamination from sealing materials, for instance Pyrex (Kruidhof et al., 1993). Glass seals readily react with most of the oxygen permeable membranes. Silica-containing phases react readily with perovskites containing basic elements on the A-site in the structure. Impurities such as sulphur in the gas streams can attack the membrane under the permeation experiments, forming sulphates (Aasland et al., 2000).

Apparently similar membranes, reported from different authors, could actually vary with respect to porosity, grain size, small deviations in cation stoichiometry and tracer impurities. Unfortunately, the characterisation of the oxygen permeable membranes reported is usually very limited in the literature.

3.3 Experimental

3.3.1 Membrane preparation

The synthesis and characterisation of powders used for membrane preparation are described in Chapter 2.4.2. Preparation of green bodies is described in Chapter 2.4.3.

Membranes for oxygen permeation measurements were green bodies of Ø13 mm of composition $SrFe_{1-x}Cr_xO_{3-\delta}$. The choice of sintering conditions was based on dilatometry experiments. Generally, a temperature 50 °C above the temperature of the maximum sintering rate was chosen as the sintering isotherm to obtain membranes with high density. The heating rate was set to 10 °C/min with a dwell time of 3 hours at maximum temperature. The samples were cooled to 1000 °C at 1 °C/min followed by 0.5 °C/min to room temperature. Various microstructures of the dense $SrFe_{0.97}Cr_{0.03}O_{3-\delta}$ membranes were obtained by choosing three different sintering temperatures, 1175, 1200 and 1275 °C.

The sintered disks were machined to 10 mm diameter and ground to the desired thickness, followed by polishing on a synthetic disk pad with one μm diamond paste (Struers[16]). Polished membranes were thermally etched at the chosen sintering temperature for 10 minutes. The heating and cooling rate was set to 1 °C/min. The intention of the etching was primarily to characterise the microstructure before the permeation experiments. In addition, a stable microstructure at the beginning of the experiment was wanted.

3.3.2 Characterisation of the microstructure of sintered membranes

The microstructure of dense membranes was investigated by SEM and optical microscopy. Energy Dispersive Spectroscopy, (EDS) was used for elemental analysis to check for unexpected and unidentified phases on the surface of the samples.

---

[16] www.struers.de, Willich-Schiefbahn, Germany.

The surface of the membranes which were selected for study of how the microstructure influences oxygen permeation, were characterised using a Zeiss[17] Axioplan optical microscope. The thermally etched membranes were characterised by image analysis of four representative photos (magnification; 500x). Grain boundary lengths were measured by image analysis (Kontron[18] Elektronic Imaging System, KS 400) and reported with unit $\mu m/\mu m^2$. Grain boundary lengths of the membrane surfaces were determined as a function of maximum sintering temperature. Lines were drawn along the grain boundaries and the total length was calculated. Each photo has a frame of 175 $\times 175$ µm which contains from 400-700 grains. Standard deviation of the measurement of grain boundary length was estimated to maximum ± 0.003 $\mu m/\mu m^2$.

Membranes with different topographies were obtained by grain pull out during grinding and polishing. The surface area was investigated using white light interference microscope (WYKO[19] NT2000)[20]. The interference microscope splits a beam of white light into a reference beam and a beam that hits the surface. When these beams are recombined in the microscopes lens system, they interfere and create regions of varying intensity due to specimen topography. This interference appears as a pattern of light and dark areas. The optical profile instrument provides depth measurements with a resolution as high as 0.1 nm. The topography results are reported as a surface area index. This is the ratio of surface area to measured micrograph area. Ten surface photos, with frames of 45×59 µm, were collected for each sample to obtain representative data for the surface area index. Standard deviation of the surface area index was calculated to maximum ± 0.008.

The density of polished and thermally etched membranes were determined by the Archimedes method, as described in Chapter 2.4.5. Micrographs of sintered samples with a density < 90 % showed almost completely dense surfaces. In that respect, surface micrographs give a misleading impression of the bulk density for some of the samples of $SrFe_{1-x}Cr_xO_{3-\delta}$. Density variations

---

[17] www.zeiss.de, Jena, Germany.
[18] www.kontron.com, Eching, Germany.
[19] www.veeco.com, Watford, England.
[20] The surface characterisation was performed at SINTEF Materials Technology, Oslo, Norway.

between the surface and the bulk of these materials are discussed in Chapter 2.5.1.

3.3.3 Oxygen permeation measurements

The oxygen permeability measurements were performed in a quartz reactor, as shown in Figure 3.1 (Vigeland et al., 1998). The cell consists of two compartments separated by the membrane disc. A mixture of 50 vol% oxygen and 50 vol% nitrogen was supplied to the feed side of the membrane (outer compartment) at a flow rate of 240 Sml/min. To the permeate side (inner compartment), He was supplied at the same flow rate. All gases were 5.0 quality, and the gas flows were controlled using mass flow controllers (Bronkhorst High-Tech[21], F-201C), calibrated for the gases in question. All gases are supplied to the quartz cell through steel tubes of 1.5 mm inner diameter. Gold rings made from Ø0.8 mm wire with 8 mm inner diameter were used as seals on both sides of the membrane to prevent gas leakages between the two compartments of the cell. A steel spring exerted a load, transferred by an alumina tube, of about 1.5 kg onto the gold rings. A fan was installed to avoid overheating of the steel spring. The ductility of gold at high temperatures (> 850 °C) resulted in a good seal which was maintained even at lower temperatures. Maximum operating temperature of the oxygen permeation measurements is determined by the melting point of gold at 1063 °C.

The lower half of the quartz cell was placed inside a vertical tube furnace[22]. The furnace has Kanthal[23] heating elements with a heated zone of 20 cm. The element is isolated with FIBROTHAL, with a water cooled steel shell on the outside. The power supply to the element is controlled by an Eurotherm[24] 902 PID-controller. The engineering design of the oxygen permeation equipment is given in Figure 3.2. The instrument coding is explained in Appendix 3. Thermocouples of type S (Pt-Pt/10%Rh), checked against a calibrated type S element with an accuracy of ± 1.5 °C, were located on each side of the

---

[21] www.bronkhorst.com, Ruurlo, The Netherlands.

[22] The engineering workshop, Hydro Research Centre, Porsgrunn, Norway.

[23] www.kanthal.se, Hallstahammar, Sweden.

[24] www.eurotherm.co.uk, Worthing, West Sussex, England.

membrane. The temperature was continuously measured on both sides of the membrane during the permeation experiment, and the data was logged with a multimeter (Fluke[25] 2620A, Hydra Data Acquisition unit). The temperature was changed at a rate of 1 °C/min with isotherms in intervals of 30 °C in the temperature range 800-1030 °C. Each isotherm was usually held for 4 hours. The membrane thickness (L) was varied from 0.9 to 2.4 mm, and approximately 35 membranes were investigated in the present work. The thickness and density of the membranes are given in Appendix 9.

The oxygen permeability of the membrane was continuously measured. The content of oxygen and nitrogen in the helium sweep gas were analysed in an on-line gas chromatograph (Chrompack[26], Micro-GC) containing two columns, PoraPlot Q and Molsieve 5Å. Helium was used as the carrier gas in the GC. The relevant column for this study was the Molsieve, giving high sensitivity (> 1 ppm) for the analysis of O_2 and N_2. The design of the GC allows reliable analysis every sixth minute. The gas analysis measurements were performed automatically[27] and the data stored in an Excel spreadsheet. The GC was frequently calibrated with a standard gas of 1000 ppm oxygen and 1000 ppm nitrogen in helium. The measured nitrogen content at the permeate side is directly related to the leakage rate past the gold seals or through the sample, while the oxygen content is the sum of contributions from the leakage and the oxygen flux through the membrane. The permeability rates were normalised to the surface area which was exposed to the gas atmosphere after sealing. All oxygen permeability data are reported in units of [mol m^{-2} s^{-1}].

Generally, a leak rate of less than 0.05 ml/min was achieved. Air leakage from the atmosphere, and inherent oxygen and nitrogen in the helium gas were accounted for by feeding He to both cell compartments at 110 °C, prior to the permeation measurements, while analysing the exhaust gas. External leakage was typically less than 5 ppm nitrogen and was of no significance to the transport behaviour of the membranes.

The exact oxygen content in the gas stream on the feed side was determined by measuring the oxygen to nitrogen ratio in the effluent stream at 110 °C,

[25] www.fluke.com, Eindhoven, The Netherlands.
[26] www.varianinc.com, Middelburg, The Netherlands.
[27] www.scisoftinc.com, (Maestro II), Charlottesville, VA USA.

prior to the oxygen permeability experiment. A period of 2-3 hours was necessary to obtain a stable level for the oxygen to nitrogen ratio.

The partial pressure of oxygen on the permeate side was determined by the oxygen flux through the membrane and any leakage. The oxygen partial pressure is assumed to be the same as the P_{O_2} in the effluent stream. This assumption is probably valid for the chosen rates of sweep gas when the gas tube is located near the membrane surface.

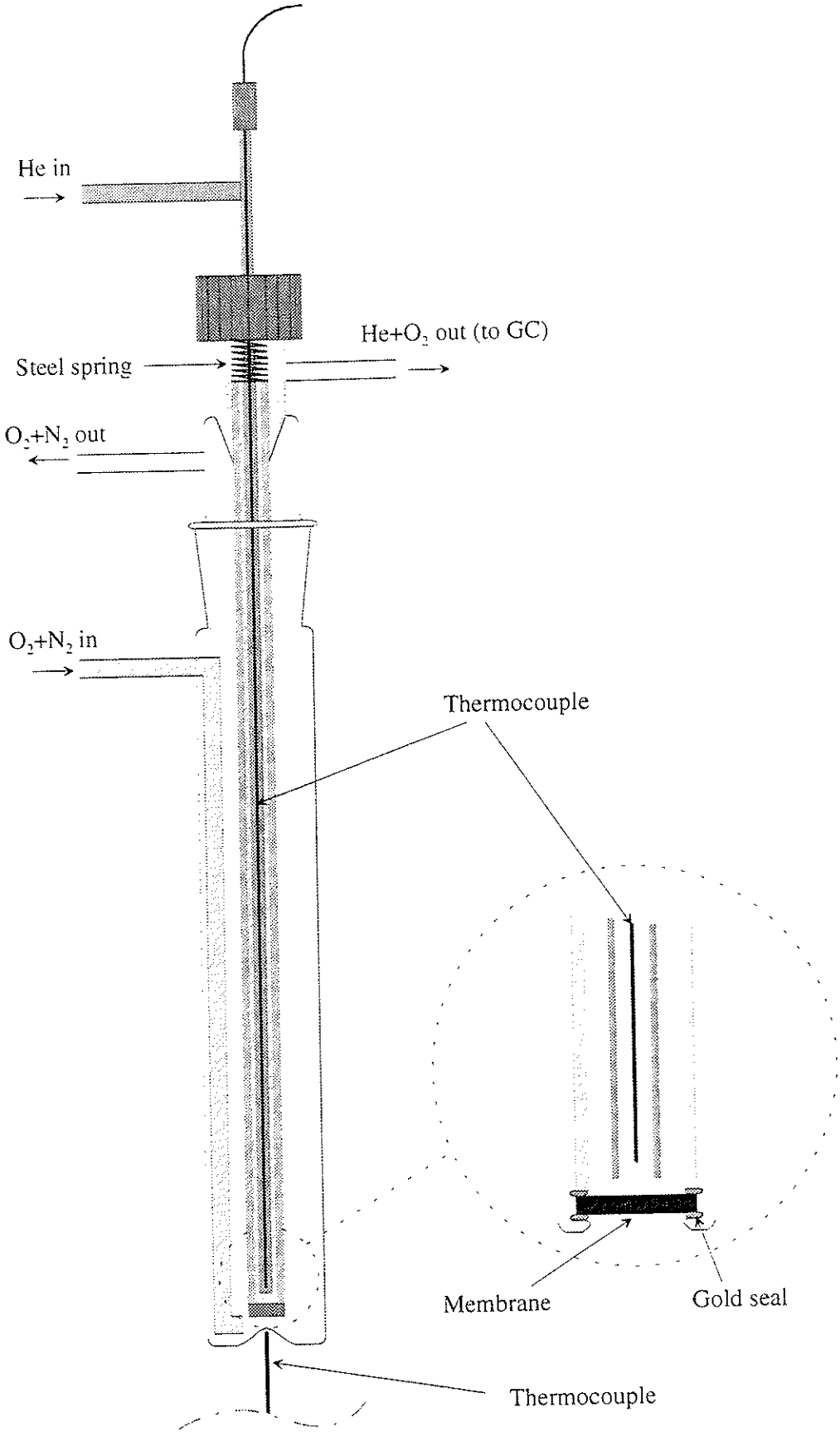

Figure 3.1 Schematic design of the quartz cell used for the measurements of oxygen permeability (Vigeland et al., 1998).

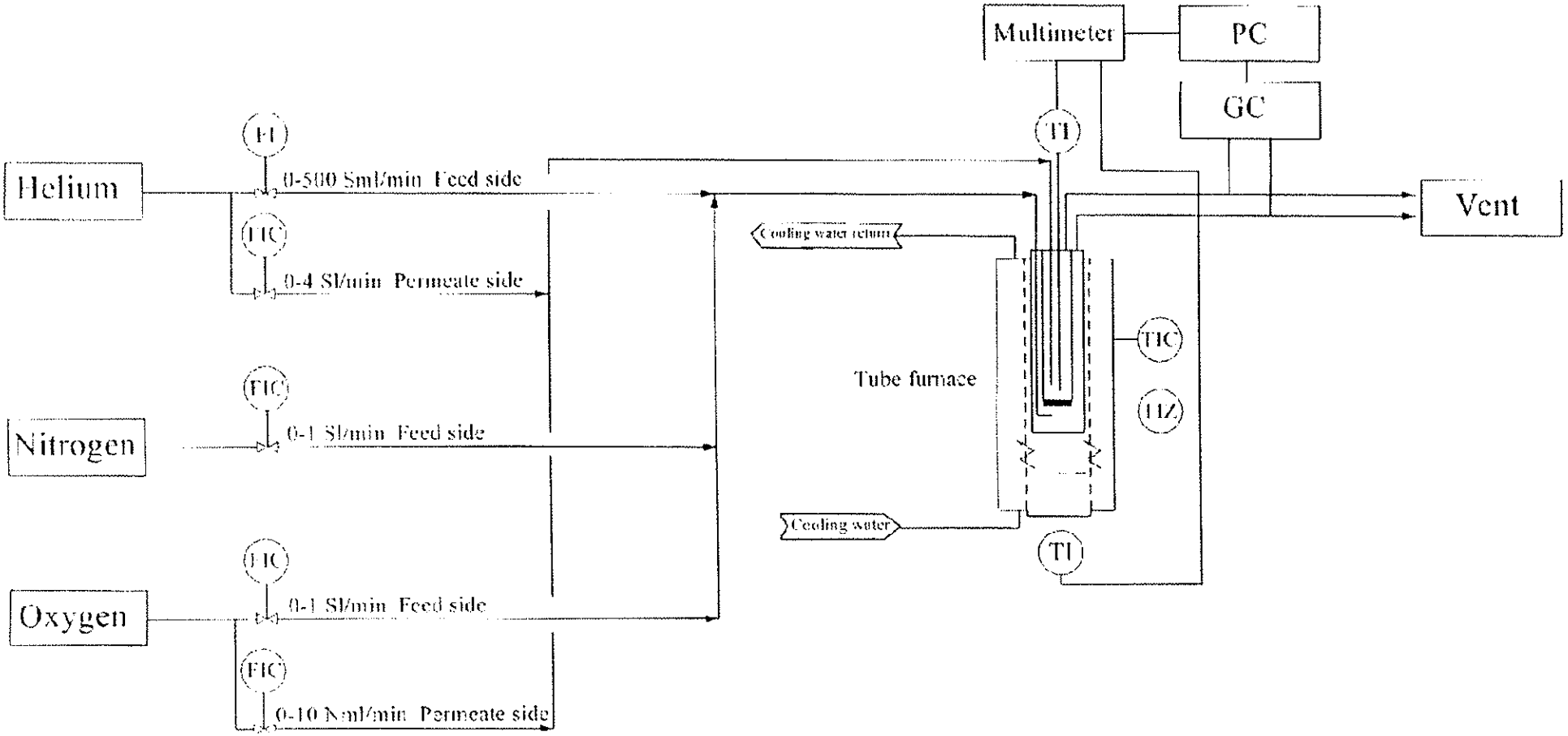

Figure 3.2 Engineering design of the oxygen permeation equipment. The instrument coding is explained in Appendix 3.

The steady-state oxygen permeation was calculated from:

$$J_{O_2} = \frac{f \cdot c_1}{A} - l_{O_2} \qquad [3.1]$$

where f is the total flow rate on the permeate side, c_1 is the oxygen concentration in the effluent stream, A is the effective membrane surface on the permeate side and l_{O_2} is the oxygen leak. The oxygen leak was calculated from:

$$l_{O_2} = \frac{f \cdot c_2 \cdot \frac{O_2}{N_2}}{A} \qquad [3.2]$$

where c_2 is the nitrogen concentration in the effluent stream and $\frac{O_2}{N_2}$ is the oxygen to nitrogen ratio at the feed side.

The measurements of the oxygen permeation in varying oxygen partial pressure gradients were performed in two ways. One way was to vary the oxygen content of the primary gas (between 20 and 87 vol%) while the total gas flow was held constant. The oxygen partial pressure on the oxygen lean side increased, due to the increased permeation from increased oxygen pressure in the feed gas. Determination of the oxygen content on the feed side after each alteration of the gas composition was done using the constant oxygen to nitrogen ratio measured prior to the experiment. Measurement of these ratios is described above.

The other method was to decrease the driving force by adding oxygen to the permeate side (0-6 Sml/min) while the helium flow was adjusted to keep the total gas flow constant. Determination of the added oxygen content was done by reducing the temperature between each alteration in oxygen addition to a range where there is negligible oxygen permeation (≈ 500 °C) , and then analysing the oxygen content with the GC. In these experiments the oxygen partial pressure on the feed side was held constant at 0.54 bar.

3.4 Results and discussion

The XRD results show that the membranes for the oxygen permeation measurements were single phase. The membranes had densities of more than 97.5 % of the theoretical value. The estimation of theoretical densities is described in Chapter 2.4.2. The Archimedes measurements showed a variation in density of ± 0.05 g/cm^3 for the different $SrFe_{0.97}Cr_{0.03}O_{3-\delta}$ membranes. The influence of porosity on the oxygen permeation could therefore be expected to be constant. The density of the membranes used in the oxygen permeation measurements are given in Appendix 9.

The increase in thickness from room temperature to the operation temperature, due to thermal and chemical expansion of $SrFe_{0.97}Cr_{0.03}O_{3-\delta}$, has not been corrected for. An average expansion coefficient of $35 \cdot 10^{-6}$ K^{-1} introduces a thickness increase of maximum 0.05 mm from room temperature to 1000 °C for membranes < 2.5 mm.

To avoid changing the microstructure during the permeation measurements, the maximum operating temperature was set to 150-250 °C below the sintering temperature. In spite of this procedure, the SEM analysis of the surface showed a change in the microstructure after the permeation experiments. This was most evident at the feed side of the membranes. Figures 3.3a-b show the oxygen rich surface of the membrane before and after the permeation experiment. The change in the microstructure on the feed surface is mainly re-crystallisation. This is not observed on the permeate side and hence indicates that the re-crystallisation depends on the P_{O_2}. The microstructural behaviour of $SrFe_{0.97}Cr_{0.03}O_{3-\delta}$ membranes after permeability experiments are further discussed in Chapter 3.4.7.

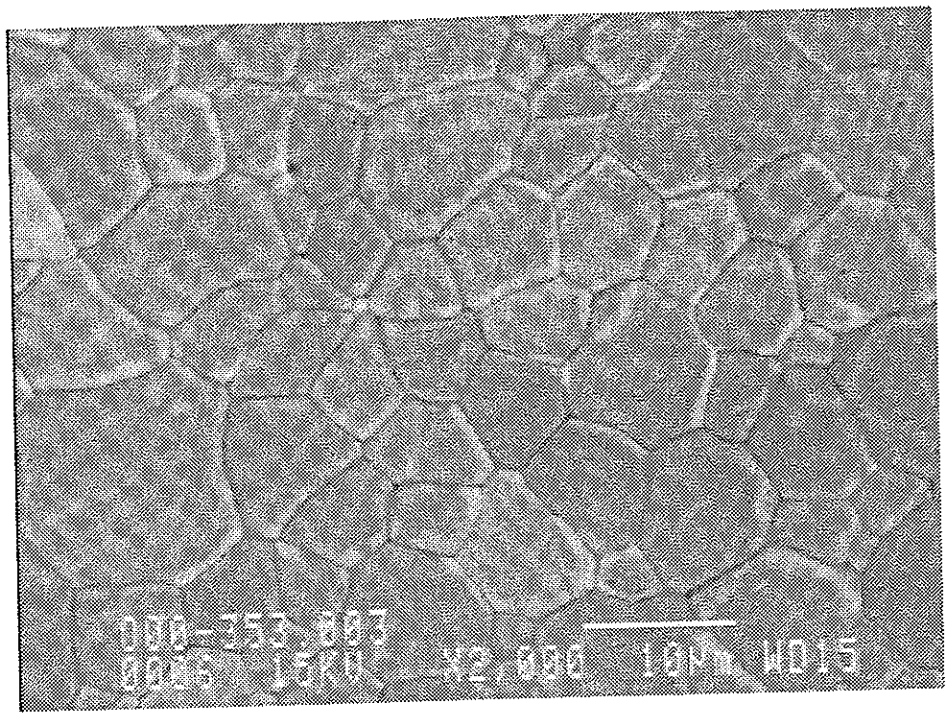

Figure 3.3a SEM micrograph of the membrane surface of $SrFe_{0.97}Cr_{0.03}O_{3-\delta}$, sintered at 1175 °C.

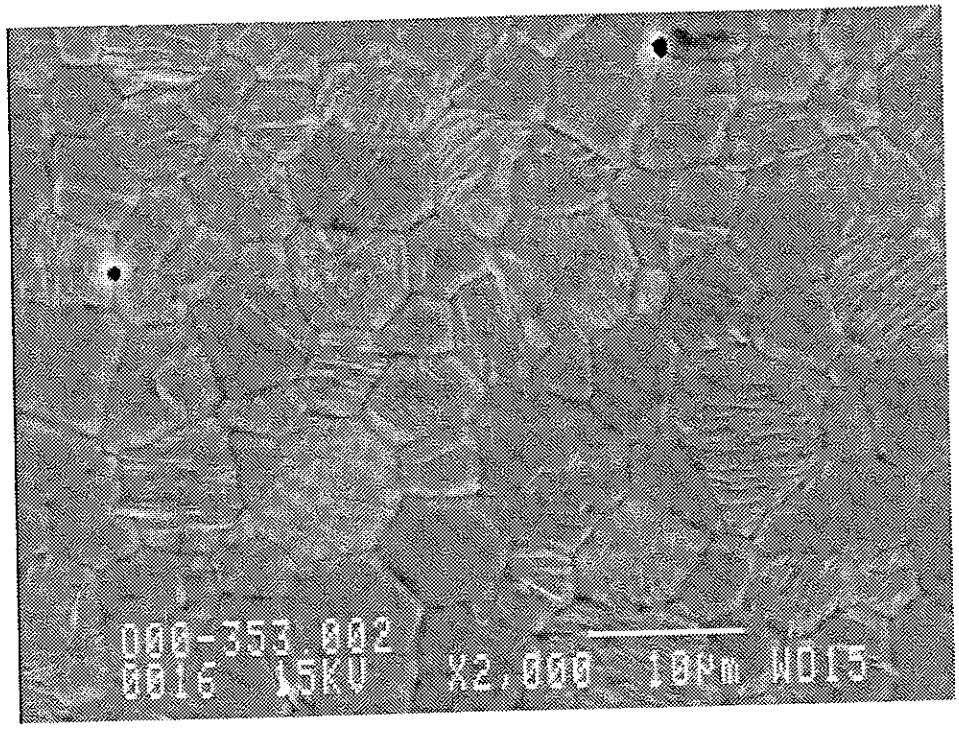

Figure 3.3b SEM micrograph of the feed side of a $SrFe_{0.97}Cr_{0.03}O_{3-\delta}$ membrane, sintered at 1175 °C. The permeation experiment was carried out in the temperature range 850-1030 °C for a total length of 100 hours.

Preliminary permeation measurements demonstrated a decreasing isothermal oxygen flux below approximately 900 °C, as would be expected from vacancy ordering. This is in agreement with other studies and will be discussed later. In view of this order-disorder phenomenon, data from experiments carried out above 900 °C are used to investigate the oxygen permeation as a function of temperature, driving force and microstructure.

It was not possible to obtain crack free membranes after the permeation experiments, even with slow cooling rates. The reason is that the membranes are constrained, and thus can not contract freely during cooling.

3.4.1 The reproducibility of the permeability measurements

After each temperature cycle the initial conditions were restored to check the reproducibility of the oxygen permeability rates. The reproducibility was also investigated for parallel membranes of the same composition and microstructure. The variation in the oxygen permeation under the same conditions for $SrFe_{0.97}Cr_{0.03}O_{3-\delta}$ membranes did not exceed 5 %, and was usually less than 3 %.

One of the major uncertainties in the permeability experiments is the determination of the effective permeation area as the deformation of the gold rings varied. Determination of the permeation area after the experiment is difficult and inaccurate, due to cracking during cooling.

Fluctuations in the flow of sweep gas or drift in the gas chromatograph also contribute to the experimental uncertainty. In selected experiments the sweep gas flow was checked using a recorder connected to the mass flow controller. No fluctuation was registered during the time measurement.

Laminar flow of the sweep gas on the permeate side of the membrane gives a stagnant film on the surface and can reduce the measured permeation by at least 10 %, as shown in Figure 3.4. No significant changes in the oxygen permeation are observed with the sweep gas tube less than 0.5 mm from the membrane surface under the chosen conditions. The inner diameter of the gas tube is 1.5 mm and the He flow was 240 Sml/min. This gives a gas velocity of 2.3 m/s and a Reynolds number of approximately 30. This result shows

that a relative high sweep gas flow is necessary to avoid a stagnant oxygen film on the membrane surface.

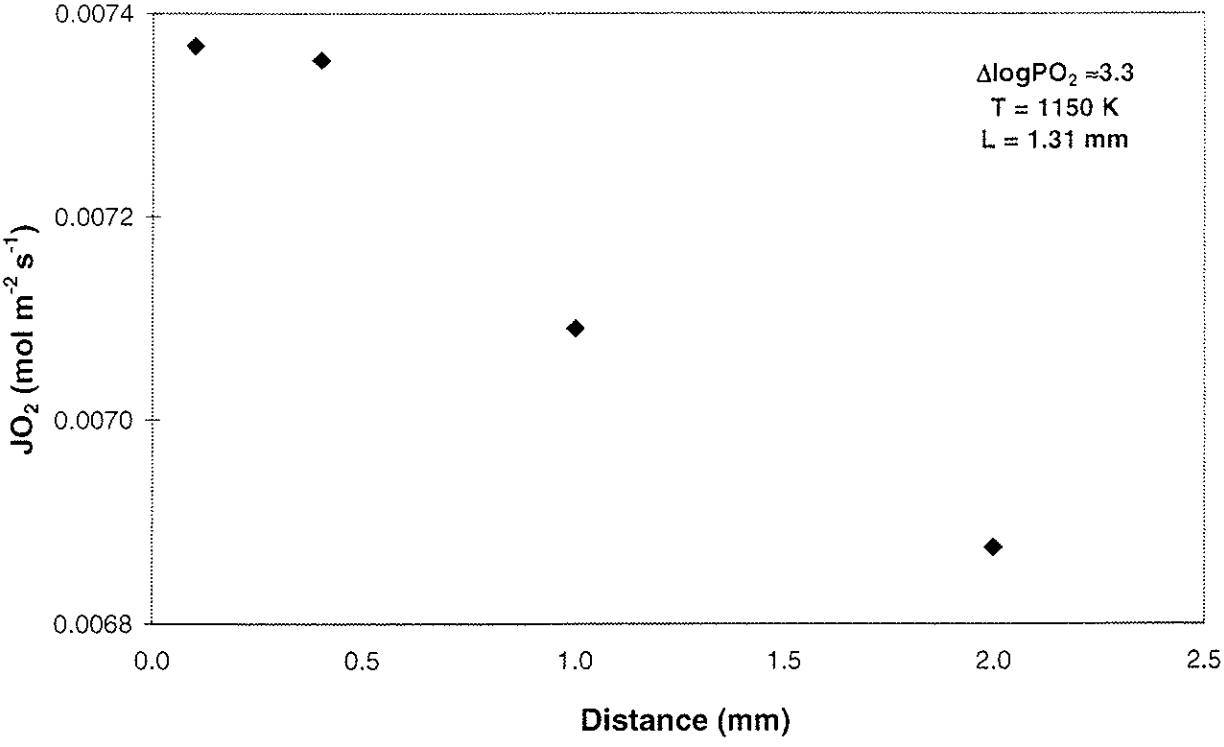

Figure 3.4 Oxygen permeation as a function of distance between the sweep gas tube and the membrane surface.

3.4.2 Oxygen permeability of $SrFeO_{3-\delta}$ and $SrFe_{0.97}Cr_{0.03}O_{3-\delta}$

A limited effort was devoted to the study of permeability differences between membranes of $SrFeO_{3-\delta}$ and $SrFe_{0.97}Cr_{0.03}O_{3-\delta}$. Figure 3.5 shows the difference in oxygen permeability for the two different compositions. The oxygen permeation decreased approximately 10 % by introducing 3 mol% chromium in the structure. The measurements have been performed on membranes with equal thickness, but the unsubstituted membrane had ≈4 % lower density. Since the influence of oxygen surface exchange limitations are unknown for $SrFeO_{3-\delta}$, it is impossible to evaluate the significance of the difference in porosity. The uncertainty in the oxygen permeation experiments is maximum ± 5 %, as discussed in Chapter 3.4.1. In view of this, the influence of 3 mol% Cr-substitution in $SrFe_{1-x}Cr_xO_{3-\delta}$ may not be significant. Kharton et al. (1998) reported that the oxygen permeability was essentially independent of chromium substitution for $SrCo_{0.90-x}Fe_{0.10}Cr_xO_{3-\delta}$ where x=0.01-0.05.

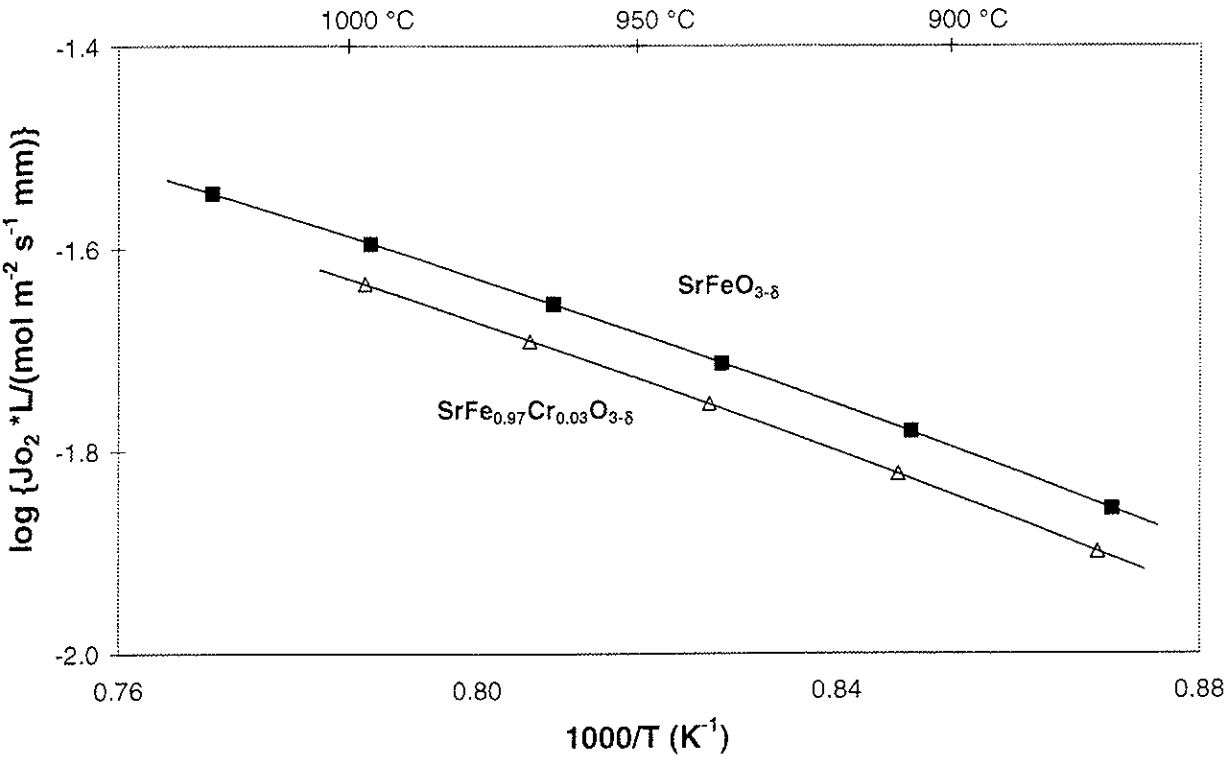

Figure 3.5 Arrhenius plot of oxygen permeation of $SrFeO_{3-\delta}$ and $SrFe_{0.97}Cr_{0.03}O_{3-\delta}$ membranes exposed to a similar driving force of $\Delta \log P_{O_2} \approx 2.1$.

3.4.3 Temperature dependence of the oxygen permeation of $SrFe_{0.97}Cr_{0.03}O_{3-\delta}$ membranes

The activation energy for oxygen permeation, limited by bulk diffusion is given by:

$$E_a (J_{O_2}) = E_a (D_v) + \Delta E_v (\delta) \qquad [3.3]$$

when the electronic conductivity does not significantly influence the transport. $E_a (D_v)$ is the activation energy for vacancy mobility and $\Delta E_v (\delta)$ is the energy related to the temperature dependent oxygen vacancy formation, given as $d\ln\delta/d(1/T)$. This can be seen from Wagner's equation [1.4].

The parameter ΔE_v is described and quantified in Chapter 4.1. According to ten Elshof et al. (1995), the ΔE_v depends on the oxygen partial pressure. In

reality, ΔE_v depends on the change in oxygen vacancy concentration and not on the oxygen partial pressure itself.

The increased oxygen permeation at higher temperatures reduces the gradient in oxygen partial pressure over the membrane. The influence of the variation in $\Delta \log P_{O_2}$ is investigated. From the Arrhenius plot in Figure 3.6 the apparent activation energy for the oxygen permeation with a fixed gradient in oxygen partial pressure is calculated to be 59 kJ/mol.

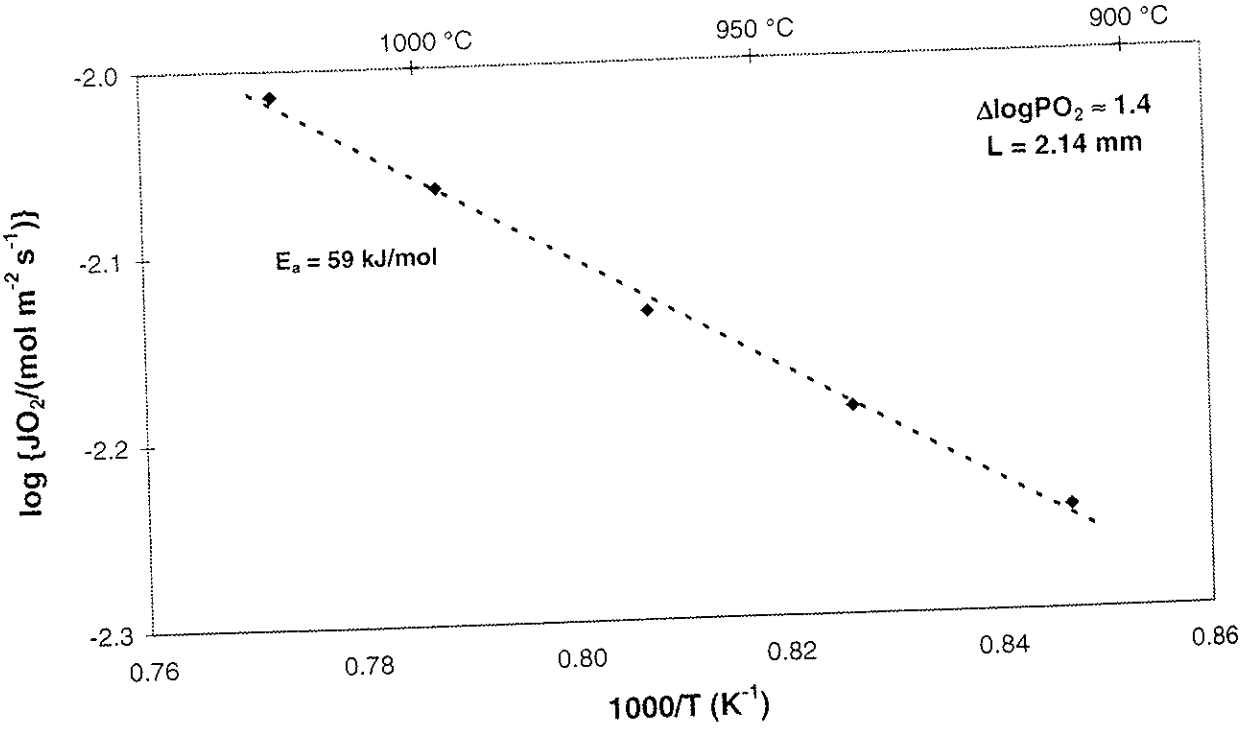

Figure 3.6 Arrhenius plot of the oxygen permeation of $SrFe_{0.97}Cr_{0.03}O_{3-\delta}$ membrane in a fixed gradient of oxygen partial pressure.

The fixed gradient is obtained by adding oxygen to the permeate side of the membrane, giving a lower driving force for this measurement compared to the experiments where the permeate side is only flushed with helium. Figure 3.7 shows an Arrhenius plot where the P_{O_2} at the permeate side is floating with the oxygen permeability. The small change in driving force due to the increased permeation at higher temperature is not significant in calculation of the activation energy. Nevertheless, some convex curvatures are observed as the driving force is slightly changed with the permeation rates.

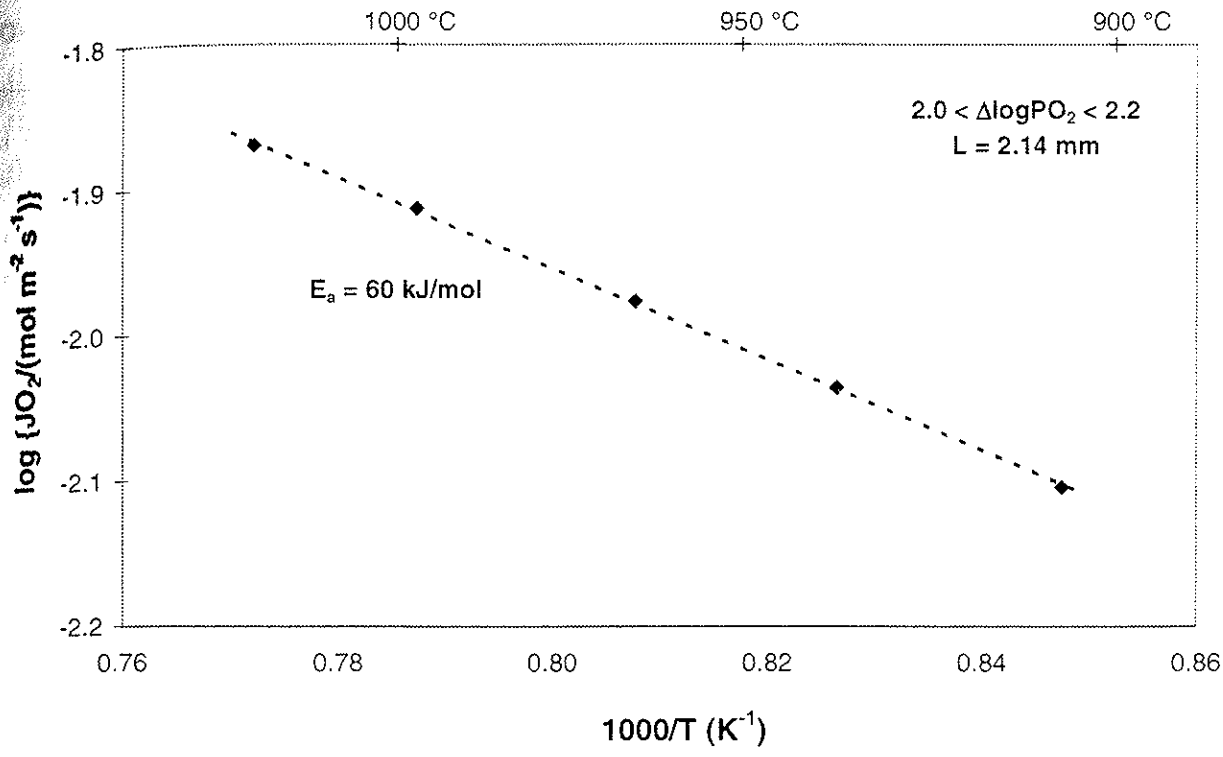

Figure 3.7 Arrhenius plot of oxygen permeation for $SrFe_{0.97}Cr_{0.03}O_{3-\delta}$ membrane where the P_{O_2} at the permeate side is floating with the oxygen permeability.

The apparent activation energies for all the permeation experiments were determined in the temperature range 900-1000 °C. The mean activation energy for oxygen permeation was calculated to 52 ± 8 kJ/mol. This is apparently independent of thickness, temperature and driving force. The comparison of apparent activation energies for the different physical parameters are given in Table 4.5.

Holt et al. (1999) reported the activation energy for the chemical diffusion coefficient ($\tilde{D}$) to be 54 kJ/mol for $SrFeO_{3-\delta}$. This value should be comparable to the activation energy for the present oxygen permeation. The method applied was transient thermogravimetry (TTG) in the oxygen partial pressure range from 0.5 bar to 1 bar. Determination of $\tilde{D}$ from electrochemical measurements reports activation energies of 51-55 kJ/mol (Larsen, 1999).

3.4.4 Thickness dependence of the oxygen permeation of $SrFe_{0.97}Cr_{0.03}O_{3-\delta}$ membranes

According to Wagner's equation, [1.4], the oxygen permeation is expected to be linearly dependent on the membrane thickness. Oxygen permeation of $SrFe_{0.97}Cr_{0.03}O_{3-\delta}$ membranes as a function of inverse thickness is plotted in Figure 3.8. The data indicate an increased surface control limiting the oxygen flux as the membrane thickness decreases.

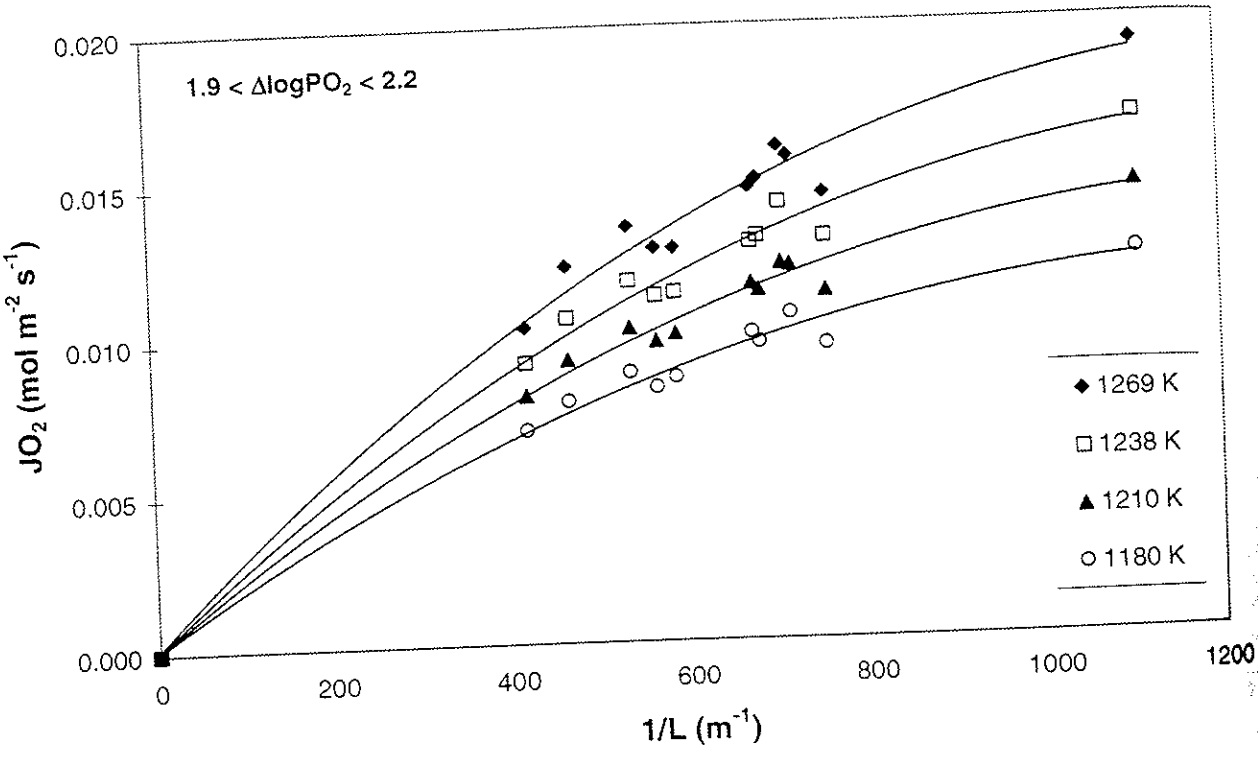

Figure 3.8 Oxygen permeability as a function of inverse thickness of $SrFe_{0.97}Cr_{0.03}O_{3-\delta}$ membranes.

The extent of surface limitation may vary with temperature and driving force across the membrane. The degree of surface exchange control at constant temperature can be investigated using the following equation:

$$1/J_{O_2} = (L_s + L)/j_b \qquad [3.4]$$

where J_{O_2} is the oxygen permeability, L_s is the apparent additional bulk thickness caused by surface exchange limitations, L is the membrane thickness and j_b is the bulk permeability rate for a membrane with 1 mm thickness (Vigeland et al., 1998). Hence, L_s << L for bulk controlled permeation. The two parameters L_s and j_b can be obtained by fitting the experimental permeation data to equation [3.4], details of which are given in Appendix 10. Similar methods of estimation the total surface exchange limitation is reported by other authors as well (Bouwmeester et al., 1994).

Oxygen permeability of $SrFe_{0.97}Cr_{0.03}O_{3-\delta}$, with different membrane thicknesses is plotted as a function of inverse temperature in Figure 3.9. A second degree polynomial has been fitted to the data. The membranes have experienced the same sintering conditions (1175 °C/3h) to get similar microstructures. The surfaces area index was in the range 1.10-1.13. The importance of the surface roughness is discussed in Chapter 3.4.6.

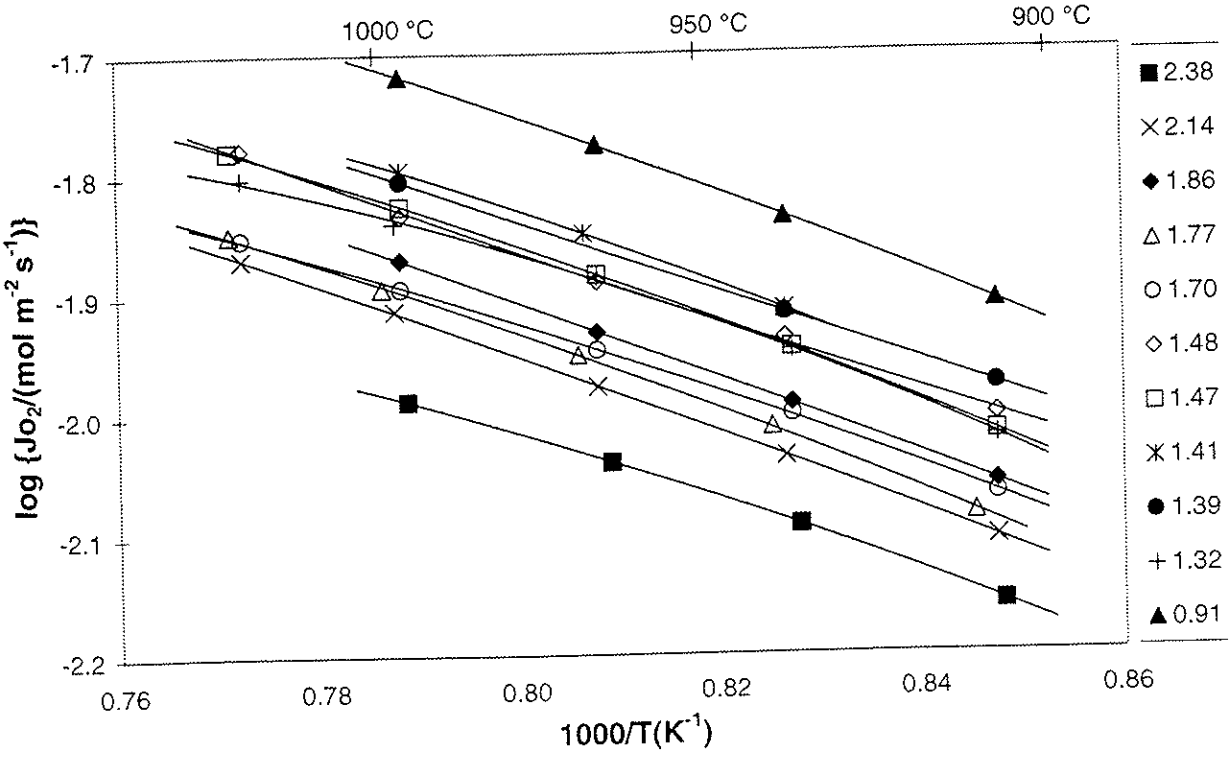

Figure 3.9 Arrhenius plot of the oxygen permeability for $SrFe_{0.97}Cr_{0.03}O_{3-\delta}$ membranes with different thicknesses. The legends next to the figure give the membrane thickness (mm).

Figure 3.10 shows the parameters L_s and j_b as a function of inverse temperature. This plot shows that L_s increases with decreasing temperature. This implies that the degree of surface exchange limitation increases as the temperature decreases. Activation energies for the bulk diffusion and surface exchange limited transport are estimated to 52 ± 8 and 57 ± 8 kJ/mol at 1273 K. Figures 3.11 and 3.12 represent the Arrhenius plots of the bulk diffusion and the surface exchange process. The surface exchange limitation is further discussed in Chapter 4.2.

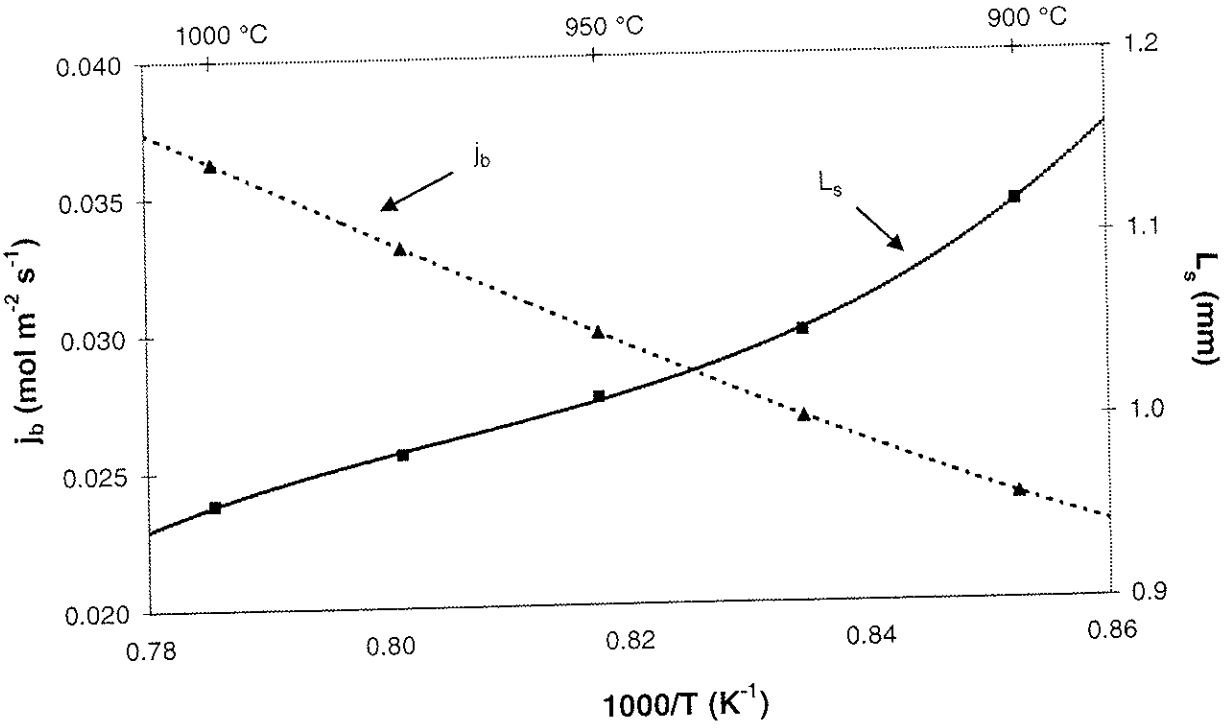

Figure 3.10 Calculated bulk permeation (j_b) for a membrane of 1 mm thickness and the apparent additional bulk thickness (L_s), related to the surface exchange limitation.

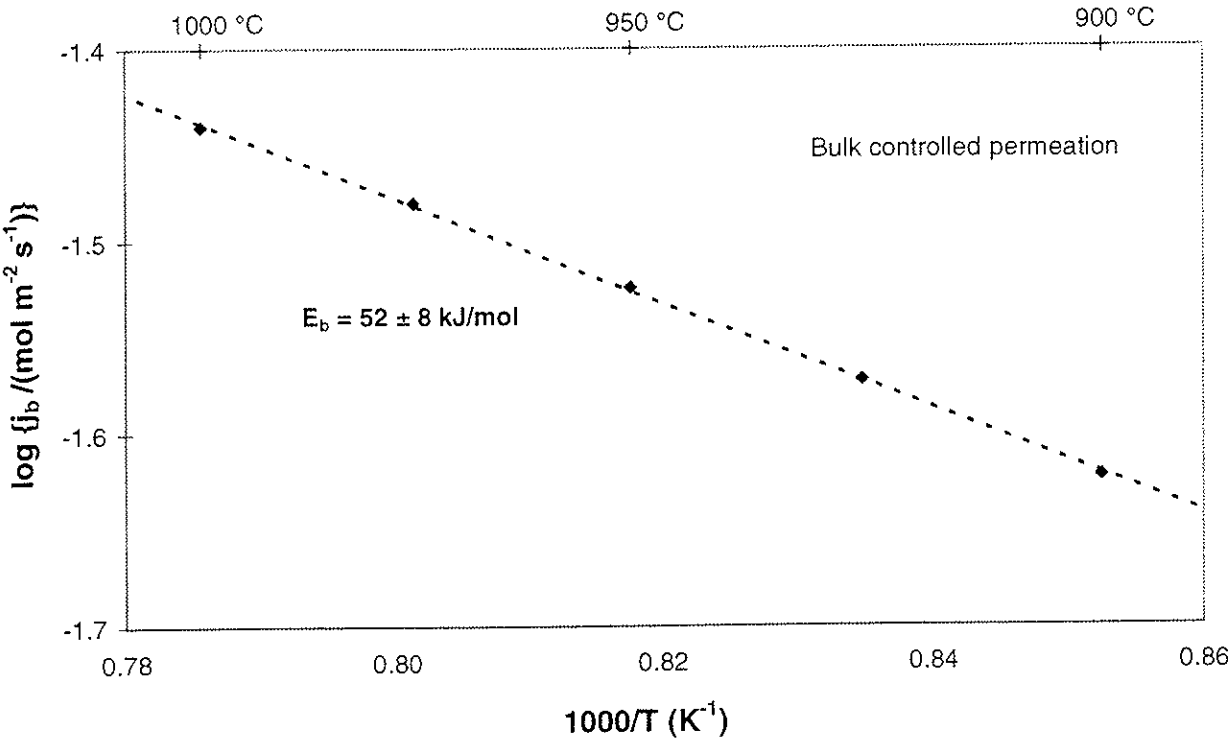

Figure 3.11 Arrhenius plot of the calculated bulk diffusion of $SrFe_{0.97}Cr_{0.03}O_{3-\delta}$ membrane with thickness 1 mm.

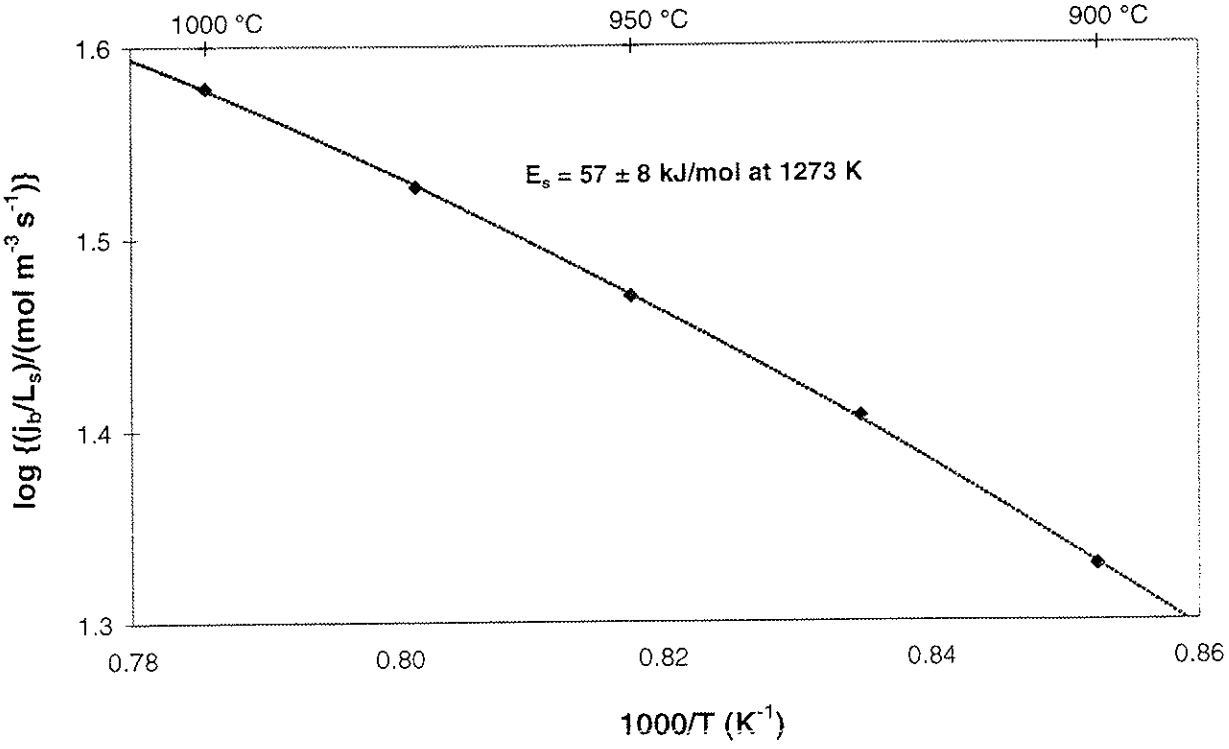

Figure 3.12 Arrhenius plot of the calculated surface exchange rate of a $SrFe_{0.97}Cr_{0.03}O_{3-\delta}$ membrane.

The equation [3.4] can be used to estimate the potential oxygen permeability rate if the surface exchange limitation is eliminated. Bulk permeability as a function of membrane thickness is obtained by setting $L_s = 0$ in the equation [3.4]. The results are plotted in Figure 3.13.

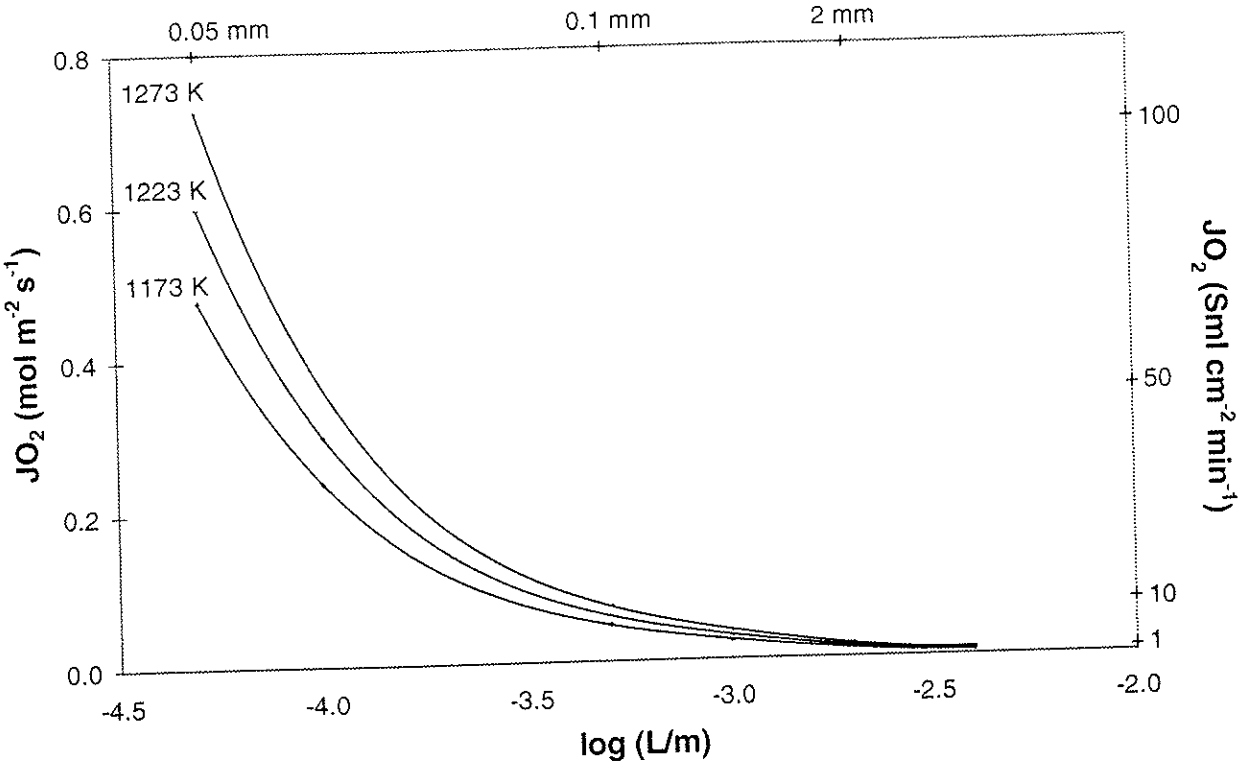

Figure 3.13 Calculated bulk limited oxygen permeation as a function of thickness of $SrFe_{0.97}Cr_{0.03}O_{3-\delta}$ membranes.

This demonstrates the possibility of obtaining oxygen permeability rates of approximately 0.7 mol m^{-2} s^{-1} or 100 Sml cm^{-2} min^{-1} for a 50 µm thick membrane at 1000 °C and $\Delta \log P_{O_2} \approx 2.0$. A way to achieve this could be to increase the surface area with a porous layer or apply a catalyst. However, the surface area must increase approximately 20 times to eliminate the surface exchange limitation. This is probably not realistic.

Chapter 4.2 describes and discusses an alternative method of estimating the surface oxygen exchange control, which also resolves the surface exchange limitations on the two membrane surfaces.

3.4.5 Oxygen partial pressure dependence of the oxygen permeation of $SrFe_{0.97}Cr_{0.03}O_{3-\delta}$ membranes

Oxygen permeability as a function of driving force of $SrFe_{0.97}Cr_{0.03}O_{3-\delta}$ are given in Figure 3.14. The permeability data is obtained on a membrane with thickness 2.14 mm and rough surfaces. The effect of surface roughness is discussed in the following section. Varying the P_{O_2} on the feed side gives apparently a higher flux through the membrane than P_{O_2} variation on the permeate side with the same driving force. This can be explained by difference in the oxygen defect concentration from the feed side to the permeate side in the two experiments. This is illustrated in Figure 3.15 for the data at 1270 K. Similar behaviour is observed for the measurements at other temperatures, given in Figure 3.14. The oxygen stoichiometry data is taken from the model, described in Chapter 4.1.

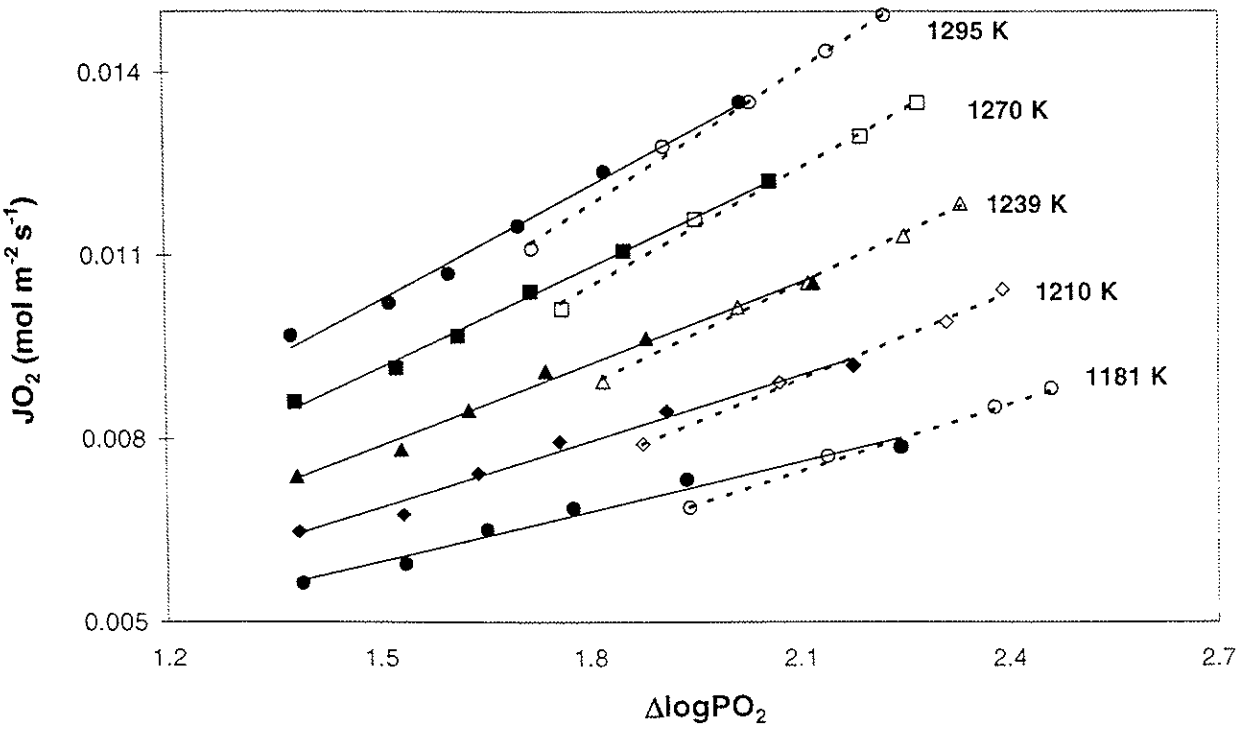

Figure 3.14 Oxygen permeation as a function of driving force for a $SrFe_{0.97}Cr_{0.03}O_{3-\delta}$ membrane of thickness 2.14 mm. Solid lines show the measurements with constant $P_{O_2} = 0.5\ bar$ at the feed side of the membrane. Dashed lines show the experiments with approximately constant $P_{O_2} \approx 0.005\ bar$ on the permeate side.

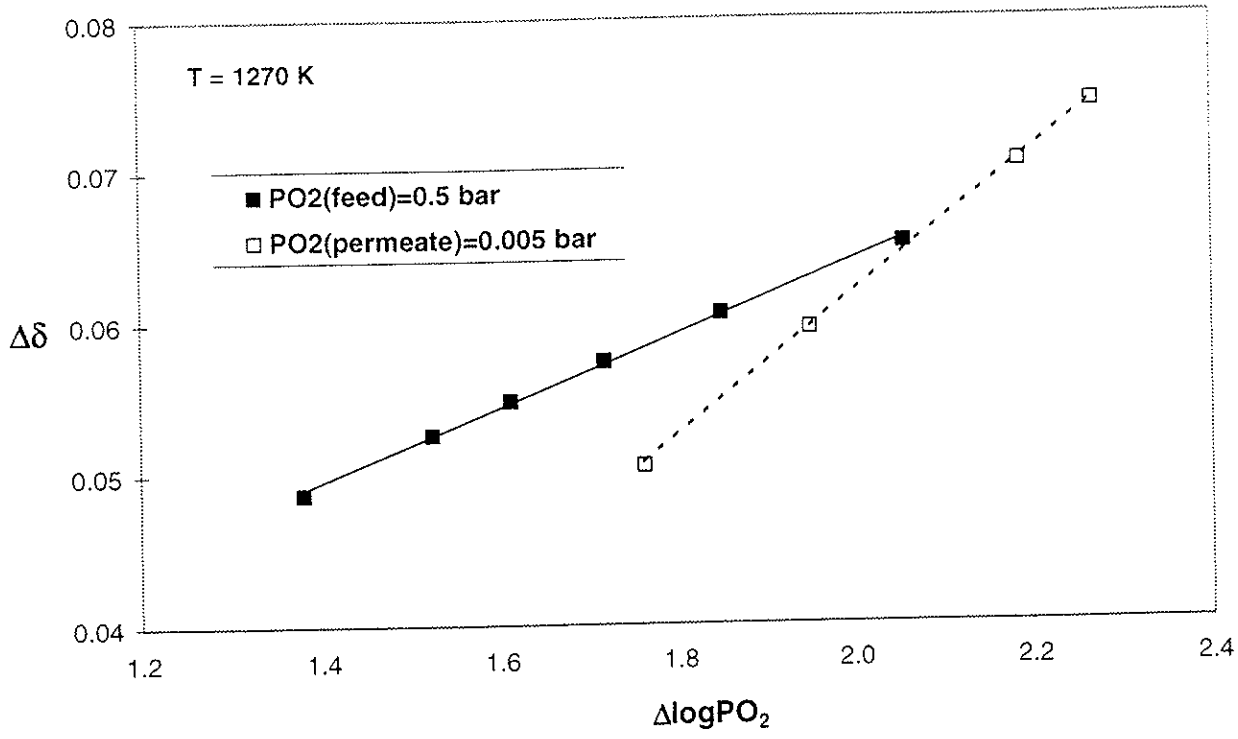

Figure 3.15 Relative change in oxygen defect concentration from the feed side to the permeate side as a function of driving force for a permeating $SrFe_{0.97}Cr_{0.03}O_{3-\delta}$ membrane. The figure explains the behaviour given in Figure 3.14.

The apparent activation energy for the oxygen permeation of $SrFe_{0.97}Cr_{0.03}O_{3-\delta}$ membranes is almost independent of the driving force. The results from oxygen permeation versus driving force were used to model the surface exchange rate as a function of temperature and P_{O_2}. Results from this approach are given and discussed in Chapter 4.2.

3.4.6 Effect of microstructure on the oxygen permeation of $SrFe_{0.97}Cr_{0.03}O_{3-\delta}$ membranes

$SrFe_{0.97}Cr_{0.03}O_{3-\delta}$ is used in this study as a model material for microstructure dependent permeability, due to the high oxygen permeation and the possibility of controlling the microstructure of the membranes. Membranes with different microstructures are made from the same batch of powder to avoid the uncertainty of varying cation nonstoichiometry and trace impurities.

A batch of membranes of composition $SrFe_{0.97}Cr_{0.03}O_{3-\delta}$ has been made with rough surfaces on both sides. Higher surface areas were obtained by grain pull out during grinding. The measured specific surface area was approximately 10 % larger than for the membranes with smooth surfaces. Micrographs of smooth and rough surfaces are shown in Figure 3.16.

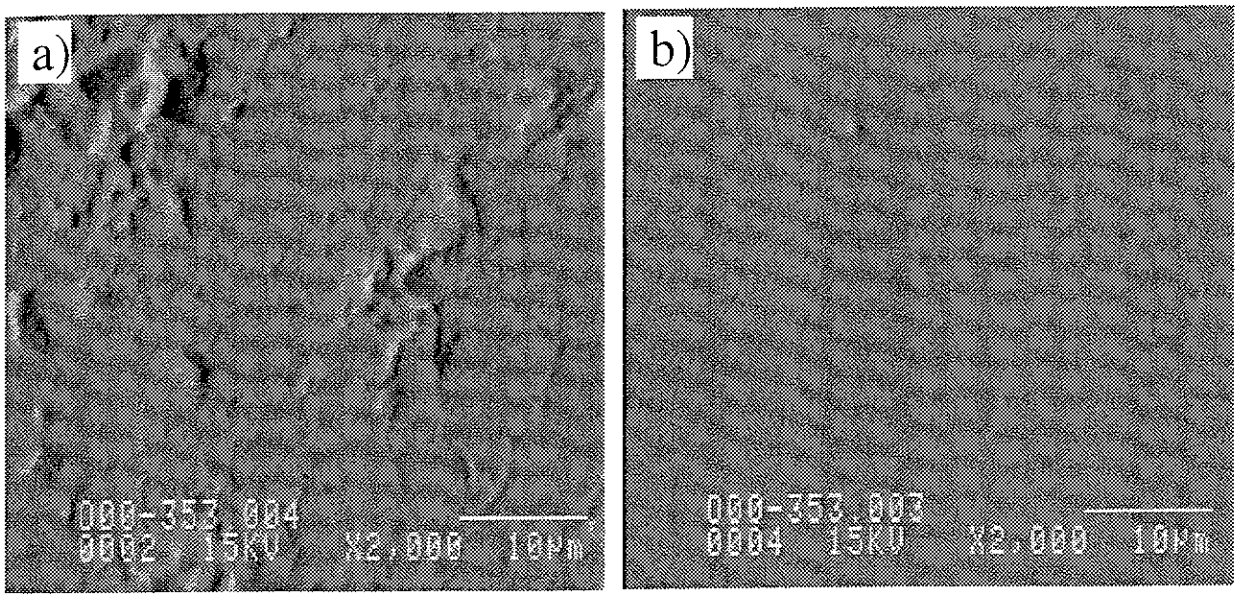

Figure 3.16 SEM micrographs of sintered (1175 °C/3 h), polished and thermally etched (1175 °C/10 min) membranes of $SrFe_{0.97}Cr_{0.03}O_{3-\delta}$ with **a)** rough and **b)** smooth surfaces. Surface area index: 1.13 and 1.01, respectively.

Membranes with dissimilar grain boundary lengths are obtained by changing the sintering profile of identical green bodies. Only dense membranes with smooth surfaces are used for this study, to make possible the measuring of grain boundary lengths. Figure 3.17 show micrographs of membranes with three different microstructures and their grain boundary lengths. The density of the membranes was measured to 98.5 ±0.5 %.

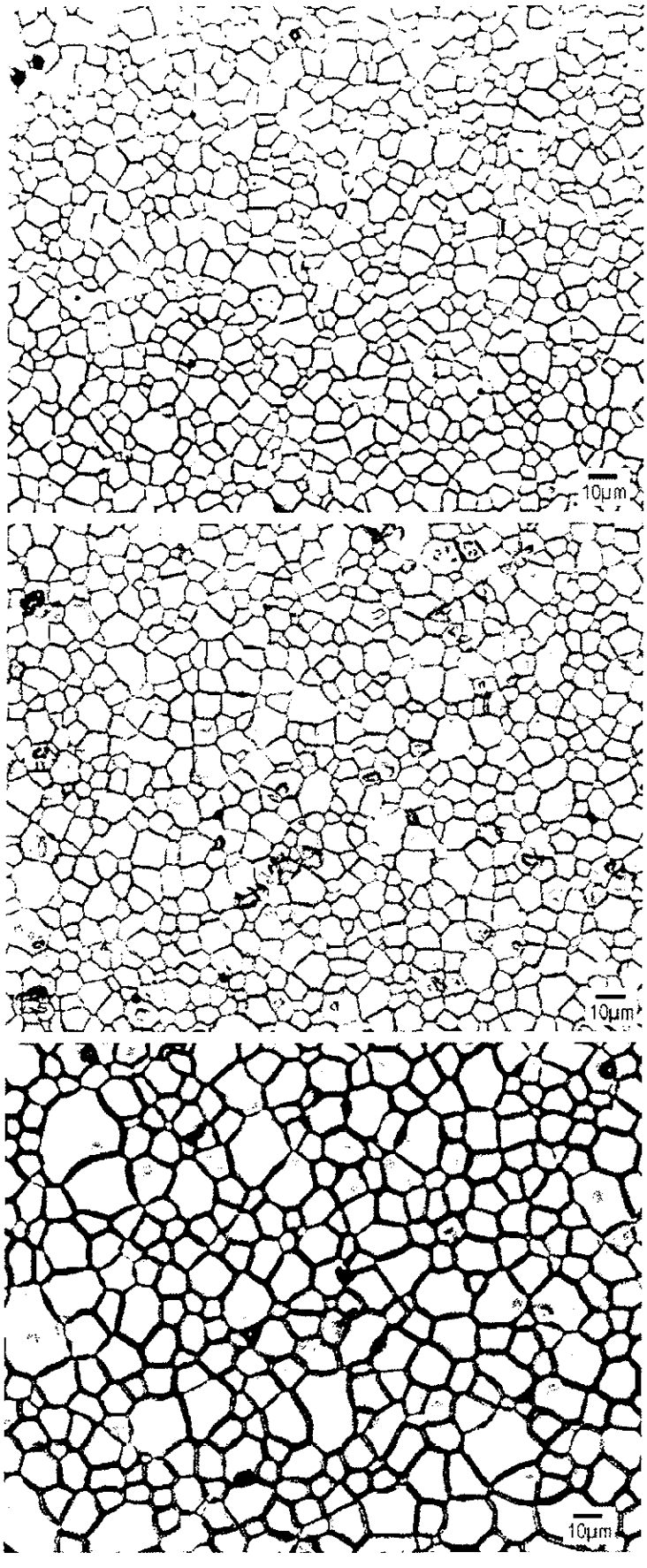

Sintered at 1175 °C/3h in air
Grain boundary length:
0.289 µm/µm^2

Sintered at 1200 °C/3h in air
Grain boundary length:
0.263 µm/µm^2

Sintered at 1275 °C/3h in air
Grain boundary length:
0.182 µm/µm^2

Figure 3.17 Optical micrographs of sintered, polished and thermally etched $SrFe_{0.97}Cr_{0.03}O_{3-\delta}$ membranes.

Figure 3.18 shows the oxygen permeability multiplied by the thickness as a function of temperature of membranes with rough surfaces and varying grain boundary length. For comparison, permeability data of membranes with smooth surfaces and varying grain boundary length are given in Figure 3.19. It is clearly seen that to roughening the surface of the membranes, i.e. increasing the surface area, results in oxygen permeability independent of the grain boundary length. These results indicate that the bulk grain boundary length has negligible influences on the oxygen permeability of these membranes. However, the grain boundaries in the surfaces seem to be an important factor for the surface exchange of oxygen.

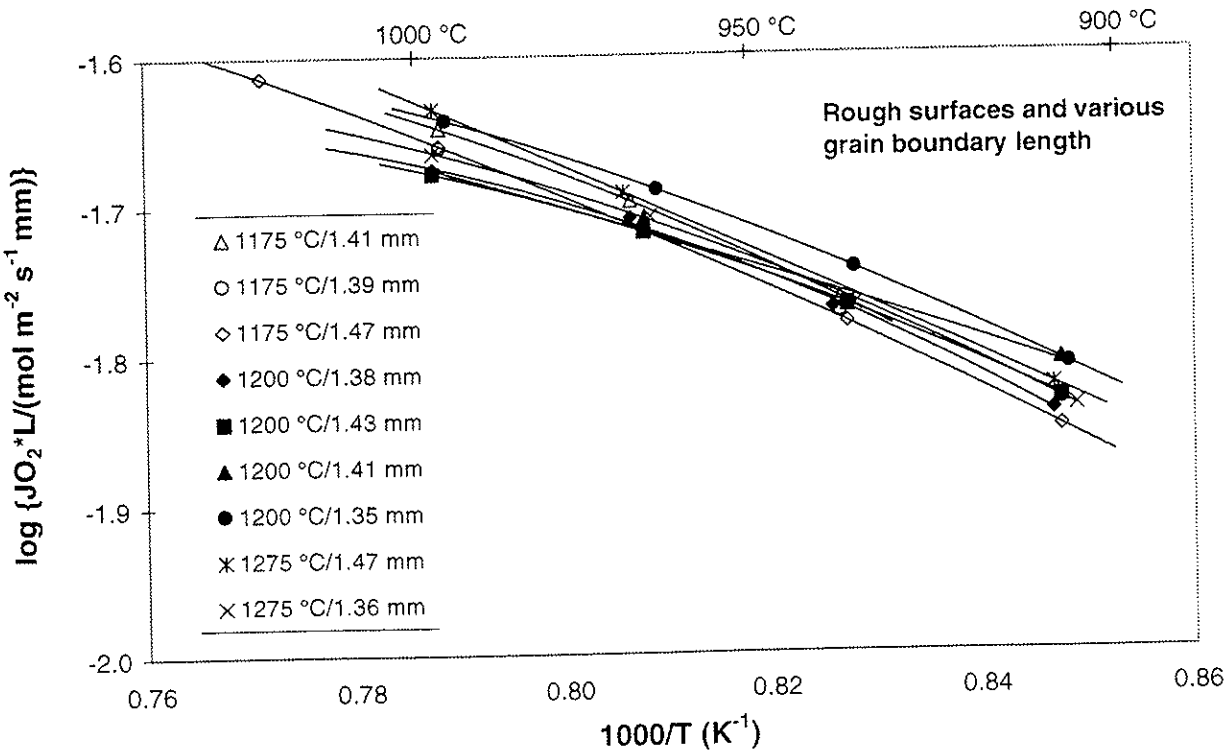

Figure 3.18 The permeability of $SrFe_{0.97}Cr_{0.03}O_{3-\delta}$ membranes with rough surfaces and varying grain boundary length. The legends give the sintering temperature and the membrane thickness. $\Delta \log P_{O_2} \approx 2.1$.

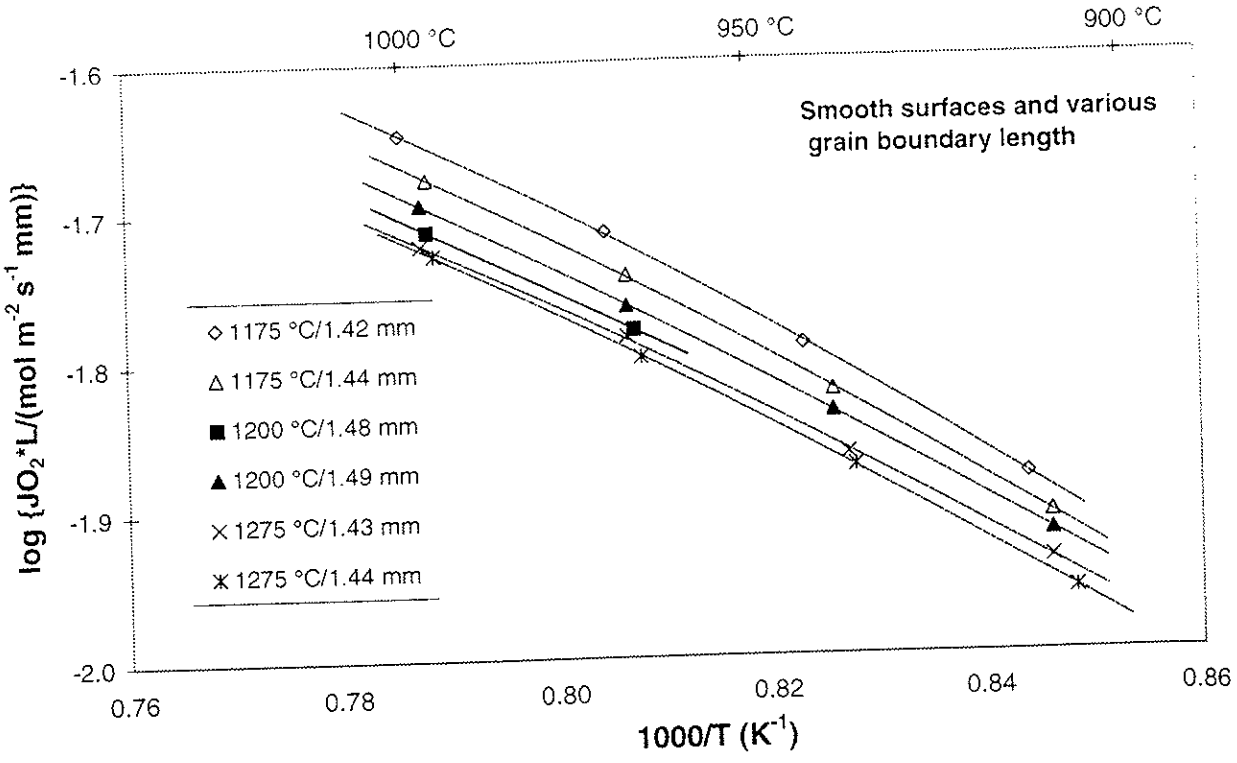

Figure 3.19 Permeability of $SrFe_{0.97}Cr_{0.03}O_{3-\delta}$ membranes with smooth surfaces and varying grain boundary length. The legends give the sintering temperature and the membrane thickness. $\Delta \log P_{O_2} \approx 2.1$.

Overall permeation indicates higher activation energies at the investigated temperature range for membranes with smooth surfaces. Representative permeability data for membranes with the two surface area indexes are compared in Figure 3.20. Based on the result of increased surface exchange limitations when reducing the temperature (Figure 3.10), there are indications that membranes with smooth surfaces have more surface exchange limitations than membranes with rough surfaces.

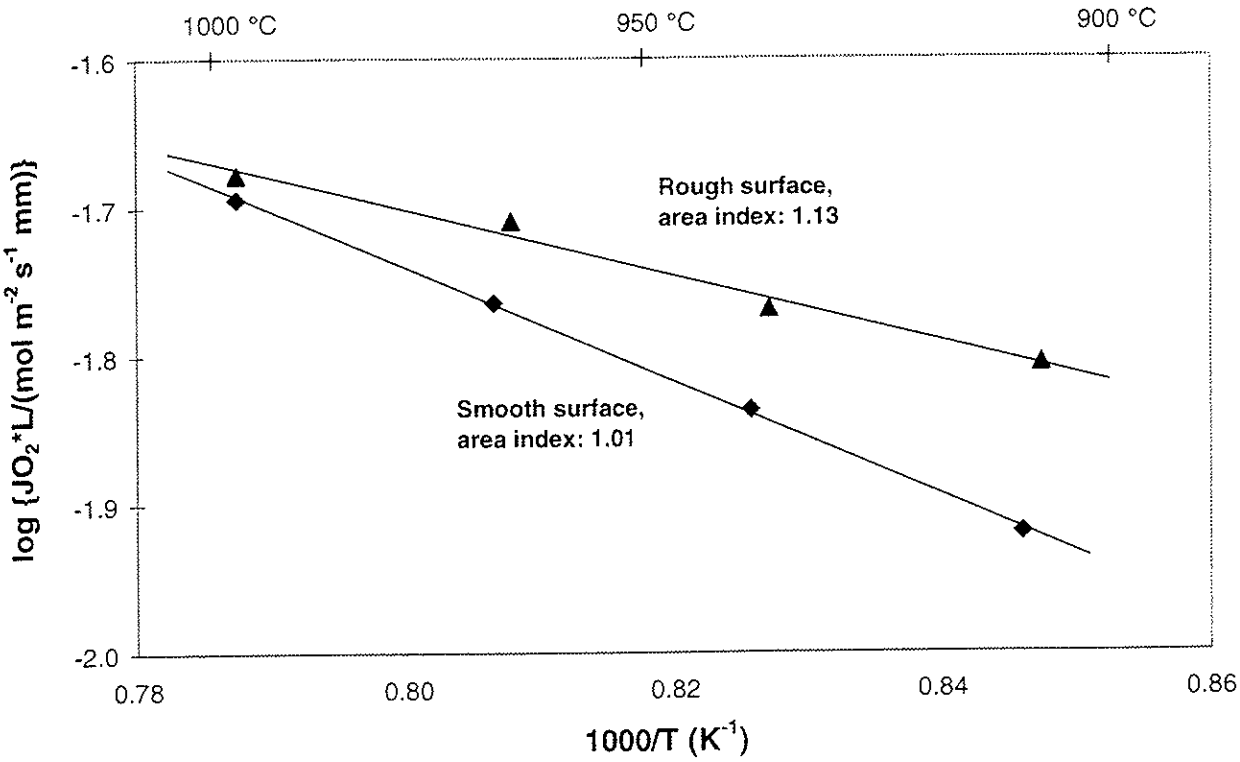

Figure 3.20 Oxygen permeation of $SrFe_{0.97}Cr_{0.03}O_{3-\delta}$ membranes with various surface roughness and equal grain boundary length. $\Delta \log P_{O_2} \approx 2.1$.

The two membranes batches with different surface area indexes are made from different lots of powder. This decreases the reliability in the evaluation of their transport behaviour. However, chemical characterisation of the membranes show identical behaviour. The grain boundaries of membranes made from the different powder batches were studied using optimised EDS line scans. No variation in composition across the grain boundaries was observed. Small deviations from stoichiometric composition may occur even though they can not be detected.

The experimental results of oxygen permeability as a function of grain boundary length are given in Figure 3.21.

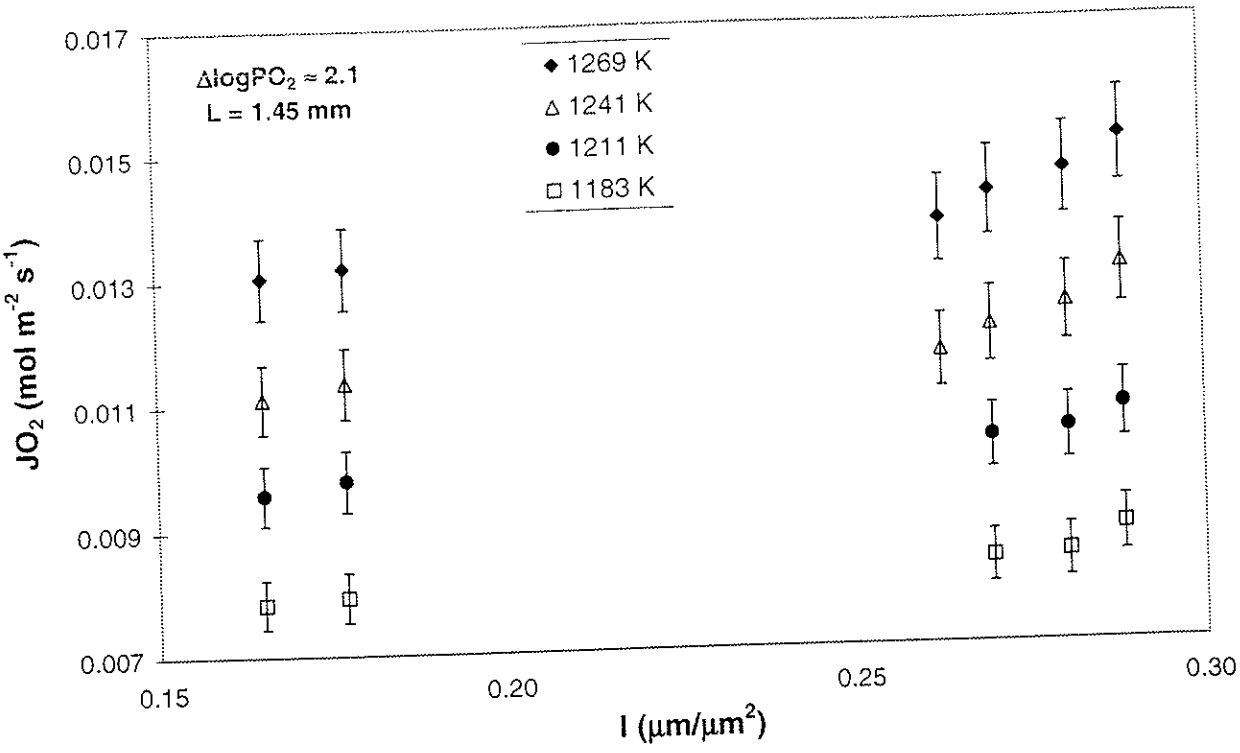

Figure 3.21 Oxygen permeation as a function of grain boundary length of $SrFe_{0.97}Cr_{0.03}O_{3-\delta}$ membranes with thicknesses, 1.45 mm.

It is clearly seen that the oxygen permeability increases with increasing grain boundary length. However, the reliability of these results is limited due to the limited number of experiments carried out. Nevertheless, a physical model has been developed to fit the data. The results and discussion of this numeric modelling of the grain boundary dependency are given in Chapter 4.3.

3.4.7 Kinetic demixing and decomposition

In some of the oxygen permeation experiments of $SrFe_{0.97}Cr_{0.03}O_{3-\delta}$ membranes, a degradation of the flux in the range 3-6 % of the initial permeation rate was observed after 100 hours in the temperature range 1063-1303 K. Degradation of the permeability as a function of time at 1269 K is plotted in Figure 3.22. The sample was thermally cycled between each data point, shown in the figure.

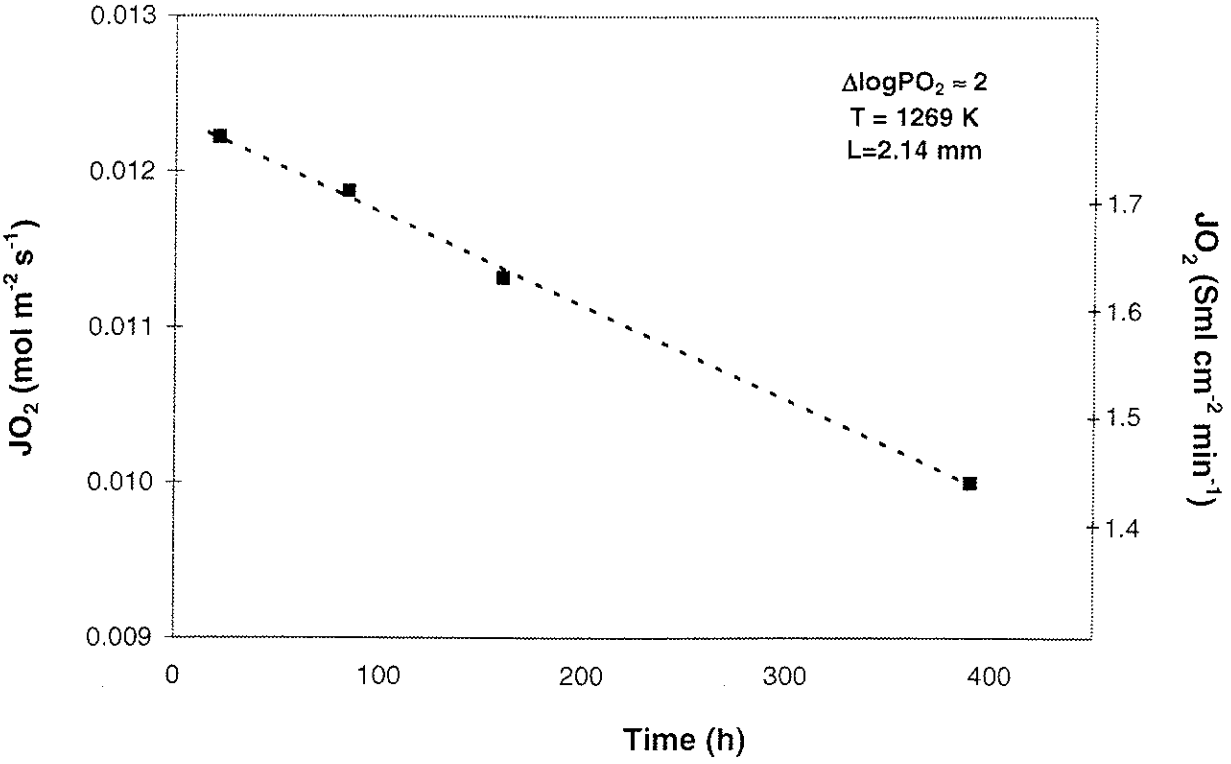

Figure 3.22 Degradation of the oxygen permeability of a $SrFe_{0.97}Cr_{0.03}O_{3-\delta}$ membrane.

SEM/EDS analysis of the membranes after the permeation experiment showed a plate-shaped secondary phase at the feed side of the membrane. The phase was not observed before the measurement. The plates were often seen to grow out of the membrane matrix as seen in Figure 3.23. Due to the thin plates and the small amount present, EDS or XRD analysis could not identify the phase. In addition, re-crystallisation can be observed in the figure, as stripes in each grain.

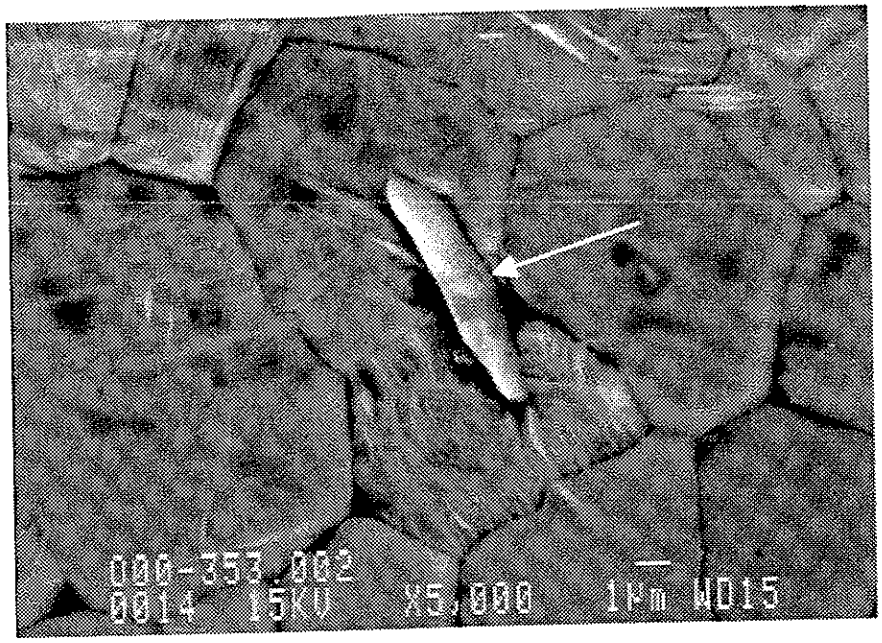

Figure 3.23 SEM micrograph of the oxygen rich side of a $SrFe_{0.97}Cr_{0.03}O_{3-\delta}$ membrane, showing a plate-shaped secondary phase. The surface has been exposed to P_{O_2} = 0.5 bar for 100 hours in the temperature range 790-1030 °C.

Known phases in the Sr-Fe-O system adjacent to the stoichiometric 1:1 phase are $Sr_4Fe_6O_{13+\delta}$ and $Sr_3Fe_2O_{7-\delta}$ (Batti, 1962; Kanamaru et al., 1972). Which phase forms during kinetic decomposition is related to cation diffusion rates. The cation diffusion data given in Appendix 11 indicate that the diffusivity of iron ions is higher than strontium ions in the perovskites at the relevant temperatures. Accordingly, it is presumably $Sr_4Fe_6O_{13+\delta}$ which forms at the oxygen rich side of the membrane. A simple test to identify the secondary phase was carried out by making a membrane from a powder with the nominal composition $Sr_{0.97}Fe_{0.97}Cr_{0.03}O_{3-\delta}$. Micrographs of the sintered membranes showed large amounts of a plate-shaped phase. This supports the assumption that $Sr_4Fe_6O_{13+\delta}$ forms during the permeability experiments. Kleveland et al. (2001) have recently reported that the $Sr_3Fe_2O_{7-\delta}$ phase also grows as plate-shaped grains. The two phases $Sr_4Fe_6O_{13+\delta}$ and $Sr_3Fe_2O_{7-\delta}$ have melting points of 1243 °C and 1510 °C, respectively. Heat treatment of a permeated membrane to 1350 °C in air, did not answer which plate-shaped phase that was observed on the feed surface. The object was to melt the $Sr_4Fe_6O_{13+\delta}$ phase if this was the one which was present. Figure 3.24 shows the membrane feed surface before and after the heat treatment at 1350 °C.

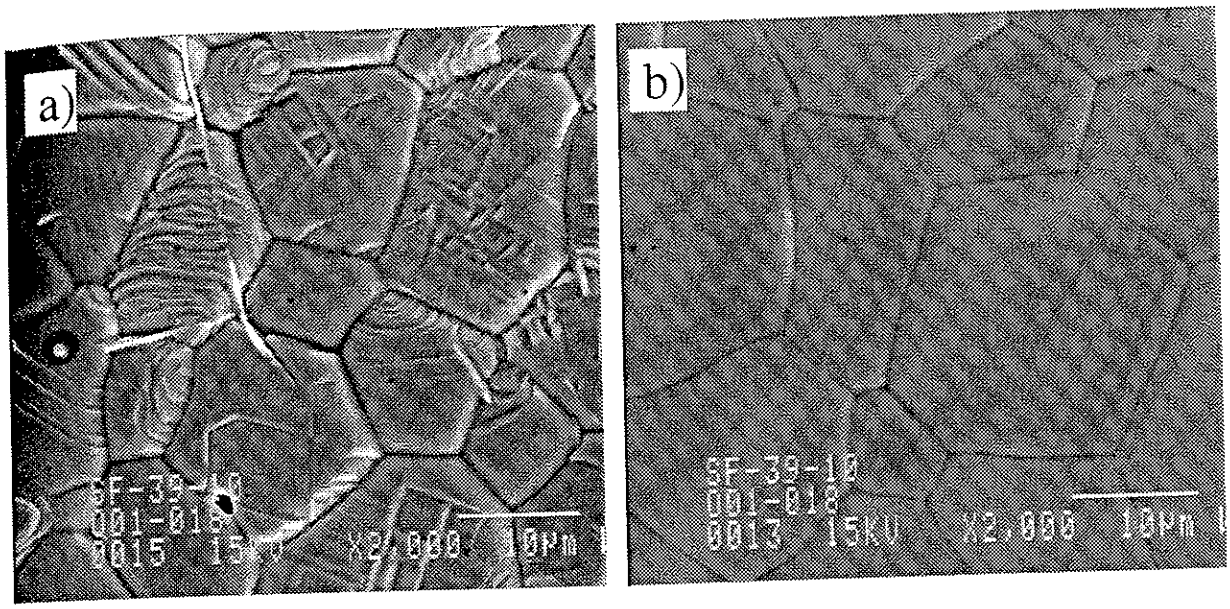

Figure 3.24 SEM micrographs of the feed side of a $SrFe_{0.97}Cr_{0.03}O_{3-\delta}$ membrane: **a)** after exposed at $P_{O_2} = 0.5$ bar and maximum 1000 °C. **b)** as a) and thereafter a heat treatment to 1350 °C/1h in air.

The micrographs show that both the re-crystallisation and the formation of the plate-shaped phase were reversible processes. Absence of the plate-shaped phase after heat treatment at 1350 °C is an indication of demixing during the permeation experiments. Another possible explanation is however that the impurity phase enters the stability region of the primary phase at $P_{O_2} = 0.21$ bar and 1350 °C.

3.4.8 Ordering processes

Representative oxygen permeability data of $SrFe_{0.97}Cr_{0.03}O_{3-\delta}$ membranes as a function of time in the temperature range 1063-1273 K are given in Figure 3.25. Below approximately 1150 K, there is a slow decrease in permeability with time, at a constant temperature. Steady state permeation could not be obtained within four hours. In contrast, steady state is reached in less than 30 minutes above 1223 K. Comparable results are reported in the literature for the $SrFe_{1-x}Co_xO_{3-\delta}$ system (Kruidhof et al., 1993; van Doorn, 1996).

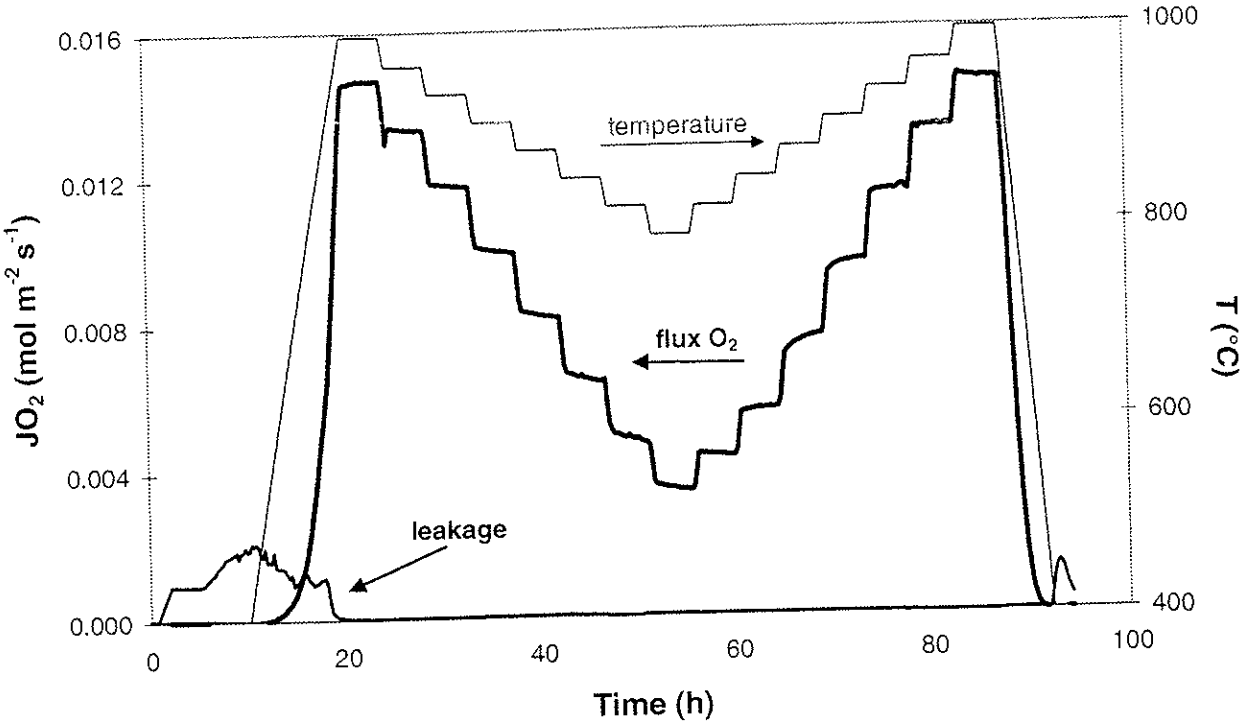

Figure 3.25 Representative example of an oxygen permeation measurement for a $SrFe_{0.97}Cr_{0.03}O_{3-\delta}$ membrane. $\Delta \log P_{O_2} \approx 2.1$

The anomaly in the temperature dependent permeability has been attributed to the occurrence of an order-disorder transition in the oxygen sublattice. According to data from Holt et al. (1999), the oxygen content was ≈ 2.55 at the permeate side of the $SrFeO_{3-\delta}$ membrane at 1173 K. The phase diagram by Mizusaki et al. (1992) indicates that this composition is near the brownmillerite phase boundary, and agrees with the assumption of oxygen vacancy ordering. Limited change in the order-disorder boundary line is assumed by substituting 3 mol% chromium in $SrFeO_{3-\delta}$.

The vacancy ordering below approximately 1173 K is a slow kinetic process, and the dynamic permeability behaviour below 1173 K is thus not investigated in further detail. Neither is the ordering process thoroughly studied. The complexity of studying the slow order-disorder process from oxygen permeation experiment is illustrated in a paper by Qiu et al. (1995).

Conclusions

Membranes of $SrFe_{0.9}Cr_{0.03}O_{3-\delta}$ exhibit reasonably high oxygen permeability ~0.015 mol m^{-2} s^{-1} at 1273 K and $\Delta \log P_{O_2} \approx 2.1$. The apparent activation energy for the overall oxygen permeation for $SrFe_{0.97}Cr_{0.03}O_{3-\delta}$ was determined to 160 ± 8 kJ/mol, which agrees with comparable results in the literature.

The oxygen permeation is partly governed by the surface exchange kinetics in the temperature range 900-1030 °C. Results from thickness dependent permeation implies approximately 50 % surface exchange limitation for a 1 mm thick membrane, slightly decreasing with temperature. The activation energy for the bulk diffusion and surface exchange control was calculated to ≈ 55 kJ/mol for both processes.

A significant increase in oxygen permeation was observed when increasing the grain boundary length in the membranes. Increased surface area depressed this effect, suggesting grain boundary dependent surface exchange kinetics. The grain boundary length in the bulk is apparently of no consequence for the oxygen permeation properties.

4 MODELLING OF BULK DIFFUSION AND SURFACE EXCHANGE RATES OF $SrFe_{1-x}Cr_xO_{3-\delta}$ MEMBRANES

4.1 Defect model of the oxygen stoichiometry for $SrFeO_{3-\delta}$

The modelling and discussion described below are based on oxygen vacancy concentration data from thermogravimetry analysis (TGA) by Norby et al. (2001). Oxygen stoichiometry data was obtained in the P_{O_2} range $1 - 1 \cdot 10^{-15}$ bar and temperatures in the range 1273 - 1473 K. The data are in agreement with other data reported in the literature (Takeda et al., 1986; Fell et al., 2001).

The oxygen defect structure of $SrFeO_{3-\delta}$ can be described with the Kröger-Vink notation as discussed by van Hassel et al. (1993). The physical model for oxygen nonstoichiometry is described by the two chosen equilibria:

Reduction of Fe(IV) and oxygen vacancy formation:

$$2Fe_{Fe}^{\cdot} + O_O^{\times} = 2Fe_{Fe}^{\times} + V_O^{\cdot\cdot} + \tfrac{1}{2}O_2(g) \qquad [4.1]$$

Charge disproportionation of Fe(III):

$$2Fe_{Fe}^{\times} = Fe_{Fe}^{\prime} + Fe_{Fe}^{\cdot} \qquad [4.2]$$

where $V_O^{\cdot\cdot}$ is a vacancy on an O^{2-} lattice position and $O_O^{\times}$ is an O^{2-} ion on a regular site. Tetra-, tri-, and divalent iron on a Fe^{3+} lattice position are represented by $Fe_{Fe}^{\cdot}$, $Fe_{Fe}^{\times}$ and $Fe_{Fe}^{\prime}$, respectively. The nonstoichiometry model could also be described for instance by equation [4.1] and the equilibrium for reduction of Fe(III) to Fe(II).

In addition, the charge neutrality condition and mass site balances are taken into account. A strontium to iron ratio of one is assumed in the calculation.

Electroneutrality: $$[Sr_A^{\cdot}] + [Fe_{Fe}^{\cdot}] = 2[V_O^{\cdot\cdot}] + [Fe'_{Fe}] \qquad [4.3]$$

Mass site balances: $$[O_O^{\times}] + [V_O^{\cdot\cdot}] = 3 \qquad [4.4]$$

$$[Fe_{Fe}^{\cdot}] + [Fe_{Fe}^{\times}] + [Fe'_{Fe}] = 1 \qquad [4.5]$$

The notation $[Sr_A^{\cdot}]$ symbolises the concentration of strontium on an A-site of an A(III)B(III)O_3 perovskite and is equal to one for $SrFeO_{3-\delta}$.

The interpretation of the charge disproportionation of Fe^{3+} implies localised conduction electrons and holes, trapped on iron sites by the local (or more extended) lattice polarisation. This is called a polaron hopping-type electrical conductivity mechanism. This thermally activated hopping process is a reasonable description for $SrFeO_{3-\delta}$, according to the literature (MacChesney et al., 1965; Poulsen et al., 1994; Smyth, 1996). Electrical conductivities of 50-100 S/cm and an activation energy of 0.1 eV are reported. A more general discussion of the electronic structure for perovskites of 3d oxides is given by Cox (1995). He indicates the conductivity mechanism for $SrFeO_{3-\delta}$ to be an activated hopping process of point defects to neighbouring lattice sites.

The equilibrium constants for the reduction of Fe(IV) and charge disproportionation of Fe(III) are given by $K_{4.1}$ and $K_{4.2}$. Introducing the equations [4.3] - [4.5] simplifies the expressions of $K_{4.1}$ and $K_{4.2}$. Two equations remain, with three unknowns:

$$K_{4.1} = \frac{(2[V_O^{\cdot\cdot}]+[Fe'_{Fe}]-1)\cdot[V_O^{\cdot\cdot}]\cdot(P_{O_2})^{\frac{1}{2}}}{K_{4.2}\cdot[Fe'_{Fe}]\cdot(3-[V_O^{\cdot\cdot}])} = e^{-\left(\frac{\Delta H_{4.1}-T\Delta S_{4.1}}{RT}\right)} \qquad [4.6]$$

$$K_{4.2} = \frac{[Fe'_{Fe}]\cdot\left(2[V_O^{\cdot\cdot}]+[Fe'_{Fe}]-1\right)}{4\cdot\left(1-[Fe'_{Fe}]-[V_O^{\cdot\cdot}]\right)^2} = e^{-\left(\frac{\Delta H_{4.2}-T\Delta S_{4.2}}{RT}\right)} \qquad [4.7]$$

The enthalpy of disproportionation, $\Delta H_{4.2}$, describes essentially the stability of Fe(III) relative to Fe(IV) and Fe(II), and $\Delta H_{4.1}$ describes the formation enthalpy of oxygen vacancies. The thermodynamic quantities, ΔH and ΔS, are determined by plotting the logarithm of Gibbs free energy versus inverse temperature.

The procedure for calculating the oxygen content was as follows: The oxygen vacancy concentration is calculated by estimating $K_{4.2}$ and then calculating the $[Fe'_{Fe}]$ from the experimental vacancy concentration data. The equilibrium constant $K_{4.1}$ is determined, and $K_{4.2}$ is further optimised until$K_{4.1}$ is constant in the P_{O_2} range of the experimental data. The equilibrium constant as a function of inverse temperature gives the thermodynamic quantities which are input data for calculation of the oxygen vacancy concentration. Figure 4.1 shows the modelled oxygen defect concentration as a function of oxygen partial pressure, and the thermodynamic quantities.

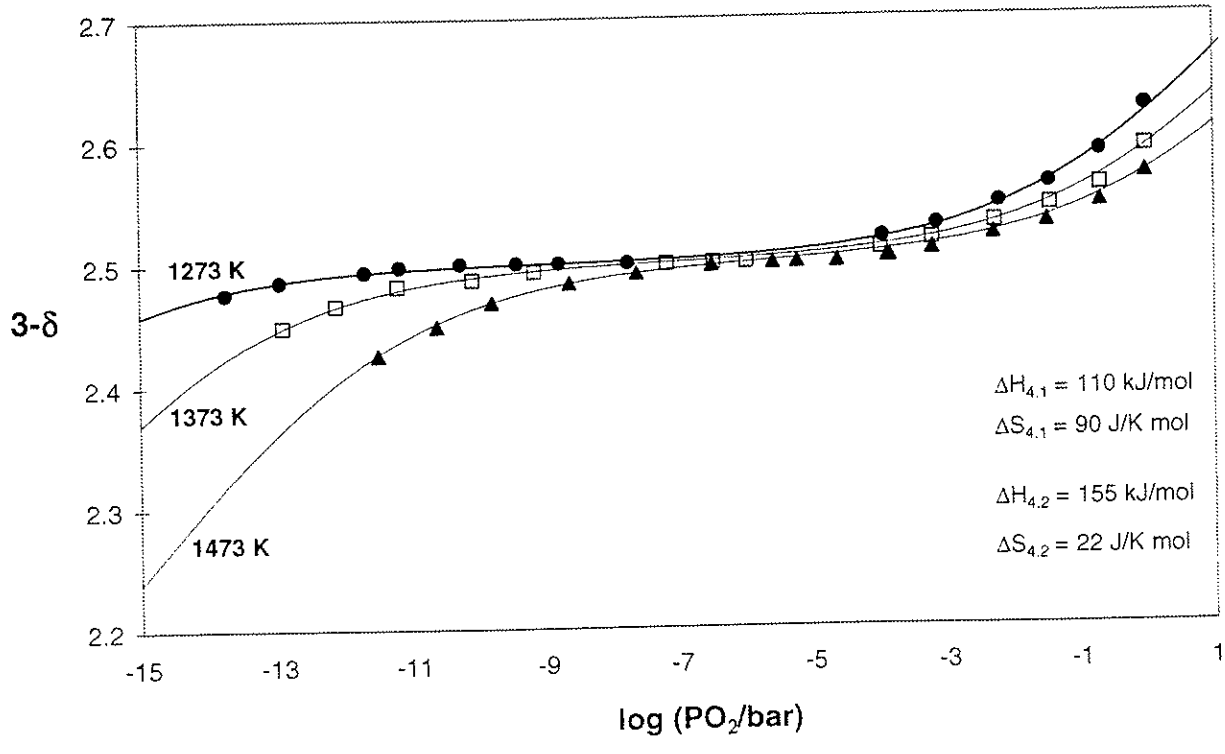

Figure 4.1 Modelled oxygen defect concentration as a function of oxygen partial pressure for $SrFeO_{3-\delta}$. Experimental data are taken from Norby et al. (2001).

$SrFeO_{3-\delta}$ is highly nonstoichiometric and a description based on a point defect model is oversimplified and can not be expected to describe the experimental data accurately (Mizusaki et al., 1985; van Hassel et al., 1993). However, the model fits well with reasonable values for the thermodynamic parameters, which are given in Table 4.1.

The thermodynamic data indicate only limited influence of the charge disproportionation, with an equilibrium constant six orders of magnitude lower than the equilibrium constant for the Fe(IV) to Fe(III) reduction. The region of almost constant oxygen defect concentration is caused by the low level of disproportionation, i.e. the high stability of trivalent iron.

Thermodynamic data for $La_{1-x}Sr_xFeO_{3-\delta}$ from Mizusaki et al. (1985) are listed in Table 4.1, along with those of the present work. The value of $\Delta H_{4.2}$ decreases presumably with increasing Sr-content indicating a decreased stability for Fe(III). The $\Delta S_{4.2}$ has a small value and is apparently independent of the Sr-content. The enthalpy and entropy changes for oxygen vacancy formation ($\Delta H_{4.1}$, $\Delta S_{4.1}$) appear to be independent of the composition. Holt et al. (1999) report lower values for the thermodynamic parameters for the oxygen vacancy formation than in the present study, but they used only the stoichiometry data at high P_{O_2} in the modelling.

Table 4.1 Thermodynamic quantities for oxygen vacancy formation and charge disproportionation of $SrFeO_{3-\delta}$, according to the equations [4.1] and [4.2]. The data is compared with literature data on $La_{1-x}Sr_xFeO_{3-\delta}$.

x	$\Delta H_{4.1}$ (kJ/mol)	$\Delta S_{4.1}$ (J/K mol)	$\Delta H_{4.2}$ (kJ/mol)	$\Delta S_{4.2}$ (J/K mol)	References
0	125	71	196	25	Mizusaki et al., 1985
0.1	113	67	163	13	"
0.25	117	75	184	31	"
0.4	105	70	125	-4	"
0.6	113	82	138	6	"
1.0	80	75			Holt et al., 1999
1.0	110	90	155	22	This study

The parameter ΔE_v given in equation [3.3] can be quantified using the results in Figure 4.1. The data are shown in Figure 4.2, in a relevant P_{O_2} range. This contribution to the apparent activation energy, given as $d\ln\delta/d(1/T)$, is used to determine the activation energy for the oxygen mobility. This is described in the following section.

The parameter ΔE_v for $SrFeO_{3-\delta}$ is calculated to 10 kJ/mol at P_{O_2} = 0.5 bar and T = 1273 K, and decreases with decreasing oxygen partial pressure. At the plateau where the oxygen defect concentration is approximately constant, the ΔE_v has decreased to almost zero. This can also be seen in Figure 4.1.

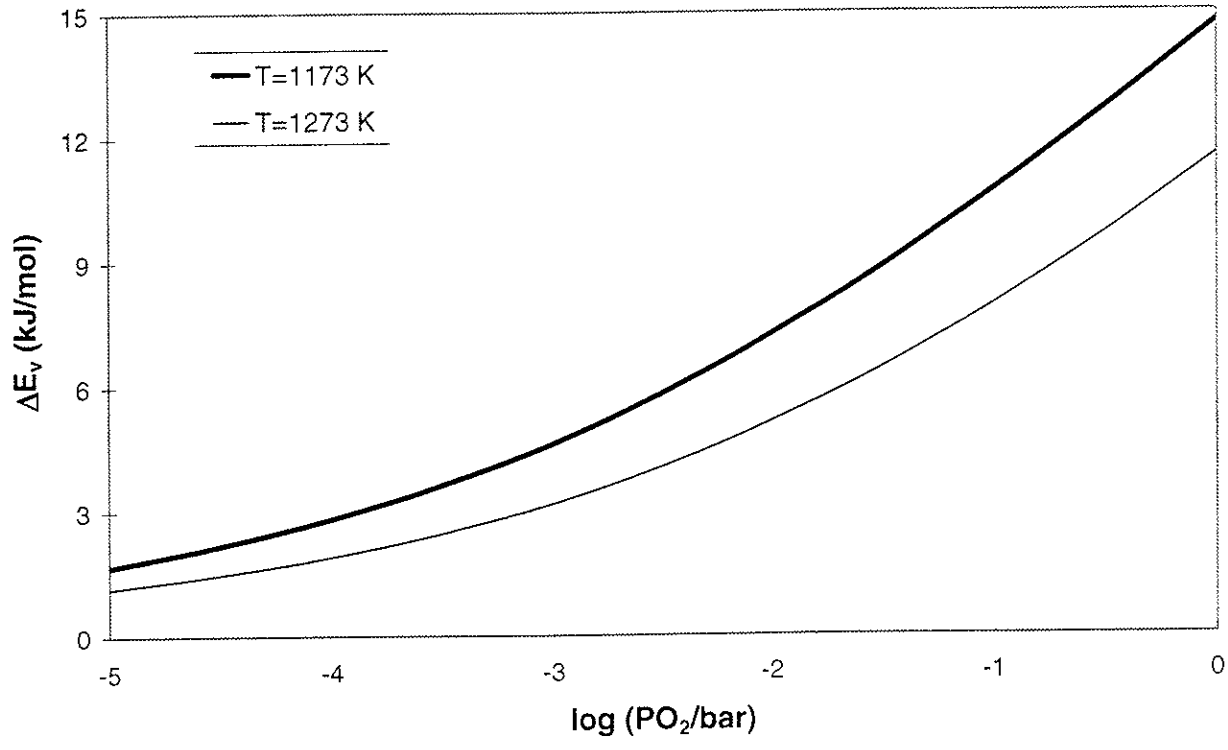

Figure 4.2 The energy change related to the vacancy formation (i.e. $d\ln\delta/d(1/T)$), observed as a contribution to the apparent activation energy for oxygen permeation.

Estimates by Ishigaki et al. (1984/1988) and ten Elshof et al. (1995) show a sharp decrease in ΔE_v with increasing Sr-content for $La_{1-x}Sr_xFeO_{3-\delta}$ ($0 \le x \le 0.4$). This is illustrated in Figure 4.3. The present value is in agreement with the literature data.

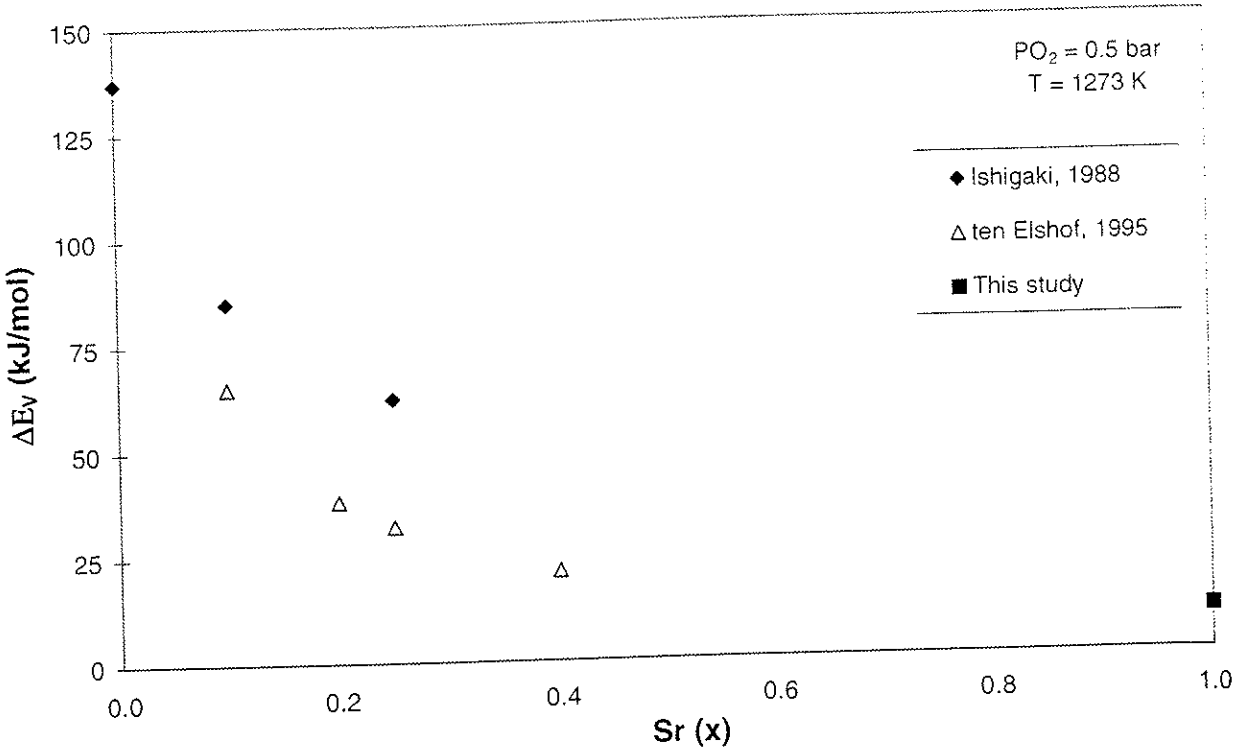

Figure 4.3 The apparent energy of oxygen vacancy formation as a function of Sr-content for $La_{1-x}Sr_xFeO_{3-\delta}$. Description of ΔE_v is given in the text.

The oxidation enthalpy is calculated for comparison with experimental data from calorimetric experiments. The parameter ΔH_{ox} describes the energy which is necessary to oxidise the disordered perovskite according to the equation:

$$4SrFeO_{2.5}\ (s) + O_2\ (g) = 4SrFeO_3\ (s) \qquad [4.8]$$

where both the red-ox equation and the disproportionation are taken into account. The oxidation enthalpy is given by:

$$\Delta H_{ox}\ (\text{kJ/mol } O_2) = 4((-[Fe^{\cdot}_{Fe}] \cdot [Fe'_{Fe}] \cdot \tfrac{1}{2}\Delta H_{4.2}) + (-\tfrac{1}{2}\Delta H_{4.1})) \qquad [4.9]$$

Figure 4.4 presents the concentration of the different oxidation states of iron as a function of oxygen stoichiometry. The $[Fe'_{Fe}]$ is equal to $[Fe^{\cdot}_{Fe}]$ for $SrFeO_{2.5}$ and the figure shows that the disproportionation is almost negligible at 1273 K.

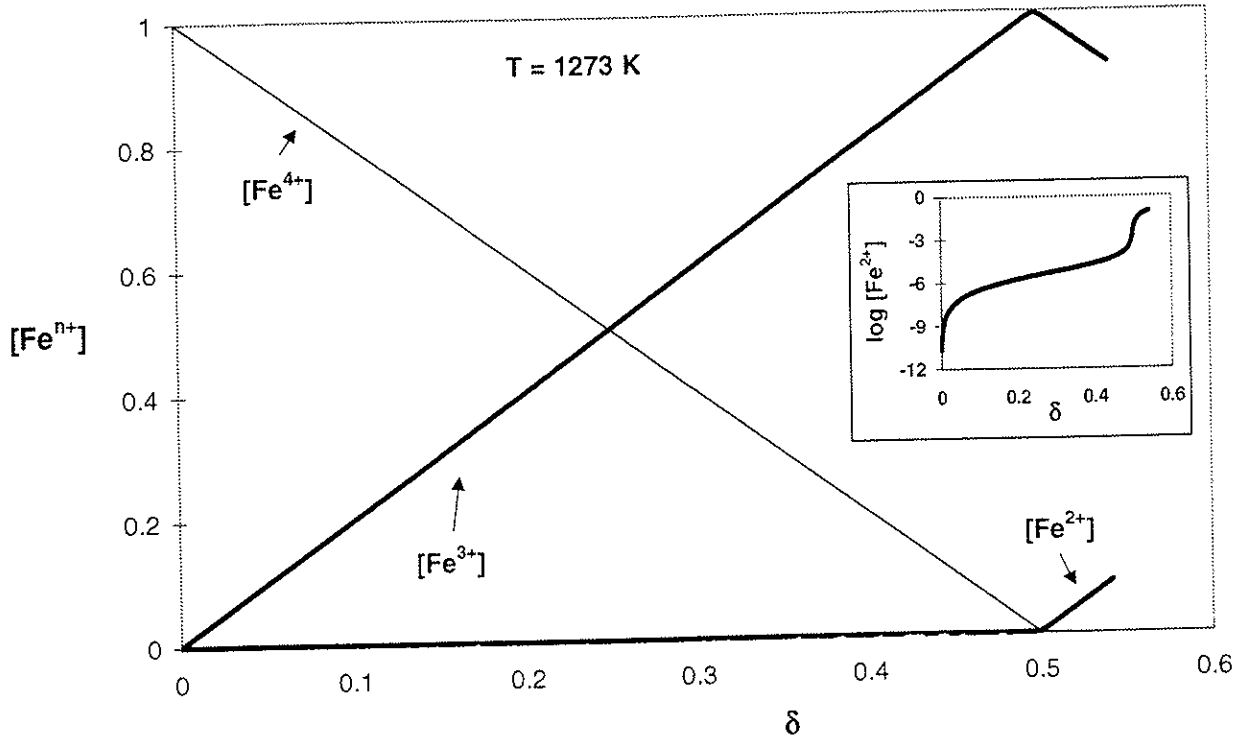

Figure 4.4 Molfraction of Fe^{n+} (n=2,3,4) as a function of oxygen vacancy concentration for $SrFeO_{3-\delta}$ at 1273 K.

The ΔH_{ox} is calculated to be -221 kJ/mol O_2 at 1273 K and is determined mainly by the Fe(IV) to Fe(III) reduction. The oxidation enthalpy is almost independent of temperature in the range 1173-1473 K, as shown in Figure 4.5. Haavik (2001) has measured the oxidation enthalpy from calorimetric studies to be -111 kJ/mol O_2 at 1200 K.

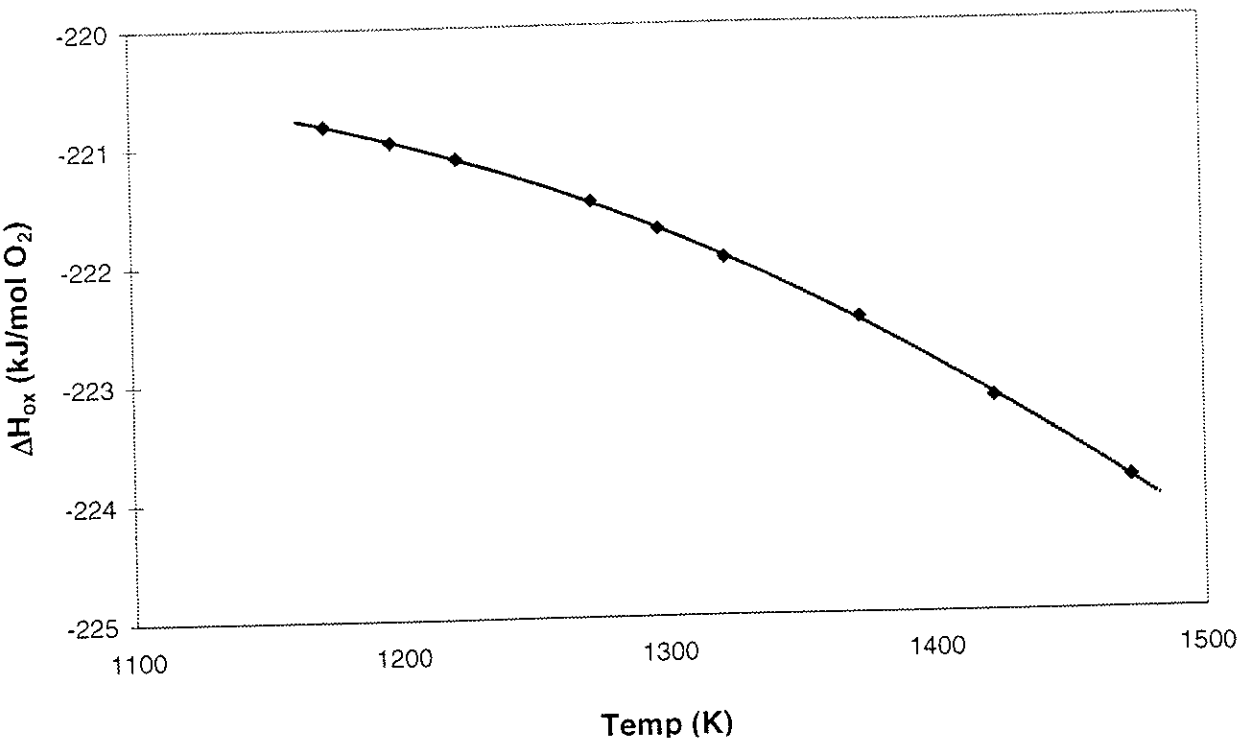

Figure 4.5 Calculated oxidation enthalpy as a function of temperature for the perovskite: $4SrFeO_{2.5} + O_2 = 4SrFeO_3$.

The oxidation entropy, ΔS_{ox}, according to equilibrium [4.8] is calculated to -180 J/(K mol O_2). Generally, the oxidation entropy is found to be -120 to -180 J/(K mol gas species).

In the present results, the free energy (ΔG_{ox}) is calculated. The data are therefore subject to some uncertainty with respect to deconvolution into ΔH_{ox} and ΔS_{ox}. However, the results are quite reasonable. The data are in accordance with the results of Mizusaki et al. given in Table 4.1, but these results are obtained from oxygen stoichiometry result as well. The oxidation entropy can be compared with oxides with similar electronic structures. The data are given in Table 4.2. Hence, the oxidation entropy by Haavik is anomalously low. The calculated free energy of oxidation by Haavik is in agreement with the present result.

Table 4.2 The oxidation entropy of some relevant oxide systems (1200 K and 1 bar).

Reaction	ΔS_{ox} (*J/K mol*)	References
$4SrFeO_{2.5} + O_2 = 4SrFeO_3$	-180	Present study
	-89	Haavik, 2001
$4/5Sr + 4/5Fe + O_2 = 2/5Sr_2Fe_2O_5$	- 213.2	Tanasescu et al. , 2000
$4FeO + O_2 = 2Fe_2O_3$	- 242.3	Barin, 1993
$6FeO + O_2 = 2Fe_3O_4$	- 220.0	Barin, 1993
$4MnO + O_2 = 2Mn_2O_3$	-210.5	Barin, 1993
$6MnO + O_2 = 2Mn_3O_4$	-240.2	Barin, 1993
$2Cu_2O + O_2 = 4CuO$	-187.8	Barin, 1993

4.1.1 Vacancy diffusion coefficient and ionic conductivity of $SrFe_{1-x}Cr_xO_{3-\delta}$

The vacancy diffusion coefficient (D_v) can be calculated from the Wagner equation [1.4] and equation [1.7], as described in Chapter 1.2. The parameter D_v describes the vacancy mobility, according to equation [1.3].

The molar volume, V_m, as a function of oxygen stoichiometry is calculated from literature data and is given in Figure A12.1 (Shin et al., 1978; Takeda et al., 1986; ICDD, 1997). However, the change in molar volume as a function of oxygen vacancy concentration is small in the relevant nonstoichiometry range ($0.4 < \delta < 0.5$). The molar volume is set constant to $3.7 \cdot 10^{-5}\ m^3/mol$ without a significant error. The bulk oxygen permeability is calculated from the membrane thickness dependent permeation results, described in Chapter 3.4.4. The oxygen stoichiometry data are calculated from the model described in Chapter 4.1.

The apparent vacancy mobility as a function of P_{O_2} for $SrFe_{0.97}Cr_{0.03}O_{3-\delta}$ is calculated from the oxygen permeation data under varying driving forces. Polynomial functions are used to fit the D_v as a function of P_{O_2}. This description is used because of the relatively complex expression of the oxygen stoichiometry as a function of P_{O_2}. The function can only be used for the range of conditions covered by experimental data, and should not be

extrapolated to higher or lower oxygen partial pressures. Description of the fitting procedure is given in Appendix 13.

Arrhenius plots of the vacancy diffusion coefficient resulted in activation energies increasing from 49 to 62 kJ/mol, with decreasing P_{O_2}, at 1273 K. The results are shown in Figure 4.6. The apparent mobility increases by a factor two from low to high P_{O_2}, as shown in Figure 4.7. Other authors assumed D_v to be independent of P_{O_2} for the $La_{1-x}Sr_xFeO_{3-\delta}$ system ($0 \leq x \leq 0.4$). This is established as a reasonable assumption for systems which contain low oxygen vacancy concentrations (Ishigaki et al., 1984/1988; ten Elshof et al., 1995; Yasuda & Hishinuma, 1995; Lane et al., 1999). According to Yasuda & Hishinuma, assuming a constant D_v for the highly nonstoichiometric $SrFeO_{3-\delta}$ is more questionable. Nevertheless, the present modelling indicates only a factor two dependence on the oxygen partial pressure. It is important to point out that the modelled vacancy concentration is based on no interaction between the vacancies. The work by Holt et al. (1999) assumed D_v to be independent of P_{O_2} for $SrFeO_{3-\delta}$. Literature data on the vacancy diffusion coefficient as a function of Sr-content for $La_{1-x}Sr_xFeO_{3-\delta}$ is shown in Figure 4.8.

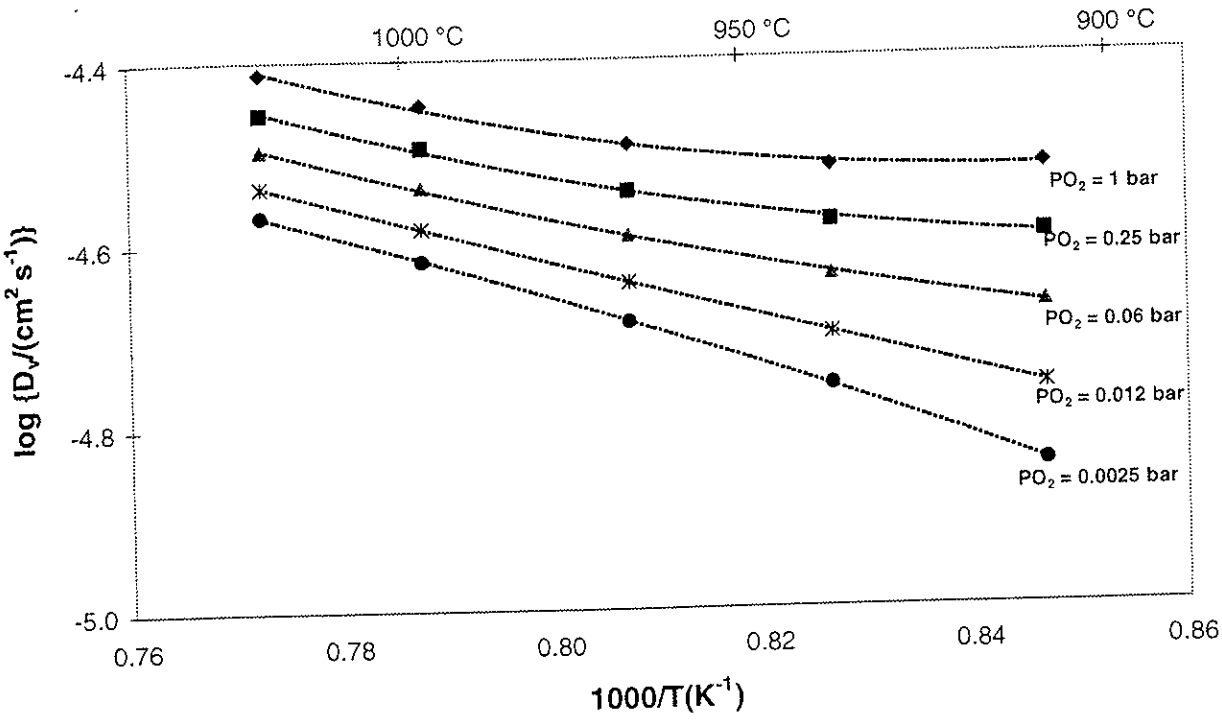

Figure 4.6 Arrhenius plots of the fitted vacancy diffusion coefficients for $SrFe_{0.97}Cr_{0.03}O_{3-\delta}$ at different P_{O_2}. The lines are a guide to the eye.

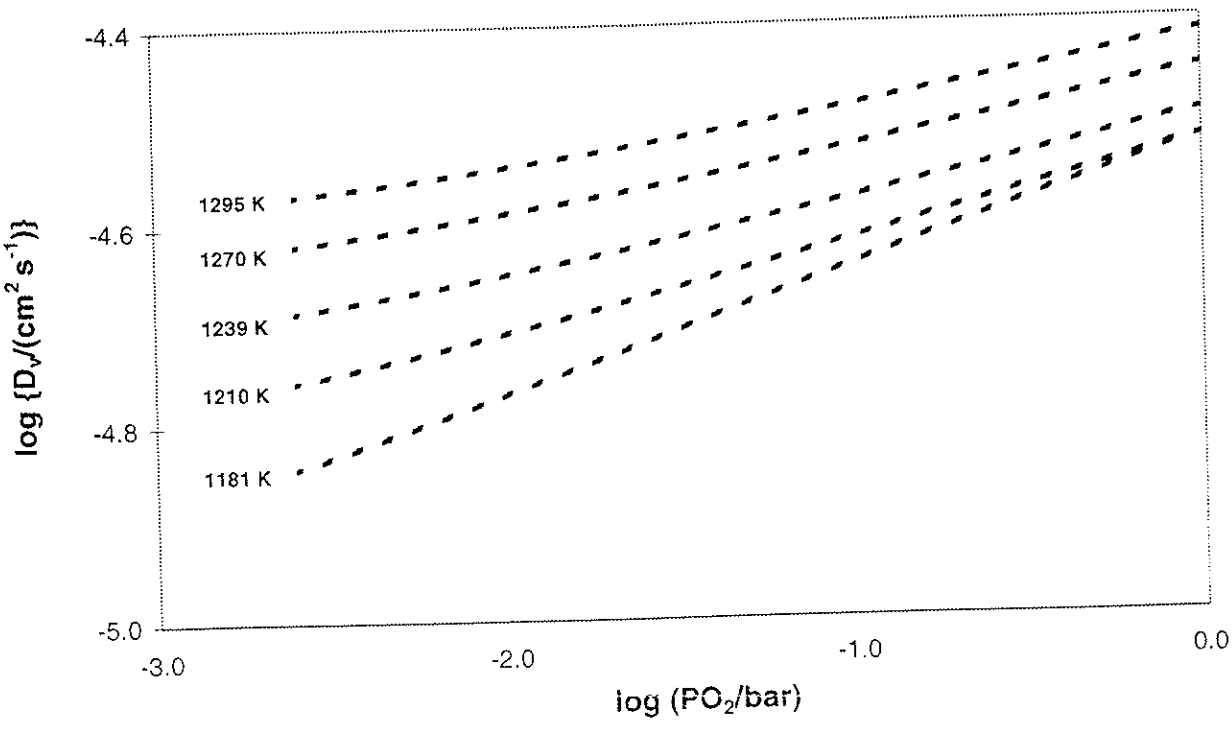

Figure 4.7 Fitted vacancy diffusion coefficients as a function of oxygen partial pressure for $SrFe_{0.97}Cr_{0.03}O_{3-\delta}$.

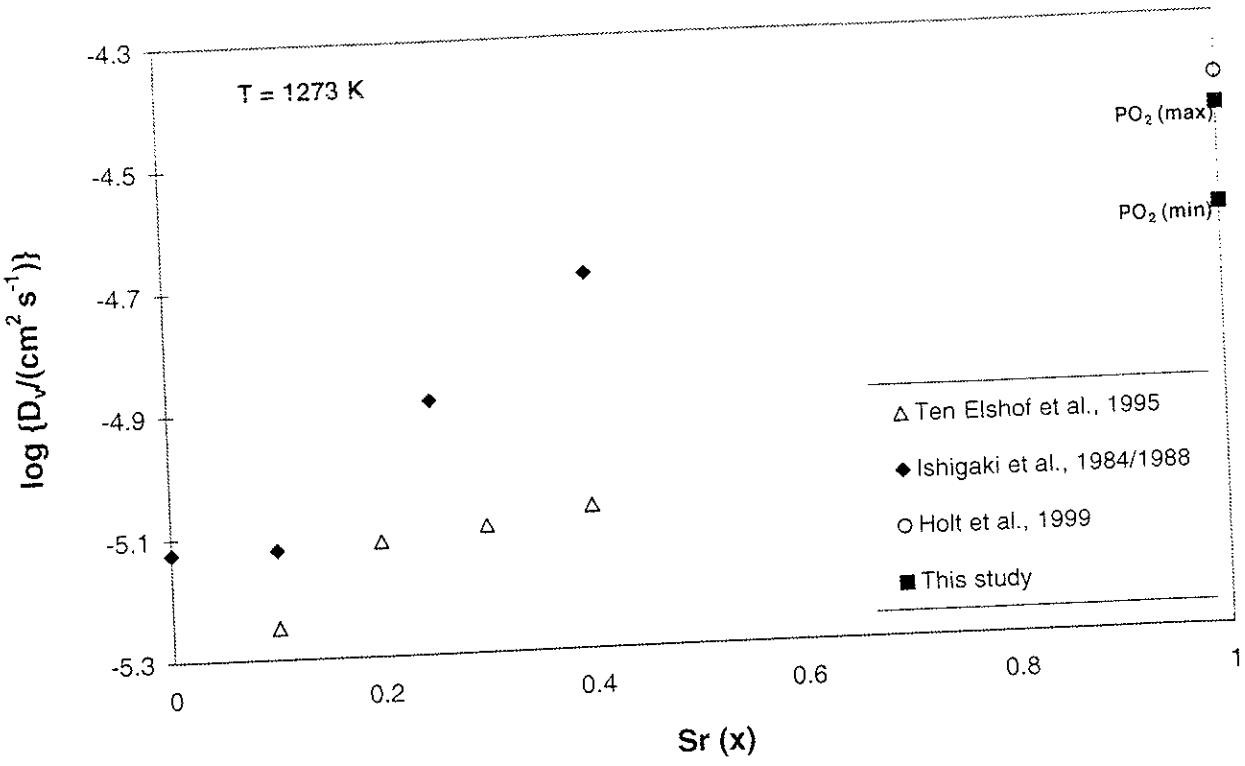

Figure 4.8 The vacancy diffusion coefficients as a function of Sr-content for $La_{1-x}Sr_xFeO_{3-\delta}$ at 1273 K.

The subject of how the oxygen partial pressure influences the vacancy mobility will be further discussed in the following section.

The ionic conductivity can be calculated by the Nernst-Einstein equation [1.5]. The estimated variation in mobility as a function of P_{O_2} is introduced in the calculation. The Arrhenius plot of ionic conductivity is given in Figure 4.9. The activation energy is calculated to 52-60 kJ/mol and is slightly dependent on the oxygen partial pressure in the relevant P_{O_2} range.

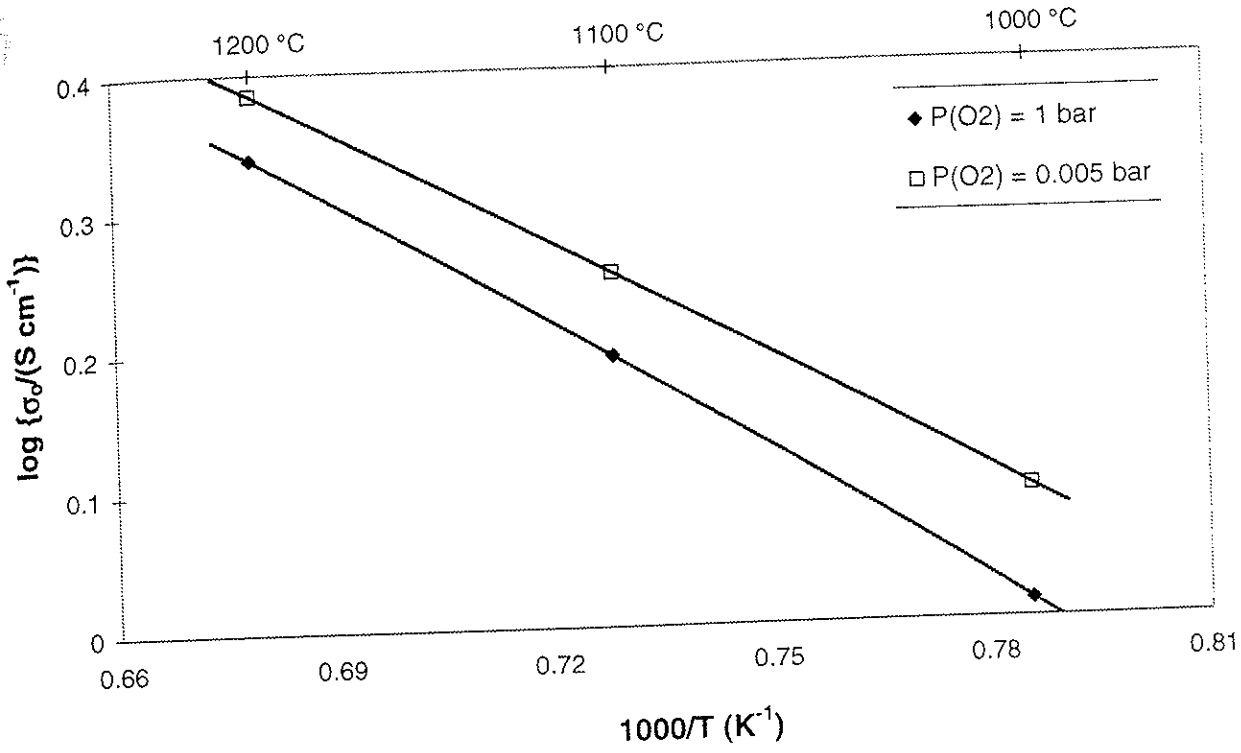

Figure 4.9 The Arrhenius plot of the calculated ionic conductivity of $SrFeO_{3-\delta}$. The data on oxygen vacancy concentration is taken from Norby et al. (2001).

It should be noticed that the value of the ionic conductivity of $SrFeO_{3-\delta}$ is comparable with the best 'molten' fast ion conductors, such as α-AgI (Tuller et al., 1980). Other studies have also presented remarkably high ionic conductivities for perovskites. Authors report conductivities above 1 S/cm at 1273 K for $SrFe_{1-x}Co_xO_{3-\delta}$ ($0 \leq x \leq 1$) (Teraoka et al., 1988[1]; Steele, 1992; Holt et al., 1999; Aasland et al., 2000).

4.1.2 Chemical diffusion coefficient of $SrFe_{1-x}Cr_xO_{3-\delta}$

The vacancy diffusion coefficient (D_v) can be directly compared to the chemical diffusion coefficient ($\tilde{D}$), using the thermodynamic enhancement factor, γ (Wagner, 1975). This is described in Chapter 1.2 through the equations [1.12] and [1.13].

The thermodynamic enhancement factor, γ_v, is calculated as a function of oxygen partial pressure for $SrFeO_{3-\delta}$. The data used in the calculation are

taken from the modelled oxygen stoichiometry, and the result is shown in Figure 4.10.

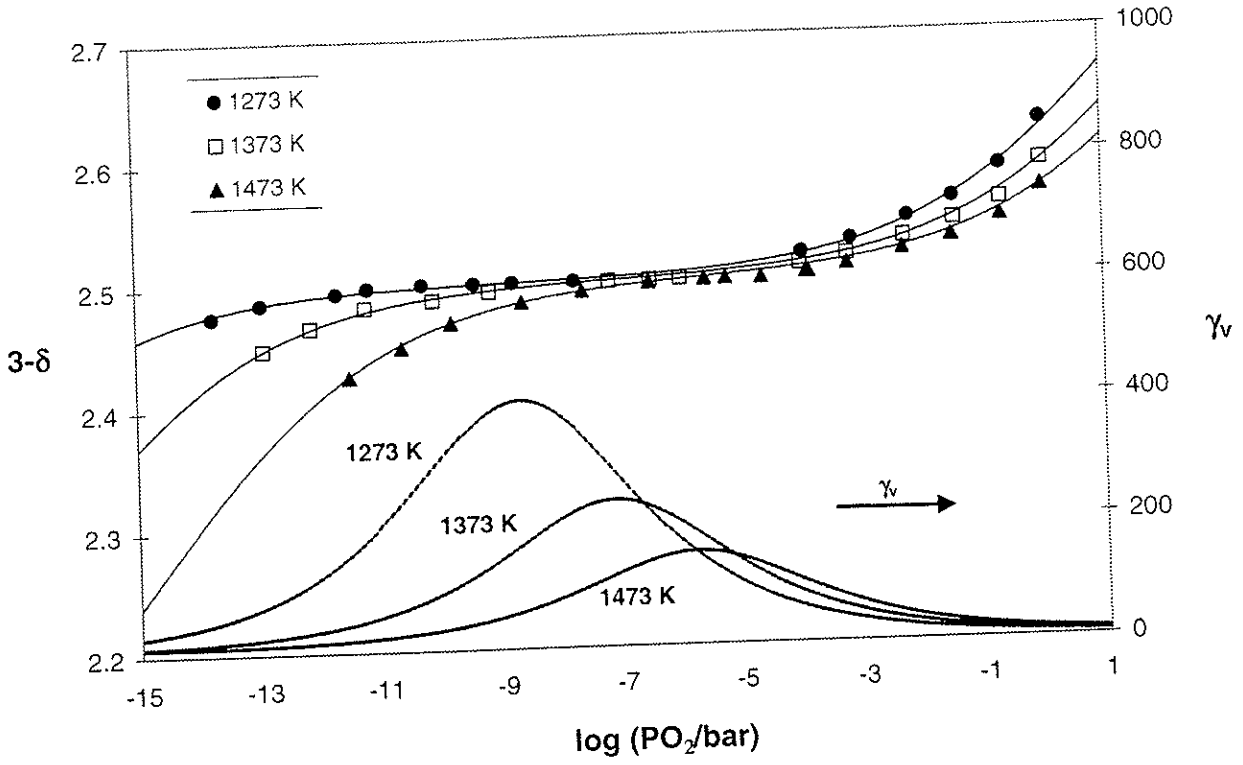

Figure 4.10 The oxygen stoichiometry and thermodynamic enhancement factor, γ_v, as a function of oxygen partial pressure for $SrFeO_{3-\delta}$. The experimental data are taken from Norby et al. (2001).

Holt et al. (1999) have reported the experimental and calculated chemical diffusion coefficient for $SrFeO_{3-\delta}$. The data are reported in Figure 4.11. The calculated data are not in agreement with the experimental data. The calculations give a decreasing $\tilde{D}$ with increasing oxygen partial pressure, while the experimental data show the opposite results. Introducing the P_{O_2} dependent D_v (Chapter 4.1.1) does not explain the discrepancy between the calculated and experimental values of $\tilde{D}$, as shown in the figure.

The experimental results are subject to uncertainty because it is not known whether there are surface exchange limitations partly controlled the transport rates. The literature data indicate increasing surface exchange rate when the P_{O_2} is increased (Lee et al., 1997, Benson et al., 1998). Permeation governed by high surface exchange limitation should then rise the slope of the experimental $\tilde{D}$ (Figure 4.11) when the surface exchange limitation increase.

This implies that surface exchange limitation probably not explain the behaviour of the experimental $\tilde{D}$.

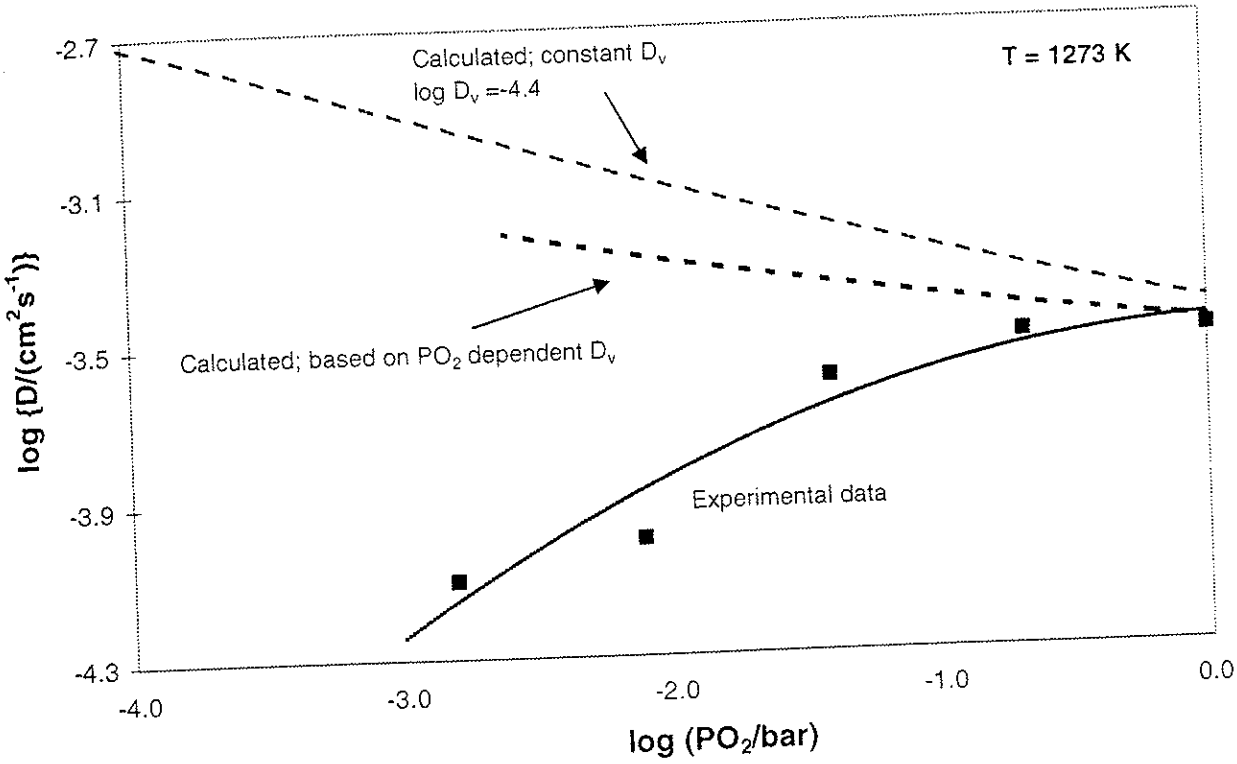

Figure 4.11 Calculated and experimental chemical diffusion coefficients ($\tilde{D}$) for $SrFeO_{3-\delta}$. Experimental data are taken from Holt et al. (1999).

The calculated results are based on the assumption of no interaction between the vacancies and is also subject to uncertainty.

Holt et al. ascribe the discrepancy to an increase in four-coordinated iron with decreasing P_{O_2} which can lead to an ordering of the vacancies. From the present oxygen permeation experiments there is no indication of vacancy ordering at 1273 K in the relevant P_{O_2} range. Notwithstanding, the oxygen vacancies probably interact to some extent for this highly defective material although it is not apparent from the permeation experiments.

The coordination numbers of oxygen are from four to six for iron ions in nonstoichiometric $SrFeO_{3-\delta}$. Pongsai et al. (2001) have calculated approximately 75 % five-coordinated iron ions for $SrFeO_{2.5}$ in the disordered state. The remaining ions are four- and six-coordinated. Under the relevant

conditions, a significant part of the oxygen sub-lattice can be inaccessible for oxygen diffusion. A coordination number of three is not energetically favourable, and as a consequence there are restrictions on where a vacancy can jump. A vacancy can not jump to a polyhedron with four-coordinated iron. The effective vacancy concentration is therefore dependent on the concentration of four-coordinated polyhedrons. The discrepancy from the measured vacancy concentration will then increase with decreasing oxygen partial pressure and increasing temperature. However, the effective vacancy concentration must change considerably in the relevant P_{O_2} range to get the calculated $\tilde{D}$ to correspond to the experimental data given in Figure 4.11.

The present status is that the poor agreement between the measured and predicted values of chemical diffusion coefficient is not well understood. Data to separate the effect of vacancy mobility and number of mobile vacancies for oxygen transport are lacking. The subject needs further investigation. If the measured $\tilde{D}$ describes the real situation, the oxygen defect concentration and mobility have to be adjusted when calculating the transport parameters.

4.2 Determination of surface oxygen exchange rates

The oxygen exchange between the gas phase and the membrane surface involves a number of possible rate determining steps. This is illustrated in Chapter 1.2. The surface exchange limitation may involve steps such as adsorption/desorption, dissociation/recombination of bonds, electron transfer, transport of electrons and ions, incorporation/removal of oxygen ions and formation of oxygen defects.

The interaction of O_2 with metal oxide surfaces is difficult to study by surface analysis techniques, because of the large background signal of lattice oxygen. In a brief outline, it is supposed that molecular adsorption is performed on stoichiometric surfaces and dissociative adsorption is promoted by oxygen nonstoichiometric surfaces. The latter is probably due to the charge transfer (Henrich & Cox, 1996). The present status is that physical mechanisms that limit the surface oxygen exchange in oxides are not well understood (De Souza & Kilner, 1999).

It is advantageous to have a quantitative idea of the possible rate determining steps, while considering the overall surface oxygen exchange limitation. The sketch of possible rate determining steps, given in Chapter 1.2 can be visualised as follows. The first adsorption step is assumed to be fast and simply influenced by the oxygen flow to the membrane surface, provided that no stagnant film of gas is formed. A stagnant film can be formed when the gas contains less oxygen than the ambient gas. This is not likely at the feed side in the present permeation experiments. From kinetic gas theory, the flow of oxygen molecules at the feed side of the membrane is calculated to approximate 80,000 times the measured oxygen permeation (De Boer, 1968). Intuitively, the second step of breaking chemical bonds in molecular oxygen would be of more hindrance. The dissociation energy of an O_2 molecule is calculated to 494 kJ/mol at room temperature (Porterfield, 1993). The barrier for dissociation depends of the oxygen stoichiometry on the metal oxide surface. A qualified guess of the activation energy for this step is thus difficult. The third step involves two processes, the charge transfer and the incorporation of oxygen ions into the surface layer. The charge transfer is considered to be fast because of the high electronic conductivity of $SrFe_{0.97}Cr_{0.03}O_{3-\delta}$. The second process of finding a vacant position for the oxygen ion is probably a process with higher barrier, and can be rate determining.

A numeric expression of the Wagner equation [1.4] and equation [1.16], defined for the two membrane surfaces, is solved in order to estimate the surface exchange limitations. The modelling is based on oxygen permeability data of $SrFe_{0.97}Cr_{0.03}O_{3-\delta}$ and nonstoichiometry data for $SrFeO_{3-\delta}$. Detailed description of this modelling is given in Appendix 14.

Some representative results of surface exchange flux, $J_{O_2}^{ex}$, are shown in Figure 4.12. The open symbols show the exchange fluxes which are set constant and the filled symbols the calculated exchange fluxes, on the opposite surface of the membrane. The exchange rates were calculated to be nearly twice the measured permeation rate for this membrane thickness at 1270 K. The exchange rate is higher at the feed surface than at the permeate surface, which implies greater surface exchange limitation at the permeate side. The exchange rate gives the maximum oxygen permeation rate. The exchange rate is equal to the permeation rate when all of the available driving force is lost in the surface process.

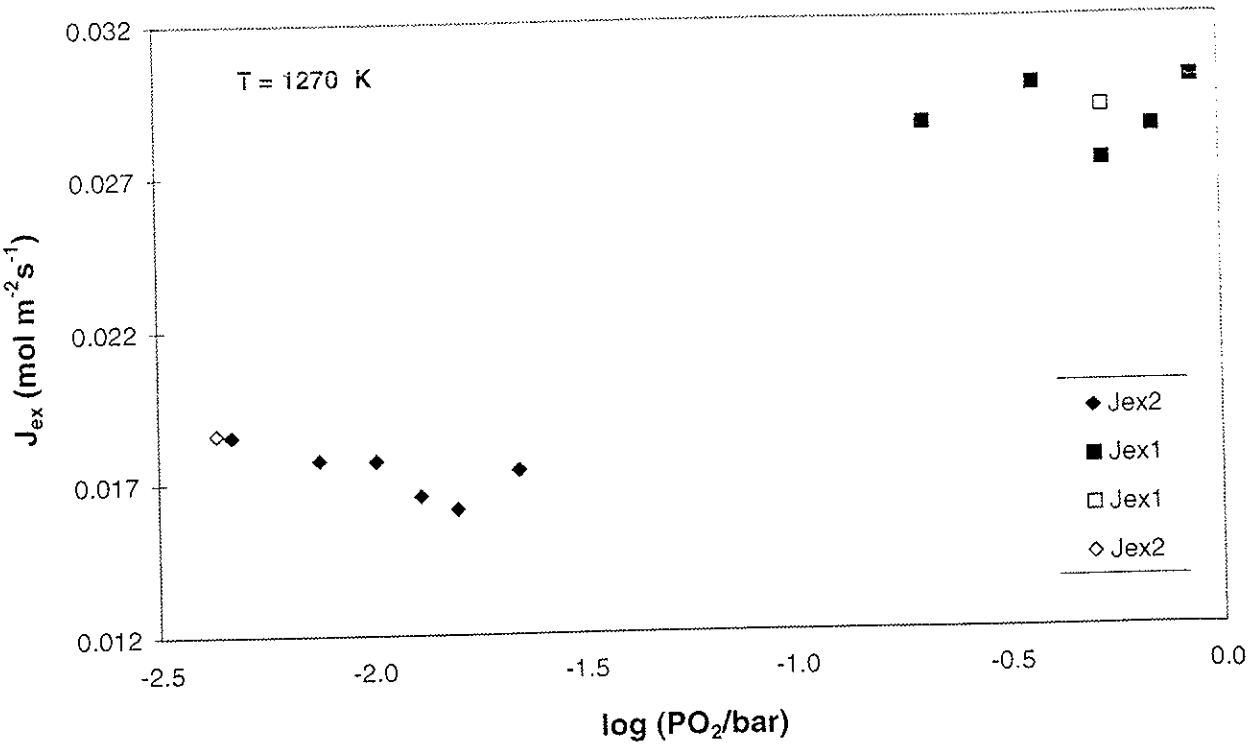

Figure 4.12 Modelled apparent surface exchange rate, $J_{O_2}^{ex}$ as a function of P_{O_2} for $SrFe_{0.97}Cr_{0.03}O_{3-\delta}$. Membrane thickness 2.14 mm.

Figure 4.13 shows the surface exchange rate as a function of P_{O_2} at all temperatures which were modelled. The scatter in the data of calculated $J_{O_2}^{ex}$ is probably due to uncertainty in the determination ofP_{O_2}. The uncertainty in measuring temperature is less, and is likely to be systematic. The main weakness of the modelling is that the results are based on permeation experiments for one single membrane thickness.

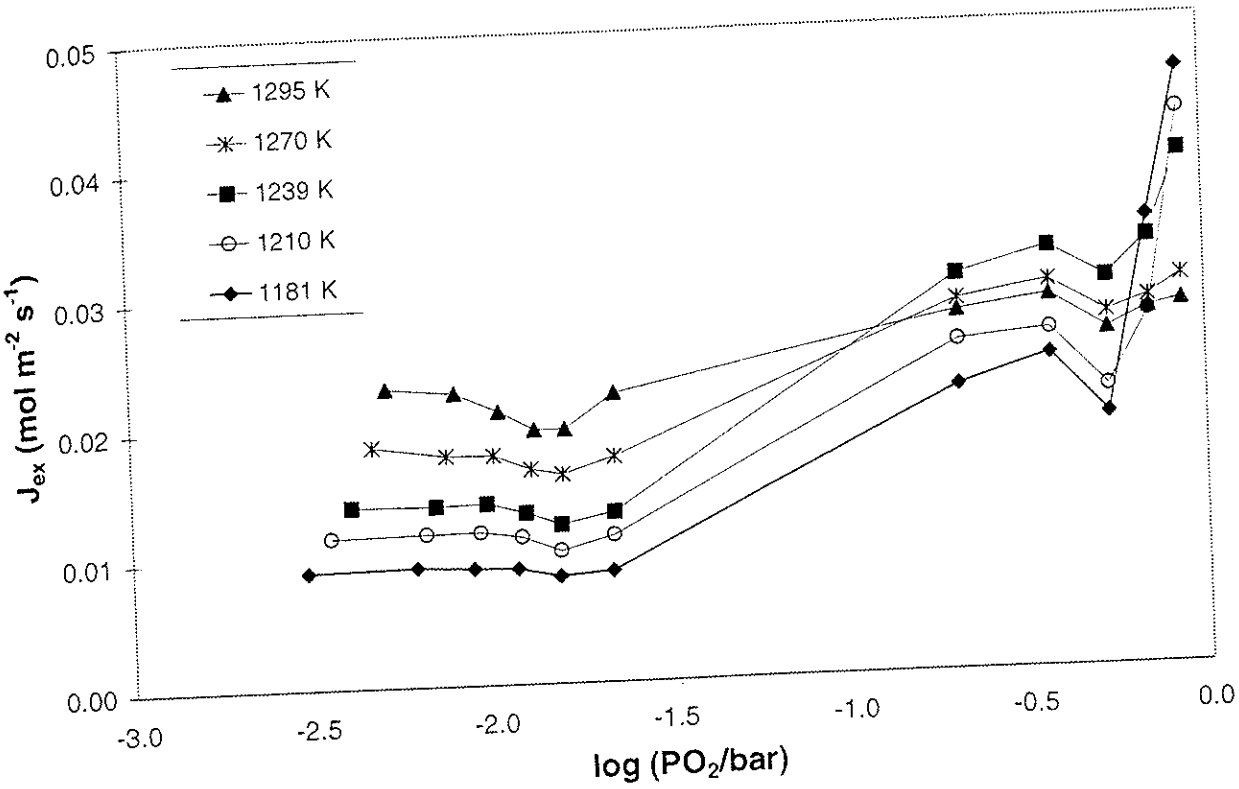

Figure 4.13 The apparent surface exchange rate as a function of P_{O_2} for $SrFe_{0.97}Cr_{0.03}O_{3-\delta}$. Membrane thickness, 2.14 mm.

At low P_{O_2} the exchange rate increases with increasing temperature. The apparent activation energy is calculated to 98 ± 8 kJ/mol for $0.003 < P_{O_2}(\text{bar}) < 0.021$. The exchange rate increases with decreasing temperature at $P_{O_2} = 0.9$ bar. These results imply different rate determining step on the two surfaces. At the feed side, the membrane surface is oxidised. This is an exothermic process. The permeate membrane surface is reduced, which is endothermic. This indicates that the oxidation and reduction processes give a major contribution to the rate determining of the oxygen surface exchange rates.

The chemical potential drop through a permeating membrane is plotted in Figure 4.14. The chosen driving force is typical for the majority of the present permeation experiments. The figure shows that the highest potential drop is through the bulk. The oxygen exchange limitation is higher on the permeate surface than the feed surface at all temperatures. The potential drop on the two surfaces approach each other when the temperature increases. The result is not influenced significantly by changing the model input parameters as

long as they remain within a reasonable range. The trend in the potential drop is similar for the other driving forces which are applied.

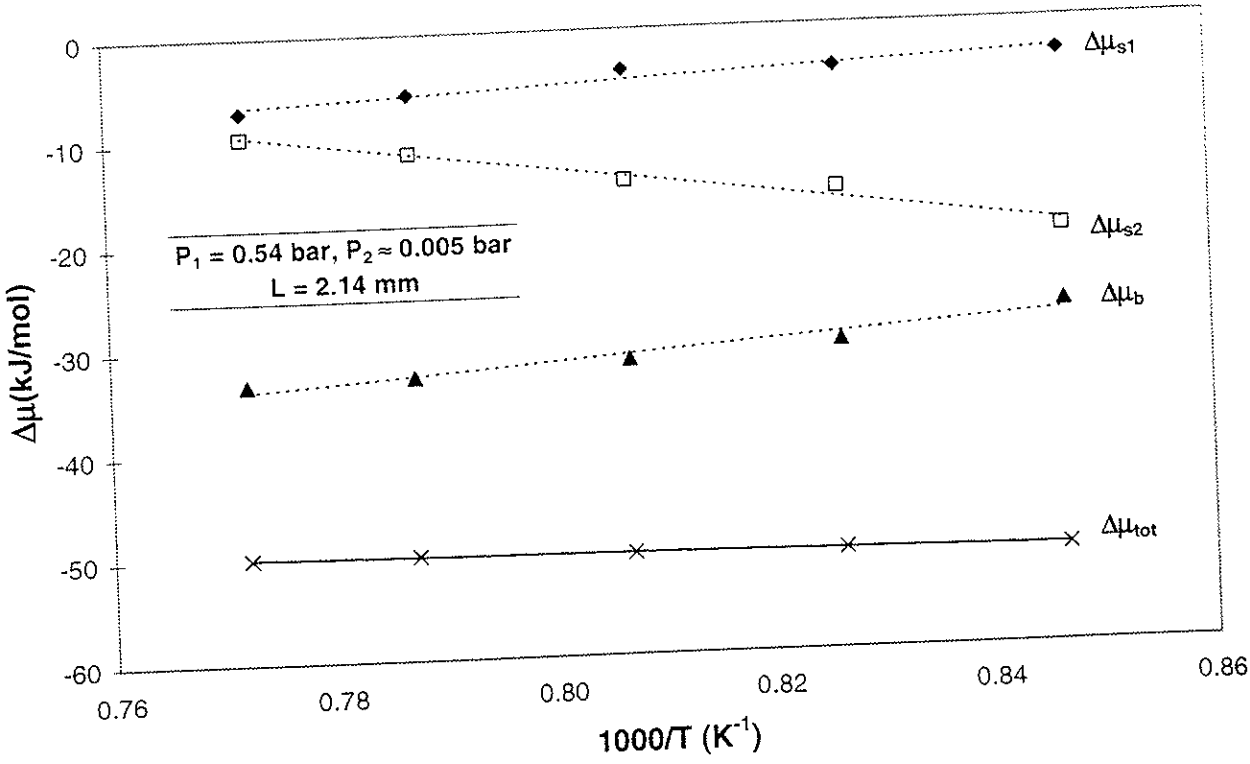

Figure 4.14 The chemical potential drop on the feed surface ($\Delta\mu_{s1}$), permeate surface ($\Delta\mu_{s2}$) and through the bulk ($\Delta\mu_b$) as a function of inverse temperature. Membrane of $SrFe_{0.97}Cr_{0.03}O_{3-\delta}$ with thickness 2.14 mm and driving force, $\Delta\mu_{tot}$.

Figure 4.15 shows the total chemical potential drop on both membrane surfaces, and compared with the results obtained from permeability experiments for membranes with different thicknesses (Chapter 3.4.4). The figure illustrates adequate agreement between the two methods used to determine the surface exchange limitation. The discrepancy is less than 10 % at the highest temperature, but increases at lower temperature. The thickness dependent experiments are based on membranes with thicknesses in the range $0.9 < L(mm) < 2.4$. These results are believed to have the highest uncertainty due to the relative narrow membrane thickness range which was investigated.

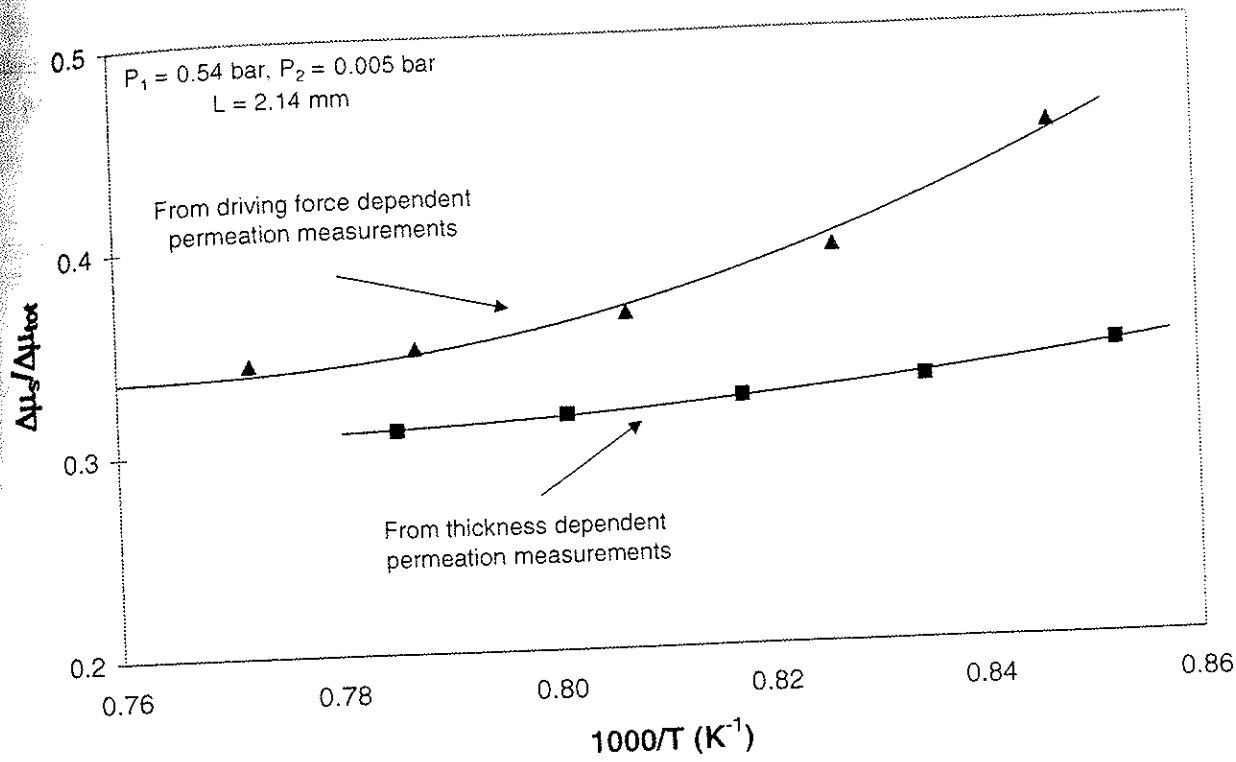

Figure 4.15 The fraction of the total chemical potential drop on the two membrane surfaces, as a function of inverse temperature. Membrane of $SrFe_{0.97}Cr_{0.03}O_{3-\delta}$ and thickness 2.14 mm.

The oxygen chemical potential profile through the membrane is plotted in Figure 4.16. The calculation of the profile through the bulk is performed by dividing the chemical potential drop into 20 segments and calculating x for each chemical potential in the range $0 < x < L$. A detailed description is given in Appendix 15.

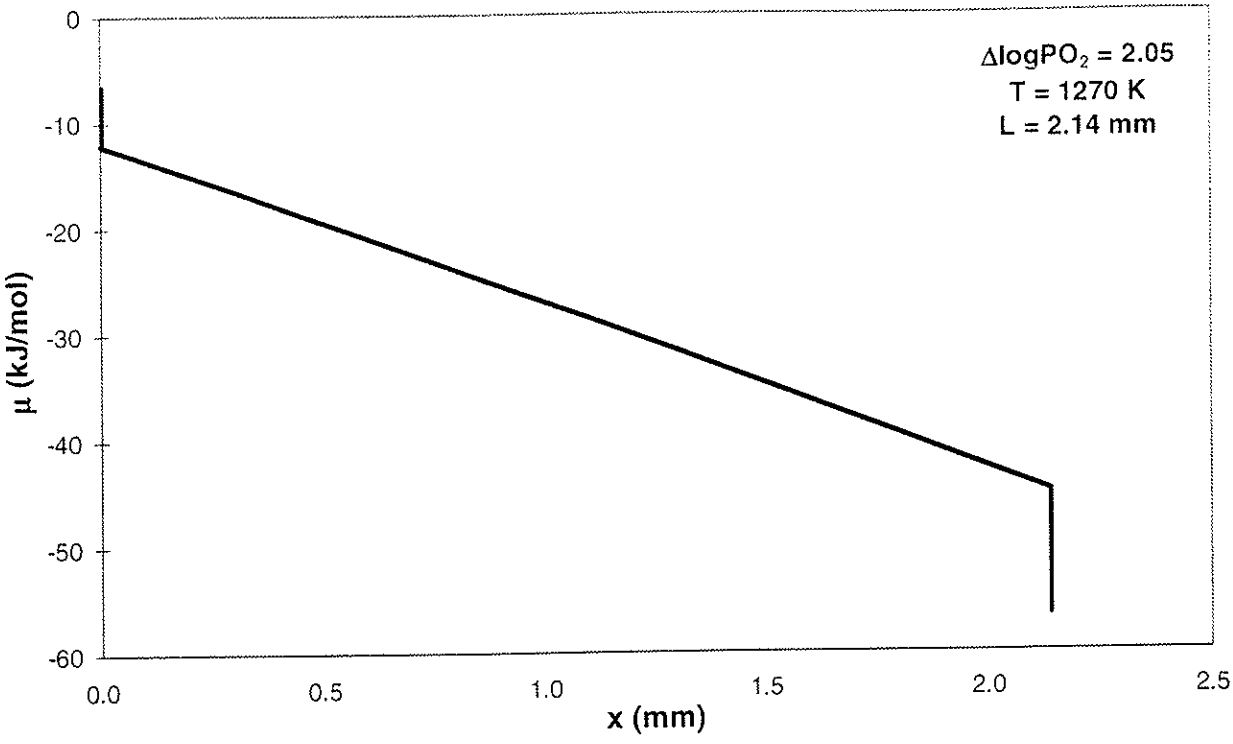

Figure 4.16 Calculated chemical potential profile of oxygen as a function of position x in the membrane of $SrFe_{0.97}Cr_{0.03}O_{3-\delta}$ with thickness 2.14 mm.

The relationship between the exchange flux ($J_{O_2}^{ex}$) and the tracer surface exchange coefficient (k^*) is given in equation [1.20] (Kilner, 1994; Bouwmeester & Burggraf, 1997). The calculated tracer surface exchange coefficient (k^*) as a function of inverse temperature at P_{O_2} = 0.007 bar is given in Figure 4.17.

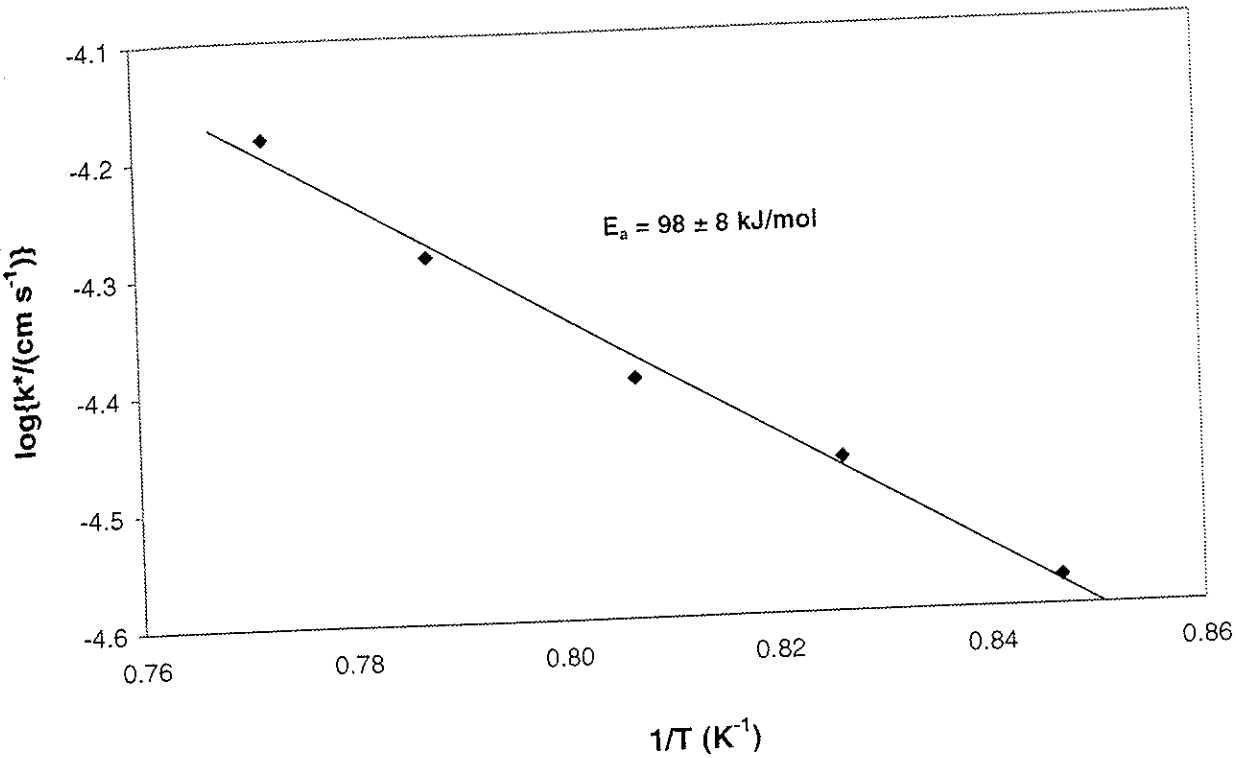

Figure 4.17 Arrhenius plot of the calculated tracer surface exchange coefficient for $SrFe_{0.97}Cr_{0.03}O_{3-\delta}$ at $P_{O_2} = 0.007$ bar.

The estimated tracer surface exchange coefficient is in the range of $6 \cdot 10^{-5} - 2 \cdot 10^{-5}$ cm/s at the stated temperatures, in the low P_{O_2} region. These values are reasonable compared to results from isotopic exchange experiments for the $La_{1-x}Sr_xFeO_{3-\delta}$ system (Ishigaki et al., 1984/1988; ten Elshof et al., 1995). The literature data and the results of this study are reported in Figure 4.18. The data show an increased k^* with increasing Sr-content.

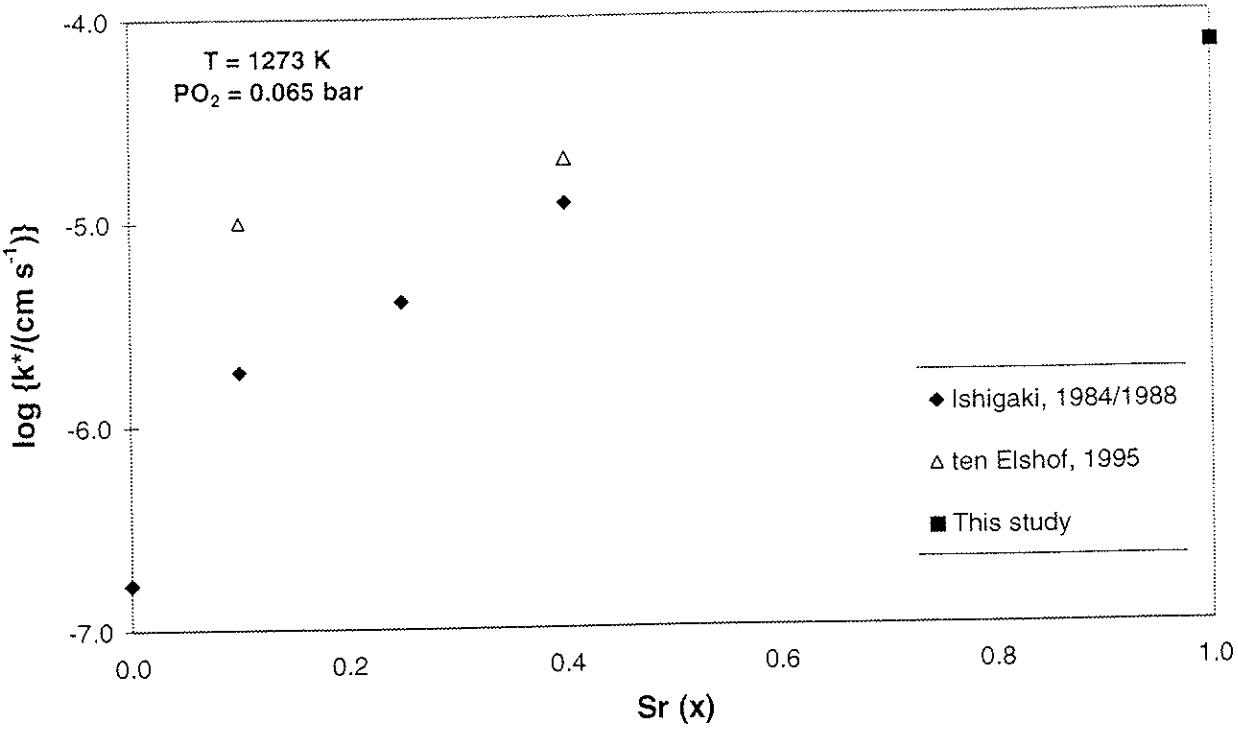

Figure 4.18 The tracer surface exchange coefficient as a function of Sr-content for $La_{1-x}Sr_xFeO_{3-\delta}$.

The relationship between k^* and D^* can be expressed by the notation L_c, according to equation [1.23]. Kilner et al. report a correlation between k^* and D^* specific to the structure type, for perovskites and fluorites (Kilner, 1994; De Souza & Kilner, 1999). This may imply that accessibility of oxygen vacancies is the rate determining step in the surface exchange process for the investigated materials. The characteristic thickness as a function of Sr-substitution in $La_{1-x}Sr_xFeO_{3-\delta}$ is plotted in Figure 4.19 (Ishigaki et al., 1984/1988; ten Elshof et al., 1995). The L_c increases with increasing Sr-substitution and the value for $SrFeO_{3-\delta}$ fits well with the literature data.

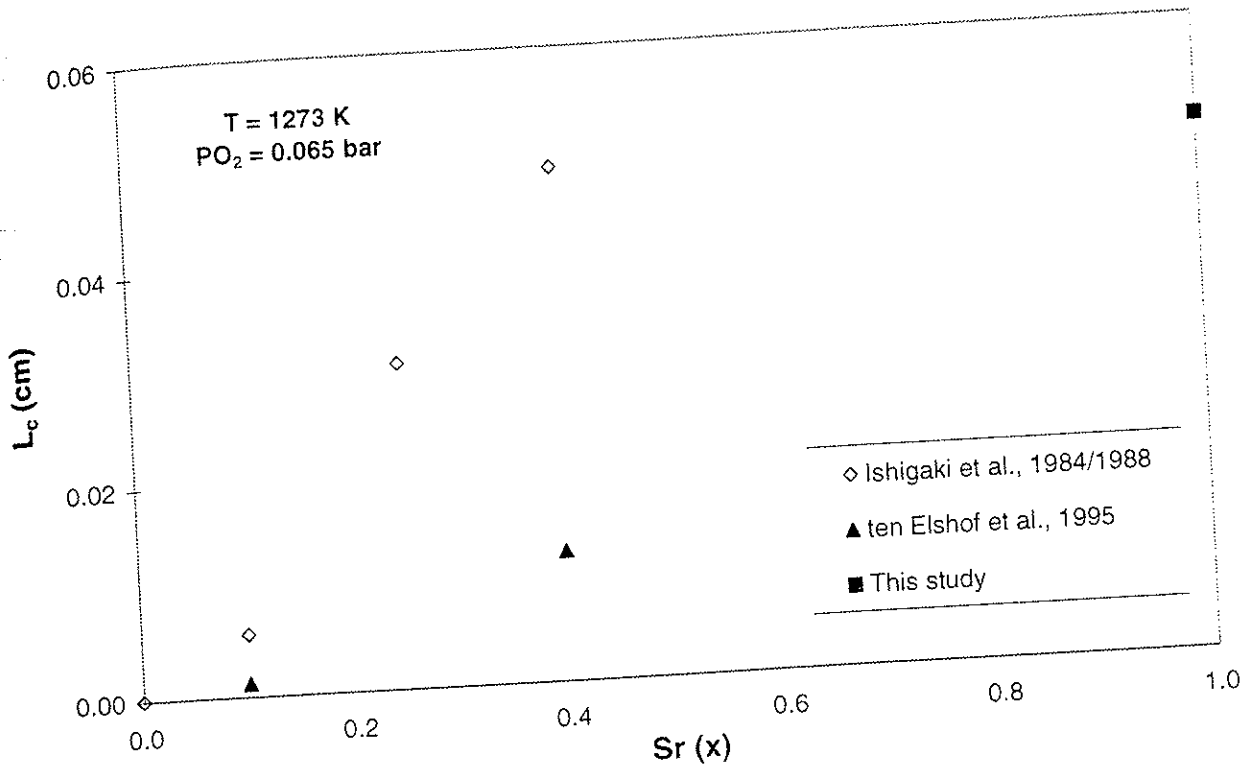

Figure 4.19 Characteristic thickness, L_c, as a function of Sr-content for $La_{1-x}Sr_xFeO_{3-\delta}$.

4.3 Model for microstructure dependent permeation

The model is based on an equivalent circuit for the oxygen transport, shown schematically in Figure 4.20. The model has two pathways for oxygen bulk diffusion through the sample: One is transport along the grain boundaries, the other goes through grains and across grain boundaries. Additionally, the model describes the influence of grain boundaries on the surface oxygen exchange kinetics on both the feed and permeate side of the membrane.

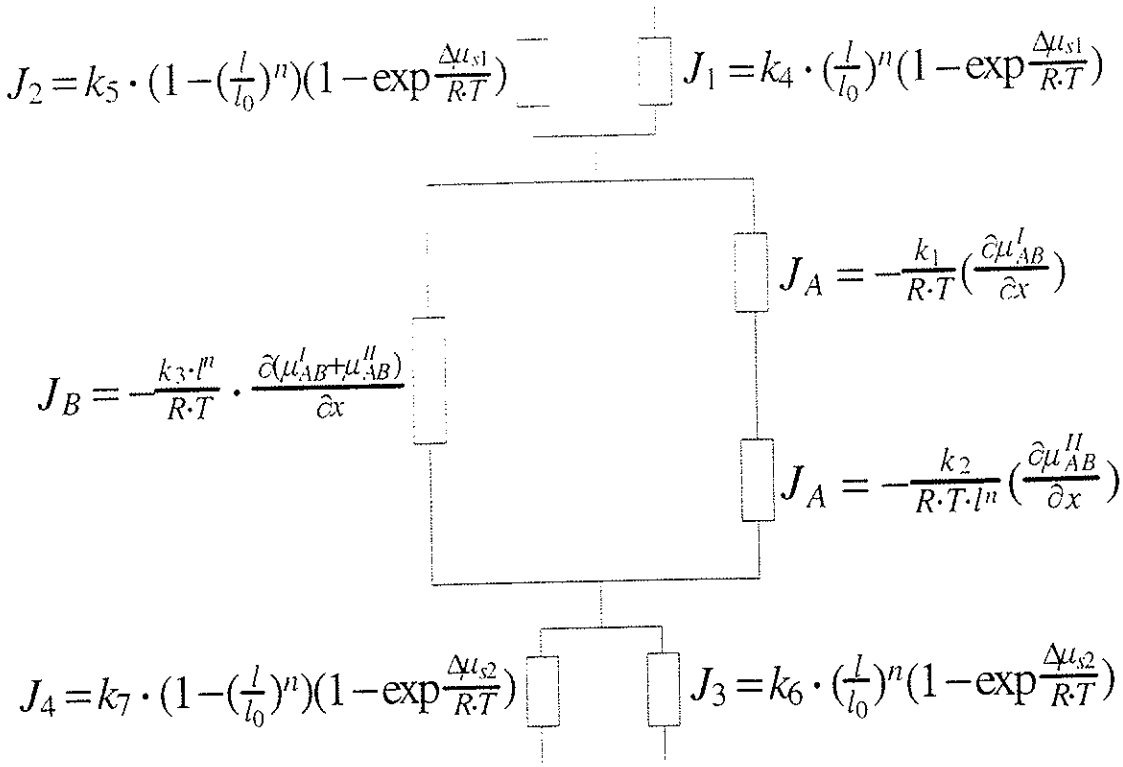

Figure 4.20 Diagram of the different oxygen chemical potential drop and the associated permeability equations of an oxygen permeable membrane.

The following equations describe the oxygen permeation of the membrane:

$$J_A = -\frac{k_1}{R\cdot T}\left(\frac{\partial\mu^I_{AB}}{\partial x}\right) \qquad [4.10]$$

where the constant k_1 is related to the bulk transport through grains (intra grain), and $\frac{\partial\mu^I_{AB}}{\partial x}$ is the chemical potential gradient of O_2 across the total number of grains through the thickness of the membrane.

$$J_A = -\frac{k_2}{R\cdot T\cdot l^n}\left(\frac{\partial\mu^{II}_{AB}}{\partial x}\right) \qquad [4.11]$$

where the constant k_2 is connected to the bulk transport by traversing the grain boundaries, l is the grain boundary length, and $\frac{\partial \mu_{AB}^{II}}{\partial x}$ is the chemical potential gradient across the grain boundaries through the thickness of the membrane. The exponent n describes the permeability dependency of the grain boundary length.

$$J_B = -\frac{k_3 \cdot l^n}{R \cdot T} \cdot \frac{\partial(\mu_{AB}^{I} + \mu_{AB}^{II})}{\partial x} \qquad [4.12]$$

where the constant k_3 is related to the bulk transport along the grain boundaries (inter grain). Thus the calculated oxygen permeability, J_C, of the membrane is given by:

$$J_C = J_A + J_B \qquad [4.13]$$

The oxygen permeability across the feed surface, J_1, can be represented as:

$$J_1 = k_4 \cdot (\frac{l}{l_0})^n (1 - \exp \frac{\Delta \mu_{s1}}{R \cdot T}) \qquad [4.14]$$

where the constant k_4 is related to the surface oxygen exchange transport along the grain boundaries. The characteristic grain boundary length, l_0 is estimated to be 1000 $\mu m/\mu m^2$, based on a grain boundary width of 10^{-3} μm. The oxygen permeability on the feed surface can also be described as:

$$J_2 = k_5 \cdot (1 - (\frac{l}{l_0})^n)(1 - \exp \frac{\Delta \mu_{s1}}{R \cdot T}) \qquad [4.15]$$

where the constant k_5 is related to the surface oxygen exchange transport in the absence of grain boundaries. Similar expressions describe the surface exchange kinetics on the permeate surface:

$$J_3 = k_6 \cdot (\frac{l}{l_0})^n (1 - \exp \frac{\Delta\mu_{s2}}{R \cdot T}) \qquad [4.16]$$

$$J_4 = k_7 \cdot (1 - (\frac{l}{l_0})^n)(1 - \exp \frac{\Delta\mu_{s2}}{R \cdot T}) \qquad [4.17]$$

The total oxygen permeability is consequently:

$$J_C = J_1 + J_2 = J_3 + J_4 \qquad [4.18]$$

The total available driving force, $\Delta\mu_{tot}$ across the membrane is given by:

$$\Delta\mu_{tot} = \Delta\mu_{s1} + \Delta\mu_{AB}^{I} + \Delta\mu_{AB}^{II} + \Delta\mu_{s2} \qquad [4.19]$$

where $\Delta\mu_{s1}$ and $\Delta\mu_{s2}$ are the drop in the chemical potential on the feed and permeate surface respectively.

Table 4.3 gives a description and units of the constants $k_1 - k_7$, given in equations [4.10]-[4.17].

Table 4.3 Description of coefficients in the model of grain boundary length dependent oxygen permeability, according to equations [4.10] - [4.17].

coefficient	unit	Description
k_1	$\frac{mol}{m \cdot s}$	intra grain, bulk
$\frac{k_2}{l^n}$	$\frac{mol}{m \cdot s}$	traverse grain boundaries, bulk
$k_3 \cdot l^n$	$\frac{mol}{m \cdot s}$	inter grain (along grain boundaries), bulk
k_4	$\frac{mol}{m^2 \cdot s}$	surface exchange, feed side - along grain boundaries
k_5	$\frac{mol}{m^2 \cdot s}$	surface exchange, feed side - no grain boundaries
k_6	$\frac{mol}{m^2 \cdot s}$	surface exchange, permeate side - along grain boundaries
k_7	$\frac{mol}{m^2 \cdot s}$	surface exchange, permeate side - no grain boundaries

Simplification of the model

The results presented in Chapter 3.4.6 show that the grain boundary length (in the surface) has a major effect on the surface exchange process. The permeation data on membranes with various surface roughness and grain boundary length give no information on variation in bulk transport with different microstructure. Hence, the two bulk potential drops in the model

described above (Figure 4.20) can not be separated. The equations [4.11] and [4.12] are in this manner eliminated in the present numeric modelling.

The calculation of $\frac{\partial \mu_{AB}}{\partial x}$ is performed for membrane with thickness, L = 1.45 mm. Detailed description is given in Appendix 15. The chemical potential as a function of position x is shown in Figure 4.21. The results give almost straight lines at the relevant temperatures. The numeric calculation of grain boundary dependent permeation is simplified by introducing a linear chemical potential drop across the bulk of the membrane.

In summary, the bulk permeation in the present modelling is described by the equation:

$$J_A = -\frac{k_1}{L}\left(\frac{\Delta \mu_{AB}}{R \cdot T}\right) \qquad [4.20]$$

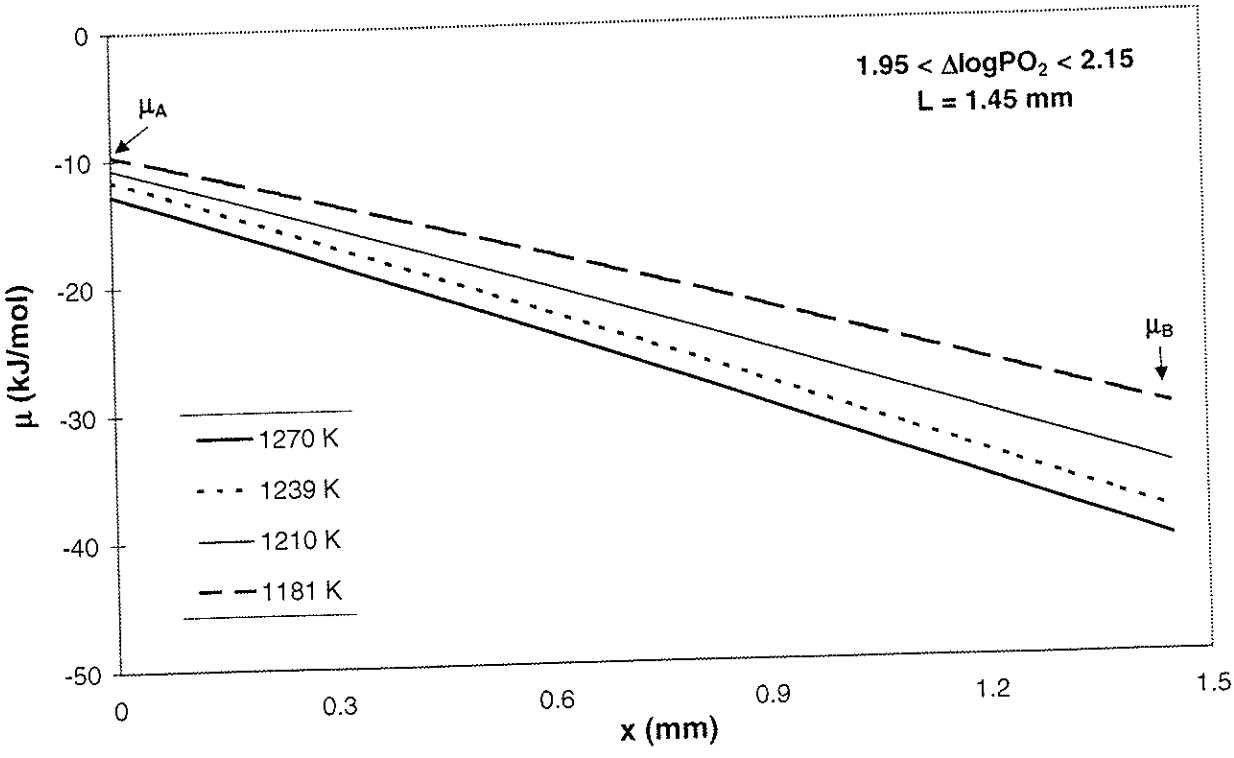

Figure 4.21 Calculated bulk chemical potential of oxygen as a function of position x in the membrane of $SrFe_{0.97}Cr_{0.03}O_{3-\delta}$ with thickness 1.45 mm.

Equations [4.11] - [4.20] are solved numerically by iteration of the chemical oxygen potential drop across the bulk ($\Delta\mu_{AB}$) from initial estimates of the coefficients $k_1 - k_7$ and exponent n. The modelled potential drop at $l = 0.29$ $\mu m/\mu m^2$, presented in Chapter 4.2, is recalculated to the relevant thickness and fixed in the modelling of the similar grain boundary length. Results of the fitting coefficients are given in Table 4.4. The results of calculated permeability as a function of grain boundary length with various exponent n are given in Figure 4.22. With reasonable values of n, the best fit to the experimental data is obtained when the permeation is proportional to the grain boundary length on the surfaces to the n'th power (n > 2). A reasonable explanation for this behaviour is lacking in the present study.

Modelling with a proportional factor to the grain boundary length did not fit the experimental data.

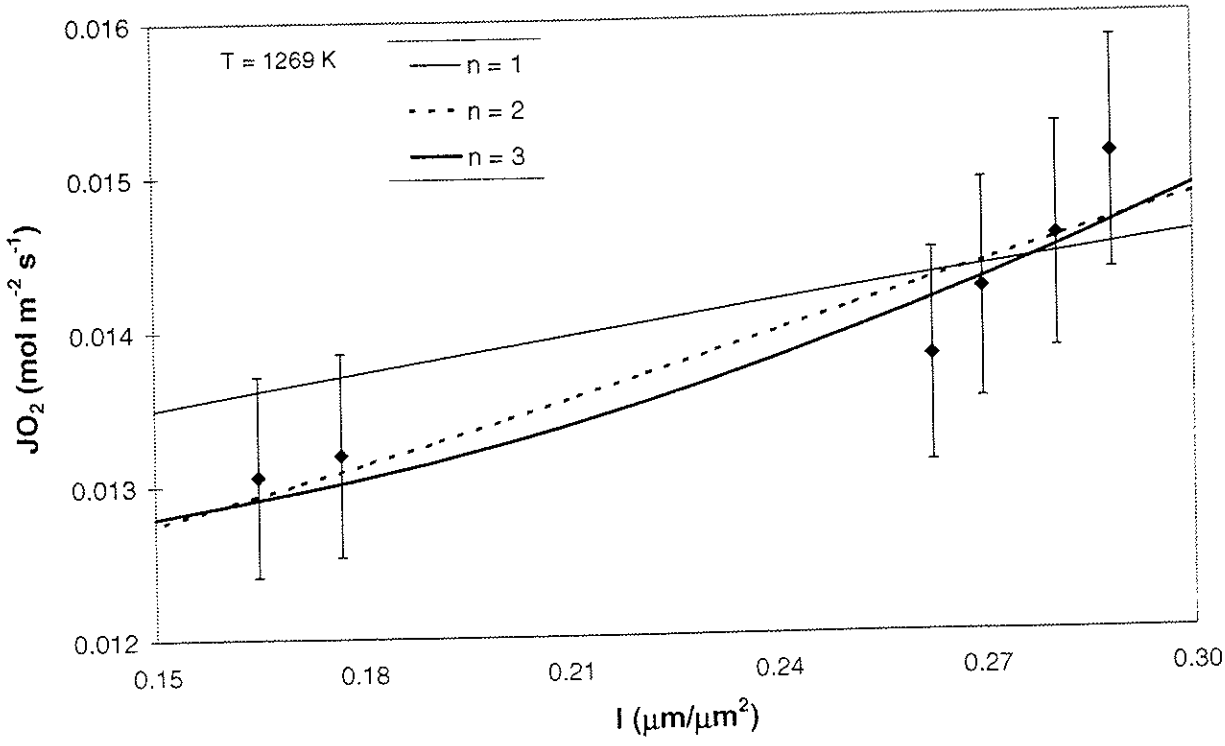

Figure 4.22 Calculated oxygen permeability as a function of grain boundary length of $SrFe_{0.97}Cr_{0.03}O_{3-\delta}$ membranes of 1.45 mm thickness and various exponent n. $\Delta \log P_{O_2} \approx 2.1$

Table 4.4 Results of regression coefficients for the grain boundary length dependent oxygen permeation, according to the equations [4.11] - [4.20].

T (K)	n	k_1	k_4	k_5	k_6	k_7
1269	1	$7.70 \cdot 10^{-6}$	20	0.026	18	0.015
1269	2	$7.80 \cdot 10^{-6}$	2000	0.032	80000	0.0137
1269	3	$7.80 \cdot 10^{-6}$	$4.00 \cdot 10^{8}$	0.0224	$1.76 \cdot 10^{8}$	0.0161
1241	3	$6.90 \cdot 10^{-6}$	$4.95 \cdot 10^{8}$	0.0269	$1.39 \cdot 10^{8}$	0.0129
1211	3	$6.63 \cdot 10^{-6}$	$8.00 \cdot 10^{7}$	0.029	$9.50 \cdot 10^{7}$	0.0105
1183	3	$6.45 \cdot 10^{-6}$	$4.28 \cdot 10^{7}$	0.0295	$6.07 \cdot 10^{7}$	0.00826

Figure 4.23 shows the results of modelled oxygen permeability as a function of grain boundary length at different temperatures. The experimental data indicate an increased effect of the grain boundary length with increasing temperatures.

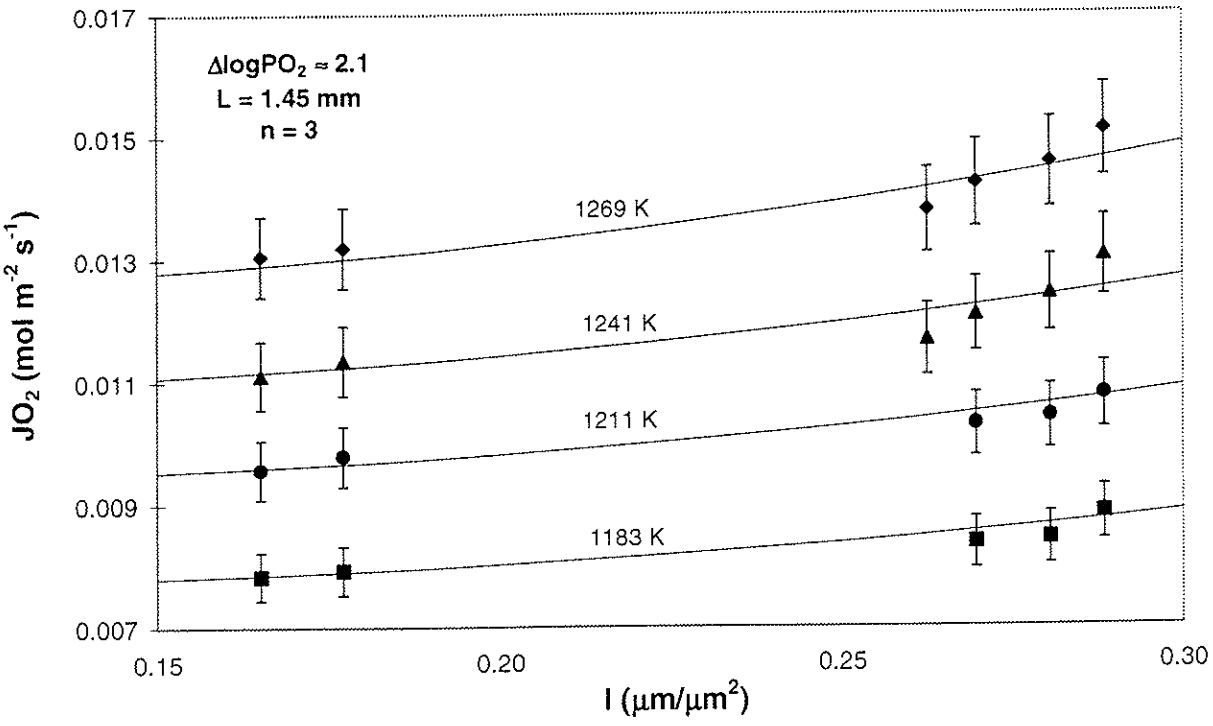

Figure 4.23 Calculated oxygen permeability as a function of grain boundary length of $SrFe_{0.97}Cr_{0.03}O_{3-\delta}$ membranes with thickness 1.45 mm.

The fraction of the chemical potential drop across the bulk, and on the two surfaces as a function of grain boundary length at 1269 K are given in Figure 4.24.

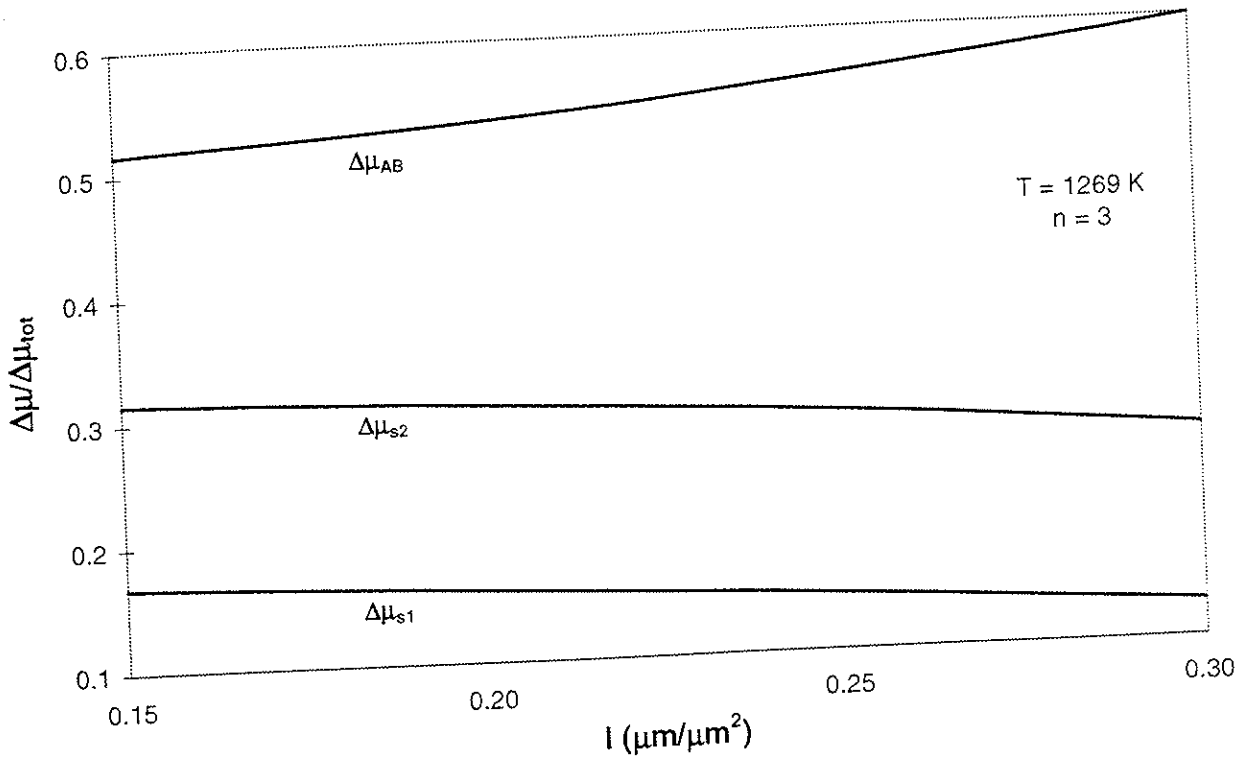

Figure 4.24 Calculated chemical potential of oxygen as a function of grain boundary length of $SrFe_{0.97}Cr_{0.03}O_{3-\delta}$. $\Delta \log P_{O_2} \approx 2.1$.

The uncertainty in the modelling is large because of the limited number of experiments. The abrupt change in permeation at the largest grain boundary length does probably not describe the real situation. Nevertheless, the results show an increase in oxygen permeation with increasing grain boundary length.

Variation in membrane density is within 0.5 % and can not explain the abnormal grain boundary dependent permeation results. Most of these results can be explained by the presumed uncertainty of 5 % in the oxygen permeation measurements. The uncertainty in grain boundary length measuring is less than 2 %.

The present results of enhanced permeation with increasing grain boundary length is not in agreement with the work of Kharton et al. (1998). A discussion of that paper is given in Chapter 3.2. However, the present study concludes that the increased grain boundary length enhances the surface exchange kinetics. Kharton et al. reported the reduced permeability with increasing grain boundary length to be due to higher bulk resistance. Additionally, they observed considerable surface exchange limitation.

4.4 Conclusions

The simple point defect model describes the oxygen stoichiometry for $SrFeO_{3-\delta}$ with reasonable values of the thermodynamic quantities.

Modelling of the surface oxygen exchange rate shows that the permeation is partly limited by the surface exchange kinetics. The oxygen exchange rate is higher on the feed side than on the permeate side, which indicates a higher resistance on the permeate surface. The surface exchange limitation of the permeation increases when decreasing the temperature on the permeate side, while the opposite is observed on the feed surface. This indicates that the oxidation and reduction of the oxide surfaces give a major contribution to the rate determining step of the oxygen surface exchange process. The total surface exchange limitation increases with decreasing temperature, and hence is in agreement with the evaluation of surface exchange kinetics from the experiments of oxygen permeability as a function of membrane thickness.

A significant increase in the oxygen permeability was observed when increasing the grain boundary lengths in the membranes. Increased surface area masks this effect, suggesting grain boundary dependent surface exchange kinetics. Modelling of the grain boundary dependency gave an adequate fit to the experimental data. The best fit is obtained when the permeation is proportional to the grain boundary length on the surfaces to the n'th power (n > 2). A reasonable explanation for this behaviour is lacking in the present study.

Table 4.5 summarises the activation energies for the different physical parameters related to the oxygen permeation of $SrFe_{0.97}Cr_{0.03}O_{3-\delta}$.

Table 4.5 Activation energies for the different physical parameters related to oxygen permeation of $SrFe_{0.97}Cr_{0.03}O_{3-\delta}$ at 1273 K.

Measurements	Physical parameters		E_a (kJ/mol)
Oxygen permeation	J_{O_2}	overall permeation	60 ± 8
Oxygen permeation, modelled from thickness dependency (Ch. 3.4.4)	j_b	bulk diffusion	52 ± 8
Oxygen permeation, calculated from thickness dependency and eq. [1.4]	D_v	bulk, activation energy of vacancy migration	49-62
TGA, nonstoichiometry model	δ	bulk, $d\ln\delta/d(1/T)$	2-10 *
Oxygen permeation, calculated from D_v and the Nernst-Einstein relation	σ_i	bulk, ionic conductivity	52-60
Oxygen permeation, modelled from driving force dependency	$J^{ex}_{O_2(II)}$	surface exchange rate, permeate side	98 ± 8
Oxygen permeation, modelled from thickness dependency (Ch. 3.4.4)	$\frac{j_b}{L_s}$	total surface exchange rate	57 ± 8

* The apparent energy required for oxygen vacancy formation (ΔE_v) decreases as the vacancy concentration increases, in the relevant P_{O_2} range (1.0 - 10^{-5} bar).

REFERENCES

Aasland, S., Tangen, I. L., Wiik, K. and Ødegård, R.
Oxygen Permeation of $SrFe_{0.67}Co_{0.33}O_{3-\delta}$.
Solid State Ionics, **135** (2000) 713.

Adamczyk, Z. and Nowotny, J.
Effect of the surface on gas/solid equilibration kinetics in nonstoichiometric compounds.
Solid State Phenom. **15-16** (1991) 285.

Anderson, H. U.
Review of p-type doped perovskite materials for SOFC and other applications.
Solid State Ionics, **52** (1992) 33.

Atkins, P. W.
"Physical Chemistry"
Oxford University Press, Oxford, 1986.

Atkinson, A.
"Diffusion in Ceramics" in "Material Science and Technology - A Comprehensive Treatment", Vol. 11: Structure and Properties of Ceramics. 295-337.
Eds., Cahn, R. W., Haasen, P. and Kramer, E.
VCH Publishers, Wienheim, 1994.

Barin, I.
"Thermochemical Data of Pure Substanes"
Eds., Schulz, G. and Ryan-Bugler, P.
VCH Publishers, Wienheim, 1993.

Batti, P.
Diagramma d`equilibrio del sistema $SrO-Fe_2O_3$.
Ann. Chim. **52** (1962) 941.

Belzner, A., Gür, T. M. and Huggins, R. A.
Oxygen chemical diffusion in strontium doped lanthanum manganites.
Solid State Ionics, **57** (1992) 327.

Benson, S. J., Waller, D., Lane, J. A. and Kilner, J. A.
Oxygen Transport and Non-Stoichiometry in $La_{0.6}Sr_{0.4}Fe_{0.8}Co_{0.2}O_{3-\delta}$.
Presented at the 11th International Conference on Solid State Ionics, Hawaii, 1997.
www.eng.hawaii.edu/~ssi11/SSI-11Papers/C21.pdf

Benson, S., Charter, R. J. and Kilner, J. A.
Oxygen Diffusion and Surface Exchange in the Mixed Conducting Perovskite $La_{0.6}Sr_{0.4}Fe_{0.8}Co_{0.2}O_{3-\delta}$.
Proc. Electrochem. Soc., **97-24** (1998) 596.

Bocquet, A. E., Dobson, J. F., Healy, P. C., Myhra, S. and Thompson, J. G.
X-ray photoelectron spectra of High T_c bismuth compounds.
Phys. Stat. Sol. B, **152**(1989) 519.

Boroomand, F., Wessel, E., Bausinger, H. and Hilpert, K.
Correlation between defect chemistry and expansion during reduction of doped $LaCrO_3$ interconnects for SOFCs.
Solid State Ionics, **129** (2000) 251.

Bouwmeester, H. J. M., Kruidhof, H. and Burggraaf, A. J.
Importance of the surface exchange kinetics as rate limiting step in oxygen permeation through mixed-conducting oxides.
Solid State Ionics, **72** (1994) 185.

Bouwmeester, H. J. M. and Burggraf, A. J.
"Dense ceramic membranes for oxygen separation" in "The CRC Handbook of Solid State Electrochemistry", 481-553.
Eds., Gellings, P. J. and Bouwmeester, H. J. M.
CRC Press Inc., Florida, 1997.

Encyclopædia Britannica
www.britannica.com, 2000.

Cannon, R. M. and Carter W. C.
Interplay of Sintering Microstructures, Driving forces, and Mass Transport Mechanisms.
J. Am. Ceram. Soc., **72** [8] (1989) 1550.

Chemical Week
www.chemweek.com, 2000.

Cox, P. A.
"Transition Metal Oxides. An introduction to their electronic structure and properties."
Oxford University Press, New York, 1995.

Crank, J.
"The Mathematics of diffusion"
Oxford University Press, New York, 1975.

Davies, V. de L.
"Støperiteknikk" In Norwegian.
Tapir Forlag, Trondheim, 1970.

De Boer, J. H.
"The Dynamical Character of Adsorption."
Oxford University Press, New York, 1968.

De Souza, R. A. and Kilner, J. A.
Oxygen transport in $La_{1-x}Sr_xMn_{1-y}Co_yO_{3\pm\delta}$ perovskites.
Part II. Oxygen surface exchange
Solid State Ionics, **126** (1999) 153.

Deng, H., Zhou, M. and Abeles, B.
Diffusion-reaction in mixed ionic-electronic solid oxide membranes with porous electrodes.
Solid State Ionics, **74** (1994) 75.

Deng, H., Zhou, M. and Abeles, B.
Transport in solid oxide porous electrodes: Effect of gas diffusion.
Solid State Ionics, **80** (1995) 213.

Diethelm, S., Closset, A., Nisancioglu, K., Herle, J. V., McEvoy, A. J. and Gür, T.
Simultaneous determination of chemical diffusion and surface exchange coefficients of oxygen by the potential step technique.
J. Electrochem. Soc., **146** [7] (1999) 2606.

DOE (U. S. Department of Energy) Techline.
www.fetc.doe.gov/publications/press, 1999.

Fell, H. J., Budd, M, Svendsen, J. A., Glenne, R. and Julsrud, S.
The transient electrochemical characterisation of $SrFeO_{3-\delta}$.
In preparation.

Garino, T. J. and Bowen, H. K.
Kinetics of Constrained-Film Sintering.
J. Am. Ceram. Soc., **73** [2] (1990) 251.

Gellings, P. J. and Bouwmeester, H. J. M.
Ion and mixed conducting oxides as catalysts.
Catalysis today, **12** (1992) 1.

German, R. M. and Churn, K. S.
Sintering Atmosphere Effects on the Ductility of W-Ni-Fe Heavy Metals.
Met. Trans., **15A** (1984) 747.

German, R. M.
"Sintering Theory and Practice"
John Wiley & Sons, New York, 1996.

Gordes, P., Christiansen, N, Jensen, E. J. and Villadsen, J.
Synthesis of perovskite-type compounds by drip pyrolysis.
Journal of Materials Science, **30** (1995) 1053.

Haavik, C.
Thermochemical studies of $Fe_{1-y}O$, Fe_3O_4 and $SrFeO_{3-\delta}$: interplay between experiment and modelling.
PhD. Thesis, University of Oslo, Norway, 2001.
In preparation.

Handwerker, C. A., Dynys, J. M., Cannon, R. M. and Coble R. L.
Dihedral Angles in Magnesia and Alumina: Distributions from Surface Thermal Grooves.
J. Amer. Ceram. Soc., **73** (1990) 1371.

Hansen, H. L.
Determination of oxygen permeability in cobalt substituted strontium ferrate.
M. Sc. Thesis, Norwegian University of Science and Technology, Trondheim, Norway, (1999). In Norwegian.

Harmer, M. P. and Zhao, J.
Effect of Pores on Microstructure Development. Ceramic Microstructures '86 Pask, J. A. and Evans, A. G. (eds.)
Plenum Press, New York, (1988) p. 455-464.

Henrich, V. E. and Cox, P. A.
"The surface science of metal oxides."
Cambridge University Press, Cambridge, 1996.

Holt, A., Larring, Y. and Norby, T.
Phase transitions and chemical diffusion coefficients of $Sr_4Fe_{6-x}Co_xO_{13}$.
Proc. Nordic Seminar on "Diffusion and concentration of mobile species in fuel cell materials." (eds. Zachau-Christiansen, B.), Geilo, Norway (1998).

Holt, A., Norby, T. and Glenne, R.
Defects and transport in $SrFe_{1-x}Co_xO_{3-\delta}$.
Journal Ionics, **5** (1999) 434.

Hong, J.-O., Teller, O., Martin, M. and Yoo, H.-I.
Demixing of mixed oxide (A,B)O in an oxygen potential gradient: numerical solution of the time evolution of the demixing process.
Solid State Ionics, **123** (1999) 75.

Horita, T., Ishikawa, M., Yamaji, K., Sakai, N., Yokokawa, H. and Dokiya, M.
Cation diffusion in (La,Ca)CrO3 perovskite by SIMS.
Solid State Ionics, **108** (1998) 383.

Horita, T., Ishikawa, M., Yamaji, K., Sakai, N., Yokokawa, H. and Dokiya, M.
Calcium tracer diffusion in (La,Ca)CrO_3 by SIMS.
Solid State Ionics, **124** (1999) 301.

Ishigaki, T., Yamauchi, S., Mizusaki, J., Fueki, K., Naito, H. and Adachi, T.
Diffusion of Oxide Ions in $LaFeO_3$ Single Crystal.
J. Solid State Chem., **55** (1984) 50.

Ishigaki, T., Yamauchi, S., Kishio, K., Mizusaki, J. and Fueki, K.
Diffusion of Oxide Ion Vacancies in Perovskite-Type Oxides.
J. Solid State Chem., **73** (1988) 179.

Iwahara, H.
Oxygen separation from gas mixture - by selectively passing through membrane of lanthanum strontium cobalt oxide.
Japan Patent 56-92103 (1981).

Jacobson, A. J., Yang, Y. L., Lee, T. H., Kim, S. and Abeles, B.
Oxygen permeation studies of diffusion and surface exchange in mixed conducting oxide electrode materials.
In *Proceedings of the Fifth International Symposium on SOFC*, Aachen, Germany, (1997) 493.

Jagannathan, K. P., Tiku, S. K., Ray, H. S., Ghosh, A. and Subbarao, E. C.
Technological Applications of Solid Electrolytes. In "Solid Electrolytes and their Applications", Eds. Subbarao, E. C.
Plenum Press, New York, 1980.

J. E. Sinor Consultants Inc.
www.edj.net/sinor/sfr498art2.html

Kanamaru, F., Shimada, M. and Koizumi, M.
Crystallographic properties of and Mössbauer effect in $Sr_4Fe_6O_{13}$.
J. Phys. Chem. Solids, **33** (1972) 1169.

Kang, D., Thorogood, R. M., Allam, R. J., Topham, A. K. J. and Russek, S. L.
High temperature oxygen production with steam and power generation.
US Patent 5,565,017 (1996).

Kawada, T., Horita, T., Sakai, N., Yokokawa, H. and Dokiya, M.
Experimental determination of oxygen permeation flux trough bulk and grain boundary of $La_{0.7}Ca_{0.3}CrO_3$.
Solid State Ionics, **79** (1995) 201.

Kharton V. V., Tikhonovich, V. N., Shuangbao, L., Naumovich, E. N., Kovalevsky, A. V., Viskup, A. P., Bashmakov, I. A. and Yaremchenko, A. A.
Ceramic Microstructure and Oxygen Permeability of $SrCo(Fe,M)O_{3-\delta}$ (M = Cu or Cr) Perovskite Membranes.
J. Electrochem. Soc., **145** [4] (1998) 1363.

Kilner, J. A., Steele, B. C. H. and Ilkov, L.
Oxygen self-diffusion studies using negative-ion secondary ion mass spectrometry (SIMS).
Solid State Ionics, **12** (1984) 89.

Kilner, J.
Isotopic exchange in mixed and ionically conducting oxides.
Proc. 2nd Int. Symp. Ionic and Mixed Conducting Oxide Ceramics, Vol. **94-12**, Eds.; Ramanarayanan, T. A., Worrell, W. L. and Tuller, H. L.
The Electrochemical Society. Pennington, NJ., (1994) 174.

Kingery, W. D. and Francois, B.
The sintering of Crystalline Oxides,
I. Interactions Between Grain Boundaries and Pores.
"Sintering and Related Phenomena", p. 471-498.
Gordon and Breach, New York, 1967.

Kingery, W. D., Bowen, H. K. and Uhlmann, D. R.
"Introduction to Ceramics" Second Edition
John Wiley & Sons, New York, 1976.

Kleveland, K., Einarsrud, M. A. and Grande, T.
Sintering behaviour, microstructure and phase composition of $Sr(Fe,Co)O_{3-\delta}$ ceramics.
J. Am. Ceram. Soc., Accepted.

Klug, H. P. and Alexander, L. E.
"X-ray diffraction procedures for polycrystalline and amorphous materials"
John Wiley & Sons, New York, 1974.

Kofstad, P.
"Nonstoichiometry, Diffusion and Electrical Conductivity in Binary Metal Oxides"
John Wiley & Sons, New York, 1972.

Kokhanovskii, L. V., Vashuk, V. V., Villkotskaya,E.F., Vitushko, S. I. and Zinkevich, M. V.
Synthesis, structure and some physiochemical properties of $SrCo_{1-x}Fe_xO_{3-\delta}$.
Inorg. Matter., **35** [3] (1999) 282.

Kruidhof, H., Bouwmeester, H. J. M., van Doorn, R. H. E. and Burggraaf, A. J.
Influence of order-disorder transitions on oxygen permeability through selected nonstoichiometric perovskite-type oxides.
Solid State Ionics, **63-65** (1993) 816.

Lane, J. A., Benson, S. J., Waller, D. and Kilner, J. A.
Oxygen transport in $La_{0.6}Sr_{0.4}Co_{0.2}Fe_{0.8}O_{3-\delta}$.
Solid State Ionics, **121** (1999) 201.

Larsen, T.
Determination of oxygen transport coefficients in strontium ferrate.
M. Sc. Thesis, Norwegian University of Science and Technology, Trondheim, Norway, (1999). In Norwegian.

Lee, T. H., Yang, Y. L. and Jacobsen, A. J.
Surface modifications of dense $SrCo_{0.8}Fe_{0.2}O_{3-\delta}$ membranes.
Ceramic Membranes I (1997) 72.

Lifshitz, I. M. and Slyozov, V. V.
The kinetics of precipitation from supersaturated solid solutions.
Phys. Chem. Solids, **19** (1961) 35.

Ma, B., Balachandran, U., Park, J. H. and Segre, C. U.
Determination of chemical diffusion coefficient of $SrFeCo_{0.5}O_x$ by the conductivity relaxation method.
Solid State Ionics, **83** (1996) 65.

Ma, B., Balachandran, U., Park, J.-H. and Segre, C. U.
Electrical Transport Properties and Defect Structure of $SrFeCo_{0.5}O_x$.
J. Electrochem. Soc., **143** [5] (1996) 1736.

MacChesney, J. B., Sherwood, R. C. and Potter, J. F.
Electric and Magnetic Properties of the Strontium Ferrates.
J. Chem. Phys., **43** [6] (1965) 1907.

Machkova, M., Brashkova, N., Ivanov, P., Carda, J. B. and Kozhukharov, V.
Surface behavior of Sr-doped lanthanide perovskites.
Applied Surface Science, **119** (1997) 127.

Maier, J.
On the correlation of macroscopic and microscopic rate constants in solid state chemistry.
Solid State Ionics, **112** (1998) 197.

Manning, P. S., Sirman, J. D. and Kilner, J. A.
Oxygen self-diffusion and surface exchange studies of oxide electrolytes having the fluorite structure.
Solid State Ionics, **93** (1997) 125.

Mazanec, T. J. and Velenyi, L. J.
Process for separating oxygen from an oxygen-containing gas by using a bi-containing mixed metal oxide membrane.
US Patent 5,160,713 (1992).

McColm, I. J. and Clark, N. J.
"High Performance Ceramics"
Blackie, Glasgow, 1988.

Messing, G. L., Zhang, S. C. and Jayanthi, G. V.
Ceramic Powder Synthesis by Spray Pyrolysis.
J. Am. Ceram. Soc., **76** [11] (1993) 2707.

Miura, N., Okamoto, Y., Tamaki, J., Morinaga, K. and Yamazoe, N.
Oxygen semipermeability of mixed-conductive oxide thick-film prepared by slip casting.
Solid State Ionics, **79** (1995) 195.

Mizusaki, J., Yoshihiro, M., Yamauchi, S. and Fueki, K.
Nonstoichiometry and Defect Structure of the Perovskite-Type Oxides $La_{1-x}Sr_xFeO_{3-\delta}$.
J. Solid State Chem., **58** (1985) 257.

Mizusaki, J., Okayasa, M., Yamauchi, S. and Fueki, K.
Nonstoichiometry and Phase Relationship of the $SrFeO_{2.5}$-$SrFeO_3$ System at High Temperature.
J. Solid State Chem., **99** (1992) 166.

Monceau, D., Petot, C. and Petot Ervas, G.
Kinetic Demixing Profile Calculation under a Temperature Gradient in Multi-component Oxides.
J. Eur. Ceram. Soc., **9** (1992) 193.

Nataraj, S., Moore, R. B. and Russek, S. L.
Production of synthesis gas by mixed conducting membranes.
European Patent Application, EP 0 926 096 A1 (1998).

Norby, T., Holt, A, Glenne, R. and Bakken, E.
The defect structure of strontium ferrate, $SrFeO_{3-\delta}$.
To be submitted to *Ionics*.

Nowotny, J. and Wagner, J. B. jr.
Influence of the Surface on the Equilibration Kinetics of Nonstoichiometric Oxides.
Oxid. Met., **15** (1981) 169.

ICDD
Collected from Powder Diffraction Files (PDF-2):
Number; 33-0677, 33-0678, 39-0954, 40-0906.
ICDD (1997) Release A6.

Pei, S., Kleefisch, M. S., Kobylinski, T. P., Faber, J., Udovich, C. A., Zhang-McCoy, V., Dabrowski, B., Balachandran, U., Mieville, R. L. and Poeppel, R. B.
Failure mechanisms of ceramic membrane reactors in partial oxidation of methane to synthesis gas.
Catalysis Letters, **30** (1995) 201.

Pongsai, B., Stølen, S. and Allan, N.
Configurationally averaged lattice energy simulation of structure and energetics of the order-disorder transformation in $Sr_2Fe_2O_5$.
To be submitted to *J. Mater. Chem.*

Porterfield, W. W.
"Inorganic Chemistry: a unified approach."
Academic Press, California, 1993.

Poulsen, F. W., Lauvstad, G. and Tunold, R.
Conductivity and Seebeck measurements on strontium ferrates.
Solid State Ionics, **72** (1994) 47.

Prasad, R.
Ceramic Membranes for Syngas Production.
Presentation at *Eurogas '99 Conference*,
Rühr-Universitat Bochum, Germany, May 1999.

Praxair Technology, Inc.
www.Praxair.com, 2000.

Prigogine, I.
"Thermodynamics of irreversible processes."
John Wiley & Sons, New York, 1967.

Qiu, L., Lee, T. H., Liu, L. M., Yang, Y. L. and Jacobson, A. J.
Oxygen permeation studies of $SrCo_{0.8}Fe_{0.2}O_{3-\delta}$.
Solid State Ionics, **76** (1995) 321.

Rahaman, M. N.
"Ceramic Processing and Sintering"
Marcel Dekker, Inc., New York, 1995.

Rao, C. N. R. and Gopalakrishnan, J.
"New Directions in Solid State Chemistry"
Cambridge University Press, Cambridge, 1997.

Rauch, W. L. and Meilin, L.
Effect of Microstructure and Dopant on the Electrochemical Properties
of Barium Cerate-Based Electrolytes.
Ceramic Membranes I (1997) 146.

Rhines, F. N., Birchenall, C. E., Hughes, L. A.
Behavior of Pores during the Sintering of Copper Compacts.
Journal of Metals, Trans. AIME, **188** (1950) 378.

Routbort, J. L., Rothman, S. J., Chen, N. and Mundy, J. N.
Site selectivity and cation diffusion in $YBa_2Cu_3O_{7-\delta}$.
Phys. Rev., **B43** (1991) 5489.

Sagdahl, L., Einarsrud, M. A. and Grande, T.
Sintering of $LaFeO_3$ Ceramics.
J. Amer. Ceram. Soc., **83** [9] (2000) 2318.

Sagdahl, L.
Sintering and swelling in $La_{0.9\pm y}Sr_{0.1}FeO_{3-\delta}$.
Presentation at ninth Norwegian meeting on "Perovskite related oxides-Oxygen permeating membranes"
Sundvolden, Norway, November, 2000.

Sakai, N., Yamaji, K., Horita, T., Negishi, H. and Yokokawa, H.
Chromium diffusion in lanthanum chromites.
In *Proceedings of the 12th International Conference on Solid State Ionics*. Halkidiki, Greece (1999) 199.

Sakai, N., Yamaji, K., Horita, T., Yokokawa, H., Kawada, T. and Dokiya, M.
Oxygen Transport Properties of $La_{1-x}Ca_xCrO_{3-\delta}$ as an Interconnect Material of a Solid Oxide Fuel Cell.
J. Electrochem. Soc., **147** [9] (2000) 3178.

Sasaki, H., Suzuki, M. and Kajimura, A.
Oxide Ionic Conductivity of Doped Lanthanum Chromites.
In Proceedings of the Second European SOFC Forum, Oslo, Norway, (1996) 513.

Schmalzried, H., Laqua, W. and Lin, P. L.
Crystalline Oxide Solid Solutions in Oxygen Potential Gradients.
Z. Naturforsch., **34A** (1979) 192.

Schmalzried, H. and Laqua, W.
Multicomponent Oxides in Oxygen Potential Gradients.
Oxidation of Metals, **15** [3/4] (1981) 339.

Schmalzried, H
"Solid state reactions"
Second Edition
Verlag Chemie. Weinheim, Germany, 1981.

Shannon, R. D.
Revised effective ionic-radii and systematic studies of interatomic distances in halides and chalcogenides.
Acta Cryst. A, **32** (1976) 751.

Shin, S., Yonemura, M. and Ikawa, H.
Order-disorder transition of $Sr_2Fe_2O_5$ from brownmillerite to perovskite structure at an elevated temperature.
Mat. Res. Bull., **13** (1978) 1017.

Skoog, D. A. and West, D. M.
"Fundamentals of analytical chemistry"
Holt-Saunders, New York, 1976.

Smyth, D. M., Chang, E. K. and Liu, D. H.
Travels through perovskite space.
Phase Transitions, **58** (1996) 57.

Steele, B. C. H., Kilner, J. A., Dennis, P. F., Mc Hale, A. E., van Hemert, M. and Burggraaf, A. J.
Oxygen surface exchange and diffusion in fast ionic conductors.
Solid State Ionics, **18-19** (1986) 1038.

Steele, B. C. H.
Oxygen ion conductors and their technological applications.
Mat. Sci. and Eng., **B13** (1992) 79.

Steele, B. C. H.
Ceramic ion conducting membranes.
Solid State & Materials Science, **1** (1996) 684.

Takeda, Y., Kanno, K., Takada, T., Yamamoto, O., Takano, M., Nakayama, N. and Bando, Y.
Phase Relation in the Oxygen Nonstoichiometric System, $SrFeO_x$ ($2.5 \leq x \leq 3.0$).
J. Solid State Chem., **63** (1986) 237.

Tanasescu, S. Totir, N. D. and Marchidan, D. I.
Thermodynamic properties of $SrFeO_{2.5}$ and $SrMnO_{2.5}$ brownmillerite-like compounds by means of EMF-measurements.
Solid State Ionics, **134** (2000) 265.

ten Elshof, J. E., Bouwmeester, H. J. M. and Verweij, H.
Oxygen transport through $La_{1-x}Sr_xFeO_{3-\delta}$. I. Permeation in air/He gradients.
Solid State Ionics, **81** (1995) 97.

ten Elshof, J. E., Bouwmeester, H. J. M. and Verweij, H.
Oxygen transport through $La_{1-x}Sr_xFeO_{3-\delta}$.
II. Permeation in air/CO, CO_2 gradients.
Solid State Ionics, **89** (1996) 81.

ten Elshof, J. E.
"Dense inorganic membranes."
PhD. Thesis, University of Twente, Enschede, The Netherlands, (1997).

ten Elshof, J. E., Lankhorst, M. H. R. and Bouwmeester, H. J. M.
Chemical diffusion and oxygen exchange of $La_{0.6}Sr_{0.4}Co_{0.6}Fe_{0.4}O_{3-\delta}$.
Solid State Ionics, **99** (1997) 15.

ten Elshof, J. E., Lankhorst, M. H. R. and Bouwmeester, H. J. M.
Oxygen Exchange and Diffusion Coefficients of Strontium-Doped Lanthanum Ferrites by Electrical Conductivity Relaxation.
J. Electrochem. Soc., **144** [3] (1997) 1060.

Teraoka, Y., Zhang, H. M., Furukawa, S., and Yamazoe, N.
Oxygen permeation through perovskite-type oxides.
Chem. Lett., (1985) 1743.

Teraoka, Y., Zhang, H. M., Okamoto, K. and Yamazoe, N.
Mixed ionic-electronic conductivity of $La_{1-x}Sr_xCo_{1-y}Fe_yO_{3-\delta}$ perovskite-type oxides.
Mat. Res. Bull., **23** (1988) 51.

Teraoka, Y., Nobunaga, T. and Yamazoe, N.
Effect of Cation Substitution on the Oxygen Semipermeability of Perovskite-type Oxides.
Chem. Lett., (1988) 503.

Tuller, H. L., Button, D. P. and Uhlmann, D. R.
Fast ion transport in oxide glasses.
J. Non-Cryst. Solids **40** (1980) 93.

Ullmann's Encyclopedia of Industrial Chemistry
Fifth Edition, Volume A17
VCH Verlagsgesellschaft, Weinheim, Germany, 1991.

van Doorn, R. H. E.
"Oxygen Separation with Mixed Conducting Perovskite Membranes."
PhD. Thesis, University of Twente, Enschede, The Netherlands, (1996).

van Doorn, R. H. E., Bouwmeester, H. J. M. and Burggraaf, A. J.
Kinetic decomposition of $La_{0.3}Sr_{0.7}CoO_{3-\delta}$ perovskite membranes during oxygen permeation.
Solid State Ionics, **111** (1998) 263.

van Hassel, B. A., Kawada, T., Sakai, N., Yokokawa, H., Dokiya, M. and Bouwmeester, H. J. M.
Oxygen permeation modelling of perovskites.
Solid State Ionics, **66** (1993) 295.

Vigeland, B., Glenne, R., Breivik, T. and Julsrud, S.
Oxygen permeability of dense mixed-conducting oxides.
Hydro Report 98P_DK9 (1998). Confidential.

Wagner, C.
Beitrag zur Theorie des Anlaufvorgangs.
Z. Phys. Chem. B, **21** (1933) 25.

Wagner, C.
Beitrag zur Theorie des Anlaufvorgangs II.
Z. Phys. Chem. B, **32** (1936) 447.

Wagner, C.
Theorie der alterung von niederschlägen durch umlösen (Ostwald-reifung).
Z. Electrochem., **65** (1961) 581.

Wagner, C.
Equations for Transport in Solid Oxides and Sulphides of Transition Metals.
Progress in Solid-State Chemistry, **10** (1975) 3.

Wang, S., Jiang, Y., Zhang, Y., Li, W., Yan, J. and Lu, Z.
Mixed conducting oxide anodes for solid oxide fuel cell.
In *Proceedings of the 12th International Conference on Solid State Ionics*. Halkidiki, Greece (1999) 152.

Whittermore, O. J. Jr. and Sipe, J. J.
Pore Growth during the Initial Stages of Sintering Ceramics.
Powder Technology, **9** (1974) 159.

Yasuda, I., Ogasawara, K. and Hishinuma, M.
Oxygen tracer diffusion in (La,Ca)$CrO_{3-\delta}$.
In *Proc. 2nd Int. Symp. on Ionic and Mixed Cond. Oxide Ceramics*, **94** [12] (1994) 164.

Yasuda, I. and Hishinuma, M.
Electrical conductivity and chemical diffusion coefficient of Sr-doped lanthanum chromites.
Solid State Ionics, **80** (1995) 141.

APPENDICES

Appendix 1 Relationship between the chemical diffusion coefficient, $\tilde{D}$, and the self-diffusion coefficient D_o

$$J_{O_2} = -\frac{D_o c_o}{4RT}\frac{\partial \mu_{o_2}}{\partial x} \qquad [A1.1]$$

$$J_{O_2} = -\frac{1}{2}\tilde{D}\frac{\partial c_o}{\partial x} \qquad [A1.2]$$

Combining the Wagner equation [A1.1] and Fick's first law [A1.2] gives:

$$\tilde{D} = \frac{1}{2}\frac{c_o D_o}{RT}\frac{\partial \mu_{o_2}}{\partial c_o} \qquad [A1.3]$$

$$\tilde{D} = \frac{1}{2}\frac{c_o D_o}{RT}\frac{1}{c_o}\frac{\partial c_o}{\partial \ln c_o}\frac{\partial \mu_{o_2}}{\partial c_o} = \frac{1}{2}\frac{D_o}{RT}\frac{\partial \mu_{o_2}}{\partial \ln c_o} \qquad [A1.4]$$

By introducing $\partial \mu_{o_2} = \partial RT \ln P_{o_2}$:

$$\tilde{D} = D_o\left(\frac{1}{2}\frac{\partial \ln P_{O_2}}{\partial \ln c_o}\right) \qquad [A1.5]$$

The expression in the brackets is named the *thermodynamic enhancement factor*, γ_o (Bouwmeester & Burggraaf, 1997). It is important to point out that γ_o is different from the *thermodynamic activity coefficient*, γ_o^*. By introducing $\partial \mu_{o_2} = \partial RT \ln a_{o_2}$ and $a_o = \gamma_o^* \cdot c_o$ in the equation [A1.4] we get the expression (Schmalzried, 1981; Atkins, 1986):

$$\tilde{D} = D_o\left(1 + \frac{\partial \ln \gamma_o^*}{\partial \ln c_o}\right) \qquad [A1.6]$$

Appendix 2 Chemicals used in the present study

Chemical	Manufacturer	Purity
$Sr(NO_3)_2$	Merck, 1.07872	p.a., > 99 %
$Fe(NO_3)_3$	Fluka, 44949	p.a., > 99 %
$Cr(NO_3)_3$	Merck, 1.02481	p.a., > 98 %
$Co(NO_3)_2$	Fluka, 60833	p.a., > 99 %
$SrCO_3$	Strem Chemicals	p.a., >99.9 %
Fe	Merck, 1.03819	p.a., > 99.5 %
Cr	Fluka, 27060	> 99 %
Co	Merck, 1.12211	p.a., > 99 %
Citric acid	Merck, 1.00244	p.a., > 99.5 %
EDTA	Merck, 1.08417	p.a., > 99.4 %
Na-hexametaphosphate	Fluka, 71600	purum, 65-70% P_2O_5
Paraffin wax	Fluka, 76228	purum
MMA/BMA copolymer	Rohm and Haas, B-66	p.a., 100 %
EMA copolymer	Rohm and Haas, B-72	p.a., 100 %
n-hexane	Merck, 1.04367	p.a., > 99 %
Diamond paste	Struers, DP-suspension	
HNO_3	Hydro Chemicals	technical, > 65 % [28]
Isopropanol	Fluka, 59309	> 99.5 %
Isooctane	Merck, 1.04718	p.a., > 99.8 %
O_2	Hydro Gas	> 99.999 %
Pressurised air	Hydro Gas	> 99.999 %
N_2	Hydro Gas	> 99.999 %
5 % H_2 in N_2	Hydro Gas	> 99.999 % [29]

[28] Residue on ignition, 0.0005 %

[29] Purity of the mixed gases

Appendix 3 Explanation of the instrument codes

The instrument codes given below are used in Figures 2.8 and 3.2.

FI:	Flow Indicator (Rotameter)
FIC:	Flow Indicator Controller (Mass flow controller)
TI:	Temperature Indicator
TIC:	Temperature Indicator Controller
TIZ:	Temperature Indicator for shutdown
PI:	Pressure Indicator

Appendix 4 Weight loss of $SrFeO_{3-\delta}$ while heating

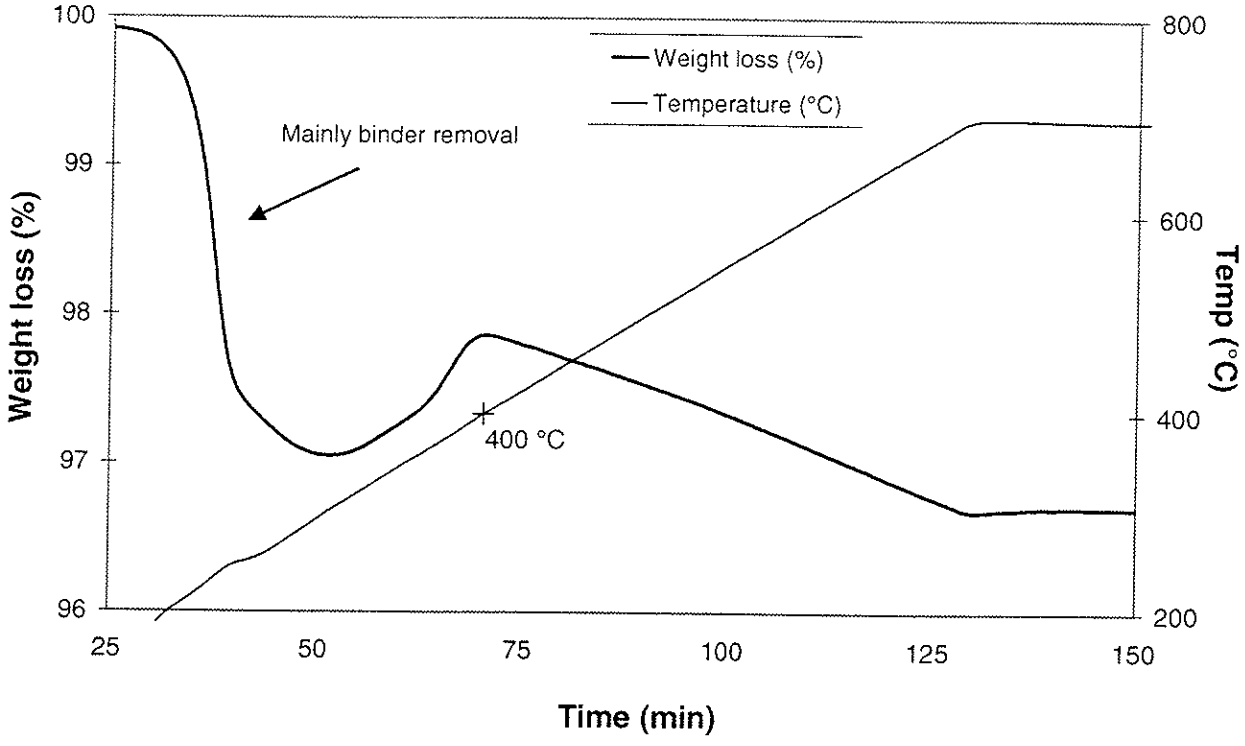

Figure A4.1 Weight loss of $SrFeO_{3-\delta}$ while heating in flowing air (TGA). Heating rate: 5 °C/min.

Appendix 5 Calculation of the maximum pore pressure in the $SrFeO_{3-\delta}$ material.

The calculation is based on results of oxygen loss as a function of temperature for $SrFeO_{3-\delta}$. The TGA measurements are performed in air at a heating rate of 5 °C/min from 950-1000 °C for a sample of 363.5 mg. The data are given in Table A5.1. The sample was in thermodynamic equilibrium with the surrounding atmosphere during the experiment. The data are used to estimate an oxygen flux in each element of the membrane.

A membrane plate of a finite thickness of 0.375 cm and infinite extension is assumed. The plate is divided into 11 elements.

The pressure, P_x is calculated from the permeation equation:

$$J_{O_2} = \frac{k}{L} \ln(\frac{P_x}{P_1}) \qquad [A5.1]$$

where k is a constant which is calculated from the oxygen permeation measurement of $SrFeO_{3-\delta}$ (Chapter 3.4.2) and extrapolated to the relevant temperature where the swelling phenomenon is observed. The values of k are given in Figure A5.1. The constant L is the membrane thickness.

The oxygen flux in each element is equal to the oxygen loss within the element added to the flux from all the preceding elements. The pressure in each element is calculated from equation [A5.1] where P_1 is the pressure in the preceding element. The results at relevant conditions of temperature, sample geometry and heating rates are given in Figures A5.2 and A5.3.

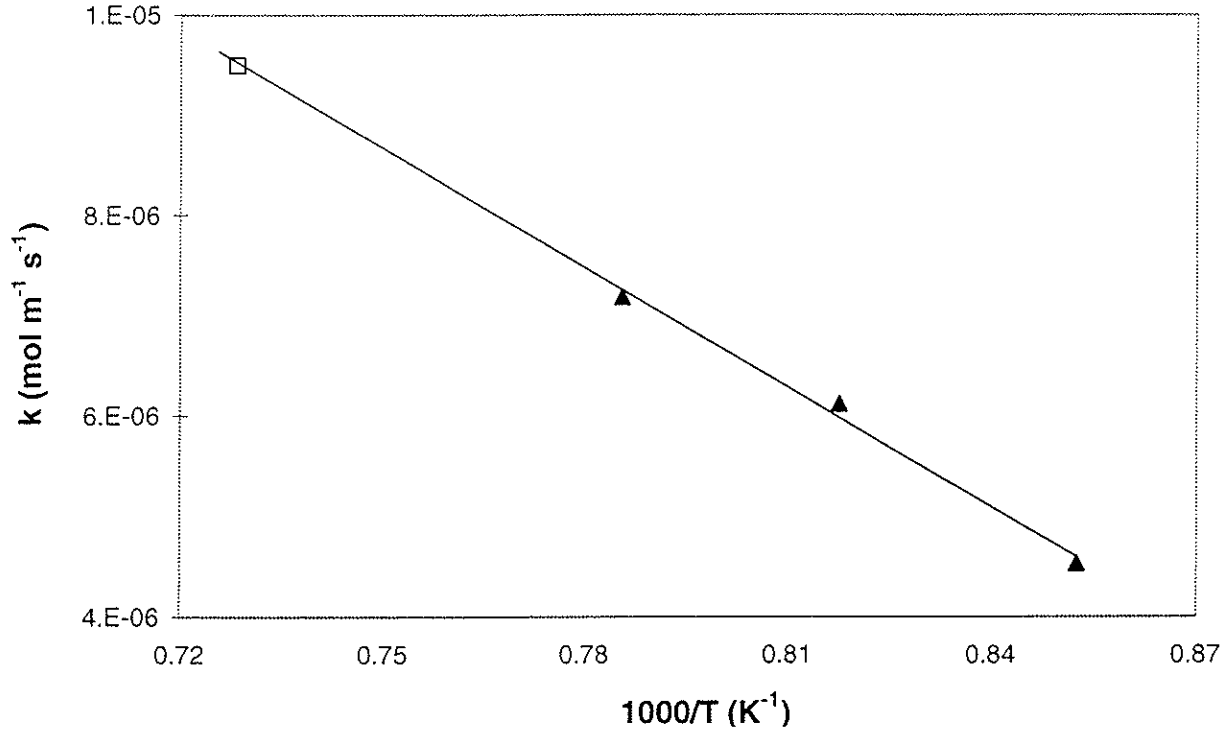

Figure A5.1 The constant k, given in equation [A5.1], as a function of inverse temperature.

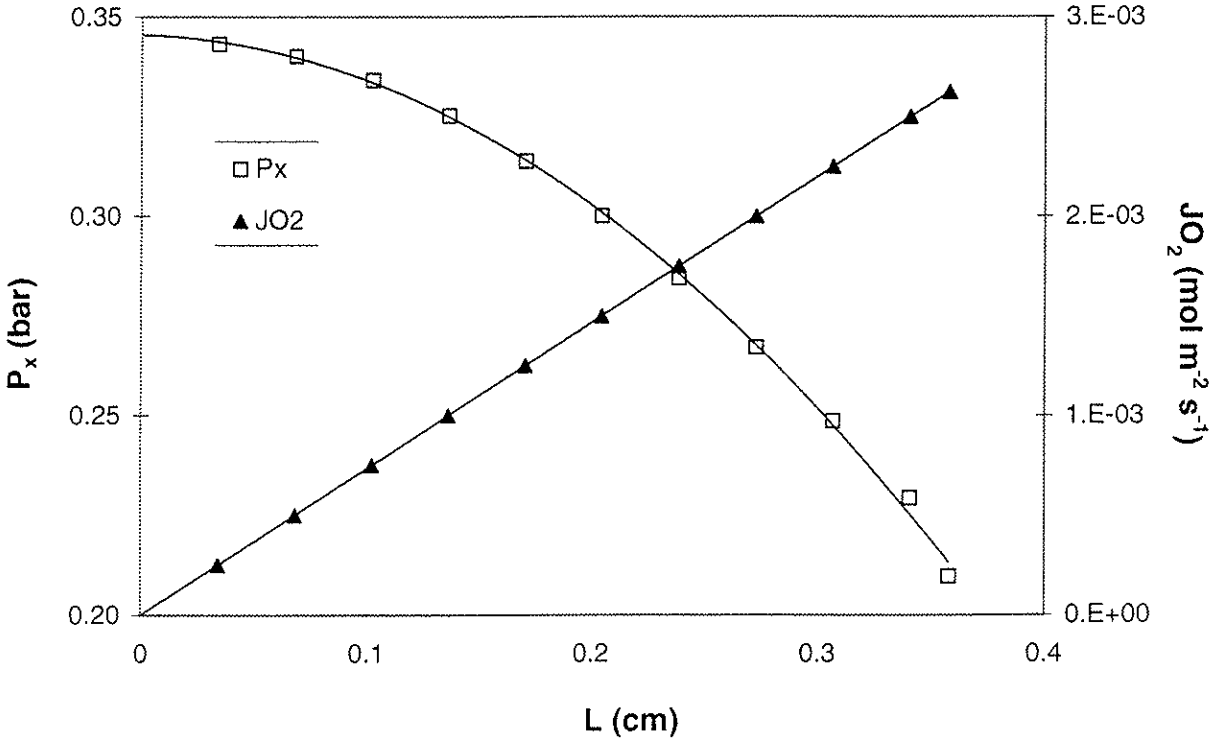

Figure A5.2 The calculated oxygen pressure and permeation across a 0.375 cm $SrFeO_{3-\delta}$ membrane plate with infinite extension during heating at a rate of 10 °C/min.

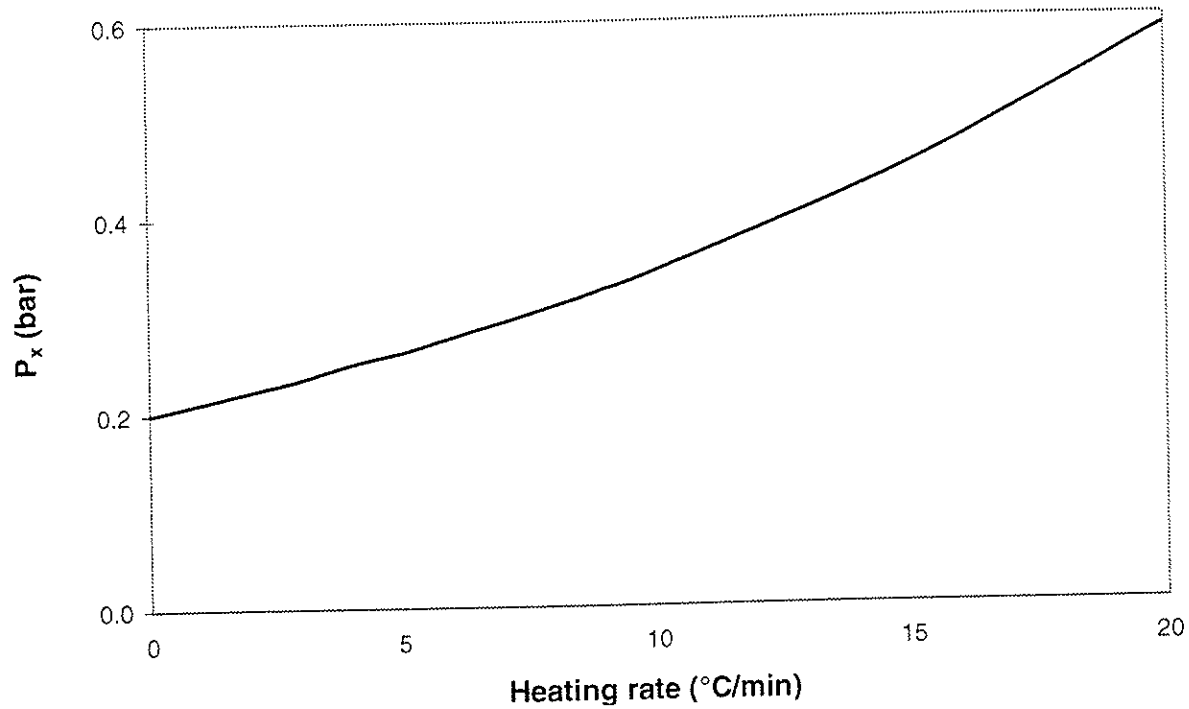

Figure A5.3 The calculated pressure as a function of the heating rate for an empty volume separated from the surrounding atmosphere by a 0.375 cm $SrFeO_{3-\delta}$ membrane plate with infinite extension.

Table A5.1 TGA results from dynamic weight loss of $SrFeO_{3-\delta}$ at 950-1000 °C, during heating at 5 °C/min.

Data	Values	Units
time	5	min
w_{tot}	363.5	mg
D_x	5.46	g/cm^3
Δw	0.47	mg
M_w (O_2)	32	g/mol
V	0.06658	cm^3
N_{loss}	1.5E-05	mol O_2
J_{loss}	7.4E-07	mol/cm^3 s

Appendix 6 Sintering behaviour of $SrFe_{0.67}Co_{0.33}O_{3-\delta}$ powder with different particle size distribution.

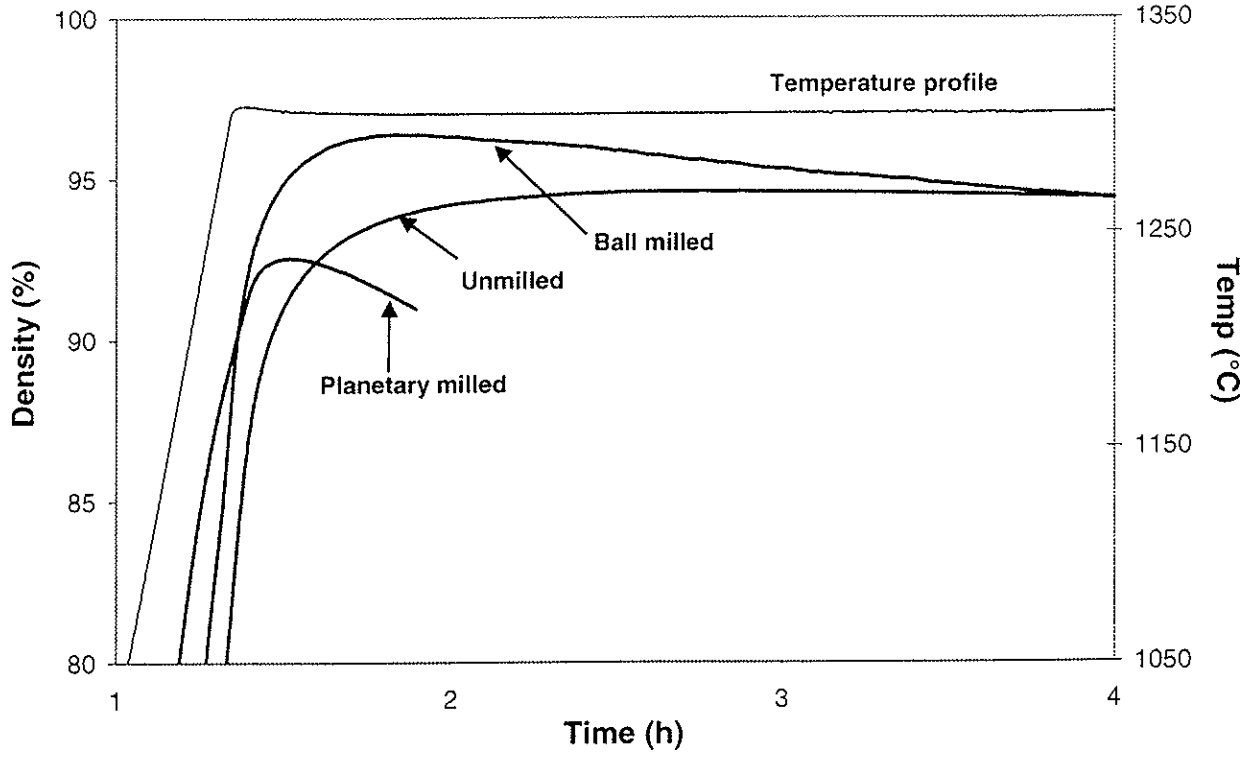

Figure A6.1 Sintering behaviour of $SrFe_{0.67}Co_{0.33}O_{3-\delta}$ powder with different morphology.

Appendix 7 Result of the linear chemical expansion measurement of $SrFeO_{3-\delta}$

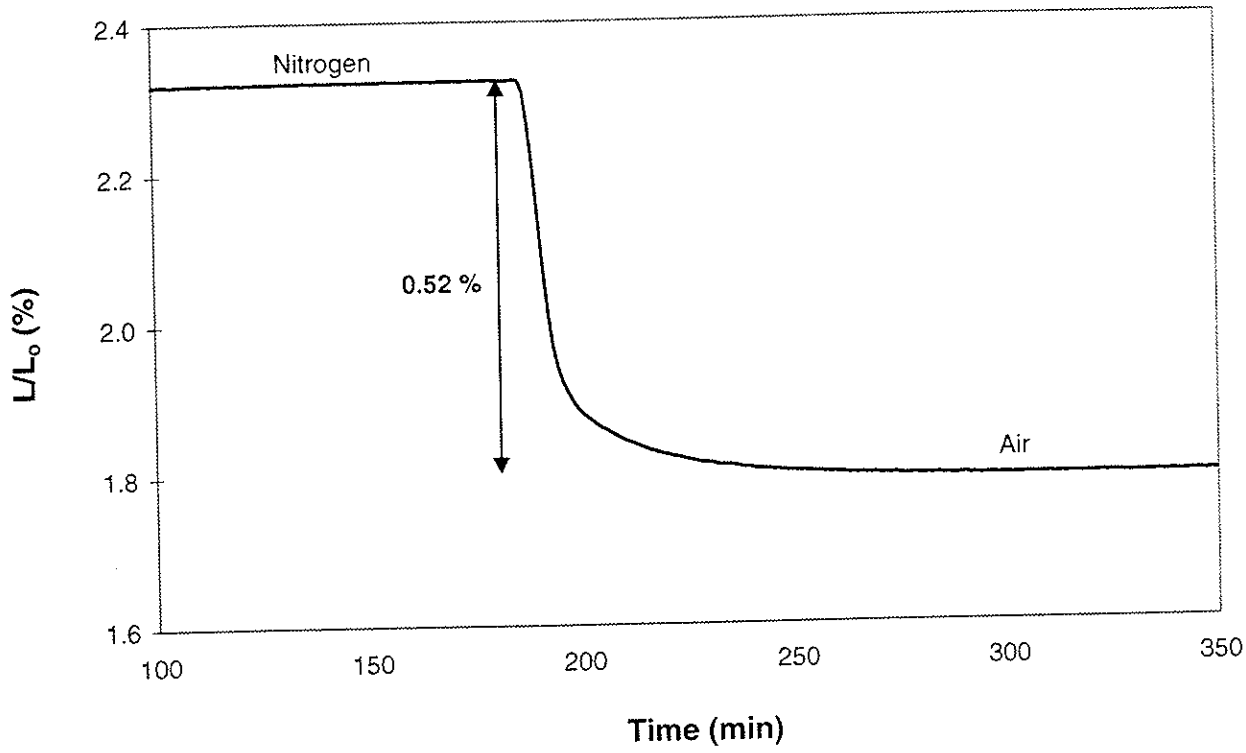

Figure A7.1 Chemical expansion of $SrFeO_{3-\delta}$ membrane at 900 °C and $\Delta \log P_{O_2} \approx 3.3$.

Appendix 8 The phase relations of $SrFeO_{3-\delta}$ as a function of oxygen stoichiometry and temperature

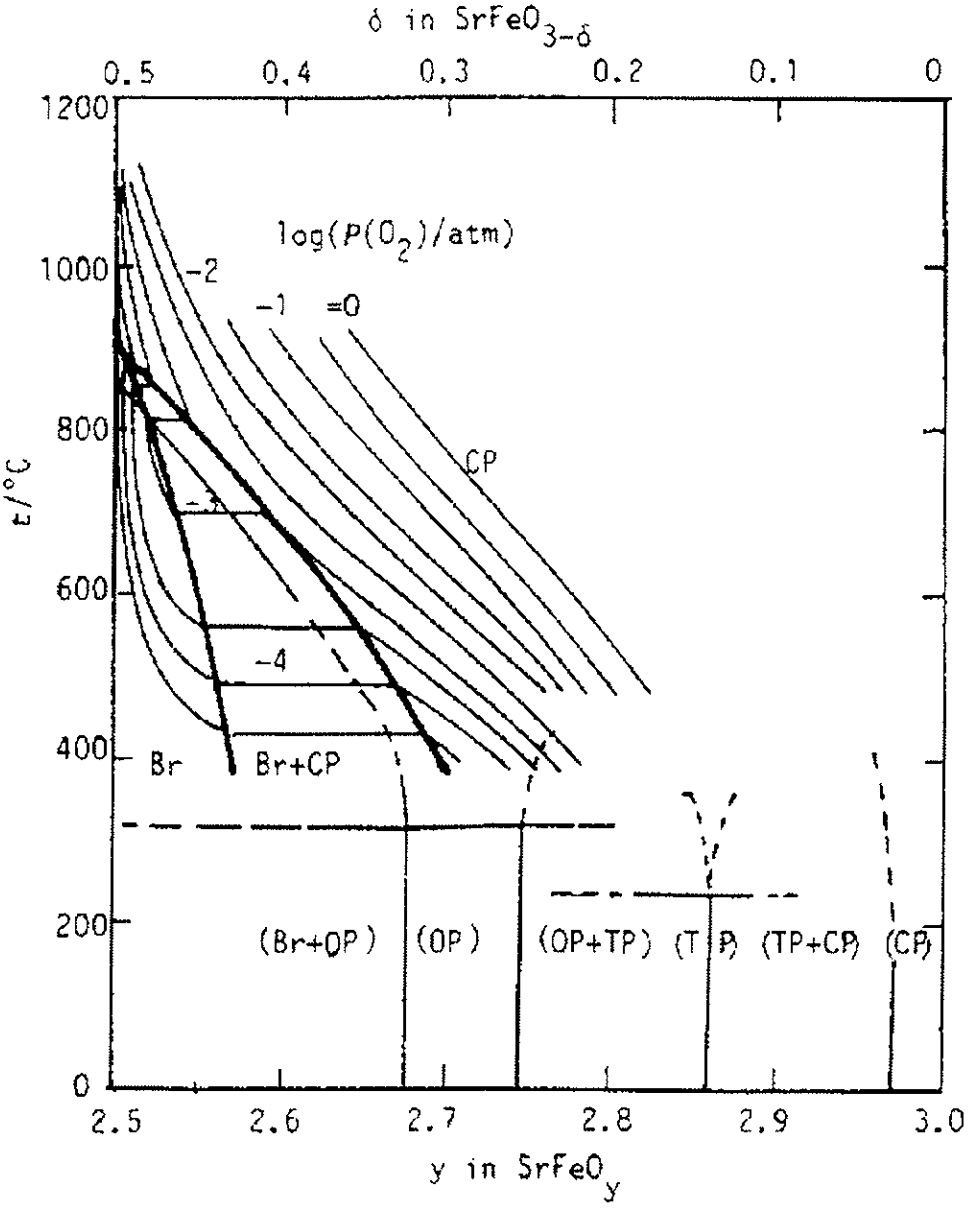

Figure A8.1 The phase diagram of $SrFeO_{3-\delta}$, representing the phase relations as a function of oxygen content and temperature. (Takeda et al., 1986; Mizusaki et al., 1992).

Appendix 9

Properties of $SrFe_{0.97}Cr_{0.03}O_{3-\delta}$ membranes used in the oxygen permeation experiments. Crystallographic density is calculated to be $D_x = 5.34$ g/cm^3.

Sample code	Green density (g/cm^3)	Sintering conditions	Membrane density (g/cm^3)	Total porosity (%)	Membrane thickness (mm)
SF-39-2	3.17	1175 °C/3h	5.26	1.5	1.43
SF-39-3	3.16	1175 °C/3h	5.27	1.3	1.42
SF-39-4	3.17	1175 °C/3h	5.27	1.3	1.44
SF-39-6	3.11	1200 °C/3h	5.28	1.1	1.48
SF-39-7	3.14	1200 °C/3h	5.26	1.5	1.49
SF-39-8	3.13	1275 °C/3h	5.23	2.1	1.43
SF-39-10	3.21	1275 °C/3h	5.24	1.9	1.44
SF-41-4	3.28	1175 °C/3h	5.26	1.5	0.91
SF-41-5	3.23	1175 °C/3h	5.27	1.3	1.70
SF-41-6	3.21	1175 °C/3h	-		1.47
SF-41-7	3.25	1175 °C/3h	5.26	1.5	1.48
SF-41-9	3.26	1175 °C/3h	5.28	1.1	2.14
SF-41-10	3.15	1175 °C/3h	5.30	0.7	1.32
SF-41-14	3.26	1175 °C/3h	5.29	0.9	1.77
SF-42-3	3.28	1175 °C/3h	5.26	1.5	1.41
SF-42-4	3.27	1175 °C/3h	5.25	1.7	1.39
SF-42-5	3.29	1200 °C/3h	5.25	1.7	1.38
SF-42-8	3.23	1275 °C/3h	5.27	1.3	1.47
SF-42-10	3.28	1275 °C/3h	5.24	1.9	1.36
SF-42-11	3.21	1200 °C/3h	5.20	2.6	1.43
SF-42-12	3.22	1200 °C/3h	5.23	2.1	1.41
SF-42-13	3.16	1200 °C/3h	5.21	2.4	1.35
SF-42-14	3.23	1175 °C/3h	5.23	2.1	2.38
SF-42-15	3.21	1175 °C/3h	5.24	1.9	1.86
SF-42-16	3.18	1175 °C/3h	5.23	2.1	0.92
SF-40-11*	3.19	1270 °C/6h	5.14	5.9	1.43

Code	SF-39-2	SF-39-3	SF-39-4	SF-39-6	SF-39-7	SF-39-8	SF-39-10
grain boundary length (μm/μm^2)	0.290	0.289	0.281	0.263	0.270	0.177	0.165

* $SrFeO_{3-\delta}$. $D_x = 5.46$ g/cm^3

Appendix 10 Estimation of the surface exchange limitation for $SrFe_{0.97}Cr_{0.03}O_{3-\delta}$ membranes.

The oxygen permeation should depend on membrane thickness (L) as described by the expression:

$$1/J_{O_2} = (L_s + L)/j_b \qquad [A10.1]$$

where the apparent additional bulk thickness L_s is proportional to the degree of surface control. The permeation rate of a bulk controlled process is defined as j_b for a membrane with unit thickness. The two parameters L_s and j_b are obtained by fitting the experimental permeation data for different membrane thicknesses to equation [A10.1].

Oxygen permeation data were selected from membranes with the same thermal history. These data are given as Arrhenius plots in Figure A10.1, with second degree polynomials fitted to the data. Parameters of these are given in Table A10.1.

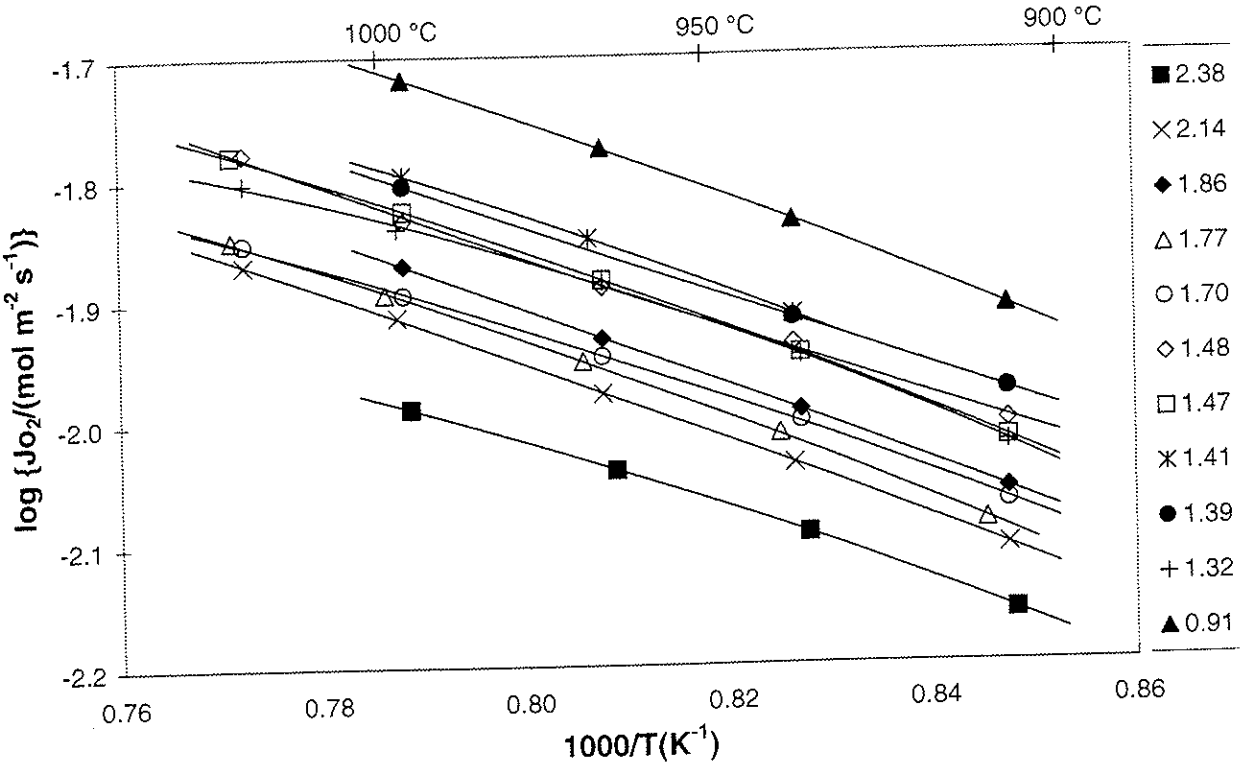

Figure A10.1 Arrhenius plots of oxygen permeation of $SrFe_{0.97}Cr_{0.03}O_{3-\delta}$. The legend gives the membrane thickness.

Table A10.1 Parameters for the polynomial fits to oxygen permeability data versus inverse temperature of $SrFe_{0.97}Cr_{0.03}O_{3-\delta}$ membranes with thickness L.

$$\log \{Jo_2/(\text{mol m}^{-2}\,\text{s}^{-1})\} = a + b\cdot T^{-1} + c\cdot T^{-2}$$

L (mm)	a	$b\cdot 10^3$	$c\cdot 10^6$
2.38	-5.593	11.473	-8.7515
2.14	-1.3422	1.5528	-2.8941
1.86	-0.9036	0.5658	-2.2754
1.77	-3.553	7.087	-6.3268
1.70	-3.7439	7.2676	-6.2416
1.48	2.2983	-7.4379	2.7913
1.47	-3.7727	7.7611	-6.7128
1.41	-5.9163	13.1211	-10.0165
1.39	0.6693	-3.3711	0.2931
1.32	-8.0235	18.0042	-12.8858
0.91	-3.1821	6.5632	-5.9708

The polynomials are used to calculate oxygen permeation at selected temperatures in the range 1173 - 1273 K. These results are shown in Figure A10.2 as a function of thickness. Linear fits yield the parameters L_s and j_b. Parameters of the linear fits are displayed in Table A10.2 and A10.3 and give the parameters L_s and j_b in the investigated temperature range.

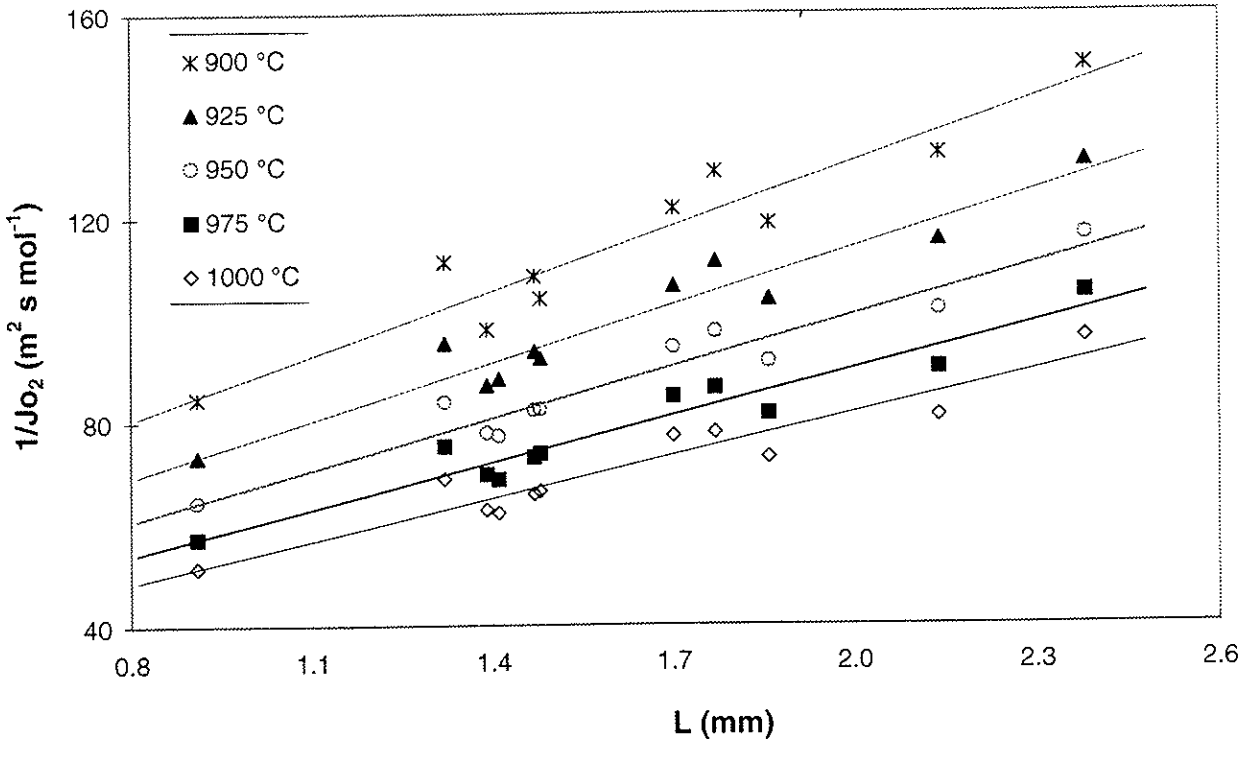

Figure A10.2 Inverse oxygen permeation as a function of membrane thickness for $SrFe_{0.97}Cr_{0.03}O_{3-\delta}$.

Table A10.2 Parameters for the linear fits to inverse oxygen permeability data versus thickness of $SrFe_{0.97}Cr_{0.03}O_{3-\delta}$ membranes. The membrane thickness is given in mm.

$$1/J_{O_2} = a + b \cdot L, \quad L_s = \frac{a}{b}, \quad j_b = \frac{1}{b}$$

Temperature (K)	a	b
1173	46.875	41.929
1198	39.182	37.388
1223	33.884	33.434
1248	29.719	30.218
1273	26.391	27.584

Table A10.3 Parameters for the linear fits (L_s and j_b) to inverse oxygen permeation of $SrFe_{0.97}Cr_{0.03}O_{3-\delta}$ versus membrane thickness.

$$1/J_{O_2} = (L_s + L)/j_b$$

Temperature (K)	L_s (mm)	j_b (mol m^{-2} s^{-1})
1173	1.12	0.024
1198	1.05	0.027
1223	1.01	0.030
1248	0.98	0.033
1273	0.96	0.036

Appendix 11 Cation diffusion in perovskites

Introduction

The cation diffusion is of major importance in understanding both the sintering process and the kinetic demixing and decomposition. Measurement of cation diffusion is generally carried out by chemical inter-diffusion of a pair of ions or by isotopic tracer diffusion (Atkinson, 1994; Kilner, 1994).

Cation inter-diffusion occurs when two ions migrate in opposite directions in a sub-lattice. Occurrence of cation migration (charge and mass transport) requires a different species to diffuse in the opposite direction to avoid long-range charge separation. Diffusion of the two species will be coupled so that the transport of the slower species is increased and that of the faster species is retarded. The diffusion coefficient is therefore a material parameter which characterises the rate of the inter-diffusion process for particular species in a particular phase. A description of the chemical diffusion coefficient is given in Chapter 1.2.

Experimental

The chemical inter-diffusion coefficients of cations ($\tilde{D}$) were determined using a profile fitting technique. Two dense polished membranes which differ in one or two of their constituent cations, were pressed together with a specific pressure of approximately 50 g/cm^2. The pressure was exerted by the alumina weight placed on top of the membrane pairs, with platinum foils in between to avoid chemical reactions. The sample pairs were then annealed at elevated temperature (900-1000 °C) for a period of 600-800 hours in stagnant air. After a high temperature treatment, some of the sample pairs had fused together to form a single pellet. The membrane pairs were cut transversely into two pieces, and the cross section was polished with diamond pastes to a roughness of one micron. The inter-diffusion of cations were determined across the interfacial surface, using X-ray fluorescence analysis (EDS). Profiles were recorded in the range of 150 μm in each direction from the interface between the two sample compositions. The line-scan was performed with a step size of 6 μm and a counting time of 60 seconds at each position. The diffusion coefficient was obtained by fitting the profile of the diffusing ion using a solution to Fick´s second law which was appropriate to the boundary conditions of the experiment. A solution for a semi-infinite source

of initial concentration c_0, in contact with semi-infinite volume of zero initial concentration is (Crank, 1975):

$$c(x,t) = \frac{c_0}{2}\mathrm{erfc}\left[\frac{x}{2\sqrt{\tilde{D}t}}\right] \qquad [A11.1]$$

where erfc is the complementary error function, erfc z = 1-erf z = $\frac{2}{\sqrt{\pi}}\int_{x}^{\infty} e^{-t^2}dt$

Results and discussion

Limited inter-diffusion experiments are performed in this study. Annealing was only carried out at two different temperatures. In some of the diffusion-couples, poor contact was observed after the heat treatment. The limited data are preliminary and subject to high uncertainty. Several experiments, specially at higher temperatures, are needed to determine the cation inter-diffusion coefficients and their activation energies in La-Sr-Fe-Co-O perovskites.

B-cation diffusion

The chemical inter-diffusion coefficient of iron ions in $SrCoO_{3-\delta}$ is estimated to be 10^{-11} cm^2/s at 950 °C.

Depth profile analysis of tracer chromium in $La_{0.95}Sr_{0.05}CrO_3$ indicated a significant contribution of grain boundary diffusion to the overall chromium diffusion (Sakai et al., 1999). The tracer coefficients were estimated to be 10^{-17} and 10^{-11} cm^2/s at 950 °C for the bulk and grain boundary diffusion, respectively. Routbort et al. (1991) report the tracer diffusion of cobalt in the perovskite phase $YBa_2Cu_3O_{7-\delta}$ to be 10^{-11} cm^2/s at 950 °C.

The tracer diffusion coefficient of iron and cobalt in MgO are extrapolated to 10^{-12} and 10^{-13} cm^2/s, respectively (Kingery et al., 1976).

A-cation diffusion

It was not possible to detect La-Sr inter-diffusion lengths in either $SrCoO_{3-\delta}/LaCoO_{3-\delta}$ or $SrFeO_{3-\delta}/LaFeO_{3-\delta}$ couples, by EDS analysis for samples annealed at 950 °C for 845 hours.

Horita et al. (1999) measured calcium tracer diffusion in $(La,Ca)CrO_3$ to be approximately 10^{-15} cm^2/s at 1000 °C for bulk diffusion and five to six orders of magnitude larger for grain boundary transport. The measured inter-diffusion of Sr-Ca ions in $(La,Ca)CrO_3$ was similar to the tracer bulk diffusion coefficient (Horita et al., 1998).

The investigated $(La,M)CrO_3$ (M = Ca, Sr) materials contained a liquid phase at the grain boundaries (Horita et al., 1998/1999; Sakai et al., 1999). The liquid phase enhances the sintering properties, but will alter the grain boundary diffusion coefficient. The reported diffusion coefficients are thus subject to uncertainty with regard to cation diffusion in the perovskite structure.

To summarise, the present experiments indicate that the inter-diffusion of iron and cobalt ions are faster than inter-diffusion of strontium and lanthanum ions at the investigated temperatures. Literature data on $(La,Ca)CrO_3$ shows the opposite results of higher tracer diffusion coefficients of A-cation than B-cation (Horita et al., 1998/1999; Sakai et al., 1999).

Appendix 12 The molar volume as a function of oxygen vacancy concentration for $SrFeO_{3-\delta}$

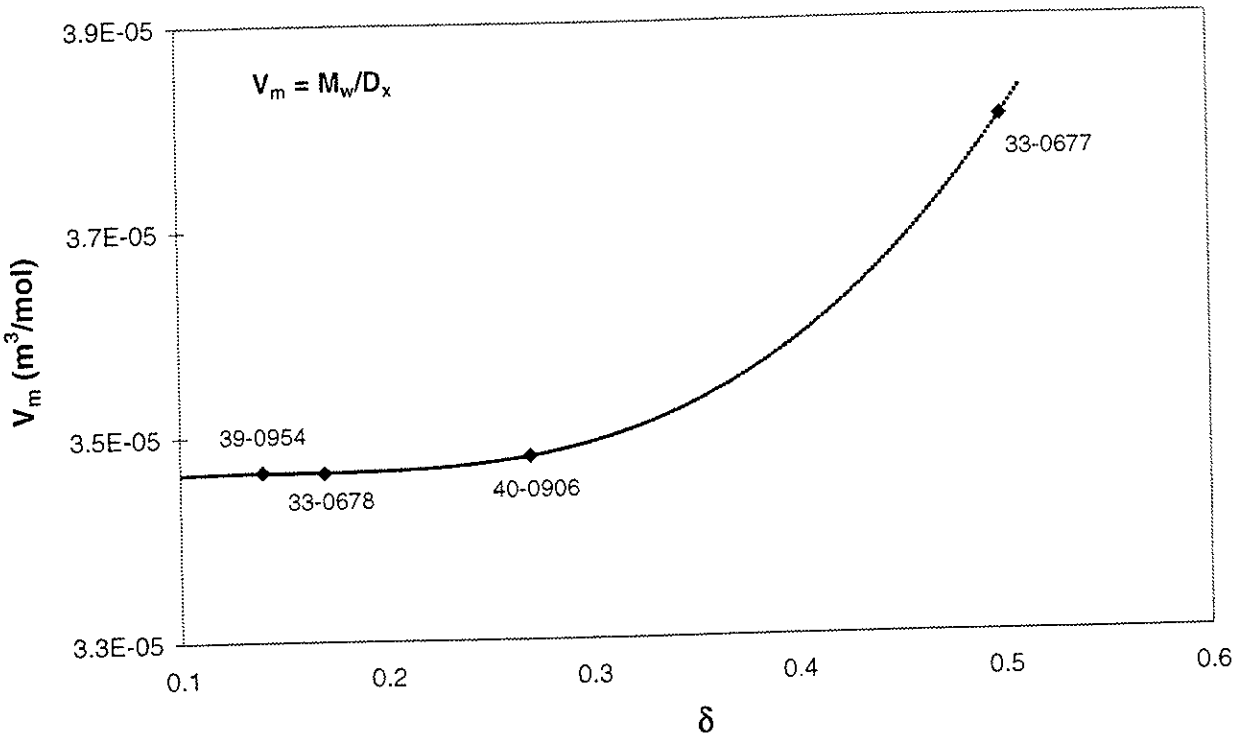

Figure A12.1 Molar volume as a function of oxygen vacancy concentration of $SrFeO_{3-\delta}$. The numbers next to the data points are the numbers from PDF-2 Database (Shin et al., 1978; Takeda et al., 1986; ICDD, 1997).

Appendix 13 Estimation of the oxygen vacancy coefficient as a function of P_{O_2} for $SrFe_{0.97}Cr_{0.03}O_{3-\delta}$

The experimental data for oxygen permeation versus driving force have been used to estimate the D_v as a function of P_{O_2}. A linear fit of D_v to the P_{O_2} is assumed, this means the regression parameter, d in equation [A13.3] is set to zero. The fitting constants in equation [A13.2] are obtained from the modelling of oxygen stoichiometry, described in Chapter 4.1. Apparent membrane thicknesses are used to describe the bulk permeation, as discussed in Chapter 3.4.4. The constants given in Table A13.1 are obtained by solving the Wagner equation, [A13.1] for the relevant conditions.

$$J_{O_2} = -\frac{1}{4LV_m}\int_{\ln P''_{O_2}}^{\ln P'_{O_2}} D_v \cdot \delta \, d\ln P_{O_2} \qquad [A13.1]$$

$$3-\delta = a(\ln P_{O_2})^2 + b(\ln P_{O_2}) + c \qquad [A13.2]$$

$$D_v = d(3-\delta)^2 + e(3-\delta) + f \qquad [A13.3]$$

$$a*(\ln P_{O_2})^6 - b*(\ln P_{O_2})^5 - c*(\ln P_{O_2})^4 -$$

$$d*(\ln P_{O_2})^3 - e*(\ln P_{O_2})^2 + f*(\ln P_{O_2}) + g* \qquad [A13.4]$$

Table A13.1 Fitting parameters in the estimation of D_v as a function of oxygen partial pressure.

T (K)	1295	1270	1239	1210	1181
L (mm)	3.08	3.10	3.13	3.17	3.26
a	0.00075	0.00079	0.00083	0.00086	0.00091
b	0.01823	0.0189	0.01975	0.02061	0.02163
c	2.59576	2.60299	2.61259	2.62233	2.63299
d	0	0	0	0	0
e	$1.50 \cdot 10^{-8}$	$1.40 \cdot 10^{-8}$	$1.30 \cdot 10^{-8}$	$1.34 \cdot 10^{-8}$	$1.57 \cdot 10^{-8}$
f	$-3.53 \cdot 10^{-8}$	$-3.31 \cdot 10^{-8}$	$-3.10 \cdot 10^{-8}$	$-3.24 \cdot 10^{-8}$	$-3.86 \cdot 10^{-8}$
a*	0	0	0	0	0
b*	0	0	0	0	0
c*	$8.438 \cdot 10^{-15}$	$8.737 \cdot 10^{-15}$	$8.956 \cdot 10^{-15}$	$9.911 \cdot 10^{-15}$	$1.300 \cdot 10^{-14}$
d*	$4.102 \cdot 10^{-13}$	$4.181 \cdot 10^{-13}$	$4.262 \cdot 10^{-13}$	$4.750 \cdot 10^{-13}$	$6.181 \cdot 10^{-13}$
e*	$3.165 \cdot 10^{-12}$	$3.248 \cdot 10^{-12}$	$3.374 \cdot 10^{-12}$	$3.728 \cdot 10^{-12}$	$4.574 \cdot 10^{-12}$
f*	$4.425 \cdot 10^{-11}$	$4.194 \cdot 10^{-11}$	$4.038 \cdot 10^{-11}$	$4.706 \cdot 10^{-11}$	$6.588 \cdot 10^{-11}$
g*	$1.470 \cdot 10^{-09}$	$1.326 \cdot 10^{-09}$	$1.159 \cdot 10^{-09}$	$1.049 \cdot 10^{-09}$	$9.970 \cdot 10^{-10}$

Appendix 14 Modelling of the oxygen exchange flux of $SrFe_{0.97}Cr_{0.03}O_{3-\delta}$ as a function of temperature and oxygen partial pressure.

From the experimental values of oxygen permeability versus driving force and the model for oxygen stoichiometry[30], numerical expressions for the Wagner equation [A14.3] and the oxygen surface exchange flux equations [A14.1] and [A14.2] are solved. An expression of D_v versus P_{O_2} is obtained by modelling the permeation data versus driving force using the L_s to express the bulk permeation (see Appendices 10 and 13). The three following equations are solved with molecular oxygen chemical potentials related to the illustration given in Figure 1.6.

$$J_{O_2} = J^{ex}_{O_2(I)}(1 - \exp(\tfrac{\mu_A - \mu_1}{RT})) \qquad [A14.1]$$

$$J_{O_2} = J^{ex}_{O_2(II)}(1 - \exp(\tfrac{\mu_2 - \mu_B}{RT})) \qquad [A14.2]$$

$$J_{O_2} = -\tfrac{1}{4LRT}\int_{\mu_A}^{\mu_B} D_v \cdot c_v d\mu \qquad [A14.3]$$

An expression for the vacancy concentration (c_v) as a function of oxygen partial pressure is given in Chapter 4.1, and an estimation of the vacancy diffusion coefficient, D_v, is given in Appendix 13. The $J^{ex}_{O_2(I)}$ and $J^{ex}_{O_2(II)}$ are the two exchange rates on the two surfaces of the membrane. In the permeation experiment where μ_1 is constant and μ_2 is varied, $J^{ex}_{O_2(I)}$ is a real constant at constant temperature. In the permeation experiment where μ_2 is constant and μ_1 is varied, $J^{ex}_{O_2(II)}$ is approximately constant at constant temperature. (A small variation in μ_2 occurs due to the μ_1 dependent oxygen permeation. An estimation has shown that this can be neglected.)

---

[30] The modelled oxygen vacancy concentration is calculated for the composition $SrFeO_{3-\delta}$.

A numerical solution of $J_{O_2}^{ex}$ as a function of oxygen partial pressure is found by initially estimating a value for $J_{O_2(I)}^{ex}$ (using the data where μ_1 is constant and μ_2 is varied) and adjusting μ_A by means of equation [A14.1]. By fitting equation [A14.3], μ_B is derived and then equation [A14.2] gives $J_{O_2(II)}^{ex}$ as a function of μ_2. Iterations are done until the error parameter (deviation between the measured and calculated permeation) approaches zero. The same procedure is then carried out with the other data set. Values of $J_{O_2(I)}^{ex}$ and $J_{O_2(II)}^{ex}$ are set until agreement is obtained between the two data sets.

Appendix 15 Calculation of the chemical potential of oxygen as a function of position in the bulk of $SrFe_{0.97}Cr_{0.03}O_{3-\delta}$ membranes

The chemical potential of oxygen through the membrane bulk with thickness L is divided into 20 step,

$$\Delta\mu = \frac{\mu_B - \mu_A}{20}$$

and $\mu_n = n\Delta\mu$ where $n = [1.....20]$

$x_A \ldots x_n \ldots x_B$

$\mu_A \ldots \mu_n \ldots \mu_B$

The positions $x_A = 0$ and $x_B = L$, and x_n are calculated. The total driving force is $\Delta\mu_{AB} = \mu_B - \mu_A$. The ratio of surface exchange limitation on the two surfaces of the membrane are taken from the modelling of $J_{O_2}^{ex}$ (Chapter 4.2).

Based on theWagner equation, the position x_n can be calculated:

$$J_{O_2} = -\frac{1}{4}\frac{D_v \delta}{V_m RT}\frac{d\mu_{O_2}}{dx} \qquad [A15.1]$$

$$J_{O_2}\int_{x_A}^{x_n} dx = -\frac{1}{4V_m RT}\int_{\mu_A}^{\mu_n} \delta D_v \, d\mu_{O_2} \qquad [A15.2]$$

$$x_n = -\frac{1}{4V_m RT J_{O_2}}\int_{\mu_A}^{\mu_n} \delta D_v \, d\mu_{O_2} \qquad [A15.3]$$

The input parameter $\Delta\mu_{AB}$ is changed until the calculated x_B is in agreement with the membrane thickness L for the corresponding oxygen permeability and temperature.

Appendix 16 The phase diagram of $SrO\text{-}Fe_2O_3$

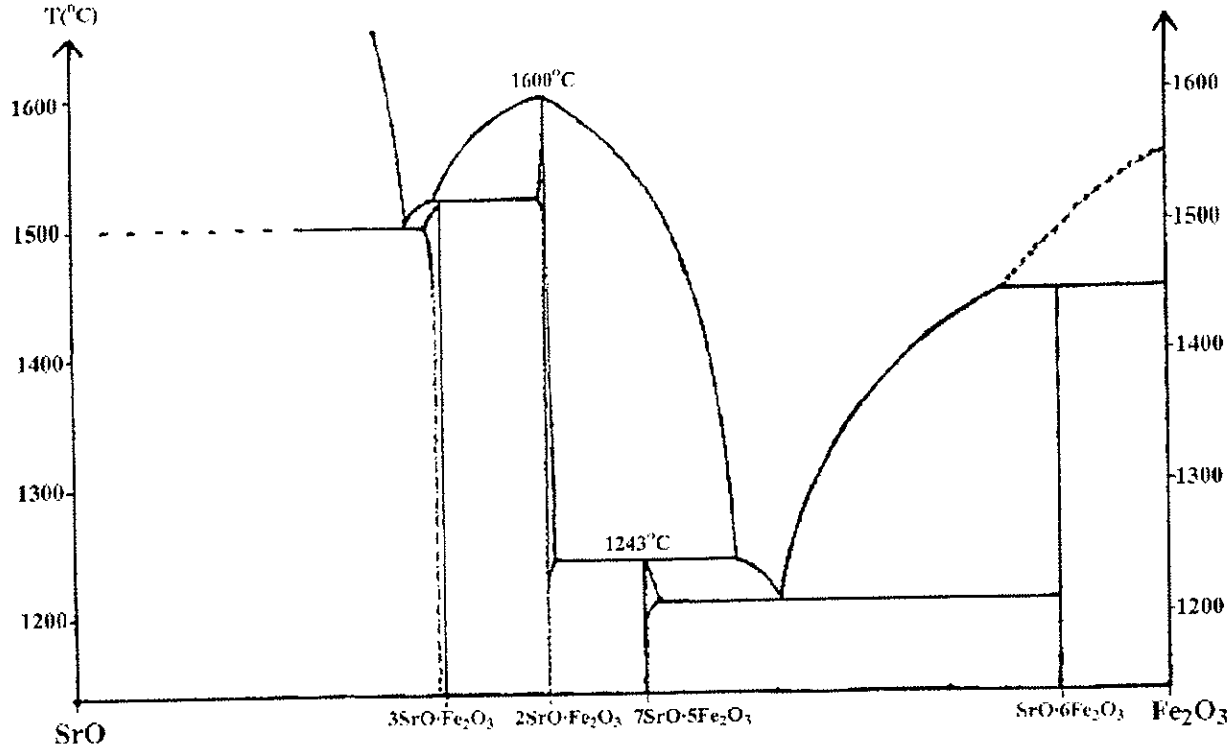

Figure A16.1 The phase diagram of the system $SrO\text{-}Fe_2O_3$ as a function of temperature (Batti, 1962).

Later on, Kanamaru et al. (1972) have shown that the reported phase, $7SrO\cdot 5Fe_2O_3$ was actually $Sr_4Fe_6O_{13+\delta}$ with a small amount of SrO.